Order and disorder in the charge and spin structures of $YFe_2O_{4-\delta}$ and $Ni_{0.42}Mn_{0.58}TiO_3$

Von der Fakultät für Mathematik, Informatik und Naturwissenschaften der RWTH Aachen University zur Erlangung des akademischen Grades eines Doktors der Naturwissenschaften genehmigte Dissertation

vorgelegt von

Diplom-Physiker

Thomas Müller

aus Mechernich, Deutschland

Berichter: Juniorprofessor Dr. Manuel Angst
Universitätsprofessor Dr. Uwe Klemradt

Tag der mündlichen Prüfung: 09. Feburar 2018

Abstract

$YFe_2O_{4-\delta}$

The main part of this thesis is dedicated to the determination of the charge order crystallographic structures of $YFe_2O_{4-\delta}$ at 160 K and 200 K. $YFe_2O_{4-\delta}$ is above the charge ordering transition isostructural to $LuFe_2O_{4-\delta}$ with the space group $R\bar{3}m$. The structure is characterized by an alternating stacking of triangular Yttrium layers and Fe bilayers each triangular, with a mean iron valence of 2.5. The arrangement of the Fe^{2+} and Fe^{3+} ions on the triangular lattice leads to frustration which is resolved at lower temperates through charge order. $LuFe_2O_{4-\delta}$ was long time the primary example for a charge order driven ferroelectric material but was found to be not ferroelectric. The isostructural $YbFe_2O_{4-\delta}$ is indicated to show ferroelectricity by one recent report, although much weaker than predicted for $LuFe_2O_{4-\delta}$. In the series of the $RFe_2O_{4-\delta}$ ferrites $YFe_2O_{4-\delta}$ is of special interest because it is the upper end member in regard of the ionic radius of the rare earth ion, which determines the intra and inter Fe bilayer spacing and therefore interaction strengths and ultimately the charge order.

The charge order of $YFe_2O_{4-\delta}$ at 160 K is described by a propagation vector of $\left(\frac{1}{4}\frac{1}{4}\frac{3}{4}\right)$ with a symmetry reduction from $R\bar{3}m$ to $P\bar{1}$. The charge order is found to be bimodal in contrast to previous results. The charge order at 200 K is incomplete with a seven times enlarged supercell based on a propagation vector of $\left(\frac{2}{7}\frac{2}{7}\frac{3}{7}\right)$ again with spacegroup $P\bar{1}$ in contrast to a previously suggested monoclinic cell.

Based on this charge ordered cell possible magnetic structures are evaluated using single crystal neutron diffraction. In contrast to the observation of well separated phases in X-ray diffraction, in neutron diffraction at 200 K and 160 K a superposition of the two CO-phases is observed, although the phases observed in X-ray diffraction are dominant. This is most likely due to the larger sample volume and different cooling times. The magnetic cell based on the 200 K charge-order structure is characterized by a propagation vector of $\left(\frac{5}{14}\frac{5}{14}\frac{18}{14}\right)_{\text{hex}}$. The magnetic cell based on the 160 K charge order cell is based on a propagation vector of $\left(0\frac{1}{2}\frac{1}{2}\right)_{\text{CO}}$. Both cells have the magnetic spacegroup $P_s\bar{1}$. The magnetic phases show no metamagnetic transitions up to 24 T in contrast to $LuFe_2O_{4-\delta}$.

$Ni_{0.42}Mn_{0.58}TiO_3$

The smaller part of the thesis is dedicated to another mechanism of multiferroicity, a vortex like arrangement of spins having a toroidal moment breaks both space and time inversion and is intrinsically magnetoelectric. Such an toroidal moment can be induced in specific materials by the application of crossed electric and magnetic fields.

$Ni_{0.42}Mn_{0.58}TiO_3$ is of particular interest because it is so far the only material in which a toroidal moment can be induced in absence of long range magnetic order, since it is an XY-spin glass. Single crystals of $Ni_{0.42}Mn_{0.58}TiO_3$ were grown by the optical floating zone method and the the Ni/Mn-ratio was confirmed by powder and single crystal X-ray diffraction. The spin glass behavior is proved by a magnetic memory test and the observation of a frequency shift in the AC-susceptibility. A magnetoelectric effect as reported in the literature could not be reproduced after magnetoelectric field cooling. Neutron diffraction shows diffuse magnetic scattering along (00ℓ) with enhanced intensity at the positions expected for $NiTiO_3$ and $MnTiO_3$. Polarization analysis confirms the spin direction in the $\mathbf{c}_{hex}$-plane but an evaluation of the toroidal state could not be performed due to experimental problems.

Zusammenfassung

$YFe_2O_{4-\delta}$

Die Bestimmung der Ladungsordnungsstruktur von $YFe_2O_{4-\delta}$ bei 200 und 160 K bildet den Hauptteil dieser Arbeit. Oberhalb der Ladungsordnungstemperatur ist $YFe_2O_{4-\delta}$ isostrukturell zu $LuFe_2O_{4-\delta}$, beide kristallisieren in der Raumgruppe $R\bar{3}m$.

$YFe_2O_{4-\delta}$ kann als eine Schichtstruktur beschrieben werden, in der sich Schichten von Yttrium, das in einem Dreiecksgitter angeordnet ist, abwechseln mit Doppelschichten von Eisen, welches ebenfalls innerhalb einer Schicht ein Dreiecksgitter bildet. Die Verteilung von Fe^{2+} und Fe^{3+} im Dreiecksgitter mit einer durchschnittliche Eisenvalenz von 2.5 führt zu Frustration, welche bei tiefen Temperaturen durch Ladungsordnung aufgelöst wird.

$LuFe_2O_{4-\delta}$ war lange Zeit das primäre Beispiel für ein Ferroelektrikum, in dem die Ferroelektrizität durch Ladungsordnung erzeugt wird, später stellte sich heraus, dass es nicht ferroelektrisch ist, wohingegen $YbFe_2O_{4-\delta}$ eine schwache Ferroelektrizität zeigt, gemäß einer vor kurzem veröffentlichten Studie. $YFe_2O_{4-\delta}$ ist besonders interessant, da Yttrium die seltene Erde mit dem grössten Ionenradius in der $RFe_2O_{4-\delta}$-Familie ist. Der Ionenradius bestimmt das Verhältnis der Abstände innerhalb der Eisen-Doppelschicht und zwischen verschiedenen Doppelschichten. Jenes Verhältnis entscheidet welche Art von Ladungsordnung realisiert wird.

Die Ladungsordnung von $YFe_2O_{4-\delta}$ bei 160 K ist gekennzeichnet durch den Propagationsvektor $\left(\frac{1}{4}\frac{1}{4}\frac{3}{4}\right)$ und einer Symmetrieverringerung zur triklinen Raumgruppe $P\bar{1}$. Die von uns bestimmte Ladungsordnung weist nur zwei verschiedene Eisen-Valenzen auf.

Im Gegensatz dazu ist die Ladungsordnung bei 200 K unvollständig und besteht aus einer 7-fach vergrösserten Zelle, basierend auf dem Propagationsvektor $\left(\frac{2}{7}\frac{2}{7}\frac{3}{7}\right)$ wiederum mit der Raumgruppe $P\bar{1}$ im Gegensatz zur vorher vorgeschlagenen monoklinen Symmetrie.

Basierend auf diesen beiden Ladungsordnungen habe ich mittels Neutronenstreuung mögliche magnetische Strukturen untersucht. Im Gegensatz zu den wohl separierten Phasen, welche mittels Röntgenstreuung beobachtet werden, fand ich dabei eine Superposition der 160 K und 200 K Ladungsordnungen, wobei die jeweilige Phase, welche in der Röntgenstreuung beobachtet wurde, dominant ist. Dies ist wahrscheinlich durch das sehr viel grössere Probenvolumen und die unterschiedliche Abkühlrate bedingt.

Die magnetische Zelle bei 200 K basiert auf dem Propagationsvektor $\left(\frac{5}{14}\frac{5}{14}\frac{18}{14}\right)_{\text{hex}}$, wohingegen die magnetische Zelle bei 160 K auf dem Propagationsvektor $\left(0\frac{1}{2}\frac{1}{2}\right)_{\text{CO}}$ basiert, in der Notation der 160 K Ladungsordnungszelle. Beide Zellen haben die magnetische Raumgruppe $P_s\bar{1}$. Die magnetischen Phasen weisen in Feldern bis 24 T keine metamagnetischen Phasenübergange auf im Gegensatz zu $LuFe_2O_{4-\delta}$.

$Ni_{0.42}Mn_{0.58}TiO_3$

Der kleinere Teil der Arbeit beschäftigt sich mit einem anderen Prinzip das Multiferroizität erzeugen kann. Eine Anordnung von Spins in einem Wirbel erzeugt ein toroidales Moment, welches weder unter Paritätstransformation noch Zeitumkehr invariant und intrinsisch magnetoelektrisch ist. Solch ein toroidales Moment kann in bestimmten Materialien durch die Anwendung von gekreuzten magnetischen und elektrischen Feldern induziert werden.

$Ni_{0.42}Mn_{0.58}TiO_3$ ist interessant, weil es bist jetzt das einzige Material ist, in dem ein toroidales Moment induziert werden kann, obwohl es keine langreichweitige magnetische Ordnung aufweist, denn unterhalb von 10 K ist $Ni_{0.42}Mn_{0.58}TiO_3$ ein XY-Spin-Glas.

$Ni_{0.42}Mn_{0.58}TiO_3$ Einkristalle wurden mittels Zonenschmelzverfahren gezüchtet und das Ni/Mn-Verhältnis mittels Einkristall- und Pulverröntgendiffraktometrie bestimmt. Die Spin-Glas Eigenschaft wurde mittels eines magnetischen Memory-Test und der Frequenzverschiebung der AC-Suszeptibilität verifiziert. Ein magnetoelektrischer Effekt, wie er in der Literatur beobachtet wurde, ließ sich nach Kühlung in gekreuzten magnetischen und elektrischen Feldern nicht reproduzieren.

In Neutronendiffraktometrie zeigen sich diffuse Linien entlang (00ℓ) mit erhöhter Intensität an den Positionen, welche man für $NiTiO_3$ und $MnTiO_3$ erwartet. Durch Polarisationsanalyse wurde bestätigt, dass die magnetischen Momente in der $\mathbf{c}_{hex}$-Ebene liegen. Eine toroidale Phase konnte wegen Problemen mit dem Instrument nicht untersucht werden.

Contents

1 Introduction

Multiferroic materials showing more than one ferroic order offer a rich range for possible applications [1]. For example magnetoelectric multiferroics can be used to switch the magnetization with an electric field instead of an electric current [2]. This would be very beneficial for the miniaturization process of data storage. Unfortunately, materials being at the same time ferromagnetic and ferroelectric are rare, and materials having these properties at room temperature are even rarer. Ferroic orders are deeply connected to symmetry breaking [3]. A requirement for ferroelectricity is the breaking of spatial inversion symmetry while ferromagnetism needs the breaking of time inversion.

The reason for the small amount of magnetoelectrics lies in the conflicting mechanisms for ferroelectricity and ferromagnetism. A ferromagnet is characterized by a phase transition between a phase without magnetic order and a low temperature phase, which shows a spontaneous magnetization in the absence of a magnetic field [4]. The spontaneous magnetization is created by alignment of spins through exchange coupling, which is prevented at higher temperature due to the thermal energy. In the classical picture with localized moments as suggested by Weiss in 1907 [5] below the Curie Temperature T_c the molecular field, i.e. exchange energy, is so strong that it leads to a parallel alignment of the localized spins [6] and the thermal behavior is well described by the Curie-Weiss law $\chi = \frac{C}{T-T_c}$.

In a bandview picture, necessary to described non-localized electrons in classical ferromagnets like Fe or Ni, the energy necessary to elevate electrons from bands where all electrons are paired to non-full bands, conquers ferromagnetism [6]. In Fe the Fermi energy lies in a region where the 4s and 3d band overlap, the high density of states of the 3d band at the Fermi level lowers the band energy necessary to reverse a spin direction to a level where the gain by exchange energy is enough to polarize the band leading to a spontaneous magnetization [6]. In completely filled bands this is not possible.

A ferroelectric material on the other hand has a phase transition from a paramagnetic state to one with a spontaneous magnetization. Ferroelectrics have to be insulators, which is incompatible with metallic ferromagnets. It is further found that the occupation of the d-shells destroys the tendency for a distortion, which removes the inversion symmetry, which is the driving force in classical perovskite ferroelectrics like $BaTiO_3$ [6, 7]. This has led to a search for novel mechanism for ferroic orders.

$LuFe_2O_{4-\delta}$ was one candidate for a ferroelectric antiferromagnetic material, where the ferroelectricity was suggested to be due to charge ordering [8]. While $LuFe_2O_{4-\delta}$ was found to be not magnetoelectric [9–12], the mechanism could be applicable to other compounds. Magnetite seems to be an example where charge order creates switchable polarization states [13–16].

There exist several isostructural compounds to $LuFe_2O_{4-\delta}$ using different rare earth ions instead of Lu. And the mechanism suggested for $LuFe_2O_{4-\delta}$ could be applicable to them and it seems that the isostructural $YbFe_2O_{4-\delta}$ shows a weak ferroelectricity [17], although it is unclear if it is based on the charge order mechanism. Beside a possible application as a ferroelectric, recently the application of $LuFe_2O_{4-\delta}$ in gas sensing has been suggested, due to the strong dependence of magnetic and electrical properties in regard to the oxygen off-stoichiometry δ [18]. Considering other members of the $RFe_2O_{4-\delta}$-family Yttrium is interesting considering it has the strongest deviation of the rare earth ion size from Lu. The rare earth ion size changes the spacing between Fe-layers inside the bilayer and between different bilayers and the ratio seems to be responsible for establishing different charge orders [19]. $YFe_2O_{4-\delta}$ is after $LuFe_2O_{4-\delta}$ one of the better studied compounds, but all the studies so far were based on powders or tiny crystallites retrieved from powder. During my diploma thesis I have grown highly stoichiometric single crystals of $YFe_2O_{4-\delta}$, showing for the first time 3D-charge-ordering in X-ray diffraction and also 3D-magnetic-ordering [20]. While the samples were characterized, by macroscopic measurements, X-ray diffraction and neutron diffraction, the structure of the charge ordered phases and also the magnetic structure were not solved. The main part of this thesis, Section 4.7 and 4.8, focuses on the establishment of the complex low temperature charge order structures of $YFe_2O_{4-\delta}$.

The smaller part of this thesis is dedicated to another ferroic order and mechanism for multiferroicity. A vortex arrangement of spins obeying a toroidal moment breaks both space and time inversion and is intrinsically magnetoelectric [21]. That such an arrangement cannot only exits in magnetically order systems like $Co_3B_7O_{13}Br$ [22] or Cr_2O_3 [23], was shown by Yamaguchi *et al.* [24] who proved the existence of toroidal moments below 10 K in the spin glass $Ni_{0.42}Mn_{0.58}TiO_3$ with the room temperature space group $R\bar{3}$. $Ni_{0.42}Mn_{0.58}TiO_3$ is an XY-spin glass, where the spins lie in the $\mathbf{c}_{hex}$ plane and shows a toroidal order and a magnetoelectric effect [24]. A linear magnetoelectric effect in a spin glass is also observed in $BaCo_6Ti_6O_{19}$ although it can not be explained by toroidal moments due to the direction of the induced polarization [25]. A more detailed introduction into $Ni_{0.42}Mn_{0.58}TiO_3$ and toroidal moments is given in Chapter 3.

2

Experimental Techniques & Theory

This chapter explains the experimental methods used to synthesize and study $YFe_2O_{4-\delta}$ and $Ni_{0.42}Mn_{0.58}TiO_3$ and gives some theoretical background necessary to understand the scattering experiments.

2.1 Synthesis

2.1.1 Powder synthesis

The powders, used in this thesis mainly to obtain polycrystalline rods for single crystal growth, were all synthesized by solid state reactions between stoichiometric ratios, in regard to the metal ions, of the starting materials, which are Ye_2O_3 and Fe_2O_3 for $YFe_2O_{4-\delta}$ and NiO, MnO_2 and TiO_2 $Ni_{0.42}Mn_{0.58}TiO_3$. The starting materials were dried for several days at 120 °C to remove moisture, which would lead to false amounts while weighting in stoichiometric ratios. The stoichiometric mixture was then ball milled to reduce the grain size and obtain a homogeneous mixture of the powders. Afterwards it was calcined in a tube furnace with a flow of CO_2/CO for $YFe_2O_{4-\delta}$ and a flow of air for $Ni_{0.42}Mn_{0.58}TiO_3$. Following the calcination the powders were again ball milled to reduce the grain size before forming rods for single crystal growth, which were hydrostatically pressed at 30 MP and had a size of 8 mm diameter and typically 10 cm length. These were sintered again and then used for both feed and seed during crystal growth.

2.1.2 Single crystal growth

All single crystal growths reported in this thesis were done with the floating zone method [26, 27] in an optical four mirror furnace (Model FZ-T-10000-H-VI-VP0 Crystal Systems Corporation, Japan), which is shown in Figure 2.1b. The floating zone method was previously used for $YFe_2O_{4-\delta}$ [20, 28] and as well for the isostructural $RFe_2O_{4-\delta}$ members, most prominent $LuFe_2O_{4-\delta}$ [29–31] and $YbFe_2O_{4-\delta}$ [32–34] and also for the synthesis fo $Ni_{0.42}Mn_{0.58}TiO_3$ [35, 36]. In the furnace four halogen lamps (1000 or 1500 W) are focused by ellipsoidal mirrors to create a hot zone.

Two polycrystalline rods are arranged on top of each other as shown in Figure 2.1a inside a

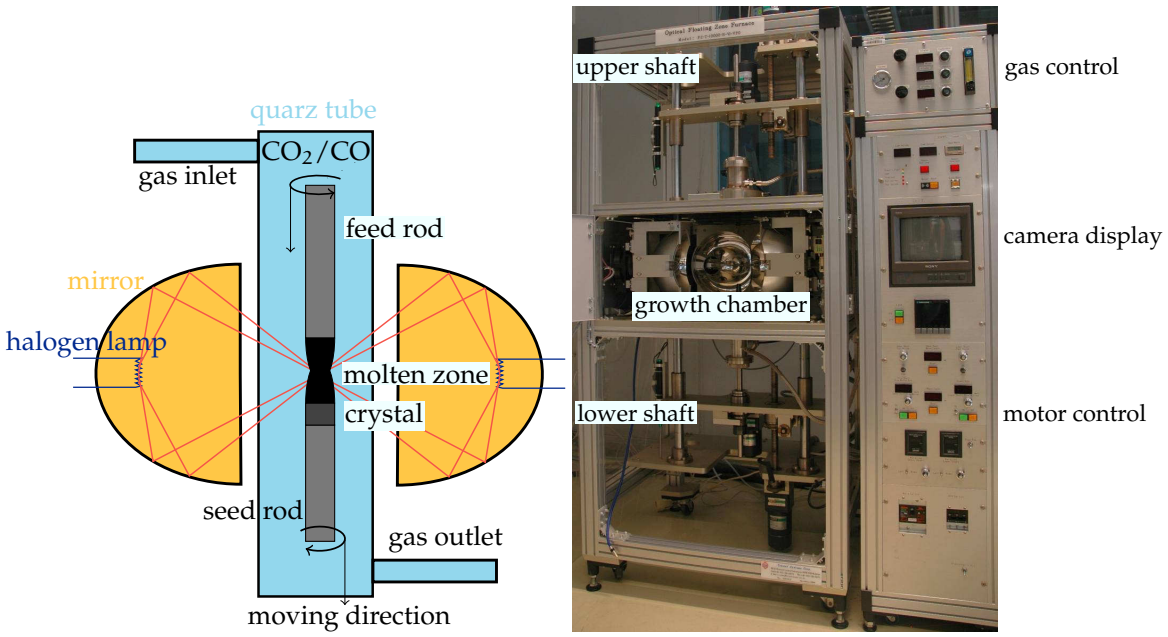

(a) shematic view (b) picture

Figure 2.1: Mirror furnace (Model FZ-T-10000-H-VI-VP0), in the schematic view only 2 lamps are shown.

quartz glass tube. The rods are moved into the hot focus of the lamps and connected through the melt. The seed and feed rod are rotating in opposite directions to mix the material, form the solidification surface and equalize the heat distribution. Afterwards both rods move vertically through the focus point, creating a floating zone of molten material. As the lower shaft, the seed, is moved out of the focus material crystallizes at the solidification surface, since it is energetically favorable for the atoms to form a crystal lattice the growth of crystallites is enhanced. Over the time larger crystallites may suppress smaller crystallites and a single crystal is obtained, this can be enhanced for example through necking, where the size of the grown part is continuously decrease until only one crystallite propagates along the growth direction, but this was not used in this thesis. The convex crystallization front also suppresses crystallites on the outside of the seed. $YFe_2O_{4-\delta}$ is reported to solidify at 1398 K[1] [37] while for $Ni_{0.42}Mn_{0.58}TiO_3$ the melting point is not reported. For the pure compounds, which were also grown for comparison, the melting points lie at 1633 K for $MnTiO_3$ [38] and at 1962 K for $NiTiO_3$ [39].

The quartz glass tube seals the growth environment and allows to apply a specific atmosphere at the molten zone, for $YFe_2O_{4-\delta}$ the growth is performed in a flow of a CO_2/CO-mixture to fine tune the oxygen stoichiometry, while the growth of $Ni_{0.42}Mn_{0.58}TiO_3$ is performed in air.

The detailed procedure for the growth of $YFe_2O_{4-\delta}$ can be found in my diploma thesis [20] and is published in [40], a quick summary is given in Section 4.2, while the procedure for $Ni_{0.42}Mn_{0.58}TiO_3$ is given in Section 3.2.

[1] This is not the melting point since, there exist a thermal hysteresis between melting and solidification.

2.2 Macroscopic methods

2.2.1 DC Magnetometry

The Magnetization measurements presented in this thesis were either performed with the Vibrating sample Magnetometer (VSM) option of a Quantum Design PPMS [41] or the Reciprocating Sample Option (RSO) of a Quantum Design MPMS [42]. Both options are based on the induction a magnetic sample creates following Faradys law [43] if it is moved in a static magnetic field. In contrast to the PPMS, in the MPMS the induced current is transfered through superconducting wires to coils to create a magnetic field whose flux is detected by a superconducting quantum interference device (rf-SQUID), the details can be found in [44].

2.2.2 AC Magnetometry

The PPMS AC Susceptibility option is used to test whether the magnetization of the sample shows a time dependent response to magnetic fields, as for example the frequency dependent freezing temperature in spin glasses [45]. It allows to apply an oscillating magnetic field of up to 10 Oe with a frequency between 10 Hz and 10 kHz. The measurements yield an in-phase real part susceptibility χ' and an out of phase susceptibility χ''. A short introduction to AC magnetization measurements can be found in [46].

2.2.3 DC Magnetometry in electric fields

Measurements with applied electric field were performed using the DC option of the MPMS where the sample does not vibrate in the magnetic field but is moved in discrete steps. For measurements with AC electric field Liming Wang and Markus Schmitz [47] modified the MPMS ACMS option. They disconnected the AC excitation coils and connected their power supply to an amplifier, which could output a Voltage up to 200 V, which is applied to the sample and can be controlled by the normal ACMS measurements commands, details can be found in [47]. To apply a DC electric field to the sample I have written a Delphi program for the External Device Control Option of the MPMS, which gives out a constant current on the AC coil connections to the amplifier, which produces a voltage that can be set with the normal MultiVu programming interface of the MPMS. The voltage is applied to the sample trough silver paste contacts on opposing surfaces.

2.3 Scattering Theory and Experiments

Scattering is an unique tool to explore the microscopic properties of materials. In this thesis single crystal X-ray diffraction is used to determine the crystallographic structures of $YFe_2O_{4-\delta}$ and $Ni_{0.42}Mn_{0.58}TiO_3$. Neutron diffraction is used to explore the spin structures of $YFe_2O_{4-\delta}$. Inelastic scattering is not relevant for the experiments in this thesis and will not be discussed.

2.3.1 General scattering Theory

To understand the basic principles of the scattering experiments in the later part of this thesis, a recapitulation of the theory behind an elastic scattering process of a neutron is given in this section. This approach is not valid for X-ray scattering, since the particle number is not conserved, but the received results also apply to X-ray scattering. The general Schrödinger equation is:

$$i\hbar\frac{\partial}{\partial t}\Psi(\mathbf{x},t) = \mathbf{H}\Psi(\mathbf{x},t) \tag{2.1}$$

where $\Psi(\mathbf{x},t)$ is the probability density amplitude of the neutron presence and $\mathbf{H}$ the Hamilton operator:

$$\mathbf{H}(\mathbf{x},t) = -\frac{\hbar^2}{2m}\Delta + V(\mathbf{x},t) \tag{2.2}$$

for a time independent potential $V(\mathbf{x},t) = V(\mathbf{x})$ there exist separated solutions with

$$\Psi(\mathbf{x},t) = \phi(\mathbf{x})\Omega(t) \tag{2.3}$$

$$\Psi(\mathbf{x},t) = \phi(\mathbf{x})\exp\left(-\frac{i}{\hbar}Et\right) \tag{2.4}$$

we get the Schrödinger equation for a time independent potential:

$$E\Psi(\mathbf{x}) = \left[-\frac{\hbar^2}{2m}\Delta + V(\mathbf{x})\right]\Psi(\mathbf{x}) \tag{2.5}$$

or with $E = \frac{\hbar^2\mathbf{k}^2}{2m}$ and $\mathbf{k}$ the wave vector in vacuum

$$\left(\Delta + \mathbf{k}^2\right)\Psi(\mathbf{x}) = \frac{2m}{\hbar^2}V(\mathbf{x})\Psi(\mathbf{x}) \tag{2.6}$$

if we assume there exists a function, the Green's function, solving:

$$(\Delta + \mathbf{k}^2)G(\mathbf{x},\mathbf{x}') = \delta(\mathbf{x}-\mathbf{x}') \tag{2.7}$$

then a formal Solution of Eqn. (2.6) is

$$\Psi(\mathbf{x}) = \Psi_0(\mathbf{x}) + \frac{2m}{\hbar^2}\int d^3x' G(\mathbf{x},\mathbf{x}')V(\mathbf{x}')\Psi(\mathbf{x}') \tag{2.8}$$

with $\Psi_0(\mathbf{x})$ a solution of the homogeneous equation:

$$(\Delta + \mathbf{k}^2)\Psi_0(\mathbf{x}) = 0 \tag{2.9}$$

This is nothing but the incident plane wave

$$\Psi_0(\mathbf{x}) = \varphi_0\exp(i\mathbf{k}\mathbf{x}) \tag{2.10}$$

It can be shown [48] that

$$G_\pm(\mathbf{x}-\mathbf{x}') = \frac{1}{4\pi}\frac{\exp(\pm ik|\mathbf{x}-\mathbf{x}'|)}{|\mathbf{x}-\mathbf{x}'|} \tag{2.11}$$

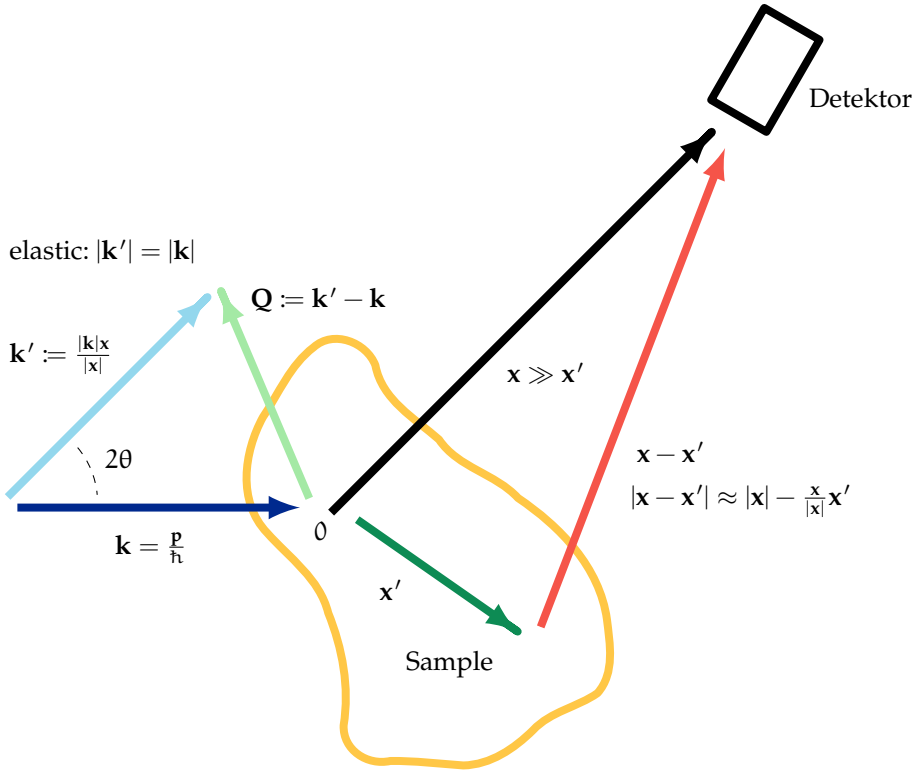

Figure 2.2: Sketch of the different vectors and relations used for the Born and Fraunhofer Approximation.

fulfills Eqn. (2.7). The general solution is a linear combination of G_+ and G_-, corresponding to outgoing and incoming spherical waves.

If we consider a weak potential as perturbation of the force-free case Eqn. (2.8) can be solved iteratively [49]. First we rename $\mathbf{x}$ in $\mathbf{x}'$ in Eqn. (2.8) and restrict ourself to the case of an outgoing wave G_+.

$$\Psi(\mathbf{x}') = \exp(i\mathbf{k}\mathbf{x}') + \frac{2m}{\hbar^2}\int d^3x'' G_+(\mathbf{x}' - \mathbf{x}'')V(\mathbf{x}'')\Psi(\mathbf{x}'') \tag{2.12}$$

we now insert this in Eqn.(2.8)

$$\begin{aligned}\Psi(\mathbf{x}) = e^{i\mathbf{k}\mathbf{x}} + \frac{2m}{\hbar^2}\int d^3x' G_+(\mathbf{x} - \mathbf{x}')V(\mathbf{x}')e^{i\mathbf{k}\mathbf{x}'} \\ + \int d^3x' \int d^3x'' G_+(\mathbf{x} - \mathbf{x}')V(\mathbf{x}')G_+(\mathbf{x}' - \mathbf{x}'')V(\mathbf{x}'')\Psi(\mathbf{x}'')\end{aligned} \tag{2.13}$$

or in a symbolic form, including higher orders of (n-fold) multiple scattering:

$$\Psi = \Psi_0 + GV\Psi_0 + GVGV\Psi_0 + GVGVGV\Psi_0 + \ldots = \sum_{n=0}^{\infty}(GV)^n\Psi_0 \tag{2.14}$$

All new terms will consist of increasing powers of the scattering potential V and can be interpreted as multiple scattering at the same potential.

In the first Born Approximation, which is the kinematical scattering theory, the series is stopped after the first substitution, i.e. multiple scattering is neglected.

$$\Psi_1(\mathbf{x}') = e^{i\mathbf{k}\mathbf{x}} + \frac{2m}{\hbar^2}\int d^3x'\, G_+(\mathbf{x}-\mathbf{x}')V(\mathbf{x}')e^{i\mathbf{k}\mathbf{x}'} \tag{2.15}$$

with an elastic scattering potential $|\mathbf{k}'| = |\mathbf{k}|$ and with finite range $\lim_{r\to\infty} |\mathbf{x}| \cdot V(|\mathbf{x}|) = 0$, with the wavevector of the scattered wave $\mathbf{k}' \coloneqq \frac{k\mathbf{x}}{|\mathbf{x}|}$ and the scattering vector (the momentum transfer) $\mathbf{Q} \coloneqq \mathbf{k}' - \mathbf{k}$ (see Fig. 2.2). If x is much larger than x', i.e. if the detector is far away from a small sample, we can replace $|\mathbf{x}-\mathbf{x}'| \approx |\mathbf{x}| - \frac{\mathbf{x}}{|\mathbf{x}|}\cdot\mathbf{x}'$ leading to the Lippmann-Schwinger-equation,

$$\Psi_1(\mathbf{x}) = e^{i\mathbf{k}\mathbf{x}} + \frac{e^{ikx}}{|\mathbf{x}|}\underbrace{\frac{2m}{4\pi\hbar^2}\int d^3x'\, V(\mathbf{x}')e^{-i\mathbf{Q}\mathbf{x}'}}_{F(\mathbf{Q})} \tag{2.16}$$

which describes the scattered beam as a stationary spherical wave. The scattering amplitude $F(\mathbf{Q})$ is therefore in the first Born approximation the Fourier transformation of the potential in regard to the momentum transfer.

$$F(\mathbf{Q}) = \frac{2m}{4\pi\hbar^2}\int d^3x'\, V(\mathbf{x}')e^{-i\mathbf{Q}\mathbf{x}'} \tag{2.17}$$

And the differential elastic scattering cross section per solid angle element is the square of the absolute value of the scattering amplitude [50]:

$$\frac{d\sigma(\mathbf{Q})}{d\Omega} = |F(\mathbf{Q})|^2 \tag{2.18}$$

The kinematic scattering theory has several shortcomings, which are treated in the dynamical scattering theory, a nice review can be found in [51]. Multiple scattering is intrinsically neglected, which is less of a problem for imperfect crystals with higher mosaicity and small samples. Extinction, the weakening of the incident beam by diffraction is also not considered but can be attributed empirically, it is also small for smaller crystals and in our X-ray experiments the extinction corrections has only a marginal influence. For neutron diffraction extinction is more important since the crystal has a larger volume and the wavelength, as well as the bandwidth is larger, which lowers the sensitivity for crystals imperfections. This also makes multiple scattering more likely but the effect is strongly reduced by the small scattering cross sections for neutrons.

Back to the kinematical theory, we now follow [52] and consider a crystalline system with a periodic arrangement of unit cells, which have the scattering density $\rho_u(\mathbf{r})$ and are connected by direct lattice vectors $\mathbf{R} = u\mathbf{a} + v\mathbf{b} + w\mathbf{c}$, where u, v, w are restricted to integer values.

The total scattering density ρ_t is the sum of $\rho_u(\mathbf{r})$ over all unit cells:

$$\rho_t(\mathbf{r}) = \sum_{uvw} \rho_u(\mathbf{r} - \mathbf{R}_{uvw}) \tag{2.19}$$

$$= \sum_{uvw} \int \rho_u(\mathbf{r}') \cdot \delta(\mathbf{r} - \mathbf{R}_{uvw} - \mathbf{r}')\, d^3r' \tag{2.20}$$

$$= \int \rho_u(\mathbf{r}') \cdot \sum_{uvw} \delta(\mathbf{r} - \mathbf{R}_{uvw} - \mathbf{r}')\, d^3r' \tag{2.21}$$

$$= \underbrace{\rho_u}_{\text{basis}} \otimes \underbrace{\sum_{uvw} \delta(\mathbf{r} - \mathbf{R}_{uvw})}_{\text{lattice}} \qquad \text{where } \otimes \text{ denotes convolution.} \tag{2.22}$$

The scattering amplitude in the first Born approximation is the Fourier transform of the scattering density:

$$F(\mathbf{Q}) = \int \rho_t(\mathbf{r}) e^{i\mathbf{Q}\mathbf{r}}\, d^3r = \mathcal{F}\left[\rho_u \otimes \sum_{uvw} \delta(\mathbf{r} - \mathbf{R}_{uvw})\right](\mathbf{Q}) \tag{2.23}$$

which can be rewritten using the convolution theorem to

$$F(\mathbf{Q}) = \underbrace{\mathcal{F}[\rho_u](\mathbf{Q})}_{\text{structure factor } F_{hk\ell}} \cdot \underbrace{\mathcal{F}\left[\sum_{uvw} \delta(\mathbf{r} - \mathbf{R}_{uvw})\right](\mathbf{Q})}_{\sum_{hk\ell} \delta(\mathbf{Q} - \mathbf{G}_{hk\ell})} \tag{2.24}$$

consisting of the Fourier transform of the scattering density of the unit cell, which is the structure factor and the Fourier transform of the direct lattice, which is the reciprocal lattice which corresponds to the Bragg condition.

For a cell with discrete atomic positions the structure factor is:

$$F_{hk\ell} = \sum_j f_j(\mathbf{Q}_{hk\ell}) \exp\left(i\mathbf{Q}_{hk\ell} \cdot \mathbf{r}_j\right) \tag{2.25}$$

with f_j the atomic form factor and $\mathbf{r}_j$ the position of the j-th atom in the unit cell. Since the neutron scatters on the point like core and not the electron cloud, the form factor for neutrons is a constant and not Q dependent. The atomic form factor for X-rays is the Fourier transform of the charge distribution of a single atom:

$$f(\mathbf{Q}) = \int_{\text{atom}} d^3r\, \rho(\mathbf{r}) \exp\left(i\mathbf{Q} \cdot \mathbf{r}\right) \tag{2.26}$$

This derivation is only valid for static electron densities. In reality the atoms in a crystal move due to their thermal energy.

Again following [52] the structure factor $F_{hk\ell}$ for a time dependent electron density is following Eqn. (2.25):

$$F_{hk\ell} = \sum_j \mathcal{F}(\underbrace{\langle \rho^{\text{atom}}(\mathbf{r}) \rangle_{\text{time}}}_{\rho^{\text{atom}}(\mathbf{r}) \otimes R(\mathbf{r})}) \cdot \exp\left(i\mathbf{Q}\langle \mathbf{r}_j \rangle\right) \tag{2.27}$$

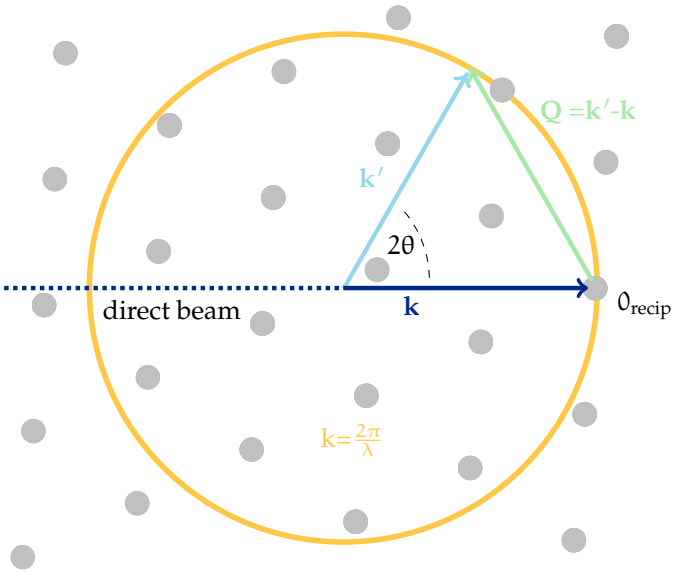

Figure 2.3: Ewald construction

where $\langle\rangle$ stands for the thermal average and $T(\mathbf{r})$ desribes the temperature smearing. With the convolution theorem this gives

$$F_{hk\ell} = \sum_j \mathcal{F}\left(\rho^{atom}(\mathbf{r})\right) \cdot \underbrace{\mathcal{F}\left(\langle T(\mathbf{r})\rangle\right)}_{\text{Debye-Waller factor}} \cdot \exp\left(i\mathbf{Q}\langle \mathbf{r}_j\rangle\right) \tag{2.28}$$

If the motion is desribed as $\mathbf{r}_j(t) = \langle \mathbf{r}_j\rangle + \mathbf{u}_j(t)$, the Debye-Waller factor can after Taylor expansion of the exponential function be expressed as

$$\mathcal{F}\left(\langle T(\mathbf{r})\rangle\right) = \exp\left(-\frac{1}{2}\langle(\mathbf{Q}\cdot\mathbf{u}_j)^2\rangle\right) \tag{2.29}$$

where $\mathbf{u}_j(t)$ describes the thermal displacement. The Debye-Waller factor therefore describes the decrease of the measured intensity with increasing atom movement along $\mathbf{Q}$ with increased temperature and also a decrease of the intensity with increasing amplitude of the scattering vector $\mathbf{Q}$.

This derivation of Eqn. (2.17) and Eqn. (2.18) has several shortcomings. First of all it is only valid for scattering probes with a rest mass such as neutrons or electrons, so it excludes X-rays. The latter scattering probe has to be described as a quantized field. Even in a semiclassical description where the atom is described in the first quantization, through conventional space and momentum operators the deviation of the scattering cross section requires second order time dependent perturbation theory. Since the quantum field theory approach leads to the same result in the first Born approximation, the deviation is omitted here, it can be found in [53, 54].

The Ewald construction is a helpful sketch to understand the basic scattering conditions, see Fig. 2.3. If one draws a sphere with the radius $|\mathbf{k}| = \frac{2\pi}{\lambda}$ and the origin of the reciprocal lattice $\mathbf{0}_{recp}$ is placed at the end of $\mathbf{k}$ on the intersection of the direct beam with the sphere, the Laue condition, $\mathbf{Q} = \mathbf{G}$, with $\mathbf{G}$ a reciprocal lattice vector, is fulfilled for any reciprocal

lattice point lying on the sphere. To observe different reflections one has therefore to rotate the crystal.

Following [55] we can write a direct-lattice vector **r** and a reciprocal-lattice vector **G** as:

$$\mathbf{R} = u\mathbf{a} + v\mathbf{b} + w\mathbf{c} \tag{2.30}$$

$$\mathbf{G} = h\mathbf{a}^* + k\mathbf{b}^* + \ell\mathbf{c}^* \tag{2.31}$$

The fundamental relation between reciprocal- and direct-lattice can then be written as:

$$\mathbf{x} \cdot \mathbf{y}^* = \begin{cases} 2\pi & \text{if } \mathbf{x} = \mathbf{y} \\ 0 & \text{else} \end{cases} \qquad \text{with } \mathbf{x}, \mathbf{y} \in \{\mathbf{a}, \mathbf{b}, \mathbf{c}\} \tag{2.32}$$

Braggs law describes the dependence of the scattering angle 2θ and the spacing of lattice planes $d_{(hk\ell)} = \frac{2\pi}{|\mathbf{Q}_{(hk\ell)}|}$. From the geometry in Fig. 2.3, with $|\mathbf{k}| = |\mathbf{k}'| = \frac{2\pi}{\lambda}$, one derives $\frac{|\mathbf{Q}|}{2} = |\mathbf{k}| \sin\theta$, which finally leads to:

$$n\lambda = 2d_{(hk\ell)} \sin\theta \qquad \text{with the wavelength } \lambda \text{ and } n \in \mathbb{Z} \tag{2.33}$$

For the hexagonal lattice the relation between $d_{(hk\ell)}$, the Miller indices h, k, l and the lattice parameters a, b, c is:

$$\frac{1}{d^2_{(hk\ell)}} = \frac{4}{3}\frac{h^2 + hk + k^2}{a^2} + \frac{\ell^2}{c^2} \tag{2.34}$$

2.3.2 Laue X-ray Diffraction

In contrast to monochromatic single crystal X-ray diffraction in Laue X-ray diffraction a spectrum of different wavelengths is used. Figure 2.4 shows on the right side the Ewald construction for this case, it is obvious that the Laue condition is fulfilled simultaneously for a lot of reflections. The Laue symmetry of the Laue pattern is characteristic for the symmetry of the chosen reflection plane, this can be used to orient single crystals and to check crystals for second grains. The left part of the Figure 2.4 shows a schematic of the back-reflection Laue pattern with the $\mathbf{c}_{\text{hex}}$ axis of $YFe_2O_{4-\delta}$ aligned along the beam path, which has a threefold symmetry. The image was measured on a MWL120 real time Laue system from Multiwire Laboratories Ltd., which has a 30x30 cm proportional wire chamber area detector. The X-ray generator uses a tungsten target and the inset of Figure 2.4 shows the Bremsstrahlungs spectrum for different electron Energies on this target assuming a flight path of 20 cm and ignoring the tails from the $L_{\alpha_{1/2}}$ emission lines above 8.5 keV. A camera system in combination with a mirror attached to the collimator allows to capture images of the sample and align the sample in the X-ray beam. A three axis goniometer offers the possibility to orient the sample under live feedback from the continuously updated Laue image. The Laue system was used to prealign the $YFe_2O_{4-\delta}$ single crystals for neutron diffraction experiments and especially for the experiment in a 30 T magnet where alignment of the sample was critical due to the small magnet opening (cf. Section 2.5).

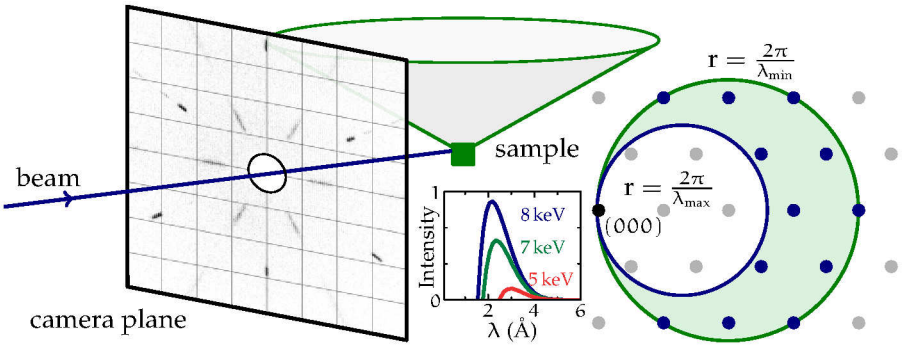

Figure 2.4: The left part of the image shows a sketch of the back reflection Laue diffraction geometry. The inset in the middle shows the the Bremsstrahlungs spectrum and the right part shows the Ewald construction for a white beam.

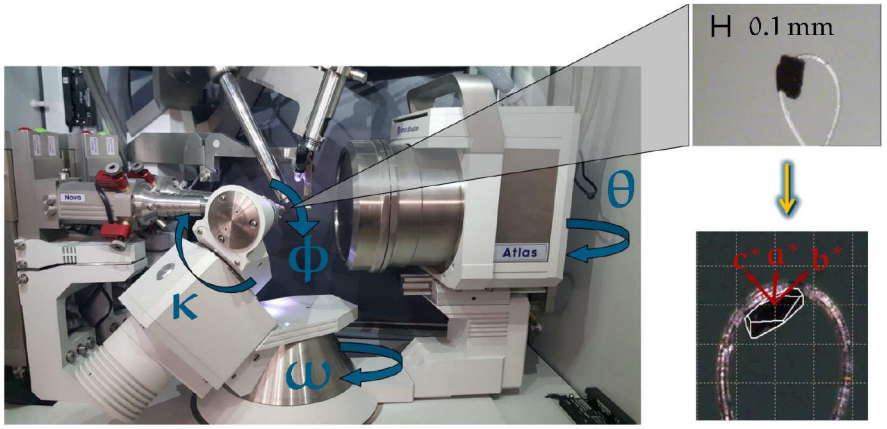

Figure 2.5: SuperNova four-circle κ diffractometer and the camera view of a single crystal with indexed facets for absorption correction.

2.3.3 SuperNova Diffractometer

Monochromatic single crystal X-ray diffraction was used to determine the charge order structure of $YFe_2O_{4-\delta}$. The inhouse single crystal X-ray diffraction experiments were performed on a Rigaku SuperNova 4-circle-Kappa-diffractometer, with a CCD area detector (Figure 2.5). The area detector allows the economic collection of a full set of unique reflections. To improve the data quality and absorption correction additional symmetry equivalent reflections were collected. An Oxford instruments liquid nitrogen Cryojet was used to control the temperature between 90 and 400 K. With the use of liquid He and an Oxford instruments Helijet temperatures down to 10 K can be reached. As wavelengths either Cu K_α (1.5418 Å) or Mo K_α (0.7107 Å) were used, the latter avoids the strong Fe fluorescence. The CrysAlis^{Pro} software package [56] was used for indexing, integration and analytical and empirical absorption correction.

2.3.4 Structure solution and refinement

In a scattering experiment only the intensity is measured and the phase information is lost, which is the crystallographic phase problem [57]. There exist several methods to overcome this, for example classical direct methods [58] as used in SIR92 [59] or charge flipping [60–62]. The latter is used in this thesis by use of the program Superflip [63]. The basic idea is that one knows that the real electron density is nowhere negative. So one starts with random phases fulfilling Friedel's law, then calculates the electron density by inverse Fourier transformation [60]. Wherever the density is negative, the sign will be flipped to positive, therefore the name chargeflipping [60]. In the Fourier transform of the new electron density the absolute values of structure factors observed in the experiment, are replaced with their measured values [60]. Based on this a new electron density is calculated and the cycle starts again [60]. Then atom positions are identified by their corresponding electron density, from which also the isotropic thermal displacement is estimated.

JANA2006 was used for merging reflections and structural refinement [64]. The refinement can either be based on the structure factors F_{obs} and F_{calc} or the square of the structure factors. For a refinement based on F the minimized function in Jana2006, as defined in [65], is:

$$P = \sum \omega(|F_{calc}| - |F_{obs}|)^2 \qquad \text{with the weighting factor} \qquad \omega_{(hk\ell)} = \frac{1}{\sigma(|F_{obs}|) + (uF_{obs})^2} \tag{2.35}$$

where u is an instability factor and is chosen to be 0.01 in all refinements in this thesis.

For a refinement based on F^2 the minimized function is:

$$P_2 = \sum \omega'(F^2_{calc} - F^2_{obs})^2 \qquad \text{with weights} \qquad \omega' = \frac{\omega}{4F^2_{obs}} = \frac{1}{4F^2_{obs} \cdot (\sigma(|F_{obs}|) + (uF_{obs})^2)} \tag{2.36}$$

Crystallographic R-values are useful to judge the quality of refined structures.

The experimental R-values which are received before refinement directly from the experimental intensities, give a first impression of the quality of a measured dataset, and validity of the chosen spacegroup. The two used values are R_σ which is based on the standard deviation and the internal residual R_{int}, which are defined as

$$R_\sigma = \frac{\sum_i \sigma(F_i)}{\sum F_i} \qquad \text{and} \qquad R_{int} = \sum_i \sum_j \frac{F^2_j - \langle F^2_i \rangle}{\langle F^2_i \rangle} \tag{2.37}$$

where i is running over all independent reflections and j over all equivalent reflections and for a specific i and $\langle F^2_i \rangle = \sum_{j=1..n} \frac{F^2_j}{n}$.

To judge the quality of the refinement, several different residuals R are in use and one has to distinguish between R factors of refinements based on F or F^2. The factor R1 gives the normed difference between observed and calculated structure factors. The R1-values for an entirely wrong structure based on a set of random intensities would be 0.83 for a cen-

trosymmetric and 0.59 for a non-centrosymmetric structure [66]. The factor based on squared structure factors is R2 and we follow the definition in [67]:

$$R1 = \frac{\sum_j ||F_{obs}| - |F_{calc}||}{\sum_j |F_{obs}|} \qquad R_2 = \frac{\sum_j |F^2_{obs} - |F^2_{calc}|}{\sum_j F^2_{obs}} \tag{2.38}$$

The weighted ωR2 value is normally two to three times higher than R1, it directly gives the weighted and normed deviation of the squared structure factors, as used in the refinement.

$$\omega R = \sqrt{\frac{\sum_j \omega(|F_{obs}| - |F_{calc}|)^2}{\sum_j \omega(F_{obs})^2}} \qquad \omega R_2 = \sqrt{\frac{\sum_j \omega(F^2_{obs} - F^2_{calc})^2}{\sum_j \omega(F^2_{obs})^2}} \tag{2.39}$$

The goodness of fit (Goof) considers also the number of used reflections n and parameters p, here $Goof_2$ is based on a refinement on F^2.

$$Goof = \sqrt{\frac{\sum_j \omega(F_{obs} - F_{calc})^2}{n - p}} \qquad Goof_2 = \sqrt{\frac{\sum_j \omega(F^2_{obs} - F^2_{calc})^2}{n - p}} \tag{2.40}$$

A refinement based on F^2 is more intrinsic since F^2 is the measured quantity. It avoids problems with reflections with near zero or negative intensity and resolves the difficulty to estimate $\sigma(F)$ from $\sigma(F^2)$ [68]. It also reduces the risk to run in local minima during the refinement [69]. In regard to the obtained standard deviations and parameters a refinement on F^2 or F will lead to the same result, if the appropriate weights are used [70]. Including the weaker reflections $F^2 < 3\sigma(F^2)$ prevents a bias in the determination of the thermal parameters and has been found to reduce the standard deviations [71, 72].

To validate anisotropic displacement parameters the Hirshfeld test can be used, which tests if the displacement parameters of two ions in a bond have similar values along the bonding direction [73].

2.3.5 Resonant Scattering

Experiments using resonant X-ray scattering will not be covered in this thesis, but results on resonant X-ray diffraction on $YFe_2O_{4-\delta}$ are discussed here shortly since the results obtained in my diploma thesis [20] are relevant for this work. The Thompson scattering approach is only valid for energies away from abortion edges, at those anomalous atomic scattering occurs which can give information about the local electronic structure [74]. It was used to probe orbital order in $LuFe_2O_{4-\delta}$ [9, 75, 76] where no anisotropy in dependence of polarization or azimuthal angle was found in the resonant scattering, which was attributed to an orbital glass state [76, 77]. For the high temperature phase of $LuFe_2O_{4-\delta}$ orbital order was excluded by XMCD measurements due to the presence of an orbital moment [9]. Theoretically orbital order is expected for the $RFe_2O_{4-\delta}$ system [78, 79]. For $YFe_2O_{4-\delta}$ a small anisotropy is observed for resonances at the Fe K-edge for $(\frac{1}{2}\frac{1}{2}\frac{3}{2})$-type reflections at 120 K, an orbital contribution could not be excluded, but if it exists it will be small [20]. As for $LuFe_2O_{4-\delta}$ [75] no additional reflections, to the charge order reflections, belonging to orbital order are observed in $YFe_2O_{4-\delta}$ [20].

2.3.6 Bond Valence Sum analysis

The X-ray scattering cross sections of Fe^{2+} and Fe^{3+} cannot be directly distinguished by laboratory X-ray diffraction, since the atomic form factors of Fe^{2+} and Fe^{3+} are too similar, as can be seen in Figure 2.6a. The electrostatic force between the iron and oxygen ions depends on the oxidation state of the iron.

Fe^{2+} has one electron more than Fe^{3+} in the 3d-orbital, which leads to a larger coulomb force shrinking the Fe^{2+}-O bond distance in comparison to the Fe^{3+}-O bond. The bond valence sum analysis allows the differentiation between Fe^{2+} and Fe^{3+} through analysis of the bonding distances to the ligand atoms. The bond valence sum method is based on two principles. First the valence of the atom is the sum of the valences of its bonds and secondly both atoms contribute equally to the bond [80]. The valence of an atom can following [81, 82] be described as,

$$\text{Valence} = \sum_i \exp \frac{d_{0i} - d_i}{0.37} \tag{2.41}$$

where d_i is the experimental bond length to the neighboring ions and d_{0i} is a tabulated [83, 84] characteristic bond length between two specific ions. The tabulated bond length is determined from experimental structures, which makes the BVS method a rather empirical approach. Since d_{0i} also depends on the valence state of the ion and its environment, the method is not quite exact. And the normal approach to distinguish different Fe valences is to calculate the valence with the d_{0i} parameter for Fe^{2+} and Fe^{3+} respectively and take the one which is significantly closer to the corresponding integer valences. The sum of all valences in a given cell should be zero, which can be used as a validity test. Nevertheless this assumes full charge disproportion of the Fe, which is still under discussion [76, 85, 86].

In the literature three studies [83, 87, 88] are found with systematic determinations of the characteristic bond lengths from published crystal data for Fe^{2+} and Fe^{3+}, the values are given in Table 2.1 together with the values for Y^{3+} determined empirically [83, 84].

	$d_{0i}(Fe^{2+})$	$d_{0i}(Fe^{3+})$
[83]	1.734(3)	1.759(3)
[87]	1.713	1.751
[88]	1.700	1.765
mean	1.716(10)	1.758(4)

	$d_{0i}(Y^{3+})$
[83]	2.019(9)
[84]	2.014
[89]	2.028 [1]
mean	2.0165(20)

Table 2.1: Characteristic bond lengths d_{0i} of Fe^{2+}, Fe^{3+} and Y^{3+}.

[1] uses 0.35 instead of 0.37 in the denominator of (2.41), not part of the mean

In this thesis the BVS method is used to deduce the charge order from the refined crystal structure in the two low temperature phases of $YFe_2O_{4-\delta}$, see Section 4.7.5 and 4.8.4.

2.3.7 Nuclear neutron scattering

Neutrons carry a magnetic moment in contrast to photons and are therefore directly influenced by the magnetic moments of the sample. Therefore neutron scattering is the best method to determine the magnetic structures of $YFe_2O_{4-\delta}$. At the structural phase transitions described in Chapters 4.7 and 4.8 also a change of the magnetic structure is observed which is already expected from the magnetization curve shown in Figure 4.6. The interaction of the neutron with the core of the atom in a crystal trough the strong force leads to nuclear scattering. Since the core is more than four orders of magnitude smaller than the typical neutron wavelength (order of Å) which is from the same size as the electron cloud, the scattering source is well described as a point source. The nuclear neutron form factor is therefore a constant and does not decrease at higher $|\mathbf{Q}|$. The definition of the scattering amplitude for nuclear scattering is similar to the one in X-ray diffraction Eqn. (2.25) but instead of the atomic form factor $f_j(\mathbf{Q})$ the $\mathbf{Q}$-independent length b is used which is related to the total scattering cross section over $\sigma = 4\pi|b|^2$ (see Eqn. (2.42)). The neutron scattering lengths from different elements and isotopes vary strongly and measured values are tabulated [90].

$$F_{(h,k,\ell)} = \sum_j b_j \exp\left(i\mathbf{Q}_{hk\ell} \cdot \mathbf{r_j}\right) \tag{2.42}$$

The basis for the scattering length is the isotropic Fermi pseudo-potential:

$$V(\mathbf{r}) = \frac{2\pi\hbar^2}{m} b\delta\left(\mathbf{r} - \mathbf{r}_j\right) \tag{2.43}$$

Considering that the scattering lengths b_j for different isotopes in the crystal vary, we have to average over this random distribution of isotopes. This is also the case for a random nuclear spin distribution. The differential cross section in the first born approximation is the square of the scattering amplitude Eqn. (2.18):

$$\frac{d\sigma(\mathbf{Q})}{d\Omega} = |F(\mathbf{Q})|^2 = \left\langle \sum_i b_i \exp\left(i\mathbf{Q}\mathbf{r_i}\right) \cdot \sum_j b_j^* \exp\left(-i\mathbf{Q}\mathbf{r_j}\right) \right\rangle \tag{2.44}$$

Calculating the average leads to a coherent part which contains the phase information and therefore the information about the crystal structure and an incoherent part which originates from superimposed scattering from a single atom which does not carry a phase information and is for us only an isotropic background,

$$\frac{d\sigma(\mathbf{Q})}{d\Omega} = \underbrace{\langle b\rangle^2 \left| \sum_i \exp\left(i\mathbf{Q}\mathbf{r_i}\right) \right|^2}_{\text{coherent}} + \underbrace{N\left\langle \left(b - \langle b\rangle\right)^2 \right\rangle}_{\text{incoherent}} \tag{2.45}$$

where N is the number of atoms [50].

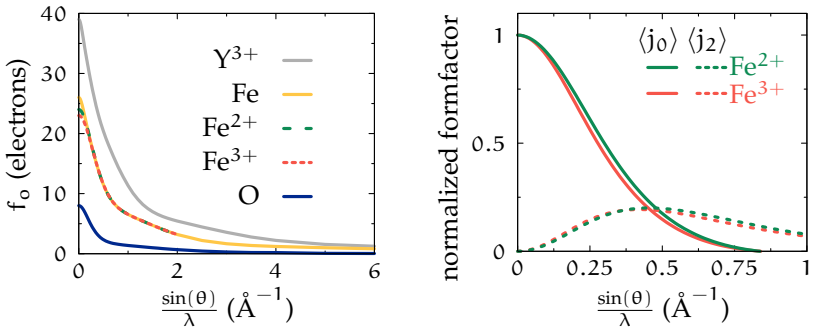

(a) X-ray form factors

(b) magnetic neutron form factors

Figure 2.6: X-ray and magnetic neutron form factors for the atoms in $YFe_2O_{4-\delta}$ (Data from [91, 92]).

2.3.8 Magnetic neutron scattering

Since the neutron carries a magnetic dipole moment $\boldsymbol{\mu}$ it interacts with external magnetic fields or the electrons in the sample via the potential:

$$V = -\boldsymbol{\mu} \cdot \mathbf{B} \tag{2.46}$$

where for the interaction of the neutron with the sample both the dipole field of the electron spin $\mathbf{B}_s = \nabla \times \frac{\boldsymbol{\mu}_e \times \mathbf{r}}{r^3}$ and the field from the orbital motion of the electron $\mathbf{B}_L = -\frac{e \cdot \mathbf{v}_e \times \mathbf{r}}{c \cdot r^3}$ have to be considered. The scattering cross section for a neutron changing the projection of the spin on the z-axis (spin quantization axis defined by a small guide field) from S_z to S_z' can be derived [50, 93, 94] as

$$\left(\frac{d\sigma}{d\Omega}\right)_{mag} = (\gamma_n r_0)^2 \left| \frac{1}{2\mu_B} \langle S_z' | \hat{\boldsymbol{\sigma}} \cdot \mathbf{M}_{\perp \mathbf{Q}} | S_z \rangle \right|^2 \tag{2.47}$$

where γ_n is the gyromagnetic ratio for the neutron, r_0 the classical electron radius and $\hat{\boldsymbol{\sigma}}$ the neutron spin operator for a definition see Appendix A.1. Here $\mathbf{M}(\mathbf{Q})$ is defined as

$$\mathbf{M}(\mathbf{Q}) = \int_{-\infty}^{\infty} \mathbf{M}(\mathbf{r}) \exp(i\mathbf{Q} \cdot \mathbf{r}) \, d\mathbf{R} \tag{2.48}$$

and only the component $\mathbf{M}_{\perp \mathbf{Q}}$ perpendicular to $\mathbf{Q}$ can be observed:

$$\mathbf{M}_{\perp \mathbf{Q}} = \hat{\mathbf{Q}} \times \mathbf{M}(\mathbf{Q}) \times \hat{\mathbf{Q}} = \mathbf{M} - (\hat{\mathbf{Q}} \cdot \mathbf{M})\hat{\mathbf{Q}} \qquad \text{with } \hat{\mathbf{Q}} = \frac{\mathbf{Q}}{|\mathbf{Q}|} \tag{2.49}$$

With factorizing the form factor over the atoms and introducing the total angular momentum $\mathbf{J} = \mathbf{L} + \mathbf{S}$ the scattering cross section can be written as

$$\left(\frac{d\sigma}{d\Omega}\right)_{mag} = (\gamma_n r_0)^2 \left| \frac{g_J}{2} f_m(\mathbf{Q}) \sum_k \langle \hat{\mathbf{J}}_{k\perp} \rangle \exp(i\mathbf{Q}\mathbf{r}) \right| \tag{2.50}$$

where g_J is the Landé g-factor $g_J = \frac{3}{2} + \frac{S(S+1)-L(L+1)}{2J(J+1)}$ [50].

In dipol approximation the magnetic form factor is given by

$$f_m(\mathbf{Q}) = \langle j_0(\mathbf{Q}) \rangle + \frac{2 - g_j}{g_j} \langle j_2(\mathbf{Q}) \rangle \tag{2.51}$$

where the spherical Bessel function j_0 describes the spin only part and j_2 the orbital contribution. The values of j_0 and j_2 have been tabulated [92] and the received normed form factors for Fe^{2+} and Fe^{3+} are plotted in Figure 2.6b.

2.3.9 The DNS instrument

DNS is a diffuse neutron scattering instrument at the FRM2 of the Heinz Maier-Leibnitz Zentrum in Garching. The only degrees of freedom are the sample rotation ω and the detector movement 2θ. It has focusing neutron guides and a pyrolytic graphite monochromator PG(002), $d = 3.355$ Å which allows a wavelength selection in the range of 2.4 to 6 Å. In our experiments the wavelength was fixed to 4.2 Å. The non-polarized flux at the sample position is up to $10^8 \frac{\text{neutrons}}{\text{cm}^2 \cdot \text{s}}$. With the use of the supermirror polarizers a polarized flux of $5 \cdot 10^6$ to 10^7 allows a $\mathbf{Q}$ up to 4.0 Å $^{-1}$. A guide field preserves the neutron polarization between the polarizing supermirror benders and the sample.

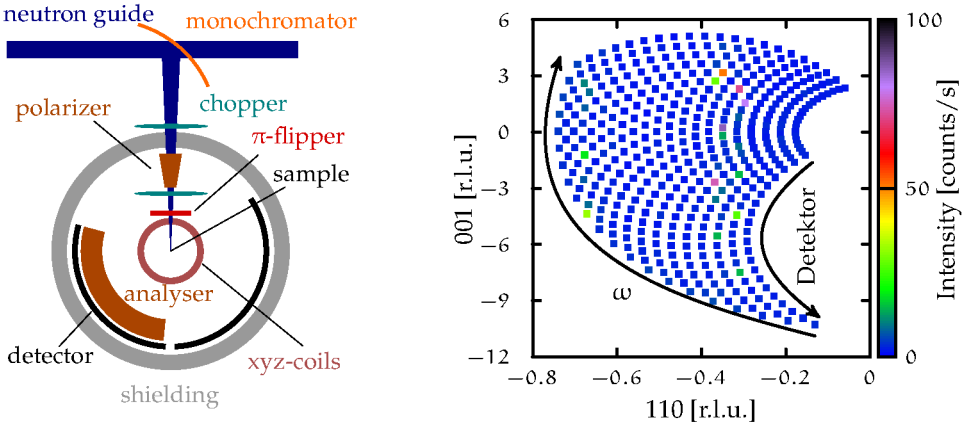

Figure 2.7: (left) Schematic view of the DNS instrument. (right) hhℓ-plane measured with a single detector bank position without interpolation and with ω-steps of 5°.

At the sample position a set of Helmholtz coils creates a small magnetic field (< 10 Oe) to turn the neutron polarization in a specified direction. A π-flipper before the Helmholtz coils is used to flip the spin of the neutrons by the application of a magnetic field perpendicular to its polarization direction over a well defined length allowing the neutron spin to perform a 180° rotation trough Lamour precession. The details about the measurements of the reciprocal hhℓ-plane of $YFe_2O_{4-\delta}$ can be found in my diploma thesis [20]. On $YFe_2O_{4-\delta}$ at DNS only the measurements of planes perpendicular to $\mathbf{c}_{hex}$ were performed during this work, see Section 4.10.1. Figure 2.7 gives an overview of the DNS instrument, the right part of the figure shows the reciprocal hhℓ-plane with large steps of the sample rotation ω and only a single detector

bank position without interpolation. The DNS instrument does not allow to efficiently collect integrated intensities from different planes, since the crystal would have to be reoriented by hand for every plane. Also through the large resolution ellipsoid axis perpendicular to the scattering plane, the exact position of the peaks is not know. Therefore we went to four-circle diffractometers to obtain the integrated intensities necessary for magnetic structural refinement. DNS was also used for neutron diffraction on $Ni_{0.42}Mn_{0.58}TiO_3$, see Section 3.6.

2.3.10 The D10 instrument

D10 was used to collect integrated intensities of the magnetic structure of $YFe_2O_{4-\delta}$ at 200 K, see Section 4.10.3. D10 is the single-crystal four-circle diffractometer at the Institute Laue-Langevin (ILL) in Grenoble, which can alternatively be used as a three-axis instrument with energy analysis As a monochromator either pyrolytic graphite or a Cu (200) crystal can be used, offering wavelengths between 1.1 and 6 Å. It offers a flux of up to $5 \cdot 10^6 \frac{\text{neutrons}}{\text{cm}^2 \cdot \text{s}}$. For fast reciprocal space mapping a 8x8 cm^2 two-dimensional microstrip detector is available which was used also to collect integrated intensities. The four circle has Euler geometry. A point ^{3}He detector with higher efficiency is available but was not used due to broad magnetic peaks which have to be separated from near charge order peaks. The general layout of the beamline is shown in Figure 2.8, where non-used detectors are omitted. Not shown is the Helium flow cryostat, which allows to control the sample temperature between 1.6 and 450 K [95]. The beam-path of the non-diffracted beam to the beamstop is also not shown.

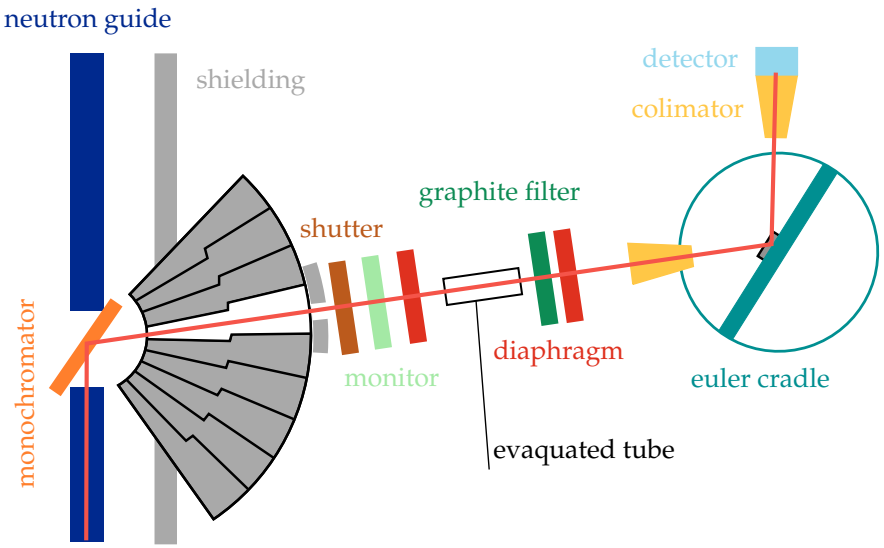

Figure 2.8: Schematic view of the D10 instrument at the Institut Laue-Langevin, reduced to the used components [96].

2.3.11 The TriCs instrument

TriCs is an instrument similar to D10, a four circle diffractometer at SINQ at the Paul-Scherrer-Institute in Villingen Switzerland. In contrast to the reactor at the ILL, SINQ is a spallation

source. The general layout can be found in [97] and differs only slightly from the D10 layout, one specialty are the detectors. TriCs has both a single tube and a 16x16 cm area detector with a radial collimator and it is possible to tilt the detectors out of the horizontal plane adding an additional degree of freedom. The tilting is not used in the four-circle mode, since one can reach every reflection with four degrees of freedom, but it is used if the four-circle cannot be used because of a mounted magnet, furnace or dilution cryostat. The instrument offers two monochromators either Germanium (311) with a wavelength of 1.18 Å or pyrolytic graphite (002) with a wavelength of 2.32 Å. The Euler four circle can be equipped with different cryostats to cover a temperature range from 5 to 800 K. The flux is up to $10^6 \frac{\text{neurons}}{\text{cm}\cdot\text{s}}$. In the meantime the instrument is now renamed to ZEBRA. It was used to collected integrated intensities of the magnetic reflections of $YFe_2O_{4-\delta}$ at 160 K, see Section 4.10.5. The TriCs area detector is larger than the D10 detector, which covers a larger portion of reciprocal space. The main disadvantage is the much lower average flux of the spallation source in comparison to the reactor at the ILL.

2.4 X-ray magnetic circular dichroism

X-ray magnetic circular dichroism (XMCD) is the difference between the scattering of left and right circularly polarized X-rays in the presence of a magnetic field, first theoretically predicted in 1965 by Bennett and Stern [98] and experimentally observed 22 years later by Schütz *et al.* [99]. The polarization vector is either parallel or antiparallel to the applied magnetic field, which breaks the time inversion symmetry, allowing dichroism. For Fe ions the effect in the soft X-ray regime is based on electric dipole transitions from 2p core states to the 3d valence states, which determine the magnetism of the so called 3d-elements in our case the iron. A small contribution of the 2p to 1s transitions is also given for L-edge transitions, but it is found to be a factor of 20 smaller than contributions from the 2p to 3d transitions [100]. XMCD is measured at element specific absorption edges and even can distinguish between different valences [101]. For 3d elements the 2p core states are split by spin orbit coupling into one state with $m_j = \frac{3}{2}$ from which transitions are responsible for the L_3-edge and one state with $m_j = \frac{1}{2}$, which corresponds to the L_2-edge. [102] Circularly left polarized light (LCP) or circularly right (RCP) polarized light carries its own angular momentum which is transfered to the photoelectron in the absorption process. For left polarized light $m_l = 1$ and for right polarized light $m_l = -1$. Through spin-orbit-coupling ($\ell + s$ at L_3 and $\ell - s$ at L_2), a part part of this angular momentum is converted to a spin moment [103], the other part is transfered as orbital moment.

The selection rules for the absorption process at the L_3 edge for the magnetization antiparallel to the photon wave vector are

$$\Delta\ell = \pm 1 \quad , \quad \Delta m_s = 0 \quad \text{and} \quad \Delta m_l = \begin{cases} 1 & \text{for RCP} \\ -1 & \text{for LCP} \end{cases} . \tag{2.52}$$

The XMCD process can be described as a two step process, first a photon excites a photoelectron from a 2p state and then this electron has to find an empty 3d valence state. The

density of states of empty 3d states both depends on the spin polarization and the orbital polarization and any imbalance in the occupation of the 3d states leads to a dichroic signal [103].

The sign of the XMCD signal is a matter of definition and as de Groot *et al.* [104] we follow the definition of Baudelet *et al.* [105]:

$$\Delta\mu(\mathbf{B}) = \mu_+(\mathbf{B}) - \mu_-(\mathbf{B}) \tag{2.53}$$

$\mu_+(\mathbf{B})$ and $\mu_-\mathbf{B})$ are the X-ray absorption spectra, for right and left polarized photons, respectively [98]. The XMCD signal $\Delta\mu$ can be measured either by switching the polarization of the incoming photon or by inversion of the magnetic field [106].

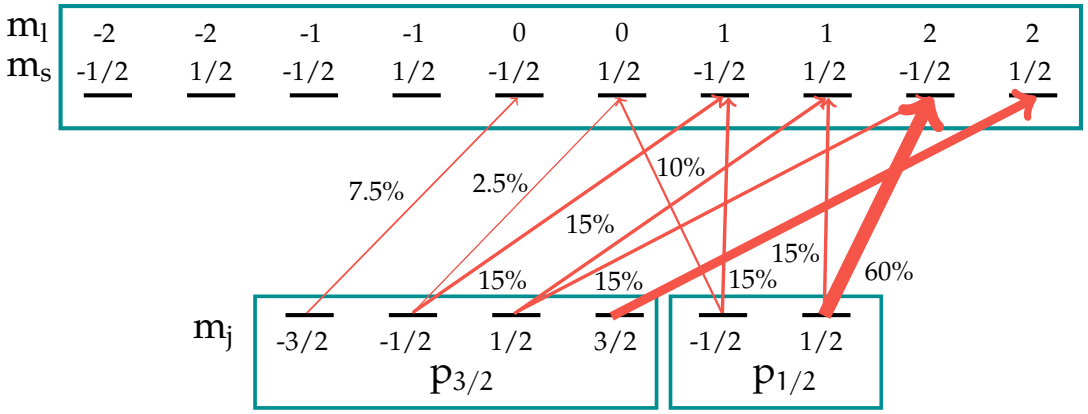

Figure 2.9: Absorption probability for the L_2 and L_3 dipol transitions for 3d elements for right-polarized light. [75, 106, 107].

Figure 2.9 shows the possible transitions for circularly right polarized light $\Delta m_l = 1$ together with the transition probabilities for both the L_3 and L_2 edges with the sample magnetized antiparallel to the photon wave vector [106]. The magnetic field does not only split the L_2 and L_3 edges, which are non-degenerate by spin orbit coupling, through the Zeeman effect [108], it also leads to a polarization of the spin states. As shown in Figure 2.10 the population of states with a spin parallel to the external field is preferred and therefore there are less free 3d states available to which a photon can be excited in comparison to an antiparallel spin polarization. The Figure 2.10 furthermore shows the transition probabilities for a right circular polarized photon for the L_2 and L_3 edge as derived from Figure 2.9. The total spin J for the $p_{3/2}$ orbital is $\ell + s$ and for the $p_{1/2}$ orbital $\ell - s$, therefore the L_2 and L_3 edge show opposite spin orbit coupling and following the transition probabilities an opposite sign of the XMCD signal between these edges is expected. So for an ideal one electron model with a spin orbit split and no orbital magnetic moment the XMCD signal at the L_2 and L_3 edge should have the same size but opposite sign, but this is rarely observed [109] and without spin orbit splitting of the L_2 and L_3 edge no XMCD signal would be observed [110]. For a left circular polarized photon the probabilities would be exchanged.

Through the application of sum rules based on the integrated XMCD signal, orbital and spin contributions to the XMCD signal can be separated. The sum rules for XMCD over the

L_3 and L_2 edges of 3d transition metal ions, originally derived by Thole *et al.* [111] and Carra *et al.* [112] confirmed by others [113, 114] can following [104, 115], under neglect of the spin quadrupole coupling, be written as:

$$m_{orb} = -\frac{4q}{3\int_{L_3+L_2}(\mu_+ + \mu_-)\,d\omega}\langle N_{3d}\rangle\,\mu_B \tag{2.54}$$

$$m_{spin} = -\frac{6p-4q}{\int_{L_3+L_2}(\mu_+ + \mu_-)\,d\omega}\langle N_{3d}\rangle\,\mu_B \tag{2.55}$$

with $\langle N_{3d}\rangle$ the number of 3d holes and:

$$p = \int_{L_3}(\mu_+ + \mu_-)\,d\omega \tag{2.56}$$

$$q = \int_{L_3+L_2}(\mu_+ + \mu_-)\,d\omega \tag{2.57}$$

By division of Eqn. (2.54) with Eqn. (2.55) one can obtain the ratio between orbital $m_{orb} = -\langle L_z\rangle\frac{\mu_B}{\hbar}$ and spin moment $m_{spin} = -2\langle S_z\rangle\frac{\mu_B}{\hbar}$:

$$\frac{m_{orb}}{m_{spin}} = \frac{2q}{9p-6q} \tag{2.58}$$

To exclude any non-field dependent part in the XMCD signal, which can be caused e.g. by sample charging or a chiral crystal structure, also the XMCD signal with negative field direction is measured, where we receive:

$$\Delta\mu(-\mathbf{B}) = \mu_-(-\mathbf{B}) - \mu_+(-\mathbf{B}) \tag{2.59}$$

The component of the XMCD signal which is induced by the magnetic field is received as,

$$2\Delta\mu = \Delta\mu(\mathbf{B}) - \Delta\mu(-\mathbf{B}) \tag{2.60}$$

while the part of the XMCD signal not influenced by the magnetic field, and which is therefore an artifact or structural, can be received as:

$$\text{art} = \Delta\mu(\mathbf{B}) + \Delta\mu(-\mathbf{B}) \tag{2.61}$$

For an ideal instrument and a centrosymmetric structure, this therm should vanish, or be at least significantly lower than the XMCD signal.

2.4.1 The 4-IDC-C beamline at APS

Our experiment at the Fe $L_{2/3}$ edge of $YFe_2O_{4-\delta}$ (see Sec. 4.4) was conducted at the soft X-ray beamline 4-ID-C at the Advanced Photon Source (APS), where also the previous experiment on $LuFe_2O_{4-\delta}$ [9, 75] was performed. Figure 2.11 gives a schematic overview of the beamline. The instrument has an undulator which allows rapid switching (0.5 Hz) between right and left circular polarized light, this allows to switch the polarization at every point of the energy scan to reduce low frequency artifacts [116]. The three mirrors in front of the spherical grating

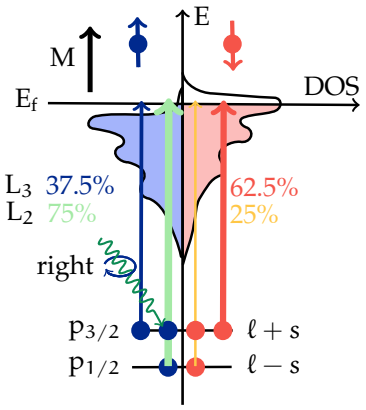

Figure 2.10: Shematic sketch showing the L_2 and L_3 edge with the absorption probabilities for right-polarized light and a photon wave vector antiparallel to the magnetic field.

monochromator and the slits in front and after the monochromator are not shown. A Kirkpatrick and Baez mirror pair [117] is used for focusing the beam. The energy can be tuned in a range of $500 - 2800\,\mathrm{eV}$ with the spherical grating monochromator, with an energy resolution of $\Delta E/E = 2 \times 10^{-4}$ and a photon flux of 1.8×10^{12} photons/second at 1350 eV. The absorption is measured either with total electron yield (TEY) or fluorescence (TFY). In TEY the current created by detached photoelectrons is measured through the electrically contacted sample, this is very surface sensitive because emitted electrons can only pass through the first 25 to 50 Å of the sample [118] and can only be used if the sample is not too isolating. TFY detects the emission by the relaxation of, through the photon beam, excited electrons. A magnetic field up to 6.5 T can be applied parallel or anti-parallel to the X-ray beam.

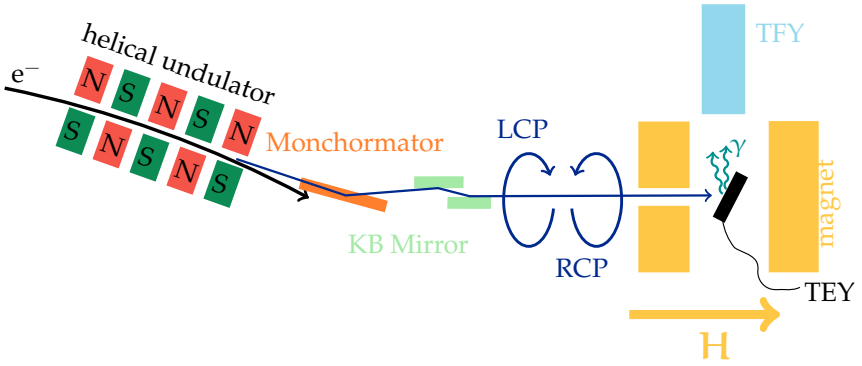

Figure 2.11: Schematic view of the 4-ID-C beamline at the Advanced Photon Source [75, 119, 120].

2.5 High magnetic field measurements

In contrast to $LuFe_2O_{4-\delta}$ the antiferromagnetic state of $YFe_2O_{4-\delta}$ cannot be switched to a ferrimagnetic state with fields up to 9 T. Non-stoichiometric $YFe_2O_{4-\delta}$ is ferrimagnetic and shows metamagnetic transitions above 16 T [121].

With a high magnetic field it should be possible to switch the antiferromagnetic state of $YFe_2O_{4-\delta}$ to a ferrimagnetic state and trough spin-charge coupling this may affect the charge ordering. In $LuFe_2O_{4-\delta}$ such a magneto structural transition is observed at 170 K [31, 122] although the metamagnetic fm-AFM transitions directly below 240 K shows no structural component [123].

To test if a magneto structural transitions exists in $YFe_2O_{4-\delta}$ we conducted an experiment at the 6-ID-C station of the Advanced Photon Source in pulsed magnetic fields up to 30 T.

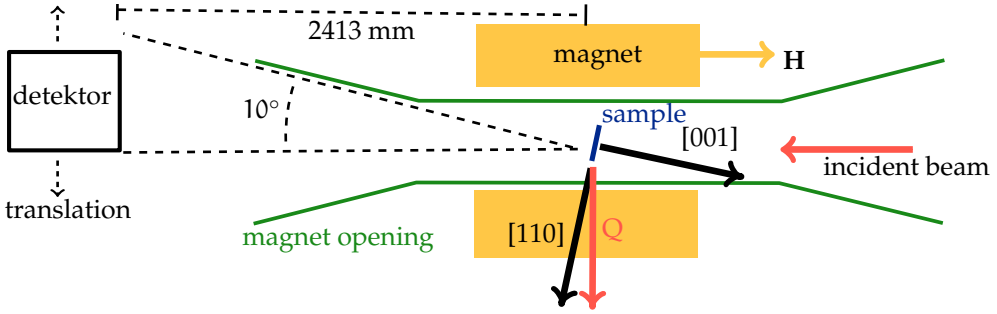

Figure 2.12: Sketch of the horizontal scattering plane at 6-ID-C (0.5° tilt is ignored for clarity).

The sample setup at 6-ID-C consists of a single large-bore solenoid cooled by a liquid nitrogen bath and a second liquid helium cryostat with a coldfinger to control the sample temperature [124]. The magnetic field lies in the horizontal scattering plane mostly parallel to the incident beam. But since the whole magnet is moved to rotate the sample, also the angle between the field and the incident beam is changed between 0 and 10°. With a discharge of the 40 kJ capacitance bank the magnet creates a 30 T pulse, with 10 ms total pulse width and a repetition time of 12 minutes [124]. The incoming and outgoing beam is restricted by the magnet opening to ±10° [125, 126]. The sample cannot be rotated independently of the magnet, the magnet rotation ω and the detector angle 2θ are the only degrees of freedom in the experiment. Either a Pilatus 100k Si or a Pixirad CdTe detector were used to detect the time resolved diffraction. The sample was prealigned using Laue X-ray diffraction. The sample was used in transmission geometry with [001] and [110] building the horizontal scattering plane. The [001]-axis was tilted 12° away from the field direction towards [110], to be able to access $(\frac{1}{2}\frac{1}{2}\frac{3}{2})$ at 160 K, taking into account the ±10° magnet opening (cf. Fig. 2.12). There was an additional 0.5° vertical offset, instead of tilting the magnet with the sample, the detector was moved accordingly. The results of the experiment can be found in Section 4.9.

3

$Ni_{0.42}Mn_{0.58}TiO_3$

3.1 Introduction

3.1.1 $Ni_{0.42}Mn_{0.58}TiO_3$ an XY-spin glass

The smaller part of this thesis is dedicated to $Ni_{0.42}Mn_{0.58}TiO_3$, which is an XY-spin glass, where the spins are restricted to the $\mathbf{c}_{hex}$ plane and obey only x and y-components and the vector spin chirality $\boldsymbol{\kappa} = \mathbf{S_1} \times \mathbf{S_2}$ [127] has only a z-component [128]. A spin glass is a random system with, in our case, competing ferromagnetic and anti-ferromagnetic interactions, which lead to a disordered spin distribution at higher temperates. Below the so called freezing temperature the system is characterized by a random, yet cooperative freezing of spins and obeys no long-range order [129]. Recently it was shown by neutron diffraction, that the correlations in $Ni_{0.42}Mn_{0.58}TiO_3$ are 2-dimensional with an intralayer correlation length of 21 Å and in-plane correlation length of 73 Å at 1.5 K [130]. By inelastic neutron scattering it was shown that the XY-spin glass state in $Ni_{0.42}Mn_{0.58}TiO_3$ obeys antiferromagnetically ordered short-range clusters with short lifetime [130]. In this XY spin glass state of $Ni_{0.42}Mn_{0.58}TiO_3$ a toroidal moment can be induced by cooling below 10 K in crossed magnetic and electric fields [24, 35]. Ferrotorodicity is a fourth ferroic order, beside ferromagnetism, Ferroelectricity and ferroelasticity, breaking both space and time reversal symmetry, as shown in Figure 3.2 [3]. Ferrotoroidic materials are intrinsically magnetoelectric [21, 131]. Both $NiTiO_3$ and $MnTiO_3$ crystallize in the $R\bar{3}$ space group, in the following in-plane is always in regard to the **c**-plane in the hexagonal representation of $R\bar{3}$. The spin glass state at low temperatures in $Ni_{0.42}Mn_{0.58}TiO_3$ is created by competing ferromagnetic Ni in-plane interactions and antiferromagnetic Mn interactions [24, 132]. Both $NiTiO_3$ and $MnTiO_3$ are antiferromagnetically ordered out of plane at sufficient low temperatures, as can be seen in the phase diagram in Figure 3.1 [24, 132]. By neutron diffraction it was shown, that for $Ni_{0.33}Mn_{0.67}TiO_3$ the spins show a deviation from the orientation along $\mathbf{c}_{hex}$, which is both field and temperature dependent (14° at 20.5 K and 80° at 4 K) [133]. The compound $Ni_xMn_{1-x}TiO_3$ changes the direction of the effective spin anisotropy from weak Ising-type to weak planar-type [134]. The phase diagram (Figure 3.1) shows that the XY-spin glass phase, with single ion easy-plane type magnetic anisotropy [134], exists only for a Nickel fraction x between and 0.4 and 0.5 and at a temperature below 10 K. $Ni_{0.42}Mn_{0.58}TiO_3$ is so far the only example of a toroidal

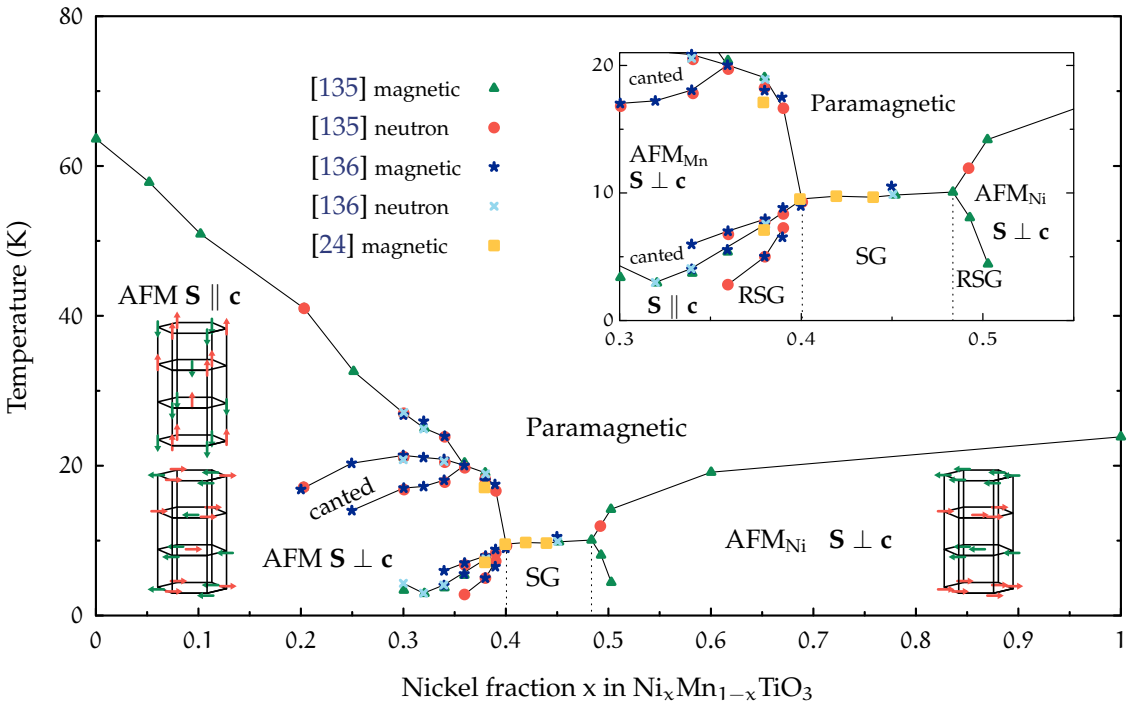

Figure 3.1: Phase diagram of $Ni_xMn_{1-x}TiO_3$ (reproduced after [24]). The data is either from magnetization measurements or neutron diffraction and is taken from [24, 135, 136]. RSG stands for reentrant spin glass, and is a mixture of the neighboring AFM-phase and the spin glass phase (SG). Spin structures reproduced from [24] based on [132]. (Reprinted with permission from Y. Yamaguchi et al., Phys. Rev. Lett. 108, 057203 (2012) Copyright (2012) by the American Physical Society [24])

spin system in a disordered state [24, 35]. To realize a toroidal state in a spin glass bot space inversion and time inversion symmetry have to be broken. A precise control of the Ni-Mn-ratio in $Ni_xMn_{1-x}TiO_3$ is essential, to reach the spin glass state.

3.1.2 A brief introduction to toroidal moments

Ferrotorodicity is a fourth ferroic order, beside ferromagnetism, ferroelectricity and ferroelasticity, breaking both space and time reversal symmetry, as shown in Figure 3.2 [3].

A toroidal moment $\mathbf{t}$ can be created by a vortex array of spins. For a discrete arrangement of magnetic moments $\mathbf{m}_\alpha$ the toroidal moment $\mathbf{t}$ is defined as:

$$\mathbf{t} = \frac{1}{2}\left\langle \sum_\alpha \mathbf{r}_\alpha \times \mathbf{m}_\alpha \right\rangle \tag{3.1}$$

where $\mathbf{m}_\alpha$ is the magnetic moment and $\mathbf{r}_\alpha$ its position vector. Analog to the magnetization, the toroidization $\mathbf{T}$, is defined as toroidal moment $\mathbf{t}$ per volume V.

$$\mathbf{T} = \frac{\mathbf{t}}{V} \tag{3.2}$$

Figure 3.3 shows four different spin systems. The antiferromagnetic spin arrangement in Figure 3.3a is the simplest example for a toroidic system with a toroidal moment $\mathbf{t} = \frac{1}{2}a s \mathbf{e}_z$

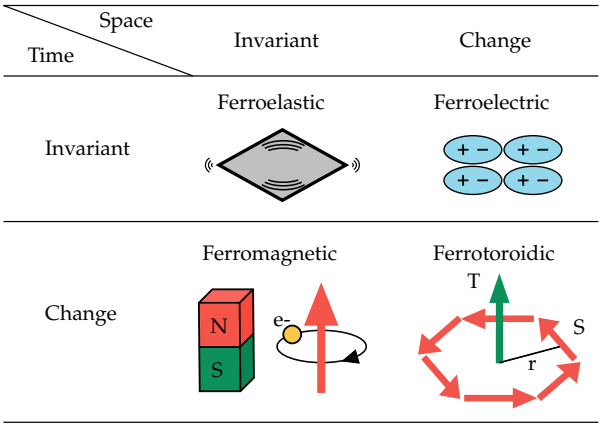

Figure 3.2: Ferroic orders and their symmetry conditions in regard of space and time. (Adapted by permission from Springer from B. Van Aken et al. "Observation of ferrotoroidic domains", Nature 449, 702 (2007) [137])

pointing out of plane, here $\mathbf{s}$ is the spin moment and $\frac{a}{2}$ is the distance of the spin from the origin. In contrast to this the antiferromagnetic spin structure in Figure 3.3b has no toroidal moment since $\mathbf{m} \parallel \mathbf{r}$. In Figure 3.3c the classical vortex like spin array is shown with a toroidal moment $\mathbf{t} = a s \mathbf{e}_z$ pointing out of the drawing plane. By space or time-reversal this structure can be transformed into Figure 3.3d, where the toroidal moment is pointing in the reverse direction $\mathbf{t} = -a s \mathbf{e}_z$.

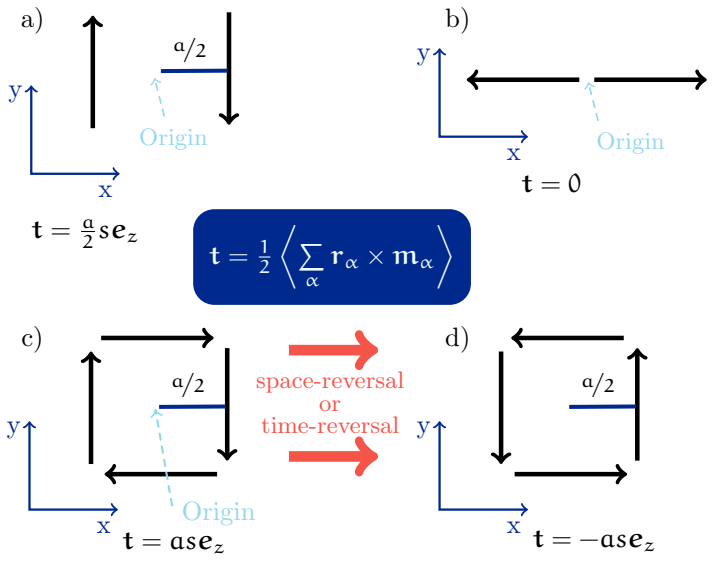

Figure 3.3: One non-toroidal (b) and three toroidal (a),(c),(d) spin configurations. (Adapted by permission from Springer from [131])

As is obvious from Figure 3.3 the definition of the toroidal moment in Eq. 3.1 clearly depends on the choice of the origin. If one changes the origin $\mathbf{r} \rightarrow \mathbf{r} + \mathbf{R}_0$ the toroidal moment is changed $\mathbf{t} \rightarrow \mathbf{t}' = \mathbf{t} + \frac{1}{2}\mathbf{R}_0 \times \mathbf{m}$ with $\mathbf{m} = \sum \mathbf{m}_\alpha$, this is the case because higher multipole mo-

ments are not necessarily extensive for non-vanishing magnetic moments [21]. As described in [131], this can be resolved by separation the magnetization in a fully compensated part

$$\mathbf{m}_\alpha^{(0)} = \mathbf{m}_\alpha - \frac{\mathbf{m}}{N} \qquad \text{with} \sum_\alpha m_\alpha(0) = 0 \tag{3.3}$$

and an uncompensated part:

$$\tilde{\mathbf{m}}_\alpha = \frac{\mathbf{m}}{N} \qquad \text{with } \mathbf{m} = \sum_\alpha m_\alpha \tag{3.4}$$

The compensated part leads to an origin independent toroidal moment

$$\mathbf{t}^0 = \sum_\alpha \frac{1}{2}\mathbf{t}_\alpha \times \mathbf{m}_\alpha \tag{3.5}$$

while the uncompensated part is origin dependent in general

$$\tilde{\mathbf{t}} = \frac{1}{2}\bar{\mathbf{R}} \times \mathbf{m} \qquad \text{with } \bar{\mathbf{R}} = \frac{1}{N}\sum_\alpha \mathbf{r}_\alpha \tag{3.6}$$

If one chooses $\bar{\mathbf{R}}$ as origin, $\tilde{\mathbf{t}}$ vanishes, of course this is a problematic choice for structural transitions, since one would like to keep the origin the same for both phases. On the other hand for non-localized moments the homogeneous magnetization density of the uncompensated part cannot create a macroscopic toroidal moment because it cannot break inversion symmetry, which allows a complete separation between dipole and toroidal contributions [131]. For infinite systems there exits a multi-valueness because one could shift the origin by a lattice vector without chaining the moment arrangement [131]. The solution for bulk periodic solids is the same as for the polarization, only differences of the toroidization are meaningful measurement quantities [131].

3.2 Single crystal growth

Single crystals of $Ni_{0.42}Mn_{0.58}TiO_3$ were grown with the floating zone method (cf. Sec. 2.1.2). Polycrystalline $Ni_{0.42}Mn_{0.58}TiO_3$ was prepared from a stoichiometric mixture of NiO, MnO_2 and TiO_2. NiO is hygroscopic and tends to oxidize to Ni_2O_3, therefore the compound labeled as NiO was heated for 10 h in Air at 1000 °C and was afterwards cooled in an Argon atmosphere to create NiO, during this procedure the color of the composition changed from gray-green to bright green, and powder X-ray diffraction confirmed NiO.

The MnO_2 and TiO_2 were dried at 120 °C for several days to remove moisture. In contrast to [35] we used MnO_2 instead Mn_3O_4, due to availability, it decompose above 600 °C to Mn_3O_4. The powder mixture was ball-milled and afterwards calcined at 1000 °C for 30 h in air. The received powder was ball-milled again and hydrostatically pressed at 30 MP into rods of 8 mm diameter and typically 10 cm length, which were used for both feed and seed. In subsequent growths crystalline seeds were used. For the floating zone growth an optical four mirror furnace was used, with a continuous flow of air. The feed and seed rods were counter rotating with 25 and 15 rpm and were moving through the lamp focus by 1.5 and 1.0 mm/h respectively. $Ni_{0.42}Mn_{0.58}TiO_3$ melts incongruently as it is reported for $MnTiO_3$ [36], but a stable zone could be established through self flux.

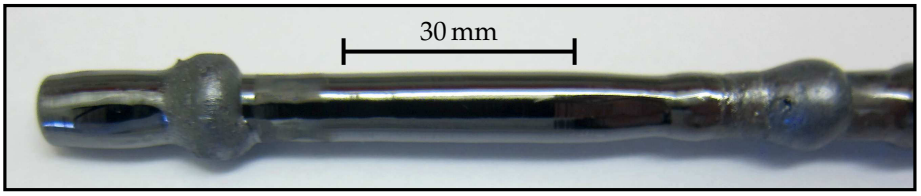

(a) Boule of $Ni_{0.42}Mn_{0.58}TiO_3$.

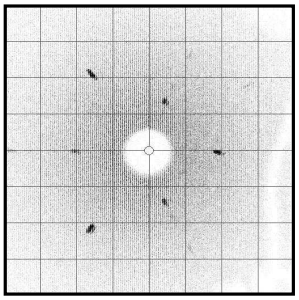

(b) $\perp$ [001]

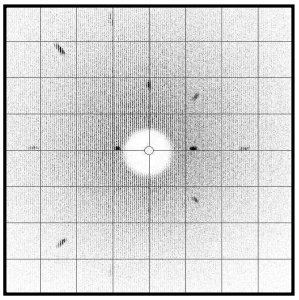

(c) $\perp$ [100]

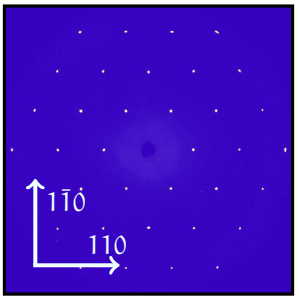

(d) hk0

Figure 3.4: Boule grown width the floating zone method, Laue images perpendicular [001] and [100] and X-ray precession image of the hk0-plane.

3.3 Chemical composition - Powder X-ray diffraction

Powder X-ray diffraction of ground crystals confirmed a single phase of $Ni_xMn_{1-x}TiO_3$. Parts from the boule right from the begin of the growth, where the self flux is not stable, show a small contamination of TiO_2. The ratio between Ni and Mn can also be determined from an evaluation of the lattice parameters. Liferovich *et al.* [138] have reported the structures of $NiTiO_3$, $MnTiO_3$ and $Ni_{0.5}Mn_{0.5}TiO_3$. Since the lattice constants between different instruments can be strongly influenced by calibration errors of the diffractometers, we have also synthesized powder of the end compounds $NiTiO_3$ and $MnTiO_3$. The a lattice parameter is almost linear to the Ni fraction x in $Ni_xMn_{1-x}TiO_3$. The c lattice parameter shows a deviation from the linear behavior, we used the lattice parameters of $Ni_{0.5}Mn_{0.5}TiO_3$ given in [138] to correct for this nonlinearity. To further strengthen the determination of the Ni fraction x, we have also grown single crystals of $NiTiO_3$ and $MnTiO_3$ and determined the lattice constants through single crystal X-ray diffraction, again the $Ni_{0.5}Mn_{0.5}TiO_3$ data from [138] was used to correct for the nonlinearity. Figure 3.5 shows the lattice parameters from powder X-ray diffraction and to which Ni fraction x they correspond. For the powdered single crystal Z1 (Figure 3.4a) the fraction is 0.403 calculated from the a lattice parameter and 0.413 calculated from the c lattice parameter. The comparison with the fractions from the feed, which was used to grown Z1, shows that the composition does not change during the growth. The single crystal X-ray diffraction gives fractions of 0.432 and 0.426 from the a and c lattice parameter respectively. Under consideration of the statistical deviations these compounds can be considered to be $Ni_{0.42}Mn_{0.58}TiO_3$ and will be called $Ni_{0.42}Mn_{0.58}TiO_3$ in the following discussion. All these Ni-fractions lie in the zone in the phase diagram of $Ni_xMn_{1-x}TiO_3$ (Figure 3.1) where the spin glass phase can be reached below 10 K.

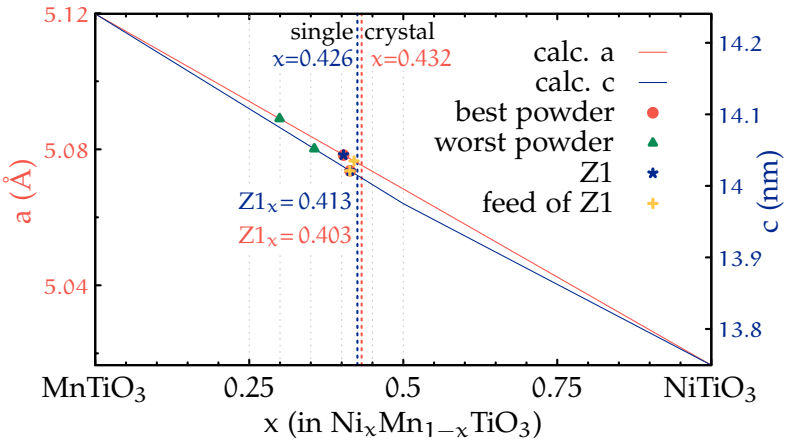

Figure 3.5: Lattice parameters of $Ni_xMn_{1-x}TiO_3$ and their corresponding Ni fractions x. Solid red and blue lines are the linearly interpolated values based on own measurements on $MnTiO_3$ and $NiTiO_3$ and the $Ni_{0.5}Mn_{0.5}TiO_3$-data from [138]. Z1 is from a ground single crystal, and the dotted lines give the corresponding Ni fraction received from single crystal x-ray diffraction.

The grown crystal was oriented using Laue X-ray diffraction and cut plate-like so that $[1\bar{1}0]$ is the surface normal. Figures 3.4b and 3.4c show Laue-images perpendicular [001] and [100] respectively of the middle part of the boule in Figure 3.4a, while Figure 3.4d shows the procession image of the hk0-plane received from single crystal X-ray diffraction data. The latter was used to confirm the sample orientation after cutting, since it is difficult to use back reflection Laue on the small side of a plate.

3.4 Magnetization measurements

To confirm the establishment of the spin glass-phase below 10 K frequency dependent AC susceptibility measurements were performed on a Quantum Design PPMS (cf. Sec. 2.2.2). Figure 3.6a shows the magnetic susceptibility at different frequencies, the shift of the transition temperature around 10 K is characteristic for a spin glass system [45, 139] and was also reported in the supplement of [24]. As in [24] the frequency dependence cannot be described by an Arrhenius law, but is well described by a Vogel-Vulcher law [140–142] with $f = f_0 \exp\left(\frac{-E_a}{k_B(T_f - T_0)}\right)$. For comparison with [24] we restrict the characteristic frequency f_0 to 10^{14}, since the fit is not very sensitive to this parameter. With this we get a Vogel–Fulcher temperature of $T_0 = 40.6 \pm 1\,K$ and $\frac{E_a}{k_B} = 9.35 \pm 0.04\,K$, which is similar to the values Yamaguchi *et al.* reported $T_0 = 34\text{~}37\,K$ and $\frac{E_a}{k_B} = 8.4\text{~}8.7\,K$.

The spin glass freezing temperature of $Ni_{0.42}Mn_{0.58}TiO_3$ shows an anisotropic behavior. The spin component in the $\mathbf{c}_{hex}$ planes freezes at 10 K while the component perpendicular freezes at 6 K [24]. Figure 3.7 shows the DC-magnetization of $Ni_{0.42}Mn_{0.58}TiO_3$ measured along the $[1,1,0]$, $[1,\bar{1},0]$ and $[0,0,1]$ axes, all measured during warming, either with previous field cooling (FW) or without (ZFC). The magnetization along $[1,1,0]$ and $[1,\bar{1},0]$ show the same behavior with a spin glass freezing point at 10 K as observed for the $[1,\bar{1},0]$ di-

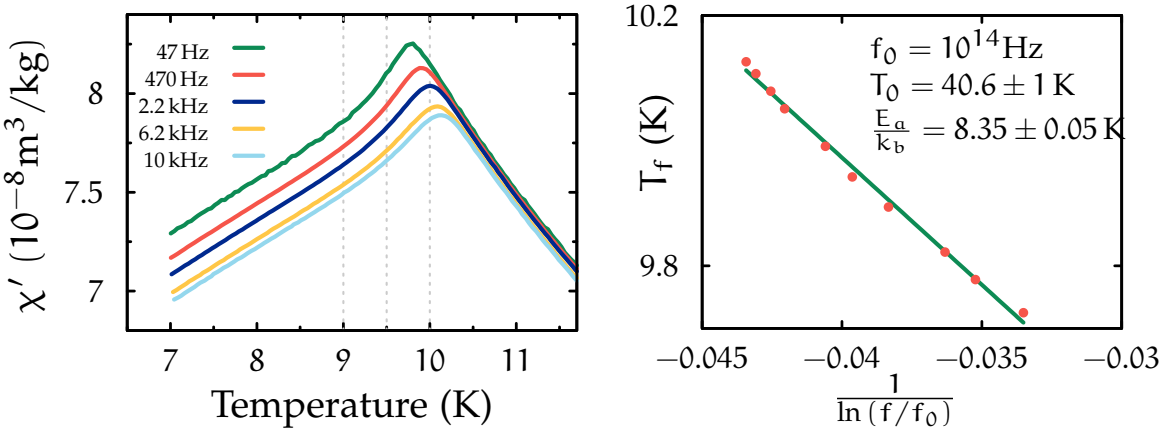

(a) Magnetic susceptibility

(b) Vogel-Fulcher-fit

Figure 3.6: AC magnetic susceptibility of $Ni_{0.42}Mn_{0.58}TiO_3$ at different frequencies with $\mathbf{H}_{ac} \parallel [1\bar{1}0]$.

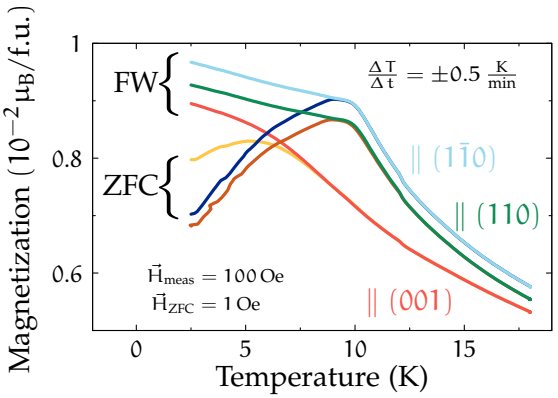

Figure 3.7: Magnetization measurement of $Ni_{0.42}Mn_{0.58}TiO_3$ with different field directions. All curves are measured in a field of 100 Oe either with previous applied cooling field (FW) or without (ZFC).

rection in [24]. Both in-plane directions were measured to have a confirmation of the crystal orientation in addition to single crystal X-ray diffraction. The magnetization in the direction perpendicular to $[1, 1, 0]$ and $[1, \bar{1}, 0]$, therefore $[0, 0, 1]$ shows a freezing point at 6 K. The small difference between the field warming and zero-field-cooling curve above 6 K is most likely given by a small in-plane contribution from a non-perfect sample alignment.

One of the most convincing tests for a spin glass is a memory test [143]. Yamaguchi *et al.* [24] have shown that the polarization induced in $Ni_{0.42}Mn_{0.58}TiO_3$ obeys a magnetoelectric memory effect. In the magnetoelectric memory test not only a time halt during cooling is made, but also the electric field is altered. The classic memory test of the magnetization characteristic for a spin glass, has not been reported on any member of the $Ni_xMn_{1-x}TiO_3$ class. For our memory test the sample was cooled in a field of 1 Oe at a rate of 1 K/min to 2.5 K with 1 h waits at 60 K and 18 K to to create a homogeneous temperature over the whole sample chamber. 18 K is well above the spin glass transition around 10 K [24]. A field of 1 Oe was

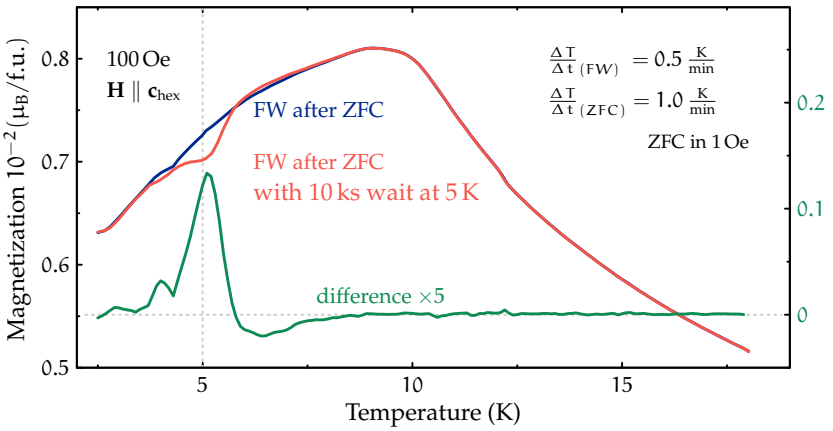

Figure 3.8: Magnetic memory test magnetization measurement of $Ni_{0.42}Mn_{0.58}TiO_3$ in $H \parallel \mathbf{c}_{hex}$. The blue curve is field warming after cooling in zero field from 18 to 2.5 K, while the red curve is measured during warming with a break of 10000 s at 5 K in the previous ZFC. The green curve is the difference of both multiplied by a factor of 5 for visibility.

chosen to have a reproducible very small field instead of a random field one gets due to the remanent magnetization of the MPMS superconducting magnet, which persist of the field is set to zero. Afterwards the magnetization was measured during warming with 0.5 K/min to 18 K in a field of 100 Oe parallel $\mathbf{c}_{hex}$. After the field was turned to 1 Oe the sample was kept for 1 h at 18 K to have the same starting conditions. During the following cooling with 1 K/min to 2.5 K the sample was held at 5 K for 10000 s. Afterwards the magnetization was measured during warming with 0.5 K/min in a field of 100 Oe. Figure 3.8 shows both magnetization measurements and the difference between the field warming without and with a break at 5 K in the previous zero field cooling. $Ni_{0.42}Mn_{0.58}TiO_3$ shows a very clear magnetic memory effect (Fig. 3.8) characteristic for a spin glass. The small dip in the magnetization around 4.2 K originates from the change of the cooling-mode of the MPMS while passing the boiling point of Helium-4.

Overall we can conclude, that the frequency shift of the AC susceptibility, the magnetic anisotropy and the memory test confirm that our sample is indeed an XY spin glass below 10 K and all these results are consistent with [24, 35].

3.5 The Magneto-electric effect in $Ni_{0.42}Mn_{0.58}TiO_3$

By cooling in crossed magnetic and electric fields below the spin glass transition a toroidal moment is induced in $Ni_{0.42}Mn_{0.58}TiO_3$ [35]. The toroidal moment $\mathbf{t}$ is coupled to the magnetization over $\mathbf{M} \propto -\mathbf{t} \times \mathbf{E}$ with application of an electric field as it is shown in Figure 3.9.

To reproduce this measurement we have cut a single crystal of $Ni_{0.42}Mn_{0.58}TiO_3$ to a 0.5 mm thick plate with face normal $[1\bar{1}0]$. A voltage of 200 V, the maximum possible voltage in our setup, was applied along $[1\bar{1}0]$ giving an electric field strength of 0.4 MV/m. Additionally a magnetic field of 9 T was applied along [110] in a Quantum Design MPMS (cf. Sec. 2.2.3)

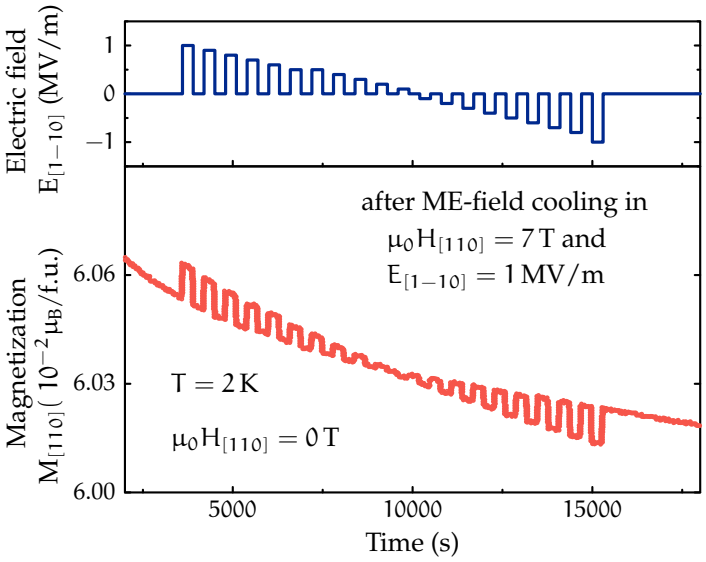

Figure 3.9: Isothermal remanent magnetization of $Ni_{0.42}Mn_{0.58}TiO_3$ at 2 K, after magneto-electric field cooling in $\mu_0 H_{[110]} = 7\,T$ and $E_{[1-10]} = 1\,MV/m$. (Reprinted by permission from Springer Nature: Yamaguchi et al. Nature Communications 4, 2063 (2013) [35]).

and the sample was cooled down to 6.4 K. A lower temperature could not be stabilized likely due to joule heating of the sample. At this temperature both the electric and the magnetic fields were turned off and the remanent magnetization was measured. An alternating voltage with an maximum amplitude of 200 V was applied to the sample to switch the magnetization. Figure 3.10 shows the time dependence of the remanent magnetization and its first derivative, together with the applied voltage pulses. The switching behavior observed by Yamaguchi *et al.* [35] (Figure 3.9) could not be observed. The peaks in the first derivative of the magnetization are measurements artifacts since they are positive for both an increase or decrease of the voltage.

The applied voltage and the corresponding electric field is lower than the one used in [24]. The electric field corresponding to 200 V is applied during the magnetoelectric field cooling of the sample and during the measurement an alternating electric field with the same maximum strength is used. Therefore the reduction of the electrical field has an quadratic influence on the magnetization changes following $\mathbf{M} \propto -\mathbf{t}\times\mathbf{E}$ and $t \propto E_{cooling}$. Nevertheless even a 10 times smaller signal than that in (Figure 3.9) would be observable, so that this cannot explain the observations. The influence of the different measurement temperature is discussed in Section 3.7. $Ni_{0.42}Mn_{0.58}TiO_3$ has two glass transitions, the first one at 9.5 ± 0.5 K is the freezing temperature for the moment parallel to the hexagonal [100]-axis, while only below 6 ± 1 K the moment along [001] freezes [134]. As observed by Yamaguchi [24], the higher temperature $8 \sim 10$ K is the magnetoelectric transition temperature.

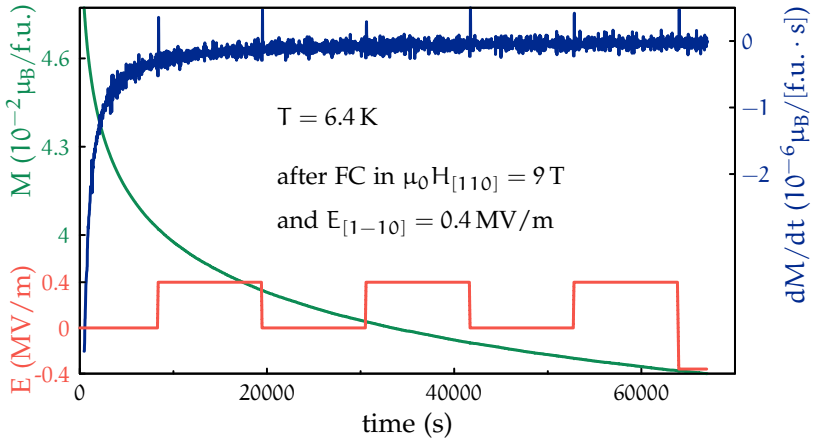

Figure 3.10: Remanent magnetization (M) of $Ni_{0.42}Mn_{0.58}TiO_3$ at 6.4 K, after magneto-electric field cooling in $H_{[110]} = 9$ T and $E_{[1-10]} = 0.4$ MV/m, under application of an varying electric field (E). The blue curve shows the numerical first derivate of the remanent magnetization.

3.6 Neutron diffraction

The main idea for the synthesis of $Ni_{0.42}Mn_{0.58}TiO_3$ was to examine the diffuse magnetic scattering related to the spin glass phase with neutron diffraction by full polarization analysis and under the influence of an electric field. During the two experiments at the DNS instrument at MLZ (cf. Sec. 2.3.9), the 5 T magnet was not operational. Due to this no magnetic field could be applied and following $\mathbf{t} \propto \mathbf{E} \times \mathbf{H}$ no toroidal moment could be induced and no magnetoelectric effect could be observed. Nevertheless we could perform neutron diffraction on the spin glass state of $Ni_{0.42}Mn_{0.58}TiO_3$. Figure 3.11 shows the reciprocal $h0\ell$-plane received from neutron diffraction. The neutron polarization was chosen pointing to the end of the detector array, so roughly parallel to the average scattering vector $\bar{\mathbf{Q}}$. With this polarization orientation all magnetic scattering, regardless of the orientation of the magnetic moment will be in the spin-flip channel, since $\mathbf{M} \perp \mathbf{Q} \rightarrow \mathbf{M} \perp \mathbf{P}$. This is just a very raw approximation, since it is only valid for reflections lying in the center of the detector array. The spin-flip channel (Figure 3.11a) shows diffuse scattering, expected in a spin glass [144], at the positions expected for pure $NiTiO_3$ and $MnTiO_3$, the latter matching the positions of nuclear reflections. The polarization analysis shows that the moments are lying in the c-plane. The non-spin-flip channel (Figure 3.11b) shows beside the structural reflections also $\lambda/2$-contaminations from imperfect monochromatization of the incoming beam. In contrast to $MnTiO_3$ where non-magnetic superstructure reflections were observed recently by neutron diffraction [145], we observe only reflections compatible with the $R\bar{3}$ space group.

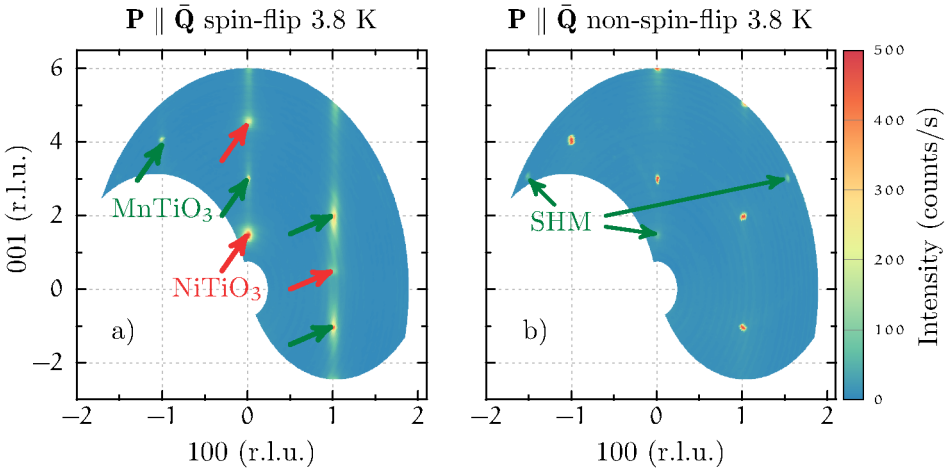

Figure 3.11: Reciprocal h0ℓ-plane of $Ni_{0.42}Mn_{0.58}TiO_3$ with neutron polarization **P** parallel the average scattering vector $\bar{\mathbf{Q}}$ in spin-flip (a) and non-spin-flip channel (b). SHM marks positions of structural reflections due to the $\frac{\lambda}{2}$- contamination.

3.7 Discussion

It is unclear why the magnetoelectric effect observed in [24] could not be observed in our samples. One possibility is, that the sample reported in [24] has a different relative amount of Ni, which is given as $x = 0.42$. Yamaguchi *et al.* [24, 35] do not specify how the amount was determined. The region in the phase diagram (Figure 3.1) in which a spin glass phase can be realized reaches from a Ni amount of 0.4 to 0.48. The $Ni_{0.42}Mn_{0.58}TiO_3$ and $MnTiO_3$ phases at room temperature and atmospheric pressure in the centrosymmetric space group $R\bar{3}$ [132] can obviously not be ferroelectric. On the other hand both are predicted to be magnetoeletric at high pressure [146, 147] or low temperature [148, 149]. For $MnTiO_3$ [150] a linear magnetoelectric effect was reported below 70 K, which also exists in a compound with $x = 0.33$ [133]. For pure $NiTiO_3$ only a high pressure phase is predicted to be magnetoelectric [151], although there are reports claiming that $NiTiO_3$ is magnetoelectric at room temperature [152]. None of these could explain a magnetoelectric effect of the type observed in [24]. The peak shift in the ACMS measurements (Figure 3.6a) shows that the sample in [24] and our sample obey a spin glass state at low temperatures. Unless there exist different phases in the spin glass region, not shown in the phase-diagram (Figure 3.1), it is unlikely that the observed differences are related to a change in the Ni/Mn-ratio between the different samples.

There are three other possible explanations, the most obvious would be a misalignment of our sample, so that either **H** or **E** is not applied in the c-plane. This is also unlikely since the alignment was checked with Laue–X-ray diffraction (Figure 3.4b and c) and single crystal X-ray diffraction (Figure 3.4d). The most likely explanation is, that during our measurements the sample was heated above the spin glass transition temperature at 10 K. The magnetization measurement in Figure 3.10, was measured at 6.4 K, which is much higher than 2 K used by Yamaguchi *et al.* (Figure 3.9). The MPMS could not hold 2 K during our measurement, which

could be due to Joule heating during the magnetoelectric field cooling, because of an imperfectly insulating sample. $NiTiO_3$ is a semiconductor [153]. Our sample was slightly larger than the one used in [35] but the applied field was significantly smaller 0.4 MV/mm to 1 MV/mm, so a possible joule heating should be similar. On the other hand the resistivity depends on the temperature, which reduces the Joule heating at 2 K. Also if the sample is the heating source, it might well be, that the temperature given by the thermometer of the MPMS is below the temperature in the sample. From Figure 3a in [35] it is clear, that the influence of the reduced electric field during cooling is linear, so we could expect a 0.16 times smaller magnetoelectric effect. Under the assumption, that the temperature dependency of the magnetoelectric effect is analog to the induced polarization (Figure 1 in [35]), the effect is reduced by a factor of 1.3 between 2 K and 6.4 K, giving a total reduction by 0.12. Even with this reduction the magnetoelectric effect would be observable in Figure 3.10. Another explanation would be that the toroidal moment leading to the magnetoelectric effect can only be induced below the spin freezing of the c-component below 6 K, but this is in contradiction to the temperature dependence of the polarization (Figure 1 in [35]). The most likely explanation is the destruction of the toroidal state by heating the sample over the spin glass transition due to joule heating caused by a conducting sample, to avoid this a smaller sample could be used or the sample could be isolated from the contacts in future measurements.

4

$YFe_2O_{4-\delta}$

The main part of this thesis in the following chapters is dedicated to the establishment of the charge and spin structures of stoichiometric $YFe_2O_{4-\delta}$.

4.1 A brief history of $YFe_2O_{4-\delta}$

$YFe_2O_{4-\delta}$ was first synthesized in 1975 by Kimizuka *et al.* [154] in a non-stoichiometric form in a CO_2/CO atmosphere. $YFe_2O_{4-\delta}$ is only metastable below 1100 °C and normally decomposes to $YFeO_3$ and FeO [154–157] during cooling. The first non-stoichiometric single crystals were grown in 1976 by Shindo *et al.* [28]. At room temperature $YFe_2O_{4-\delta}$ shows a rhombohedral crystal structure with space group $R\bar{3}m$ [154], with the lattice constants as given in Table 4.1. The structure can be understood as a stacking of triangular layers along the hexagonal c-axis (Fig. 4.1). Triangular layers of Y alternate with bilayers of Fe. A single Fe layer is again triangular and each Fe-ion is in a trigonal bipyramidal oxygen environment, while the oxygen environment for the Yttrium is octahedral. The arrangement of bi- and trivalent Fe ions on the triangular lattice leads to frustration.

The magnetization of the crystals from Shindo *et al.* [28] is characterized by a broad transition around 200 K and a strong difference in the low temperature magnetization between field warming after cooling in a field or without a field, a behavior named parasitic ferrimagnetism [158].

The first stoichiometric powder samples were prepared by Nakagawa *et al.* [161] in 1979 at room temperature they show the same $R\bar{3}m$ structure as non-stoichiometric samples. They undergo two antiferromagentic transitions with onsets at 245 and 220 K on warming, which are shifted 20 K to lower temperatures on cooling and are also structural transitions. It is reported from powder X-ray diffraction that the symmetry is lowered to monoclinic and on further cooling to triclinic [161], although a structure solution was not given. The frustration of the arrangement of Fe^{2+} and Fe^{3+} on the triangular lattice is resolved by long range charge order. The Fe^{2+} and Fe^{3+} charge ordering in stoichiometric $YFe_2O_{4-\delta}$ was analyzed in the past by electron diffraction on micro crystallites, and several different propagation vectors were suggested for different temperatures [159, 162–169]. Figure 4.3 gives an overview of the suggested phases and the propagation vectors describing them. All samples show dif-

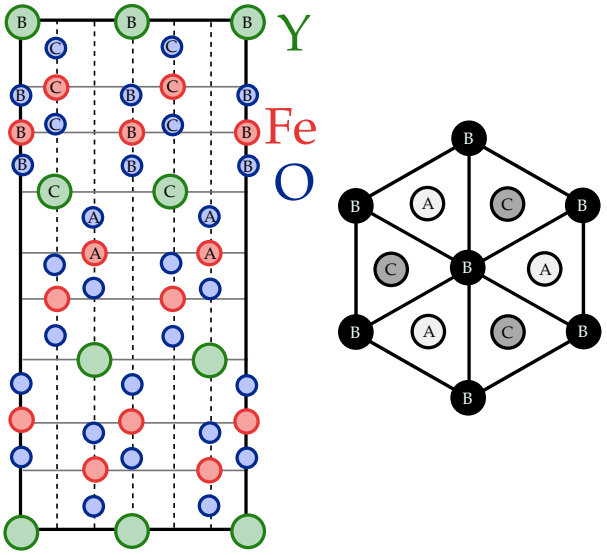

Figure 4.1: Room temperature $R\bar{3}m$ structure of $YFe_2O_{4-\delta}$ from [159] reprinted by permisson of the publisher (Taylor & Francis Ltd, `http://www.tandfonline.com`).

fuse scattering at room temperature, sometimes accomplished by superstructure reflections at $\left(\frac{1}{3}\frac{1}{3}\frac{1}{2}\right)$ [163, 168] or incommensurate modulations of it [166, 167].

Lately Blasco *et al.* [170] reported structure solutions for the charge order superstructure of stoichiometric $YFe_2O_{4-\delta}$ at 210 and 80 K based on Rietveld refinement of synchrotron powder X-ray diffraction data. Structure solution from powder diffraction is highly nontrivial without any starting point. Blasco *et al.* [170] used the room temperature structure and ISODISTORT [171] from the ISOTROPY Software Suite [172] to receive a distorted structure, the used group theory approach seems questionable, which we will discuss later.

Several Mössbauer spectroscopy studies on $YFe_2O_{4-\delta}$ are reported [160, 173–177]. At room temperature in the paramagnetic state the Mössbauer spectrum consists of two quadrupole doublets, originating from Fe^{2+} and Fe^{3+} as identified by the isomer shift [160, 173, 174]. At 373 K these lines merge to one quadrapole doublet, originating from $Fe^{2.5+}$, which is explained by an electron hopping faster than 10^8 Hz, the characteristic frequency of the Mössbauer effect [160, 174]. Below room temperature the spectra differ strongly for stoichiometric [160, 174, 175] and non-stoichiometric [173, 175, 176] $YFe_2O_{4-\delta}$. Non-stoichiometric $YFe_2O_{4-\delta}$ shows a Zeeman split into six broad lines [173] at 90 K, while the spectrum below 220 K of stoichiometric $YFe_2O_{4-\delta}$ consists of four sextets, originating from charge order of Fe^{2+} and Fe^{3+} [160, 174]. On warming at 220 K a new phase occurs with one sharp Fe^{2+} and Fe^{3+} sextett each and an additional broad line attributed to Fe^{3+} [174]. The fast decrease of the hyperfine field at 240 K indicates the Néel temperature [174]. Inazumi *et al.* [160] found that the intensity ratio of the Fe^{2+} and Fe^{3+} Mössbauer lines is 0.9, less than expected for a stoichiometric sample, while Tanaka *et al.* [174] found a ratio of 0.7. They also found that the state of the sample depends on the cooling rate, if the sample was cooled faster than 0.25 K/min between 230 and 100 K, stoichiometric $YFe_2O_{4-\delta}$ shows the same Mössbauer spectrum as a non-stoichiometric sample. During cooling the resistivity of a stoichiometric sample increases at both transitions

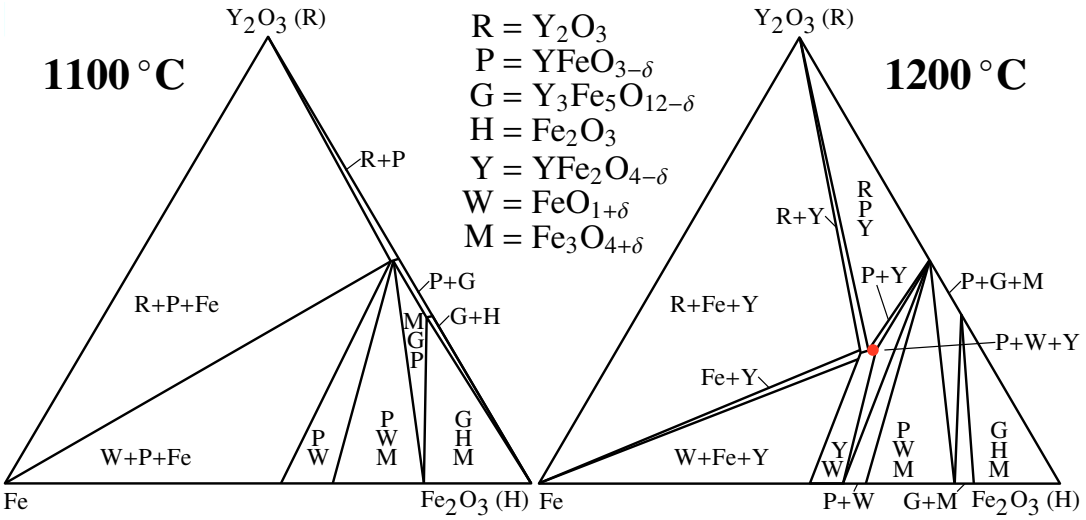

Figure 4.2: Phase diagram of the Y_2O_3-Fe-Fe_2O_3 System at 1100 °C [155] and 1200 °C [160]. The region where stoichiometric $YFe_2O_{4-\delta}$ exists, is marked in red in the 1200 °C diagram. Figure from own published work [40]. For the 1200 °C diagram ©The Physical Society of Japan.

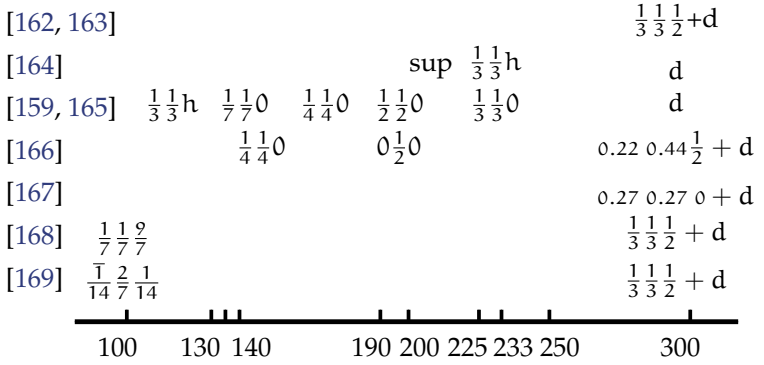

Figure 4.3: Overview of the different superstructure reflections observed in electron diffraction. d denotes diffuse scattering, h half-integer, i integer and *sup* the superposition of $(\frac{1}{3}\frac{1}{3}\mathrm{h})$, $(\frac{1}{2}\frac{1}{2}\mathrm{i})$ and $(\frac{1}{6}\frac{1}{6}\mathrm{i})$ (Brackets are omitted for visibility.).

by 1-2 orders of magnitude [178–180]. This abrupt change shows the same thermal hysteresis as the magnetization [181] and is suppressed with decreasing stoichiometry [178]. By application of pressure the transition temperatures of the structural and magnetic transition can be moved to lower temperatures, Siratori *et al.* [182] found a rate of -2.6 and -10.5 K/kbar for the high and low temperature transition respectively, while Matsumoto *et al.* [183] determined a rate of -1.2 and -3 K/kbar. The lower temperature transition is suppressed above 6 kbar [183] while the higher temperature transition vanishes above 10 kbar [182]. A substitution of Y with Lu leads to a similar effect, where a 1% substitution of Lu corresponds to a pressure of 1 kbar [182].

Neutron diffraction on non-stoichiometric single crystals below 230 K shows diffuse scattering along $(\frac{1}{3}\frac{1}{3}\ell)$ with no fine structure [184–186]. On non-stoichiometric samples with a lower oxygen deficit, the onset of three dimensional magnetic ordering is observed below the

Néel temperature and full 3D ordering is expected for the stoichiometric compound [185]. The magnetic structures are reported to be complex and incommensurate by neutron powder diffraction, but are supposed to be based on the lower symmetry charge order superstructures [185, 187].

Temperature (K)	290	222	77
a (Å)	3.513	3.534	3.574
b (Å)	3.513	3.513	3.540
c (Å)	24.779	24.771	24.505
α (deg)	90	90.23	90.43
β (deg)	90	89.54	88.82
γ (deg)	120	120.20	120.62
V (A^3)	264.83	265.74	266.78

Table 4.1: Lattice parameters of stoichiometric $YFe_2O_{4-\delta}$ from [161] and also given in [160].

4.2 Single crystal growth

The $YFe_2O_{4-\delta}$ samples used in this thesis were grown by the optical floating zone method (see Sec. 2.1.2). The procedure is published [40] and more details can be found in my diploma thesis [20]. Powdered $YFe_2O_{4-\delta}$ was synthesized following the procedure described by Shindo *et al.* [28], from a stoichiometric mixture of Fe_2O_3 (99.945%) and Ye_2O_3 (99.99%). This mixture was calcined at 1250° C for 24 h in a CO_2/Ar-H_2(4%) atmosphere with a CO_2/H_2-ratio of 3. The polycrystalline $YFe_2O_{4-\delta}$ was hydrostatically pressed at 30 MPa into rods, which were used both for the feed and seed in the floating zone growth using an optical four mirror furnace (Model FZ-T-10000-H-VI-VP0 Crystal Systems Corporation, Japan). A CO_2/CO-atmosphere was used and a growth rate of 1 mm/h with seed and feed rods counter-rotating with 10 and 20 rpm. $YFe_2O_{4-\delta}$ is only metastable below 1100 °C, therefore the grown $YFe_2O_{4-\delta}$ partly decomposes to $YFeO_3$ and FeO during cooling [155]. The decomposed part can be easily distinguished from crystalline $YFe_2O_{4-\delta}$ by optical microscopy.

Figure 4.4a shows a grown boule, with decomposed and crystalline $YFe_2O_{4-\delta}$, while 4.4b shows a small single crystal on a nylon wire used for X-ray diffraction.

The stability limit in regard to the oxygen off-stoichiometry δ in $YFe_2O_{4-\delta}$ is given by Kimizuka *et al.* [154] as $\delta = 0.095$ to $\delta = 0.000$, while Jakobs *et al.* [156] give a slightly higher lower border $\delta = 0.0885$.

X-ray powder diffraction is used to check the phase purity of polycrystalline and single crystalline powdered samples. Powder diffractograms of two polycrystalline samples and a ground non-stoichiometric ($\delta > 0.05$) single crystal are shown in Figure 4.5. The inset shows the variation of the in-plane lattice parameter of polycrystalline $YFe_2O_{4-\delta}$ with different synthesis gas ratios, already presented in [20]. The given off-stoichiometries δ are from compari-

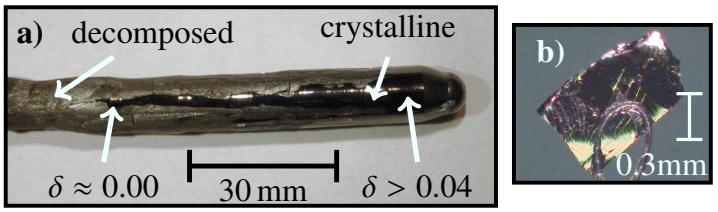

Figure 4.4: a) Grown boule, consisting of crystalline $YFe_2O_{4-\delta}$ and material decomposed to $YFeO_3$ and FeO during cooling. The last grown part (right side) was quenched, through the separation of the seed and feed rod at the end of the growth. Strong variations are observed in the oxygen off-stoichiometry δ. The given oxygen off-stoichiometry δ is determined from comparison of the magnetization with [160]. b) Tiny separated single crystal on a nylon string used for single crystal X-ray diffraction. Figure from own published work [40].

son of magnetization data with those in [160], the relation to the gas-ratio is nonlinear [156]. The decrease of the in-plane lattice parameter is also observed in $LuFe_2O_{4-\delta}$ [188, 189] and also predicted from theory [78, 79], although it is in contradiction to [160], where a small ($< 0.1\%$) volume increase is observed.

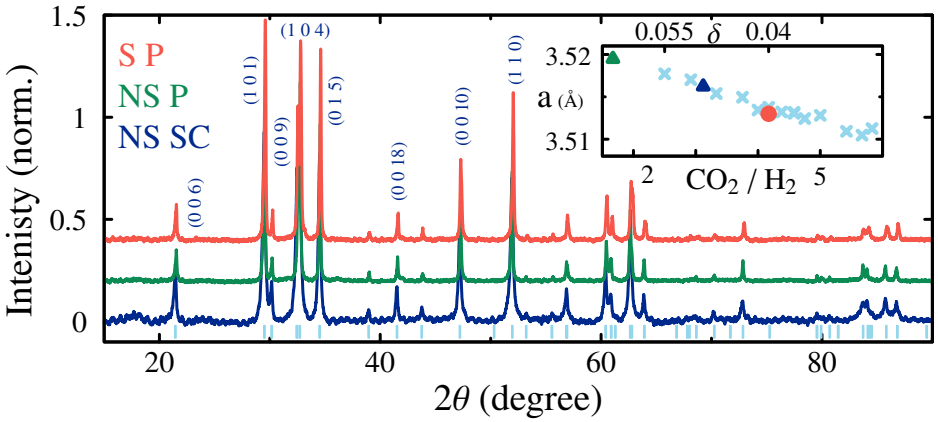

Figure 4.5: Powder diffractograms of $YFe_2O_{4-\delta}$ for the non-stoichiometric single crystal (NS SC) with the magnetization in the inset of Fig. 4.6, non-stoichiometric powder ($\delta > 0.05$) (NS P) and almost stoichiometric powder ($0.03 < \delta < 0.04$) (S P), with the two step transition as in Fig. 4.6 but a difference at low temperatures between FC and ZFC. In light blue the reflection positions for the $R\bar{3}m$ structure reported in [183] are given.
Inset: Dependency of the $R\bar{3}m$ a/b-lattice parameter on the synthesis gas mixture. The given δ is determined from comparison of the magnetization data with those from [160], the correlation to the gas ratio is nonlinear [156]. For the single crystal the gas ratio was interpolated from the lattice parameter and the powder data, since it was synthesized in a CO_2 / CO mixture. Figure from own published work [40].

4.3 Macroscopic characterization

Most samples used in this thesis were already macroscopically characterized during my diploma thesis [20], where the details can be found.

4.3.1 Magnetization

The magnetization of $YFe_2O_{4-\delta}$ is very sensitive too small changes of the oxygen stoichiometry. By comparison of the magnetization with the one measured on polycrystalline samples and reported in [160], one can estimate the stoichiometry of a given sample.

Figure 4.6 shows the magnetization of a stoichiometric $YFe_2O_{4-\delta}$ single crystal, which is characterized by two sharp first order transitions with onset at 228.5 and 180 K on cooling, which are shifted 20 K to higher temperatures on warming. There exists no difference in the field warming curve between previous cooling in a field and cooling without a field. This is in contrast to the magnetization of non-stoichiometric $YFe_2O_{4-\delta}$ (Inset of Fig. 4.6), where cooling in a field of 0.4 T, creates a 40 times larger magnetization at 20 K compared to the zero field cooled sample. The magnetization of the non-stoichiometric crystal is further characterized by a broad glassy transition around 200 K without any thermal hysteresis. The magnetization of the stoichiometric and non-stoichiometric single crystals are both conform with the results on powders [158, 160, 161, 173].

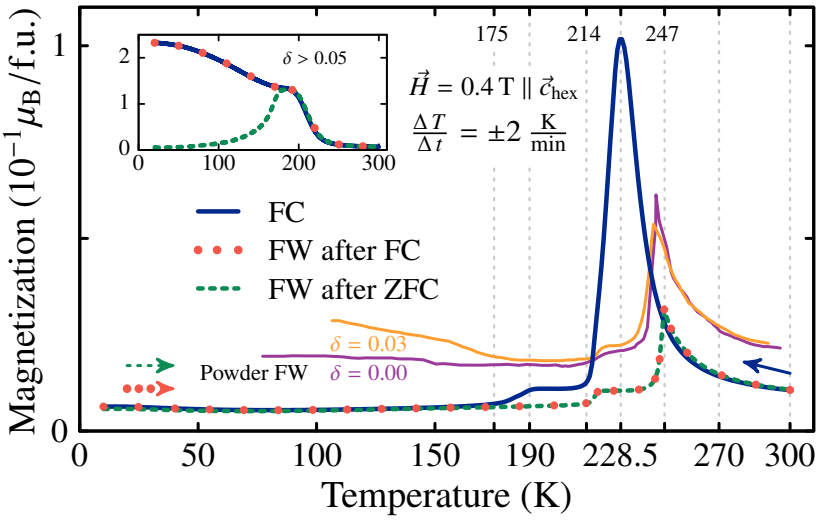

Figure 4.6: Magnetization of a 52 mg *stoichiometric* $YFe_2O_{4-\delta}$ single crystal ($0.00 \approx \delta \ll 0.03$) grown in a CO_2 / CO-ratio of 2.9±0.1, measured during field cooling (FC), field warming (FW) after cooling in a field and after cooling without a field (ZFC). The powder data measured after 0.397 T FC for $\delta = 0.00$ and $\delta = 0.03$ is scaled by a factor of 2 for clarity and taken from [160].
Inset: Magnetization of a *non-stoichiometric* $YFe_2O_{4-\delta}$ single crystal, which was grown in a CO_2 / CO-ratio of 2.6±0.1. Figure from own published work [40].

Figure 4.6 shows also the magnetization of the two most stoichiometric powders from [160]. From comparison the off-stoichiometry δ of our single crystal can be estimated to be close to 0.00 and better than 0.03. Assuming a linear behavior between the transition temperature of non-stoichiometric samples and the off-stoichiometry δ reported in [160], the off stoichiometry δ of the best crystals reported in literature [158] would be 0.5, which is much higher than the stability limit of 0.095 reported in [154].

Frequency dependent AC susceptibility measurements are not reported for $YFe_2O_{4-\delta}$. The diffuse scattering observed at room temperature indicates a partial order, where the system is ordered in the $\mathbf{c}_{hex}$-plane but the stacking of the Fe-layers is random. If the transition temperature between the magnetic states is frequency dependent, this would indicate a not fully ordered system, as it is for example observed in a spin glass transition. This can be probed with AC susceptibility measurements. Figure 4.7a shows the AC susceptibility of $YFe_2O_{4-\delta}$ along $\mathbf{c}_{hex}$ measured with frequencies between 13 and 9311 Hz, in Figure 4.8 the same data is shown zoomed in on the transition at 232 K. While the lower transition temperature shows no frequency dependence, a small shift is observed at the higher temperature transition, with an increased transition temperature at higher frequencies. On cooling the high temperature transition shows a small non-zero imaginary component χ'' (Fig. 4.7b) accompanied by a decrease of the real part χ' (Fig 4.7a). This indicates some dissipative processes in the sample, for example due to induced currents because of the reduced resistivity.

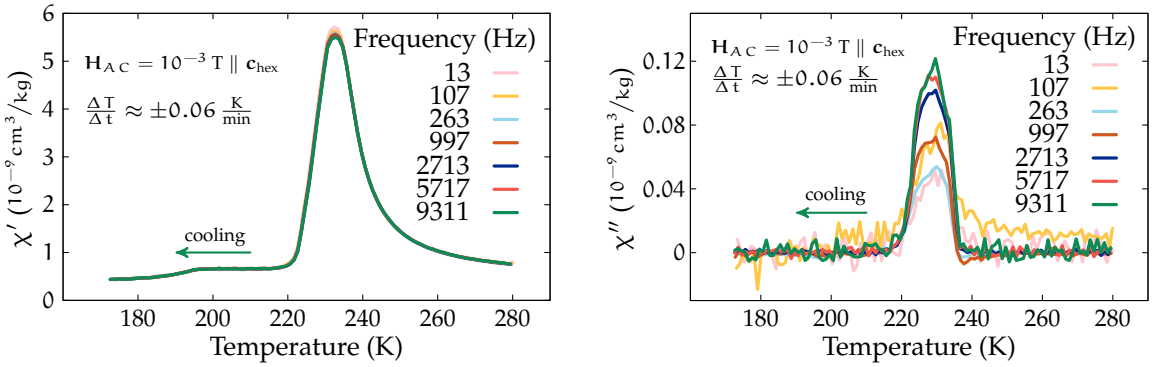

(a) real part χ'

(b) imaginary part χ''

Figure 4.7: Real and imaginary part of the AC magnetic susceptibility of $YFe_2O_{4-\delta}$ at different frequencies.

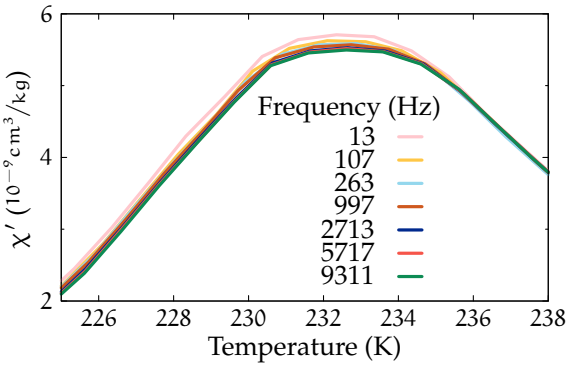

Figure 4.8: Zoom in of Fig. 4.7a, Real part χ' of the AC magnetic susceptibility of $YFe_2O_{4-\delta}$ at different frequencies.

4.3.2 Heat capacity

The specific heat was measured with a Quantum Design PPMS with Apiezon N-grease on a part of the stoichiometric sample used for X-ray and neutron diffraction. The specific heat of stoichiometric $YFe_2O_{4-\delta}$ shown in Figure 4.9 shows two peaks at 214 K and 254 K on warming. The presence of latent heat confirms the first order character of the transitions, which is also in accordance with Mössbauer spectroscopy [174]. In comparison with the powder data from [178] the transitions are more separated and there exists a strong difference at the lower temperature transition with a small peak in the single crystal data and a large continuous drop in the powder data.

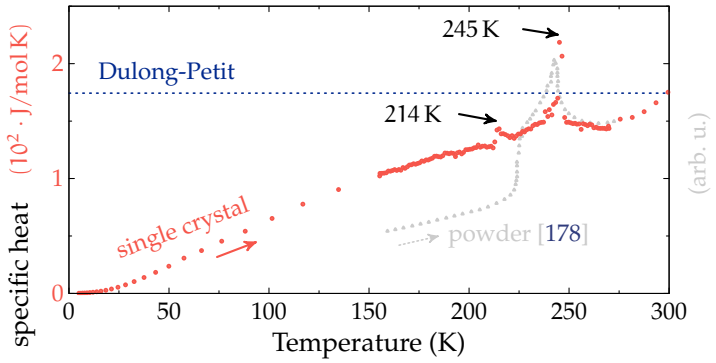

Figure 4.9: Specific heat of a stoichiometric $YFe_2O_{4-\delta}$ single crystal, measured during warming. For comparison the powder data from [178] is shown (in arbitrary units). Figure from own published work [40].

4.4 X-ray magnetic circular dichroism

X-ray magnetic circular dichroism (XMCD) is the difference between the scattering of left and right circularly polarized X-rays in the presence of a magnetic field. The XMCD signal depends on the valence of the interacting ion and also on its magnetic moment, therefore it gives direct information about the spin states of Fe^{2+} and Fe^{3+}. The experimental setup and some theoretical background can be found in Section 2.4.

Figure 4.10 shows the X-ray absorption spectrum of non-stoichiometric $YFe_2O_{4-\delta}$, which is ferrimagnetic, for both left μ_+ and right μ_- polarized light measured with total electron yield. The difference between both $\Delta\mu$ is the XMCD signal shown in green scaled by a factor of four for visibility. The light blue curve is the numerical integration of the XMCD signal. The inset of Figure 4.10 shows also the XAS and XMCD spectra but measured with total fluorescence yield, which is is less surface sensitive.

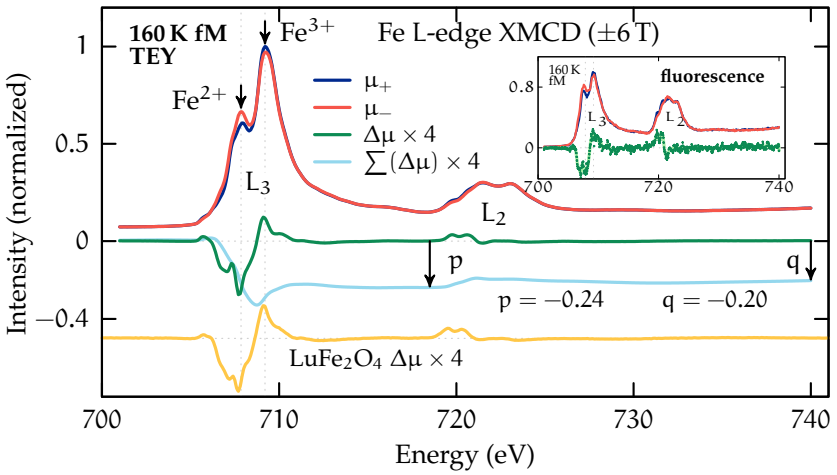

Figure 4.10: XMCD spectrum over the L_2 and L_3 edge of non-stoichiometric ferrimagnetic $YFe_2O_{4-\delta}$ at 160 K, measured with total electron yield. The inset shows the same signal received from fluorescence. For comparison the spectrum of $LuFe_2O_{4-\delta}$ is reproduced from [9] (shifted for clarity).

For the off-stoichiometric ferrimagnetic $YFe_2O_{4-\delta}$ the XMCD signal is similar to the one observed in $LuFe_2O_{4-\delta}$ [9]. At the L_3 edge it shows a larger downward peak, which belongs to the Fe^{2+} contribution and a smaller upward peak belonging to Fe^{3+}. Therefore the net magnetic moment of the Fe^{2+} ions is pointing parallel to the external field and is larger than that of the Fe^{3+} ions, which is antiparallel to the external field. Since the absolute of the dichroism belonging to Fe^{2+} is larger and the single ion moment of Fe^{2+} ($S = 2$) is smaller than that of Fe^{3+} ($S = \frac{5}{2}$), more Fe^{2+} than Fe^{3+} spins must be aligned parallel to the field [76]. In comparison to $LuFe_2O_{4-\delta}$ the Fe^{3+} dichroism signal is slightly suppressed in $YFe_2O_{4-\delta}$, which is in agreement with the observations in $Y_{0.5}Lu_{0.5}Fe_2O_4$ [190]. It is surprising, that in contrast to the Y substitution, the substitution of half the Lu in $LuFe_2O_{4-\delta}$ by Er, leads to a full suppression of the dichroism signal at the Fe^{3+} white-line. Erbium is closer to Lu in regard of the ionic radius than Y, which also results in a smaller deviation of the ratio of the

intralayer Fe–Fe distance to the bilayer thickness [19]. Differences in the oxygen between the Er and Y substituted samples in [190] could explain the stronger deviation of the Er XMCD signal, since the oxygen stoichiometry can have a huge influence on the magnetic order at least in $YFe_2O_{4-\delta}$. Another group [191] found no suppression of the XMCD signal at the Fe^{3+} position in either $ErFe_2O_4$ or $TmFe_2O_4$, which supposes that this is not an ion-sizing effect but rather generated by oxygen defects. It is also not observed in our $YbFe_2O_{4-\delta}$ sample [32, 34, 192]. Lafuerza *et al.* [193] did also not observe a supression in $YbFe_2O_{4-\delta}$, but one in $TmFe_2O_4$. They also reported a temperature dependence of the ratio of the Fe^{2+} and Fe^{3+} XMCD signal. To evaluate orbital and spin contributions to the XMCD signal sum rules as given in Eqn. (2.58) can be applied. From the numerical integration $\sum \Delta\mu$ of the XMCD signal in Fig. 4.10 $p = -0.24$ and $q = -0.2$ can be received, which lead, following Eqn. (2.58), to a ratio of orbital to spin magnetic moment of:

$$\frac{m_{orb}}{m_{spin}} = 0.42$$

This is similar to the ratios observed in $LuFe_2O_{4-\delta}$ by de Groot 0.3 [9], Kuepper 0.38 [194–197], Ko 0.34 - 0.38 [198], Lafuerza 0.3-0.5 [193] and No 0.34 [190] or 0.28 for $Y_{0.5}Lu_{0.5}Fe_2O_4$ [190]. By analyzing the XMCD signals of compounds with pure Fe^{2+} or Fe^{3+} Lafuerza *et al.* [193] estimated the error on the sum rule for the absolute orbital or spin moment to be as large as 40%, questioning the usefulness of the sum rules in case of $LuFe_2O_{4-\delta}$.

The orbital magnetic moment is pointing in the same direction as the spin magnetic moment as indicated by the negative q value [198].

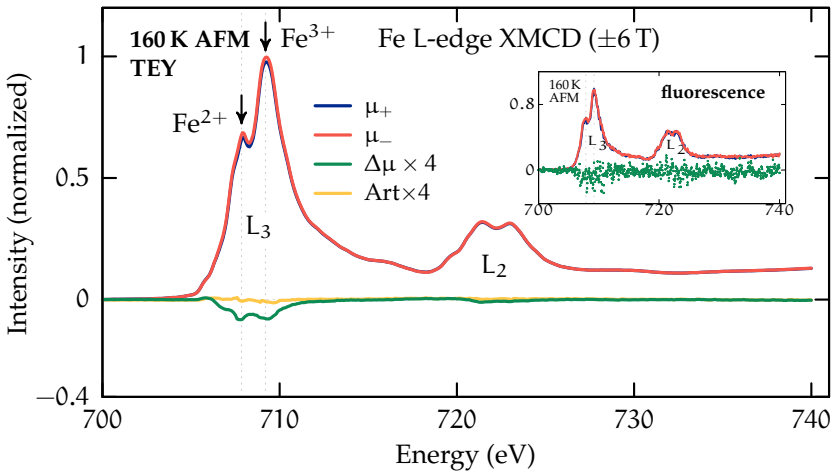

Figure 4.11: XMCD spectrum over the L2 and L3 edge of stoichiometric antiferromagnetic $YFe_2O_{4-\delta}$ at 160 K, measured with total electron yield. The inset shows the same signal received from fluorescence. μ_+ and μ_- are the XAS for left and right polarized light respectively. $\Delta\mu$ is the sum of the XMCD signal for positive and negative field directions. *Art* stands for artifact and is the difference between the XMCD signal for positive and negative field direction.

The Fe^{2+} absorption peak is much smaller than the Fe^{3+} peak in the TEY, for an equal valence distribution one would expect equal intensities. This can be explained by surface

oxidization of the sample. The fluorescence signal in the inset in Fig. 4.10 shows a much smaller difference, since fluorescence is less surface sensitive than TEY. This is also observed in $LuFe_2O_{4-\delta}$ [9, 194, 198] and is strongly reduced if the samples were prepared in situ in vacuum [190, 191, 193, 199] .

The XMCD signal of the stoichiometric $YFe_2O_{4-\delta}$ is totally field induced, because stoichiometric $YFe_2O_{4-\delta}$ is antiferromagnetic in contrast to the ferrimagnetic non-stoichiometric $YFe_2O_{4-\delta}$. The expected XMCD signal is therefore much smaller.

While the signal strength at 160 K is too weak to apply sum rules, both features at the L3 edge are negative indicating, that the nett magnetic moment of both Fe^{2+} and Fe^{3+} is parallel to the applied field (cf. Fig. 4.11).

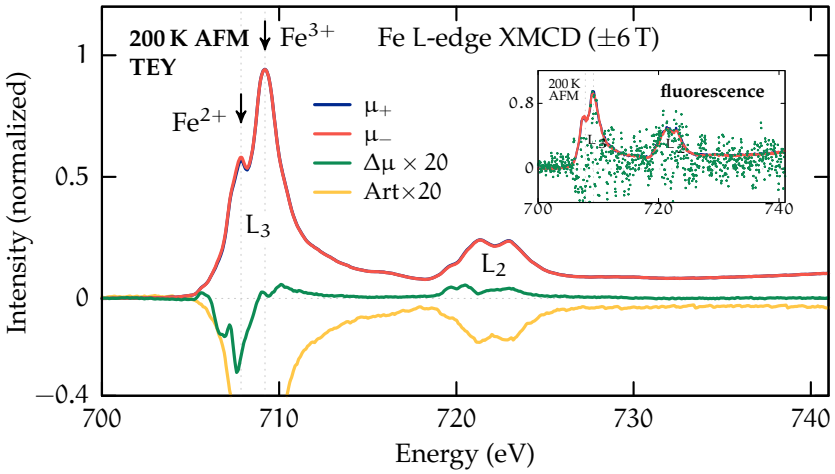

Figure 4.12: XMCD spectrum over the L_2 and L_3 edge of stoichiometric antiferromagnetic $YFe_2O_{4-\delta}$ at 200 K, measured with total electron yield. The inset shows the same signal received from fluorescence. μ_+ and μ_- are the XAS for left and right polarized light respectively. $\Delta\mu$ is the sum of the XMCD signal for positive and negative field directions. Art stands for artifact and is the difference between the XMCD signal for positive and negative field direction.

At 200 K the XMCD signal of stoichiometric $YFe_2O_{4-\delta}$ shown in Figure 4.12 has a similar form as the non-stoichiometric sample at 160 K in Figure 4.10, the Fe^{3+} peak is suppressed in contrast to the non-stoichiometric sample. Although it was not measured it is likely that the XMCD signal of non-stoichiometric $YFe_2O_{4-\delta}$ is the same at 200 K and at 160 K not considering signal strength. The yellow line in Figure 4.12 is the difference between the XMCD signal measured in positive or negative magnetic field, as defined in Eqn. (2.61), this is an artifact and should vanish. This artifact is not induced by the magnetic field and is much larger than the XMCD signal, therefore the XCMD signal at 200 K is not trustworthy, even tough its form is reasonable. Such an artifact can also be induced by a chiral structure, which would mean that the crystal structure at 200 K must be one of the Sohncke groups [200, 201] and cannot have a center of symmetry.

4.5 The room temperature structure

At room temperature our $YFe_2O_{4-\delta}$ single crystals, measured on the SuperNova diffractometer (cf. Sec. 2.3.3), show only reflections corresponding to the already reported $R\bar{3}m$ structure, with additionally diffuse lines along $\left(\frac{1}{3}\frac{1}{3}\ell\right)$ (cf. Fig. 4.13a), which are not accounted in the model. The structure was refined with Jana2006 [64] after structure solution using Superflip [63], see also Section 2.3.4. Table 4.2 shows the structure solution at 295 K in comparison to the one refined from powder data by Matsumoto *et al.* [183]. While the residuals R_{obs} and R_{all} given in Table 4.2 are acceptable, the goodness of fit is slightly away from the ideal value of one. Considering an obverse reverse twinning (twin matrix in (4.1)), leads to a second twin component with a volume fraction less than 0.001. Reflections fulfilling $h - k + \ell = 3n$ for example in the (hk1)-plane are not observed and such twinning can therefore be exclude. The mixed valence model does not account for the two-dimensional valence order inside single Fe layers, which is still present at room temperature, observed as diffuse scattering along $\left(\frac{1}{3}\frac{1}{3}\ell\right)$. The low R-value is confirmed by the good match between the observed and calculated structure factors as shown in Figure 4.14b. Table 4.3 shows the corresponding atomic positions and the thermal displacement factors. While the atomic positions found in this work are the same as in [183] there are differences observed in the thermal displacement parameters. Because of the symmetry restrictions only two of the anisotropic displacement parameters U11 and U33 are independent, the others ar given by $U22 = U11$, $U13 = U23 = 0$ and $U12 = \frac{1}{2}U11$ [202, 203]. Figure 4.14a shows the room temperature structure of $YFe_2O_{4-\delta}$, as in $LuFe_2O_{4-\delta}$ [204] the rare earth ions shows a very strong anisotropy, where U33 is unreasonable large, which is an elongation along $\mathbf{c}_{hex}$. The diffuse lines along $\left(\frac{1}{3}\frac{1}{3}\ell\right)$ are at $h = 0.333(16)$, this can be well seen in Figure 4.13b, which shows the along ℓ integrated intensity. The position of the lines will be relevant for the discussion in Section 4.11.

Parameter	this work	Matsumoto *et al.* [183]
Spacegroup	$R\bar{3}m$	$R\bar{3}m$
a (Å)	3.5153(1)	3.5136(1)
c (Å)	24.789(1)	24.7781(6)
V (Å ^{3})	265.29(4)	264.91(1)
R_{int}/R_σ	5.5/4.4	R_p 4.26
R_{obs}/wR_{obs}	4.0/5.0	R_{wp} 4.26
$R_{all}/\ wR_{all}$	4.3/5.1	R_F 4.86
$GOF_{obs}/\ GOF_{all}$	1.6/1.55	2.37
Measured Reflections	1804	powder
ρ_{calc} (g/cm^3)	4.968(7)	4.975(2)

Table 4.2: Refinement parameters at 295 K (for the definition of the powder R-values see [205])

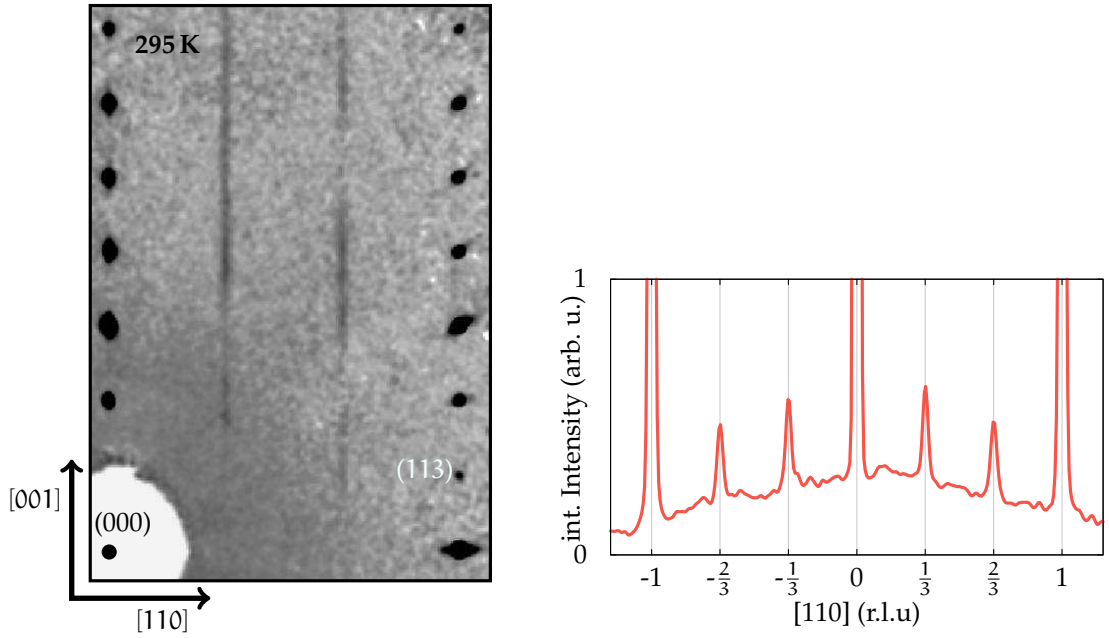

(a) R$\bar{3}$m structure

(b) integrated Intensity

Figure 4.13: (a) XRD precession image of the $hh\ell$-plane at room temperature (b) along ℓ integrated intensity (region around beamstop omitted).

$$\mathbf{T}_{\mathrm{obv/rev}} = \begin{pmatrix} -1 & 0 & 0 \\ 0 & -1 & 0 \\ 0 & 0 & 1 \end{pmatrix} \tag{4.1}$$

Param.	this work	[183]
Y:		
z	0	0
U11	0.0044(7)	0.010(1)
U33	0.065(1)	0.061(4)
Fe:		
z	0.21439(2)	0.2141(1)
U11	0.0182(2)	0.0153(8)
U33	0.010(1)	0.010(1)

Param.	this work	[183]
O1:		
z	0.2920(8)	0.2920 (2)
U11	0.015(7)	0.015(1)
U33	0.010(1)	0.005(2)
O2:		
z	0.1285(1)	0.1279(2)
U11	0.029(1)	0.026(2)
U33	0.031(1)	0.038(4)

Table 4.3: Refinement parameters at 295 K

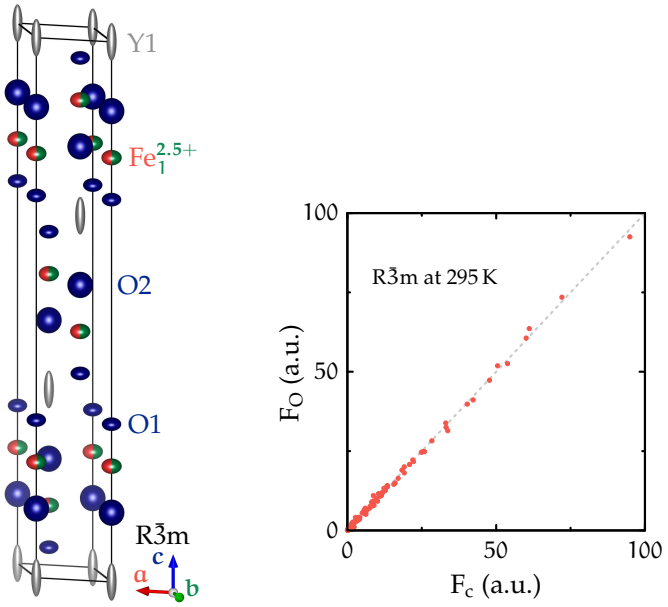

(a) R$\bar{3}$m structure

(b) F_{obs} vs F_{calc}

Figure 4.14: (a) $YFe_2O_{4-\delta}$ structure at 295 K along the [10,40,1]-axis (b) Plot of the observed structure factors F_{obs} versus the calculated F_{calc} of the R$\bar{3}$m structure at 295 K.

4.6 The crystallographic low temperature phases of $YFe_2O_{4-\delta}$

At room temperature $YFe_2O_{4-\delta}$ shows only two dimensional charge order, which is in contrast to $LuFe_2O_{4-\delta}$, which shows three dimensional charge order below 320 K. Below room temperature we have found several different phases in $YFe_2O_{4-\delta}$, as reported in my diploma thesis [20]. Below 228.5 K on cooling the charge order becomes 3D and sharp superstructure peaks are observed. Below the low temperature magnetic transition at 175 K the propagation of the charge order changes. The next part of this thesis is dedicated to the determination of these two charge order structures (Sec. 4.7 and 4.8), a common discussion if given in Section 4.11. All structure determinations are based on single crystal X-ray diffraction measured with the SuperNova diffractometer (cf. Sec. 2.3.3). Together with the CO also magnetic order is observed with the same transition temperatures. The magnetic ordering is described in Section 4.10.3 for 200 K and in Section 4.10.5 for 160 K. Additionally to these two phases if the sample is cooled directly to 100 K it is possible to get a superposition of the 200 K and 160 K phases. This seems not to be a phase on its own, if the cooling rate is slow enough, only the 160 K phase is present at 100 K. Although due to a lack of data we cannot give values for the cooling times. In one sample at 10 K a charge order with a $(\frac{1}{3}\frac{1}{3}$half-integer)-propagation was observed, which is similar to the low temperature ground state of $LuFe_2O_{4-\delta}$ [9]. Since this was never reproducible and in neutron diffraction no structural transition was found between 160 K and 4 K, this phase is no further analyzed. The existence of the superimposed phase and the additional low temperature structure are indications how close the different charge orders must be in regard of energy minimization.

4.7 The crystallographic structure at 160 K

4.7.1 A 4-fold propagation charge order

As already suggested in my diploma thesis [20], $YFe_2O_{4-\delta}$ has a commensurate charge order at 160 K. With a single propagation vector of $\left(\frac{1}{4}\frac{1}{4}\frac{3}{4}\right)$ the observed reflection pattern cannot be indexed. It is likely that as in $LuFe_2O_{4-\delta}$ [9, 75] the threefold symmetry is lost in the charge ordered phase. Figure 4.15a shows a projection image of the reciprocal $hh\ell$-plane at 160 K. In Figure 4.15b this image is overlaid with the lattice corresponding to a propagation vector of $\left(\frac{1}{4}\frac{1}{4}\frac{3}{4}\right)$ in red. There are several reflections on the $\left(\frac{1}{4}\frac{1}{4}\ell\right)$-line, which are not described by the red lattice. Assuming that the threefold symmetry is lost does not help to index them, since the propagation vectors belonging to the 120° rotations $(\bar{2}10)$ and $(1\bar{2}0)$ do not lay in the $hh\ell$-plane. The reflections in the $hh\ell$-plane which cannot be indexed by $\left(\frac{1}{4}\frac{1}{4}\frac{3}{4}\right)$ can be indexed by the blue lattice corresponding to a propagation vector $\left(\frac{1}{4}\frac{1}{4}\frac{\bar{3}}{4}\right)$. Which is the vertically mirrored red lattice, corresponding to a loss the 2-fold rotation around [110]. Beside the structural reflections of $R\bar{3}m$ there are some reflections e. g. $\left(\frac{1}{2}\frac{1}{2}\frac{3}{2}\right)$ belonging to both lattices, due to this they show a higher intensity than the first order superstructure-reflections, although they are second order.

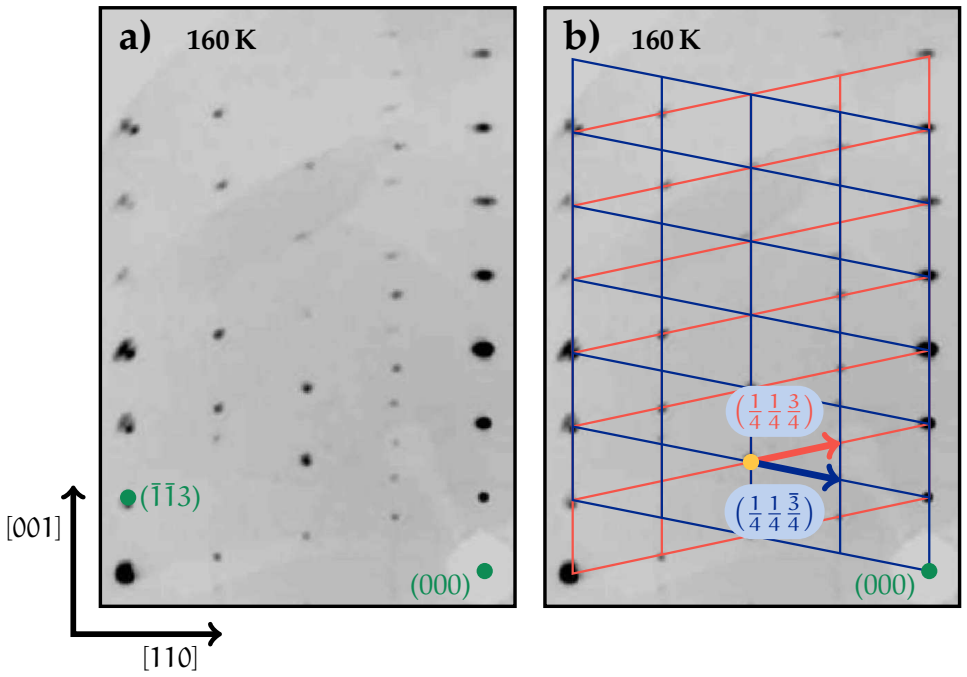

Figure 4.15: Both images show the same region of the reciprocal $hh\ell$-plane at 160 K. (b) shows additionally an overlay of the two twin lattices visible in $hh\ell$.

4.7.2 Representation analysis and basis transformations

For a k point in the first Brillouin zone of $\left(\frac{1}{4}\frac{1}{4}\frac{3}{4}\right)$ representation analysis using ISODISTORT [171] from the ISOTROPY Software Suite [172] leads to only one compatible irreducible rep-

resentation GP1 assuming a single propagation vector this leads to three structures, two with spacegroup $P\bar{1}$ and one with P1.

The transformations between the $R\bar{3}m$ structure and the superstructure without distortions can be described by the following basis transformations $\mathbf{B}$ and origin shifts $\mathbf{p}$:

$$P\bar{1}: \qquad \mathbf{B} = \begin{pmatrix} 1 & -1 & 0 \\ -2 & -2 & 0 \\ \frac{1}{3} & \frac{2}{3} & -\frac{1}{3} \end{pmatrix} \text{ and } \mathbf{p} = \begin{pmatrix} 0 \\ 0 \\ 0 \end{pmatrix} \text{ or } \begin{pmatrix} -\frac{2}{3} \\ -\frac{1}{3} \\ \frac{1}{6} \end{pmatrix} \tag{4.2}$$

the P1 structure has the same basis just lacks the inversion symmetry

$$P1: \qquad \mathbf{B} = \begin{pmatrix} 1 & -1 & 0 \\ -2 & -2 & 0 \\ \frac{1}{3} & \frac{2}{3} & -\frac{1}{3} \end{pmatrix} \text{ and } \mathbf{p} = \begin{pmatrix} 0 \\ 0 \\ 0 \end{pmatrix} \tag{4.3}$$

The basis vectors $(\mathbf{a}, \mathbf{b}, \mathbf{c})$ of the orginal direct lattice transform in the new basisvectors $(\mathbf{a}', \mathbf{b}', \mathbf{c}')$ by, the linear transformation:

$$\begin{pmatrix} \mathbf{a}' \\ \mathbf{b}' \\ \mathbf{c}' \end{pmatrix} = \mathbf{B} \cdot \begin{pmatrix} \mathbf{a} \\ \mathbf{b} \\ \mathbf{c} \end{pmatrix} \tag{4.4}$$

The Miller indexes h,k,ℓ are covariant and transform like the lattice vectors:

$$\begin{pmatrix} h' \\ k' \\ \ell' \end{pmatrix} = \mathbf{B} \cdot \begin{pmatrix} h \\ k \\ \ell \end{pmatrix} \tag{4.5}$$

The basis vectors of the reciprocal lattice $(\mathbf{a}^*, \mathbf{b}^*, \mathbf{c}^*)$ are transformed by the inverse matrix $\mathbf{B^{-1}}$ with $\mathbf{B^{-1}} \cdot \mathbf{B} = \mathbf{1}$ as given in Eqn. (4.6), where $\left[\mathbf{B^{-1}}\right]^t$ stands for the transpose of $\mathbf{B^{-1}}$.

$$\begin{pmatrix} \mathbf{a}^{*\prime} \\ \mathbf{b}^{*\prime} \\ \mathbf{c}^{*\prime} \end{pmatrix} = \left[\mathbf{B^{-1}}\right]^t \cdot \begin{pmatrix} \mathbf{a}^* \\ \mathbf{b}^* \\ \mathbf{c}^* \end{pmatrix} \quad \text{with} \quad \mathbf{B^{-1}} = \begin{pmatrix} \frac{1}{2} & -\frac{1}{4} & 0 \\ -\frac{1}{2} & -\frac{1}{4} & 0 \\ -\frac{1}{2} & -\frac{3}{4} & -3 \end{pmatrix} \tag{4.6}$$

This transformation rule is also valid for directions in direct space (u, v, w). The affine transformation of coordinates (x, y, z) is the only one affected by the origin shift in direct space $\mathbf{p}$:

$$\begin{pmatrix} x' \\ y' \\ z' \end{pmatrix} = \left[\mathbf{B^{-1}}\right]^t \cdot \begin{pmatrix} x \\ y \\ z \end{pmatrix} - \left[\mathbf{B^{-1}}\right]^t \mathbf{p} \tag{4.7}$$

In the transformation from $R\bar{3}m$ to $P\bar{1}$ the threefold symmetry and the mirror planes are lost. Writing $R\bar{3}m$ as $R\bar{3}\frac{2}{m}1$, one sees that they correspond to 120° rotations around $\mathbf{c}$ and

additional 180° rotations, around $[1,0,0]$, $[0,1,0]$ or $[-1,-1,0]$. The lost symmetry elements are twinning operations of the $P\bar{1}$ superstructure, leading to six twin domains.

The Millier indices of the triclinic cell transform between different twins following Equation 4.8 with the transformation matrices given in Eqn. (4.12) and (4.14).

$$\begin{pmatrix} h_t \\ k_t \\ \ell_t \end{pmatrix}_{\text{tric}} = \mathbf{T_i} \cdot \begin{pmatrix} h \\ k \\ \ell \end{pmatrix}_{\text{tric}} \quad \text{with} \quad i \in \{1,2,3,4,5\} \tag{4.8}$$

The twinning matrices transform from the hexagonal base to the triclinic base following Eqn. (4.9)

$$\mathbf{T}_{\text{tric}} = \mathbf{B} \cdot \mathbf{R}_{\text{hex}} \cdot \mathbf{B}^{-1} \tag{4.9}$$

Considering the nonorthogonal coordinate system the 120° rotation in reciprocal space in $R\bar{3}m$ is presented by:

$$\begin{pmatrix} h_t \\ k_t \\ \ell_t \end{pmatrix} = \mathbf{R_{120}} \cdot \begin{pmatrix} h \\ k \\ \ell \end{pmatrix} \quad \text{with} \quad \mathbf{R_{120}} = \begin{pmatrix} 0 & 1 & 0 \\ -1 & -1 & 0 \\ 0 & 0 & 1 \end{pmatrix} \tag{4.10}$$

Since $\mathbf{c}_{\text{hex}} \parallel \mathbf{c}^*_{\text{hex}} \parallel \mathbf{c}^*_{\text{tric}}$ the 120° rotation around $\mathbf{c}_{\text{hex}}$ is also a 120° rotation around $\mathbf{c}^*_{\text{tric}}$. The indices of directions in direct space transform following Eqn. (4.6), so the $\mathbf{c}_{\text{hex}}$-axis is transformed as,

$$\begin{pmatrix} 0 \\ 0 \\ 1 \end{pmatrix}_{\text{hex}} \widehat{=} \begin{pmatrix} -\frac{1}{2} \\ -\frac{3}{4} \\ -3 \end{pmatrix}_{\text{tric}} \tag{4.11}$$

Applying Eqn. (4.9) leads to the first three twin matrices for identity, 120° and 240° rotations around $\mathbf{c}_{\text{hex}}$:

$$\mathbf{T_1} = \begin{pmatrix} 1 & 0 & 0 \\ 0 & 1 & 0 \\ 0 & 0 & 1 \end{pmatrix} \qquad \mathbf{T_2} = \begin{pmatrix} -\frac{1}{2} & -\frac{3}{4} & 0 \\ 1 & -\frac{1}{2} & 0 \\ 0 & \frac{1}{2} & 1 \end{pmatrix} \qquad \mathbf{T_3} = \begin{pmatrix} -\frac{1}{2} & \frac{3}{4} & 0 \\ -1 & -\frac{1}{2} & 0 \\ \frac{1}{2} & \frac{1}{4} & 1 \end{pmatrix} = \mathbf{T_2^{-1}} \tag{4.12}$$

The twofold axes in $R\bar{3}\frac{2}{m}1$ are $[1,0,0]_{\text{hex}}$, $[0,1,0]_{\text{hex}}$ and $[-1,-1,0]_{\text{hex}}$, in the triclinic base they correspond 180° rotations around the vectors given in Eqn. (4.13).

$$\begin{pmatrix} 1 \\ 0 \\ 0 \end{pmatrix}_{\text{hex}} \widehat{=} \begin{pmatrix} \frac{1}{2} \\ -\frac{1}{4} \\ 0 \end{pmatrix}_{\text{tric}} \quad \text{and} \quad \begin{pmatrix} 0 \\ 1 \\ 0 \end{pmatrix}_{\text{hex}} \widehat{=} \begin{pmatrix} -\frac{1}{2} \\ -\frac{1}{4} \\ 0 \end{pmatrix}_{\text{tric}} \quad \text{and} \quad \begin{pmatrix} -1 \\ -1 \\ 0 \end{pmatrix}_{\text{hex}} \widehat{=} \begin{pmatrix} 0 \\ \frac{1}{2} \\ 0 \end{pmatrix}_{\text{tric}} \tag{4.13}$$

The 180° rotations can be express by the following matrices

$$\mathbf{R}_{\mathbf{180}}^{(2\bar{1}0)} = \begin{pmatrix} 1 & -1 & 0 \\ 0 & -1 & 0 \\ 0 & 0 & -1 \end{pmatrix}_{\text{hex}} \quad \widehat{=} \begin{pmatrix} \frac{1}{2} & -\frac{3}{4} & 0 \\ -1 & -\frac{1}{2} & 0 \\ 0 & 0 & -1 \end{pmatrix}_{\text{tric}} = \mathbf{T_4} = \mathbf{T_2} \cdot \mathbf{T_6} = \mathbf{T_3} \cdot \mathbf{T_5} \tag{4.14}$$

$$\mathbf{R}_{\mathbf{180}}^{(\bar{2}\bar{1}0)} = \begin{pmatrix} -1 & -1 & 0 \\ 0 & 1 & 0 \\ 0 & 0 & -1 \end{pmatrix}_{\text{hex}} \quad \widehat{=} \begin{pmatrix} \frac{1}{2} & \frac{3}{4} & 0 \\ 1 & -\frac{1}{2} & 0 \\ -\frac{1}{2} & -\frac{1}{4} & -1 \end{pmatrix}_{\text{tric}} = \mathbf{T_5} = \mathbf{T_2} \cdot \mathbf{T_4} = \mathbf{T_3} \cdot \mathbf{T_6}$$

$$\mathbf{R}_{\mathbf{180}}^{(010)} = \begin{pmatrix} 0 & 1 & 0 \\ 1 & 0 & 0 \\ 0 & 0 & -1 \end{pmatrix}_{\text{hex}} \quad \widehat{=} \begin{pmatrix} -1 & 0 & 0 \\ 0 & 1 & 0 \\ 0 & -\frac{1}{2} & -1 \end{pmatrix}_{\text{tric}} = \mathbf{T_6} = \mathbf{T_2} \cdot \mathbf{T_5} = \mathbf{T_3} \cdot \mathbf{T_4}$$

The twinning in the non-distorted case is called twinning by reticular merohedry.

If the point group of the individual is P1, there is also the possibility for type I twinning by meohedry which would be an inversion twin, where the Laue group is $P\bar{1}$ but the point group of the individual is P1.

For a distorted structure, which no longer has the $R\bar{3}m$ symmetry but is close to these, one has to distinguish two cases which can also occur together, first a general distortion of the hexagonal lattice along the hexagonal axes and second individual distortions of the twins along the axes of the twin components. For the first case, the twinning matrices are the same as for the undistorted case but the lattice parameters are different for each twin. Reflections belonging to the $R\bar{3}m$ lattice show perfect overlap, as well as reflections belonging to the second harmonic of $\left(\frac{1}{4}\frac{1}{4}\frac{3}{4}\right)$.

For the second case, where each twin has its individual distortion, the lattice parameters of all twins are the same but the twinning matrices have to be modified according to these distortions, here the twin operations belong to pseudo symmetries of the parent lattice. This case is twinning by reticular pseudo-merohedry. For this case a splitting of the structural reflections from the $R\bar{3}m$ structure will be observed. With the resolution of our in-house diffractometer the splitting of the reflections is observable but the reflections of different domains could not be separated for integration, as can be seen for example in Figure 4.15. Therefore intensity contributions of the different twins to the splitted $R\bar{3}m$ reflections, were integrated together, so a full overlap for all these reflections was realized by a large enough integration mask. This was also done for the reflections of the second harmonic of $\left(\frac{1}{4}\frac{1}{4}\frac{3}{4}\right)$ which belong to two domains. In this case it is possible to use the undistorted twin matrices as given in Eqn. (4.12) and (4.14). This will create a perfect overlap for the reflections, which were integrated together for the refinement.

4.7.3 Indexing the X-ray pattern

Using the transformation matrices $\mathbf{T_1}$ to $\mathbf{T_6}$ as given in Eqn. (4.12) and (4.14) the observed reflections at 160 K can be indexed with 6 twin domains. Figure 4.16 shows the view along the

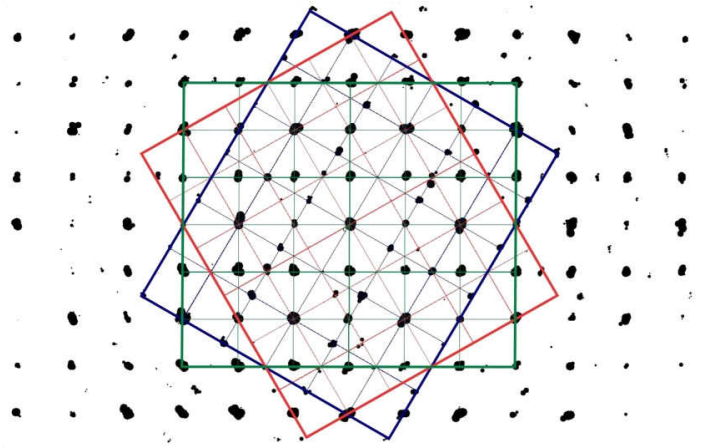

Figure 4.16: Reflections observed at 160 K view along $\mathbf{c}^*_{\mathrm{hex}}$ with the three domains arranged in a 120° pattern that are distinguishable in this view.

$\mathbf{c}^*_{\mathrm{hex}}$-axis with the three domains distinguishable in the $\mathbf{a}^*_{\mathrm{hex}}$-$\mathbf{b}^*_{\mathrm{hex}}$-plane. The CrysAlisPro software [56] automatically indexed the strongest domain with the triclinic structure we received from representation analysis for a $\left(\frac{1}{4}\frac{1}{4}\frac{3}{4}\right)$ propagation vector, which validates the approach to consider only single-q structures in representation analysis. Tables 4.4 gives the lattice parameters of this charge order cell. The CrysAlisPro software [56] can only index and integrate 4 twin components together. As for $LuFe_2O_{4-\delta}$ [9, 75], we searched for a crystal in which one domain is stronger populated than the other domains but no true single domain crystal could be found, although we scanned well above 100 crystals. Figure 4.16 shows the indexation of the reflections observed at 160 K, with four domains, the maximum the CrysAlisPro Software [56] allows, 93.5% of the reflections could be indexed with a $hk\ell$-integer tolerance of 0.125, with only one domain 67% could be indexed.

Only the strongest domain was integrated and used both for structure solution and refinement, under consideration of the twin rules.

a (Å)	b (Å)	c (Å)	α (°)	β(°)	γ (°)
6.0949(5)	7.1548(5)	8.4664(6)	103.277(6)	96.388(6)	90.223(6)

Table 4.4: Lattice parameters of the $P\bar{1}$ cell at 160 K

This cell has a 4 times enlarged volume 356.94(4) Å ^{3} compared to the primitive rhombohedral cell, which has one third of the volume of the hexagonal cell 265.29(4) Å ^{3}.

For the integration for the refinement in $P\bar{1}$ Friedel mates were considered equal, which is true even in presence of resonant scattering when a center of symmetry is present. The redundancy of 2.0 was in this case used to correct for measurement outliers following [206]. The integration mask sizes were checked visually during the integration. With the inversion center as the only symmetry element, the internal residual R_{int} defined in (4.15) only depends on the intensity differences between Friedel mates and differences between multiple measure-

ments of the same reflection with different angles, which can have a different intensity due to absorption and partial twin illumination.

$$R_{int} = \frac{\sum \left| F_o^2 - \langle F_o^2 \rangle \right|}{\sum |F_o^2|} \tag{4.15}$$

The internal residual R_{int} is minimal for an integration mask that integrates the same intensity on the Friedel pairs and multiple measurements of the same reflection. As long as the integration mask size is reasonable (not 0 or ∞) the R_{int} value can therfore give an information about the optimum choice of the integration mask size. The reflections which are structural in $R\bar{3}m$ are very broad at 160 K, because they have contributions from all 6 twin components. They could not be fully separated even using Cu-K_α-radiation and the detector placed 75 mm away from the sample, the maximum possible distance on the SuperNova diffractometer. Therefore an integration mask was chosen large enough to integrate the contributions of all domains to this $R\bar{3}m$-reflections together. The CrysAlisPro Software [56] uses a dynamical integration mask which can, additionally to the used change of the mask-size with the incident angle, be enlarge or reduced by a constant factor. Table 4.5 gives an overview of the internal residuals obtained with different integration mask sizes obtained by introducing a constant factor. The integration masks decreased by a multiplication with 0.5, were clearly too small to account for the intensities even on reflections from only one domain. For the enlarged masks, the number of outliers rejected increases and the R_{int} shows no decrease as would be expected. Therefore beside the small changes in the residual the non-modified integration mask was used. The detector was placed at 54.8 mm and the Mo-source $\lambda = 0.71073$ Å was used to decrease the splitting of structural reflections of the room temperature structure. This increases both the number of accessible reflections and the number of reflections per detector image which shortens the data collection time. The shorter wavelength compared to Cu reduces the absorption from $\mu \approx 63\,mm^{-1}$ to $\mu \approx 24\,mm^{-1}$. The Cu-K_α wavelength is also close to the Fe absorption edge around 7.1 keV which would add a strong fluorescence background.

integration mask size	0.5	1.0	1.5	2.0	2.5
internal residual R_{int}	0.052	0.033	0.036	0.039	0.033-0.040
rejected reflections	57	15	47	43	36-39

Table 4.5: Influence of different integration mask sizes on the internal residual.

The received type of charge order in the refinement was not different for the data set with the regular integration mask or by 2.5 enlarged mask.

4.7.4 Structural refinement

Based on the integration of Twin 1 a structural solution was performed using Superflip [63]. For the structure refinement with Jana2006 [64] reflections closer than 0.05° were considered to be totally overlapped, since the ideal twin matrices are used structural reflections from $R\bar{3}m$ have perfect overlap. Table 4.7 gives the atomic positions and thermal displacement

parameters received from the refinement of the 160 K superstructure of $YFe_2O_{4-\delta}$. The R-values and refinement parameters are given in Table 4.6, the good R-value is confirmed by the match between the observed and calculated structure factors as shown in Figure 4.20b.

Parameter	this work
Spacegroup	$P\bar{1}$
R_{int}/R_σ (%)	3.1/4.0
R_{obs}/wR_{obs} (%)	3.0/3.5
$R_{all}/\ wR_{all}$ (%)	3.7/3.7
$GOF_{obs}/\ GOF_{all}$	1.38/1.32
unique Reflections obs / all	1420 / 1657
parameters	132
diff. peak and hole ($e/Å^3$)	1.3 / -1.1
ρ_{calc} (g/cm^3)	4.9238

Twin	population (%)
1	0.831(18)
2	0
3	0.012(5)
4	0.034(5)
5	0.144(5)
6	0.010(1)

Table 4.6: Refinement parameters at 160 K

Site	x	y	z	U11	U22	U33	U12	U13	U23
Y1	.24412(9)	.36547(8)	.46517(8)	.0052(2)	.0057(3)	.0032(4)	-.0010(2)	.0001(2)	-.0009(2)
Y2	-.25818(9)	.12405(8)	.48322(7)	.0087(2)	.0071(3)	.0131(4)	-.0008(2)	.0013(2)	.0020(2)
Fe1	.34544(14)	.02463(13)	.13467(10)	.0063(3)	.0071(4)	.0047(4)	.000	.0007(3)	-.0011(3)
Fe2	-.11895(15)	.33013(14)	.14226(10)	.0077(3)	.0087(5)	.0042(4)	.0021(4)	.0002(3)	-.0012(3)
Fe3	.60374(16)	.50152(14)	.84772(10)	.0083(3)	.0106(5)	.0040(4)	-.0028(4)	.0008(3)	-.0006(3)
Fe4	.14546(14)	.21057(13)	.84664(10)	.0066(3)	.0071(4)	.0057(4)	.000	.0011(3)	-.0008(3)
O1	.5831(7)	.3920(6)	.6172(4)	.0066(13)	.005(2)	.005(2)	.000)	.000	.0018(16)
O2	.3897(7)	.0694(6)	.3708(5)	.0065(13)	.006(2)	.004(2)	-.0018(17)	-.000	.000
O3	.0964(7)	.1650(6)	.6165(5)	.0075(13)	.008(2)	.006(2)	.000	.000	.000
O4	.3420(6)	.0197(6)	.8836(5)	.0106(14)	.012(2)	.012(2)	.0022(18)	.000	.0024(18)
O5	-.1236(7)	.3567(6)	.3750(4)	.0063(13)	.006(2)	.005(2)	.000	.0025(16)	.000
O6	-.1413(6)	.1859(6)	.9076(5)	.0083(13)	.010(2)	.005(2)	-.0018(17)	.0018(16)	.000
O7	.2128(6)	.2726(6)	.1630(5)	.0076(13)	.006(2)	.009(2)	.000	.000	.000
O8	.2970(6)	.4530(6)	.9082(5)	.0069(13)	.010(2)	.004(2)	-.0019(17)	.000	.0024(17)

Table 4.7: Atomic positions and thermal displacement parameters of the refined 160 K structure. Values given as .000 have errors on the third decimal larger than the value.

Figure 4.17 shows the Fe environments of the 4 distinct sites in the 160 K $P\bar{1}$ structure. The view is centered on the Fe atoms shown in green for Fe^{2+} and red for Fe^{3+} with the $\mathbf{c}_{hex}$-axis pointing upwards and $[5, \bar{2}, 2]_{tric}$ as projection vector. The surrounding Oxygens of the distorted trigonal bipyramidal environment are shown in blue. For comparison, the Fe displacement ellipsoid of the room temperature $R\bar{3}m$ structure is shown in light gray and the Oxygen atoms in yellow. The most obvious observation is the strong reduction of the thermal displacements of both Oxygen and Fe ions.

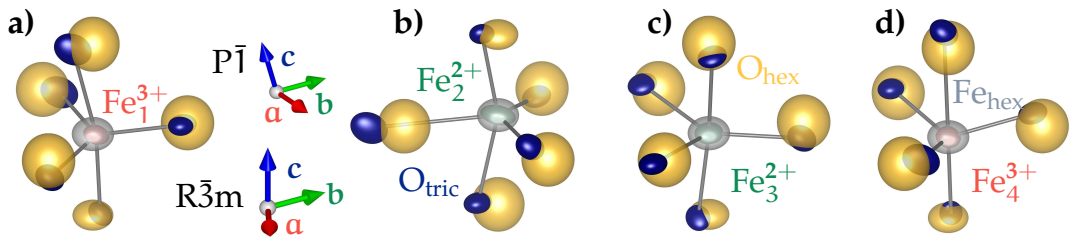

Figure 4.17: The iron environments for the four distinct Fe-positions with two different valences in the 160 K structure of $YFe_2O_{4-\delta}$. The yellow balls show the Oxygen positions of the room-temperature cell, if the Fe ion are superimposed.

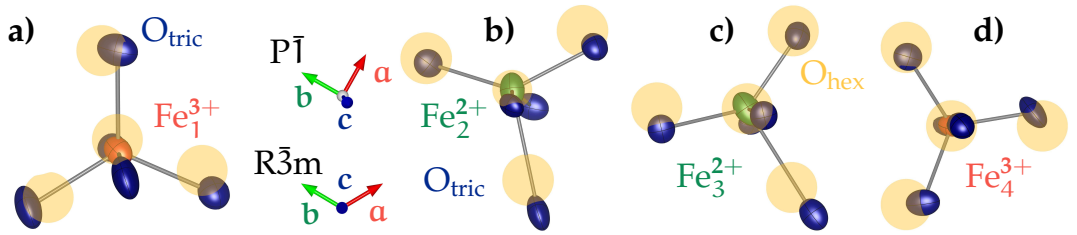

Figure 4.18: View along the $\mathbf{c}_{hex}$-axis with $[1,10]_{tric}$ pointing upwards of the distinct Fe environments at 160 K.

In the case of Fe^{2+} there exists a very strong distortion of the trigonal bipyramidal environment in the plane perpendicular to $\mathbf{c}_{hex}$. This is most obvious in the projection along $\mathbf{c}_{hex}$, as shown in Figure 4.18. The Fe^{2+}-ion is moved away from the triangle center. This can also be seen in the distortion of the bonds of a single Fe layer, which form a hexagon in the undistorted case, as shown in Figure 4.19.

If one has a look at the bond distances between Fe and O in Table 4.10, there are three bonds Fe2-O4, Fe3-O6 and Fe4-07 significantly longer than the typical Fe-O distance of 2.036 Å. Two of them are on the Fe^{2+}-ions. These Oxygens are so far away that their contribution to the BVS is marginal (0.06). The displacement of the Oxygen ion further comes along with a movement of the Fe ion closer to the other two Oxygens out of the center of the Oxygen triangle, as can be seen in the projection along $\mathbf{c}_{hex}$ shown in Figure 4.18. The long bond resulting in the small

Site	bond angle (°)			δ (°)
Fe_{hex}	118.7(1) ($O2_h$-$O2_h$)			1.3
Fe1	114.6(2) (O7-O6)	120.1(2) (O6-O4)	124.7(2) (O7-O4)	3.4
Fe2	106.0(1) (O7-O4)	117.5(1) (O8-O4)	135.0(2) (O8-O7)	10.5
Fe3	105.4(2) (O8-O6)	113.3(1) (O7-O6)	136.0(2) (O7-O8)	12.4
Fe4	109.1(2) (O8-O4)	109.6(2) (O8-O6)	115.5(2) (O6-O4)	8.6

Table 4.8: Bond angles of O-Fe-O in the triangle of the distorted triangular bipyramidal Fe environment with $\delta = \frac{1}{3}\sum|120° - \alpha_{bond}|$.

Site	bond angle (°)						mean (°)
	$O2_h$-$O2_h$	$O1_h$-$O2_h$					
Fe_{hex}	83.5(3)	96.5(3)	90.0(2)				
	O4-O4	O2-O7	O4-O7	O2-O4	O4-O6	O2-O6	
Fe1	81.7(2)	87.4(2)	88.3(2)	92.4(2)	92.8(2)	98.2(2)	90.1(1)
	O6-O4	O5-O4	O6-O7	O5-O7	O6-O8	O5-O8	
Fe2	72.4(2)	84.0(2)	88.4(2)	90.8(2)	93.6(2)	104.4(2)	89.7(1)
	O8-O6	O8-O8	O1-O6	O8-O7	O1-O7	O1-O8	
Fe3	71.0(2)	85.3(2)	89.9(2)	90.0(2)	94.2(2)	104.2(1)	89.9(1)
	O7-O4	O7-O6	O7-O8	O3-O8	O3-O6	O3-O4	
Fe4	76.2(2)	76.6(2)	76.8(2)	103.3(2)	103.4(1)	103.7(1)	92.8(1)

Table 4.9: Bond angles of O-Fe-O out of plane.

Site	bonding distance (Å)					Mean
	$O1_{hex}$	$O2_{hex}$	$O2_{hex}$	$O2_{hex}$	$O2_{hex}$	
Fe_{hex}	1.927(6)	2.042(1)	2.042(1)	2.042(1)	2.135(9)	2.070(1)
	O2	O4	O4	O6	O7	
Fe1	1.938(4)	2.116(4)	1.950(4)	1.893(4)	1.928(4)	1.965(2)
	O5	O6	O7	O8	O4	
Fe2	1.939(4)	2.007(4)	2.062(4)	1.996(4)	2.796(4)	2.160(2)
	O1	O8	O6	O7	O8	
Fe3	1.919(4)	2.038(4)	2.855(4)	1.987(4)	2.041(4)	2.168(2)
	O3	O7	O4	O6	O8	
Fe4	1.889(4)	2.598(4)	1.877(4)	1.896(4)	1.897(4)	2.031(2)

Table 4.10: Fe-O bond distances at 160 K, the gray colored distances are out-of-plane in regard to $\mathbf{c}_{hex}$.

contribution to the bond valence sum, makes one think about a change of the coordination of the Fe ion. The in-plane O-Fe-O angle, as given in Table 4.8, shows a strong deviation up to 15° from the 120° of the ideal trigonal bipyramidal environment. The most common molecular environment for a coordination of four is the tetrahedral environment, but the in-plane angles and especially the out-of-plane angles (Table 4.9) are still much closer to the ideal values of the trigonal bipyramid than to the tetrahedral angle of ≈ 109.5°, not considering the angles from the atom excluded in the tetrahedral case. Also less common environments with coordination number four like the square planar geometry or even the Seesaw geometry do not match better than the trigonal bipyramid.

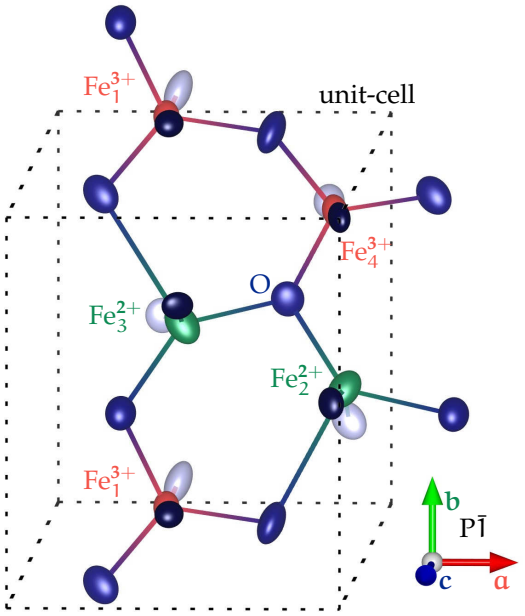

Figure 4.19: Projection of the$YFe_2O_{4-\delta}$ structure at 160 K along the $\mathbf{c}_{hex}$-axis, light blue Oxygens are below and dark above the Fe plane.

A refinement of the structure without the inversion center in spacegroup P1 was also tried. For this Friedel mates were not considered equal in the integration. The refinement was started based on the refinement results in P$\bar{1}$ the atomic positions were transformed using the inversion center and an inversion twin was introduced. To reduce the amount of free parameters the anisotropic displacement parameters of the atoms connected by inversion were kept the same this reduced the parameters from 259 to 181 in relation to 2235 unique reflections. The ratio of parameters to reflections is just on the limit where a refinement is reasonable. The limit of the ratio is often considered to be 8 for non-centrosymmetric and 10 for centrosymmetric spacegroups [207]. With the inversion twin introduced 6 of the 12 twin components refined to negative values. Therefore the twinning by inversion was removed.

Compared to a refinement in P$\bar{1}$ with the same set of reflections, the refinement in P1 converges with only minimal improved R_{obs} 3.66 vs 3.73, and the slightly worse wR_{all} of 5.03 vs 4.65. Overall the dataset is probably not large enough to directly determine if the structure

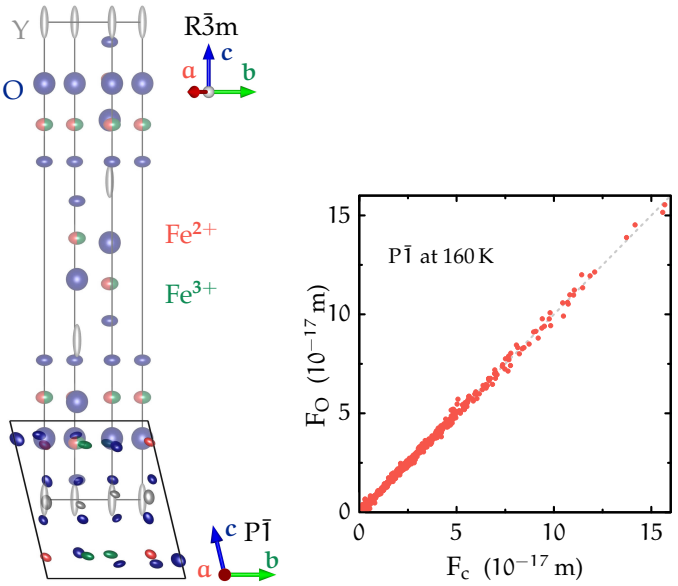

(a) comparison of R3̄m and P1̄ structures

(b) F_{obs} vs F_{calc}

Figure 4.20: (a) $YFe_2O_{4-\delta}$ structure at 160 K along the $[1,0,0]_{tric}$-axis in relation to the R3̄m structure (b) Plot of the observed structure factors F_{obs} versus the calculated F_{calc} of the R3̄m structure at 295 K.

has an inversion center or not. If one has a look at the refined domain populations given in the right part of Table 4.6, one can see that the crystal used for the refinement at 160 K is almost single domain with a volume fraction of 83% for the first domain. One domain volume fraction was fixed to zero because it refined to a small ($< 3\%$) negative value.

4.7.5 Bond valence sum analysis at 160 K

The atomic form factors of Fe^{2+} and Fe^{3+} are too similar to be directly distinguished by laboratory X-ray diffraction (cf. Fig. 2.6a). Bond valence sum analysis (see Sec. 2.3.6) was used to determine the Fe valence of the specific sites of the P1̄ structure at 160 K. For the bond valence sum calculations Oxygen atoms up to 3.05 Å away from the central Fe atom were considered. This corresponds to the atoms building the trigonal bipyramidal environment of the R3̄m structure at room temperature, which are shown in Figure 4.17. Since the characteristic bond length d_{0i} in Eqn. (2.41) depends on the valence of the Fe ion, which is not known yet, the calculations were done with the d_{0i} values for both valence states. We used the values from Brown *et al.* [83], which are considered the most reliable, as given in the green colored row of Table 4.11. The values of d_{0i} given by other authors [87, 88] were used to estimate the systematic error on the bond valence calculation, which is larger than the statistical error received from the uncertainty of the experimental bond lengths as given in Table 4.10. The bond valence sum was calculated both for the largest and smallest d_{0i} from Table 4.11 and the difference was taken as systematic error. Table 4.11 compares the results for the different Fe-sites for the calculations with the d_{0i} of Fe^{2+} and Fe^{3+}. The green colored rows are the

values closer to Fe^{2+} or Fe^{3+}. This leads to the sites Fe1 and Fe4 being Fe^{3+} and Fe2 and Fe3 sites being Fe^{2+}, conserving the mean Fe valence of 2.5. One should also mention that even using the wrong d_{0i} values e. g. the one for Fe^{2+} for site Fe1, leads to a valence higher than the mean Fe valence of 2.5. Considering a non-full charge separation as it was suggested for $LuFe_2O_{4-\delta}$ [85, 86] in contradiction to [9, 76] leads with a mixed d_{0i} value corresponding to $Fe^{2.5+}$ to valences of 2.83(06) for Fe1 or 2.10(05) for Fe2. Considering that we used a d_{0i} for $Fe^{2.5+}$ this is the lowest and highest border for the possible valence. Therefore a strong deviation from full charge separation in $YFe_2O_{4-\delta}$ is very unlikely and we are convinced of the received valence distribution $Fe1^{3+}$, $Fe4^{3+}$, $Fe2^{2+}$ and $Fe3^{3+}$. For comparison we also applied the bond valence sum analysis to the rhombohedral structure at room temperature. The bond valence sum analysis leads to valences of 2.23(07) for $d_{0Fe^{2+}}$, 2.39(04) for $d_{0Fe^{3+}}$ and 2.31(05) for $d_{0Fe^{2.5+}}$. The value is lower than one would expect, the ideal value is more than three standard deviations higher, this is also observed in $LuFe_2O_{4-\delta}$ where a valence of 2.38(3) [9] is found for the $R\bar{3}m$ structure. This might be explained by a partial order of the Fe, which is still present at room temperature as indicated by the presence of diffuse scattering along $\left(\frac{1}{3}\frac{1}{3}\ell\right)$, lowering the crystal symmetry. In [75] this was attributed to the rare trigonal bipyramidal Fe environment for which the tabulated d_{0i} [83] might not match [208], since the coordination number of the Fe ion has a huge influence on d_{0i} [87]. The non-standard d_{0i} could be resolved in the low temperature structure, through the strong distortions.

The refinement of the non-centrosymmetric structure in P1, given in Appendix A.4, shows the same charge order pattern (Tab. A.5), which still has an inversion center. The ions connected by inversion in $P\bar{1}$ have the same nominal valence in P1, the deviations for Fe1, Fe2, Fe3 and Fe4 to their counterparts connected by inversion are 0.01, 0.15, 0.13 and 0.05. Also the introduction of an inversion twin or independent harmonic displacement parameters for ions connected by inversion in $P\bar{1}$ does not change the charge order pattern. From bond valence sum analysis it is therefore very likely that not only the charge order pattern but also the triclinic crystallographic structure has an inversion center.

Site	T (K)	BVS (2+)	BVS (3+)	Multiplicity
Fe1	160	2.74(8)	2.92(4)	2
Fe2	160	2.02(6)	2.16(3)	2
Fe3	160	2.04(6)	2.17(3)	2
Fe4	160	2.72(8)	2.91(4)	2
Fe_{hex}	300	2.23(7)	2.39(4)	6

Table 4.11: Fe Bond valence sum calculations, the standard deviation is propagated from the standard deviation of the mean of d_{0i} as given in Table 2.1 and from the uncertainties of the bond lengths.

The structural refinement at 160 K also confirms that the charge modulation in $YFe_2O_{4-\delta}$ is bimodal in contrast to [209] who proposed it to be tri- or fourmodal based on XANES measurements on $LuFe_2O_{4-\delta}$. The Fe bond valence sums in $YFe_2O_{4-\delta}$ are much clearer bimodal

than the ones for $LuFe_2O_{4-\delta}$ found by X-ray diffraction 2.91(2), 2.75(2), 2.10(1) and 1.92(1) [9], where also multimodal arrangements were suggested [85, 86]. As a validity test of our bond valence sum analysis we also calculated the BVS for Yttrium and Oxygen, for the latter the different Fe valences have to be taken into account.

Site	BVS	Site	BVS
O1	2.05(3)	O5	2.04(3)
O2	2.15(3)	O6	1.92(4)
O3	2.00(2)	O7	1.84(4)
O4	1.83(3)	O8	2.06(5)

Site	BVS
Y1	3.04(3)
Y2	3.06(3)

Table 4.12: Bond valence sum calculation for Oxygen and Yttrium using the different Fe-valences

As can be seen in Table 4.12 the Oxygen valences are close to the ideal value of 2 and the Yttrium valences are close to 3, further strengthening the model.

Theoretically by use of a spin-less fermion $V - t$ model [210–213], with an Hamiltonian with one contribution from electron hopping and one from Coulomb interaction, a four fold charge order has been proposed as the one which minimizes the Coulomb Energy [214]. For the model at $T = 0$ they use mean-field calculations and at finite temperature multicanonical Monte Carlo calculations. They considered a single triangular bilayer with a per site fermion number of $\frac{1}{2}$. For the model of $RFe_2O_{4-\delta}$ where the two Fe layers are shifted in plane to each other they assumed no phase difference between the upper and lower layer, which leads to a propagation of $(\frac{1}{4}\frac{1}{4}\frac{1}{2})$.

The fourfold charge order with this propagation [214] is not the one which is realized in $YFe_2O_{4-\delta}$ at 160 K.

Figure 4.21 shows the comparison of the structure reported by [79, 214] and the one determined by X-ray diffraction in this work. In the theoretically found structure a majority of Fe^{2+} in a triangle of the upper layer leads to a placement of Fe^{3+} in the center of this triangle on the lower layer and vice versa, reducing the Coulomb energy. This is not the case in the structure found in experiment, which can be well seen in the view along $[1, \bar{1}, 0]$ in the lower part of Figure 4.21b. A more detailed discussion will follow in Section 4.11.

4.7.6 Mode decomposition

While we have so far described the low temperature structure trough a new distorted cells, it is also possible to consider the modulation of the room temperature structure. To analyze the contributions of different irreducible representations to the modulated structure mode decomposition is performed using the ISOTROPY Software Suite [172].

Table 4.13 shows the result of the mode decomposition of the distorted structure.

To analyze which modes are responsible for the expected charge order, the valence pattern found in the experiment can be decomposed into orthogonal modes corresponding to the propagation vector, its higher harmonics and the identity operation.

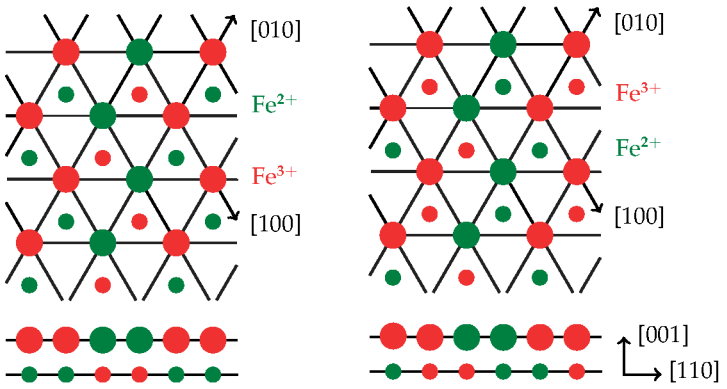

(a) Naka *et al.* [214] (b) this work

Figure 4.21: Comparison of the fourfold superstructure proposed from theory by Naka *et al.* [214] (Reprinted with permission from M.Naka et al., Phys. Rev. B 77, 224441 (2008) Copyright (2008) by the American Physical Society) (a) and the structure determined in this work by x-ray diffraction (b). The lower part is a view along $[1, \bar{1}, 0]$.

mode	GM1+	GM3+	L1-	L2-	GP1
As	0.09	0.24	0.53	0.35	1.29
Ap	0.05	0.12	0.26	0.17	0.64

Table 4.13: Mode amplitudes (sum) from mode decomposition of the distorted 160 K structure determined using ISODISTORT [171]. As is the amplitude of the triclinic CO cell and $A_p = A_s \cdot \sqrt{V_p/V_s}$ where V_p is the volume of the primitive parent structure and V_s the volume of the primitive CO supercell.

For every Fe position the valence can be decomposed into the Fourier expansion

$$\mathrm{Val}_k = \sum_{j=-n\ldots n} A_j \cdot \exp(2\pi i \cdot j\mathbf{p} \cdot \mathbf{r}_k) \text{with} \qquad \mathrm{Val} = \begin{cases} 1 & \text{for } Fe^{3+} \\ 0 & \text{for } Fe^{2.5+} \\ -1 & \text{for } Fe^{2+} \end{cases} \tag{4.16}$$

where j identifies the j-th harmonic of the propagation vector $\mathbf{p}$, and n the highest possible harmonic. $\mathbf{p}$ is the propagation vector and $\mathbf{r}_k$ the relative position of the k-th Fe ion. We use the hexagonal notation for the propagation vector and therefore have to identify the corresponding Fe positions in the non-distorted $R\bar{3}m$ cell. For this WYCKSPLIT [215] from the Bilbao crystallographic sever is used. For the 160 K phase the 6c position of Fe is split by lowering the symmetry to $P\bar{1}$ and the transformation matrix as given in Eqn. (4.2) into 8 positions from which 4 belong to (0,0,z) and 4 to (0,0,-z) with $z = 0.21435$ and are therefore connected by inversion in the parent cell, only the Fe ions belonging to (0,0,z) are used. The Fe atoms can be identified as:

$$Fe1^{3+}_{tric} = (2,1,z)_{hex} \qquad Fe2^{2+}_{tric} = (0,0,z)_{hex} \qquad Fe3^{2+}_{tric} = (1,0,z)_{hex} \qquad Fe4^{2+}_{tric} = (1,1,z)_{hex} \tag{4.17}$$

For the propagation vector of the 160 K phase $\left(\frac{1}{4}\frac{1}{4}\frac{3}{4}\right)$ the third harmonic is equivalent to the negative of $\left(\frac{1}{4}\frac{1}{4}\frac{3}{4}\right)$, therefore $n = 2$ in Eqn. (4.16). The possible modes from Eqn. (4.16) can be expressed in terms of sine and cosine, shifting the phase ϕ_i into different amplitudes for sine and cosine, as followed:

$$\mathrm{Val} = A \cdot \sin(2\pi \mathbf{p} \cdot \mathbf{r}) + B \cdot \cos(2\pi \mathbf{p} \cdot \mathbf{r}) + C \cdot \sin(2\pi \cdot 2\mathbf{p} \cdot \mathbf{r}) + D \cdot \cos(2\pi \cdot 2\mathbf{p} \cdot \mathbf{r}) + E \quad (4.18)$$

Where E corresponds to the identity operation $j = 0$ in Eqn. (4.16).

For the 4 Fe positions this leads to the equation system:

$$\begin{pmatrix} 1 \\ -1 \\ -1 \\ 1 \end{pmatrix} = \begin{pmatrix} -0.531776 & 0.846885 & -0.900706 & 0.43443 & 1 \\ 0.846885 & 0.531776 & 0.900706 & -0.43443 & 1 \\ 0.531776 & -0.846885 & -0.900706 & 0.43443 & 1 \\ -0.846885 & -0.531776 & 0.900706 & -0.43443 & 1 \end{pmatrix} \cdot \begin{pmatrix} A \\ B \\ C \\ D \\ E \end{pmatrix} \quad (4.19)$$

Solving the equation system will give the following mode contributions (A, B, C, D, E) $E = 0$ and $C = 0.482 \cdot D$, $B = 0.315$ and $A = -1.379$. So, there does not exist a single solution but D or C stays undetermined. It is reasonable to set C and D to zero, to get the most simple solution otherwise one would simply introduce a mode to compensate for another.

Mode A is the first harmonic of $\left(\frac{1}{4}\frac{1}{4}\frac{3}{4}\right)$, which is GP1 in Table 4.13. The distortion is mostly determined by the GP1 mode, although there is a significant contribution of L-modes, as shown in Table 4.13. Since the CO pattern can be described purely with the GP1 mode, the L-modes should have no effect on it. The bond valence sum analysis reveals that the L-modes do not influence the charge order pattern, the received bond valence sums for a structure where the amplitudes of the L1- and L2- modes are set to zero are 2.15, 3.10, 3.16, 1.86 for Fe1, Fe2, Fe3 and Fe4 respectively, in accordance with the charge order pattern of the distorted structure which includes the L-modes. We can therefore conclude that the charge order pattern at 160 K is based on a single mode GP1 $\left(\frac{1}{4}\frac{1}{4}\frac{3}{4}\right)$.

4.8 The crystallographic structure at 200 K

4.8.1 A 7-fold propagation charge order

The charge order at 200 K can be described with a commensurate propagation vector of $\left(\frac{1}{7}\frac{1}{7}\frac{9}{7}\right)$ if higher orders and twinning are considered in contrast to the incommensurability suggested in my diploma thesis [20]. With this propagation vector the second order reflections in the hhℓ-plane would be stronger than the first order reflections (Fig. 4.22a), which is physically unlikely. The reflections can also be described with a propagation vector of $\left(\frac{2}{7}\frac{2}{7}\frac{18}{7}\right)$ then the reflections of $\left(\frac{1}{7}\frac{1}{7}\frac{9}{7}\right)$ are third order reflections of $\left(\frac{2}{7}\frac{2}{7}\frac{18}{7}\right)$, which better accounts for the intensity distribution observed in Figure 4.22a. The three propagation vectors $\left(\frac{2}{7}\frac{2}{7}\frac{18}{7}\right)$, $\left(\frac{1}{7}\frac{1}{7}\frac{9}{7}\right)$ and $\left(\frac{2}{7}\frac{2}{7}\frac{3}{7}\right)$ give the same reciprocal lattice and the latter one will be used in the rest of this thesis to describe the CO at 200 K. As for the 160 K phase already in the hhℓ-plane not all reflections can be described with a single propagation vector and twinning has to be taken into account. The additional reflections can be described by a propagation vector with inversed ℓ-coordinate $\left(\frac{2}{7}\frac{2}{7}\frac{3}{7}\right)$, corresponding to the loss of the 2-fold rotation around [110] as in the 160 K phase. To describe all observed reflections also the twins corresponding to a loss of the threefold axis have to be considered, which reduces the symmetry to triclinic.

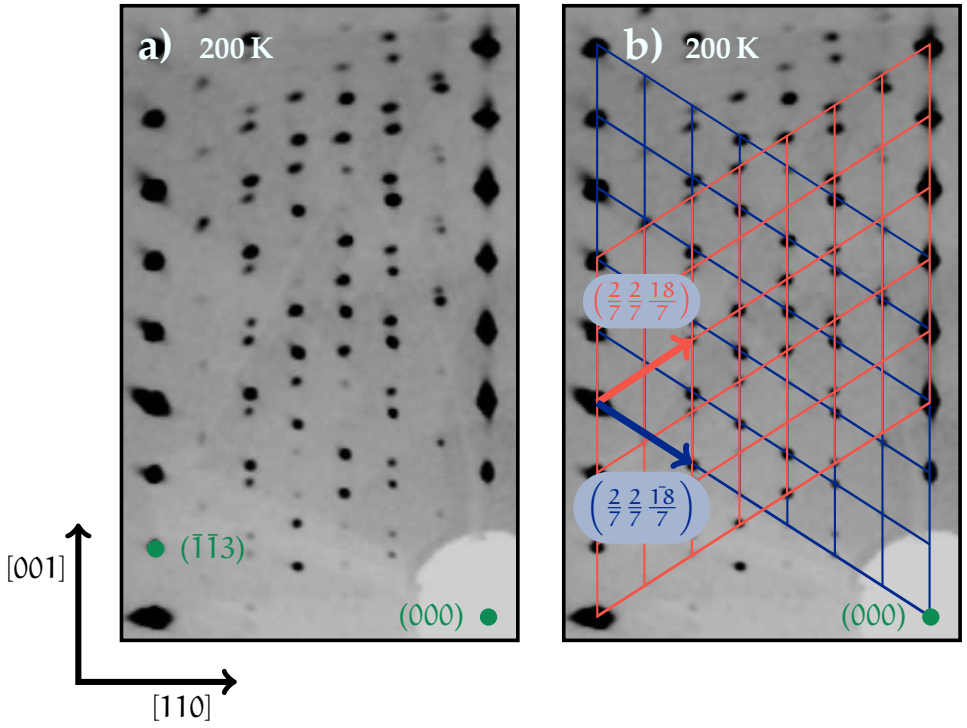

Figure 4.22: Both images show the same region of the reciprocal hhℓ-plane at 210 K. (b) shows additionally an overlay of the two twin lattices visible in hhℓ.

The CrysalisPro software [56] automatically indexed the strongest domain with the triclinic structure we received from representation analysis for a $\left(\frac{2}{7}\frac{2}{7}\frac{3}{7}\right)$ propagation, with the lattice parameters as given in Table 4.14. Again only the intensities from this domain are

used for the integration and structure refinement. With 4 domains the maximum the software allows 81% of the reflections could be indexed from which 57% can be indexed with one domain.

a (Å)	b (Å)	c (Å)	α (°)	β(°)	γ (°)
6.0810(2)	9.8365(4)	11.0621(5)	105.387(4)	100.495(3)	95.803(3)

Table 4.14: Lattice parameters of the $P\bar{1}$ cell at 200 K

4.8.2 Representation analysis and basis transformations

For a k point in the first Brillouin zone of $\left(\frac{2}{7}\frac{2}{7}\frac{3}{7}\right)$ representation analysis using ISODISTORT [171] from the ISOTROPY Software Suite [172] leads also to only one compatible irreducible representation with point groups 1 or $\bar{1}$. Assuming a single proagation vector this leads to two structures, one with spacegroup $P\bar{1}$ and one with P1. All other possibilities would be based on multiple propagation-vectors belonging to different elements of the star of $\left(\frac{2}{7}\frac{2}{7}\frac{3}{7}\right)$. The only two structures with a single propagation vector both have the same basis as given in Eqn. (4.20). Any other possible structure is at least seven times larger than this seven times enlarged cell.

$$\mathrm{P1}, \mathrm{P}\bar{1}: \qquad \mathbf{B} = \begin{pmatrix} -1 & 1 & 0 \\ \frac{5}{3} & \frac{4}{3} & \frac{1}{3} \\ \frac{7}{3} & \frac{5}{3} & -\frac{1}{3} \end{pmatrix} \text{ and } \mathbf{p} = \begin{pmatrix} 0 \\ 0 \\ 0 \end{pmatrix} \tag{4.20}$$

Since $\mathbf{c}_{\mathrm{hex}} \parallel \mathbf{c}^*_{\mathrm{hex}} \parallel \mathbf{c}^*_{\mathrm{tric}}$ the 120° rotation around $\mathbf{c}_{\mathrm{hex}}$ is also a 120° rotation around $\mathbf{c}^*_{\mathrm{tric}}$, which is given in real space in Eqn. (4.21).

$$\begin{pmatrix} 0 \\ 0 \\ 1 \end{pmatrix}_{\mathrm{hex}} \widehat{=} \begin{pmatrix} -\frac{1}{7} \\ \frac{12}{7} \\ -\frac{9}{7} \end{pmatrix}_{\mathrm{tric}} \tag{4.21}$$

The two fold axes in $R\bar{3}\frac{2}{m}1$ are $[1,0,0]_{\mathrm{hex}}$, $[0,1,0]_{\mathrm{hex}}$ and $[-1,-1,0]_{\mathrm{hex}}$, in the triclinic base they correspond 180° rotations around the vectors given in Eqn. (4.22).

$$\begin{pmatrix} 1 \\ 0 \\ 0 \end{pmatrix}_{\mathrm{hex}} \widehat{=} \begin{pmatrix} -\frac{3}{7} \\ \frac{1}{7} \\ \frac{1}{7} \end{pmatrix}_{\mathrm{tric}} \text{ and } \begin{pmatrix} 0 \\ 1 \\ 0 \end{pmatrix}_{\mathrm{hex}} \widehat{=} \begin{pmatrix} \frac{4}{7} \\ \frac{1}{7} \\ \frac{1}{7} \end{pmatrix}_{\mathrm{tric}} \text{ and } \begin{pmatrix} -1 \\ -1 \\ 0 \end{pmatrix}_{\mathrm{hex}} \widehat{=} \begin{pmatrix} -\frac{1}{7} \\ -\frac{2}{7} \\ -\frac{2}{7} \end{pmatrix}_{\mathrm{tric}} \tag{4.22}$$

The 120° rotations around $\mathbf{c}^*_{\mathrm{hex}}$ lead to the following two twin matrices:

$$\mathbf{T_1} = \begin{pmatrix} 1 & 0 & 0 \\ 0 & 1 & 0 \\ 0 & 0 & 1 \end{pmatrix} \qquad \mathbf{T_2} = \begin{pmatrix} -\frac{5}{7} & -\frac{3}{7} & -\frac{3}{7} \\ \frac{5}{7} & \frac{3}{7} & -\frac{4}{7} \\ \frac{8}{7} & -\frac{5}{7} & \frac{2}{7} \end{pmatrix} \qquad \mathbf{T_3} = \begin{pmatrix} -\frac{2}{7} & \frac{3}{7} & \frac{3}{7} \\ -\frac{6}{7} & \frac{2}{7} & -\frac{5}{7} \\ -1 & -1 & 0 \end{pmatrix} = \mathbf{T_2^{-1}} \tag{4.23}$$

While the rotations around $[1,0,0]_{hex}$, $[0,1,0]_{hex}$ and $[-1,-1,0]_{hex}$ lead to:

$$\mathbf{R}_{\mathbf{180}}^{(\bar{1}\bar{2}\bar{2})} = \begin{pmatrix} 0 & 1 & 0 \\ 1 & 0 & 0 \\ 0 & 0 & -1 \end{pmatrix}_{hex} \widehat{=} \begin{pmatrix} -1 & 0 & 0 \\ \frac{3}{7} & -\frac{1}{7} & \frac{6}{7} \\ \frac{4}{7} & \frac{8}{7} & \frac{1}{7} \end{pmatrix}_{tric} = \mathbf{T_4} = \mathbf{T_2} \cdot \mathbf{T_6} = \mathbf{T_3} \cdot \mathbf{T_5}$$

$$\mathbf{R}_{\mathbf{180}}^{(\bar{3}11)} = \begin{pmatrix} 1 & -1 & 0 \\ 0 & -1 & 0 \\ 0 & 0 & -1 \end{pmatrix}_{hex} \widehat{=} \begin{pmatrix} \frac{2}{7} & -\frac{3}{7} & -\frac{3}{7} \\ -\frac{6}{7} & -\frac{5}{7} & \frac{2}{7} \\ -\frac{9}{7} & \frac{3}{7} & -\frac{4}{7} \end{pmatrix}_{tric} = \mathbf{T_5} = \mathbf{T_2} \cdot \mathbf{T_4} = \mathbf{T_3} \cdot \mathbf{T_6} \qquad (4.24)$$

$$\mathbf{R}_{\mathbf{180}}^{(411)} = \begin{pmatrix} -1 & -1 & 0 \\ 0 & 1 & 0 \\ 0 & 0 & -1 \end{pmatrix}_{hex} \widehat{=} \begin{pmatrix} \frac{5}{7} & \frac{3}{7} & \frac{3}{7} \\ \frac{4}{7} & -\frac{6}{7} & \frac{1}{7} \\ \frac{4}{7} & \frac{1}{7} & -\frac{6}{7} \end{pmatrix}_{tric} = \mathbf{T_6} = \mathbf{T_2} \cdot \mathbf{T_5} = \mathbf{T_3} \cdot \mathbf{T_4}$$

4.8.3 Structural refinement

Considering the twin overlap at 200 K there are only totally overlapping reflections or completely separate reflections present. In contrast to the 160 K phase, reflections belong either to all domains or only one domain. The ideal twin matrices in Eqn. (4.23) and (4.24) lead to perfect superposition of the reflections belonging to all domains, these are the ones from the rhombohedral structure. In reality a peak splitting is observed but it can hardly be resolved with the SuperNova diffractometer. The integration mask size was changed automatically at higher angles. Visual inspection of the mask size during the integration process did not reveal any partial covered reflections. Increasing the integration mask by a factor up to 1.75, did not lead to a significant change of the internal R-value confirming that the assumption of a total overlap of the twin domains is justified.

The structure solution using Superflip [63] sets Yttrium Y4 at the inversion center of the $P\bar{1}$ structure, as one would also expect from representation analysis. In contrast to the 160 K phase there exists no $P\bar{1}$ structure compatible with a single propagation vector $\left(\frac{2}{7}\frac{2}{7}\frac{3}{7}\right)$, where the inversion center lies not on the Yttrium. Refining the structure with Y4 at the inversion center lead to R_{obs} values above 10%. For the case with Y4 placed in the inversion center at (0,0,0) the difference Fourier of F_{obs}-F_{calc} is shown in Figure 4.23. The map is centered at Y4 and the green color indicates too much charge while the red color indicates missing charge. From this it is clear that Y4 is not placed in the inversion center and has to be splitted, which is also confirmed by the strong reduction of the R-value from around 10% down to 5%. This is an indication for a still present grade of disorder in the 200 K structure, where 50% of the Yttrium occupies one peak and 50% the other.

The only way to resolve the split position would be to remove the center of symmetry. Lowering the symmetry to P1 will double both the amount of atomic coordinates as well as the anisotropic displacement parameters (ADP), which creates a challenging amount of parameters.

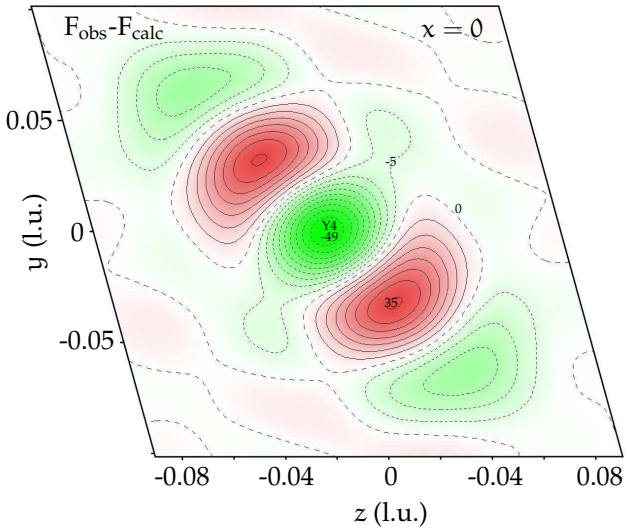

Figure 4.23: Difference Fourier map F_{obs}-F_{calc} in electrons where Y4 is placed at (0,0,0), which is the inversion center in the $P\bar{1}$ 200 K structure. The contours are in steps of 5 electrons and red is missing charge and green is too much charge.

To avoid this the ADP were handled with a pseudosymmetry, where atoms symmetry equivalent in $P\bar{1}$ were restricted to have the same ADP, while only the coordinates were refined, as suggested in [68, 216]. This was based on a dataset, which does not assume the Friedel mates to be equivalent, since the difference contains the information about the centrosymmetry [217]. Without the split position the P1 structures refines with an R-value above 7% and the same elongated anisotropic displacement parameters for Y4, which indicated the split position in $P\bar{1}$. Also the map of the observed structure factors F_{obs} shows two peaks for the Yttrium at the origin, so the disorder is not resolved by a symmetry lowering. Splitting the position in P1 leads again to an decrease of the R-value to a similar value as for the $P\bar{1}$ structure not justifying the lowering of the symmetry.

If the atomic form factors are real it is only possible to determine the Laue groups and not the point group of the system, since in this case Fridels law is fulfilled and the diffraction pattern is always centrosymmetric even if the point group of the crystal is non-centrosymetric [218]. If the atomic form factors have an imaginary part due to anomalous scattering, $F(hk\ell)$ can be distinguished from $F(\bar{h}\bar{k}\bar{\ell})$ [219, 220], although it is difficult to separate this effect from absorption correction, especially for a twinned crystal where the intensity each domain receives from the incident beam is not clear.

If the decision between centrosymmetric and non-centrosymetric cannot be clearly chosen, one should always choose the higher symmetry system [221]. One possibility to enhance anomalous scattering would be to change the wavelength from Mo to Cu to increase absorption, although this is very problematic since the analytical absorption correction does not work for a twinned crystal due to random illumination of domains. It would also induce Fe fluorescence adding substantial to the CCD background. The refinement would benefit from higher intensities since there are a lot of reflections considered unobserved due to their bad

I/sig(I) ratio. There are a lot of weak reflections because the experiment was also performed on very high scattering angles with a resolution limit of 0.38 $Å^{-1}$. If one sets a resolution limit of 0.78 $Å^{-1}$ the amount of unobserved reflections is drastically decreased together with a decrease of the crystallographic residuals as shown in Table 4.15. A measurement on a larger crystal is not suitable due to increased absorption and extinction. Long enough counting times would increase the measurement time to unreasonable times, like several months and also increase the background on the CCD. Measurements on an instrument with a Pilatus detector and evacuated beam path would avoid the background accumulation. Ideal to observe all orders of the weak superstructure reflections would be a measurement at a synchrotron.

Table 4.16 gives the atomic position refined using Jana2006 [64, 222] and Table 4.15 gives the corresponding refinement parameters. The corresponding out-of-plane bond angles are given in Table 4.18, while the in-plane angles are given in Table 4.18. In comparison to the 160 K phase the deviation from the ideal bond angles of the $R\bar{3}m$ phase seem to be slightly smaller although a broad distribution is observed.

The refinement of the 200 K structure was done on a different crystal, than the 160 K refinement since the previously used sample was lost. Form table 4.15 it is obvious, that this sample shows a much broader domain population where 3 domains obey volume fractions over 20%.

Parameter	this work
Spacegroup	$P\bar{1}$
R_{int}/R_σ (%)	11/7.7
R_{int}/R_σ (%) (resol.lim. 0.78)	4.1/1.6
R_{obs}/wR_{obs} (%)	5.2/8.7
R_{all}/ wR_{all} (%)	22/14
GOF_{obs}/ GOF_{all}	1.27/1.13
unique Reflections obs / all	6059 / 19543
parameters	230
diff. peak and hole (e/Å ^{3})	1.6 / -1.3
ρ_{calc} (g/cm^3)	4.9578

Twin	population (%)
1	0.287(12)
2	0
3	0.203(7)
4	0.291(6)
5	0.040(5)
6	0.180(5)

Table 4.15: Refinement parameters at 200 K

Figure 4.24 shows the Fe environment of the seven distinct Fe sites in the 200 K structure, together with the bonding distances. The blue atoms are the Oxygen atoms of the triclinic structure at 200 K, while the yellow atoms are the Oxygens for the rhombohedral structure at room 295 K. The bond distances with uncertainties are also given in Table 4.17. As in the the 160 K phase some of the Fe-O bond lengths are much larger than typical Fe-O distances and their contribution to the bond valence sum is marginal.

Site	occ.	x	y	z	U11	U22	U33	U12	U13	U23
Y1	1	.71863(8)	.42763(6)	.42799(5)	.0038(2)	.0181(3)	.0141(2)	-.0003(2)	.0021(2)	-.0075(2)
Y2	1	.13893(8)	.29935(6)	.27332(5)	.0041(2)	.0096(2)	.0093(2)	.000	.0020(2)	-.0007(2)
Y3	1	.56956(7)	.12134(5)	.15828(5)	.0043(2)	.0066(2)	.0069(2)	.0005(1)	.0012(1)	.0026(1)
Y4	0.5	-.00203(15)	.02213(11)	-.01537(10)	.0040(3)	.0102(5)	.0099(4)	.0006(3)	.0012(3)	.0001(3)
Fe1	1	.67616(13)	-.20910(9)	.14200(8)	.0096(3)	.0087(3)	.0077(3)	.0018(2)	-.0018(2)	.0000(2)
Fe2	1	.11731(13)	.65441(11)	.00825(9)	.0071(3)	.0216(4)	.0089(3)	.0003(3)	.0024(2)	.0018(3)
Fe3	1	.39872(12)	.23367(9)	.58430(8)	.0084(3)	.0080(3)	.0094(3)	-.0006(2)	.0009(2)	.0006(2)
Fe4	1	.96614(12)	.36246(9)	.73041(9)	.0074(3)	.0082(3)	.0123(3)	.0010(2)	.0018(2)	.0005(2)
Fe5	1	.84488(16)	.06188(10)	.41565(9)	.0256(4)	.0138(4)	.0168(4)	-.0108(3)	-.0112(3)	.0112(3)
Fe6	1	.2669(2)	-.04880(12)	.31163(13)	.0445(6)	.0191(5)	.0480(7)	.0205(4)	.0392(5)	.0241(5)
Fe7	1	.47073(17)	.48553(11)	.13363(10)	.0278(4)	.0117(4)	.0159(4)	.0050(3)	.0072(3)	.0099(3)
O1	1	.4827(6)	.3498(4)	.2307(4)	.0062(12)	.0077(14)	.0110(14)	.0019(11)	.0030(11)	.0038(12)
O2	1	.8352(6)	.2204(4)	.3457(4)	.0063(12)	.0082(15)	.0096(14)	.0011(10)	.0015(11)	.0033(12)
O3	1	-.1248(6)	.2078(5)	.0874(4)	.0069(13)	.0162(18)	.0088(14)	-.0049(12)	.000	.0031(13)
O4	1	.2227(6)	.0755(5)	.2022(5)	.0104(15)	.0079(15)	.0230(20)	.000	.0111(14)	.000
O5	1	.6649(6)	-.0834(4)	.0352(4)	.0146(15)	.0091(15)	.0063(13)	.0041(10)	.000	.000
O6	1	.3833(6)	.3568(5)	.4770(4)	.0073(13)	.0109(16)	.0093(14)	.0021(11)	.0012(11)	.0045(12)
O7	1	.4382(6)	.6378(4)	.0384(3)	.0117(13)	.0081(14)	.0098(14)	.000	.0015(11)	.0034(12)
O8	1	.8994(7)	.5114(5)	.8763(5)	.0128(17)	.0101(19)	.0440(30)	.000	.0066(19)	.0019(18)
O9	1	.0125(7)	.2350(5)	.8578(5)	.0182(19)	.0138(19)	.0350(30)	.0038(14)	.0187(18)	.0094(19)
O10	1	.2905(6)	.3409(4)	.7265(4)	.0116(14)	.0112(16)	.0114(15)	.000	.0016(12)	.0038(13)
O11	1	.5925(6)	-.0659(4)	.2746(3)	.0110(13)	.0119(16)	.0104(14)	.000	.000	.000
O12	1	.9579(6)	.4917(5)	.6215(4)	.0094(14)	.0089(16)	.0122(15)	.000	.0018(12)	.0052(13)
O13	1	.1934(6)	.0701(4)	.4766(3)	.0110(14)	.0072(14)	.0091(13)	-.0021(10)	-.0028(10)	.0027(12)
O14	1	.7109(7)	.2220(4)	.6206(4)	.0132(15)	.0121(17)	.0173(17)	.000	-.0036(13)	.0065(15)

Table 4.16: Atomic positions and thermal displacement parameters of the refined 200 K structure. Values given as .000 have errors on the third decimal larger than the value.

Site	bonding distance (Å)					Mean
	$O1_{hex}$	$O2_{hex}$	$O2_{hex}$			
Fe_{hex}	1.927(6)	2.042(1)	2.042(1)			
	O5	O10	O7	O9	O11	
Fe1	1.923(5)	2.190(5)	1.928(3)	1.936(5)	1.928(4)	1.994(2)
	O3	O8	O7	O8	O9	
Fe2	1.931(5)	1.923(4)	1.950(4)	2.330(6)	1.936(5)	2.055(2)
	O6	O11	O10	O13	O14	
Fe3	1.907(5)	2.554(4)	1.913(4)	1.899(3)	1.890(4)	2.030(2)
	O8	O9	O10	O12	O14	
Fe4	2.006(5)	2.123(5)	2.013(4)	1.970(5)	1.946(3)	2.022(2)
	O2	O13	O11	O13	O14	
Fe5	1.918(5)	2.007(4)	2.017(3)	2.091(4)	2.707(4)	2.134(2)
	O4	O13	O9	O11	O14	
Fe6	1.943(6)	2.042(4)	2.480(4)	2.108(4)	2.043(5)	2.084(2)
	O1	O7	O7	O8	O10	
Fe7	1.923(5)	2.054(4)	2.168(4)	2.237(5)	2.168(3)	2.100(2)

Table 4.17: Fe-O bond distances at 200 K, the gray colored distances are out-of-plane in regard to $\mathbf{c}_{hex}$.

Site	bond angle (°)						mean (°)
Fe_{hex}	$O2_h$-$O2_h$ 83.5(3)	$O1_h$-$O2_h$ 96.5(3)					90.0(2)
Fe_1^{3+}	O9-O10 82.3(2)	O7-O10 84.0(2)	O10-O11 87.9(2)	O5-O11 90.2(2)	O5-O9 95.6(2)	O5-O7 100.2(2)	90.0(1)
Fe_2^{3+}	O7-O8 82.8(2)	O8-O9 82.8(2)	O8-O8 84.2(2)	O3-O8 95.3(2)	O3-O9 96.4(2)	O3-O7 98.4(2)	89.9(1)
Fe_3^{3+}	O11-O13 77.6(2)	O11-O10 78.3(2)	O11-O14 79.0(2)	O6-O13 101.0(2)	O6-O10 101.5(1)	O6-O14 102.5(2)	91.2(1)
$Fe_4^{2.5+}$	O9-O10 82.2(2)	O8-O9 86.7(2)	O9-O14 90.0(2)	O8-O12 92.2(2)	O10-O12 92.8(2)	O12-O14 96.1(2)	89.9(1)
Fe_5^{2+}	O13-O14 75.8(2)	O13-O13 86.4(2)	O2-O14 88.0(2)	O11-O13 89.7(2)	O2-O11 94.0(2)	O2-O13 101.7(1)	89.5(1)
Fe_6^{2+}	O9-O14 78.5(2)	O4-O9 87.6(2)	O11-O14 87.6(2)	O4-O11 90.0(2)	O13-O14 92.3(2)	O4-O13 101.6(2)	90.0(1)
Fe_7^{2+}	O7-O10 81.6(2)	O7-O8 82.9(2)	O7-O7 84.5(2)	O1-O8 93.1(2)	O1-O10 97.8(2)	O1-O7 99.8(2)	90.1(1)

Table 4.18: Bond angles of O-Fe-O out of plane at 200 K.

Site	bond angle (°)			δ (°)
$Fe_{hex}^{2.5+}$	118.7(1) ($O2_h$-$O2_h$)			
Fe_1^{3+}	116.2(2) (O7-O11)	118.6(2) (O7-O9)	122.6(2) (O9-O11)	2.6
Fe_2^{3+}	113.6(2) (O8-O9)	121.0(2) (O7-O8)	121.3(0) (O7-O9)	2.9
Fe_3^{3+}	114.5(2) (O10-O13)	114.7(2) (O10-O14)	118.9(2) (O13-O14)	4.0
$Fe_4^{2.5+}$	116.7(2) (O8-O14)	119.0(2) (O8-O10)	123.0(2) (O10-O14)	2.4
Fe_5^{2+}	105.4(2) (O13-O14)	115.1(2) (O11-O14)	136.9(1) (O11-O13)	12.1
Fe_6^{2+}	108.8(2) (O9-O11)	123.7(2) (O9-O13)	126.4(1) (O11-O13)	7.1
Fe_7^{2+}	116.2(2) (O7-O8)	118.4(2) (O8-O10)	121.1(2) (O7-O10)	2.2

Table 4.19: Bond angles of O-Fe-O in the triangle of the distorted triangular bipyramidal Fe environment with $\delta = \frac{1}{3}\sum|120° - \alpha_{bond}|$.

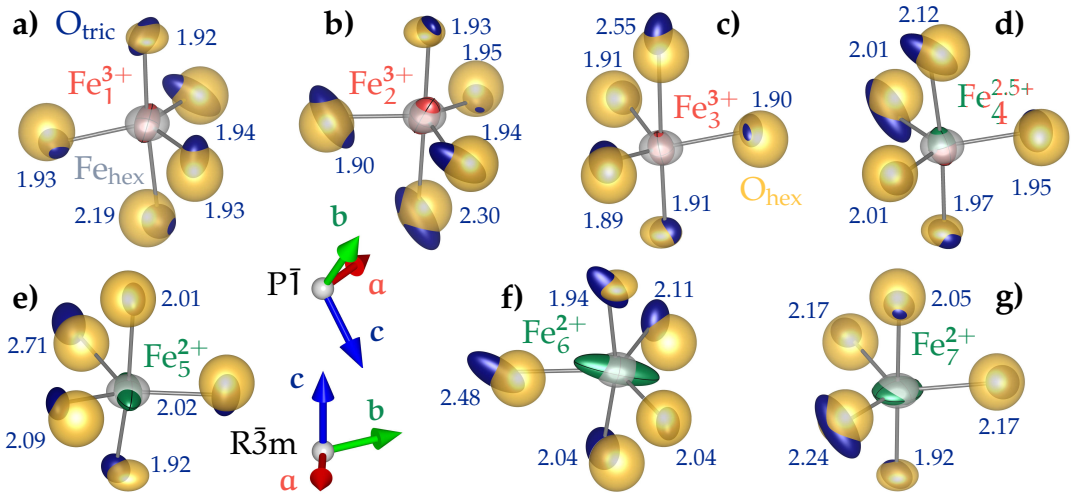

Figure 4.24: The iron environments for the seven distinct Fe-positions with different valences in the 200 K structure of $YFe_2O_{4-\delta}$. The blue numbers give the length of the Fe-O bond. (Figure made with VESTA [223].)

4.8.4 Bond valence sum analysis at 200 K

As already stated, the X-ray contrast between Fe^{2+} and Fe^{3+} is too low to be resolved directly, therefore bond valence sum analysis (see Sec. 2.3.6) is also applied to determine the Fe valence at 200 K. It is obvious from the 7 times enlarged cell with seven distinct Fe sites and a mean valence of 2.5 that there cannot be a full charge order of Fe^{2+} and Fe^{3+} as long as the structure is centrosymmetric. So at least one site must have an intermediate valence or a full spectrum of valences as suggested [170, 209] in the past should be considered.

For the bond valence sum of the Fe sites the oxygen ions building the trigonal-bipyramidal environment at room temperature were considered and the BVS was calculated for the d_{0i} of Fe^{2+} and Fe^{3+} and since no tabulated values are given for mean Fe valences, the BVS for Fe^{2+} and Fe^{3+} were averaged to account for positions with mixed valence. Table 4.20 gives the BVS for the seven Fe-sites, the green marked cells give the most likely valence for the position. Therefore Fe1, Fe2 and Fe3 are Fe^{3+} while Fe5, Fe6 and Fe7 are Fe^{2+}, Fe4 is the position with a mixed valence so $Fe^{2.5+}$. With these valences, the average Fe valence at 200,K is 2.38(20), which is lower than the expected value of 2.5. On the other hand it is comparable the Fe valence of the rhombohedral structure at room temperature of $YFe_2O_{4-\delta}$ and also $LuFe_2O_{4-\delta}$ [9]. Even when one considers all positions to be mixed the average Fe valence at 200 K is 2.41(15). Since the errorbar on the BVS is larger at 200 K than at 160 K the values can still be considered to resemble a mean valence of 2.5.

As a validity test again the BVS for the Yttrium and Oxygen sites was calculated, for the latter the different Fe valences as given in the green marked cells of Table 4.20 are used. For Yttrium the eight closest Oxygen neighbors building the octahedral environment were used for the BVS. The results are given in Table 4.21 and are close to the ideal value of three, but the deviations are larger compared to BVS at 160 K especially for Y4 with a BVS of 3.20(2). If

Site	T (K)	BVS (2+)	BVS (3+)	BVS (2.5+)	Multiplicity
Fe1	200	2.66(23)	2.84(11)	2.75(17)	2
Fe2	200	2.52(22)	2.70(10)	2.61(16)	2
Fe3	200	2.65(23)	2.83(14)	2.74(19)	2
Fe4	200	2.39(21)	2.56(10)	2.48(16)	2
Fe5	200	2.00(18)	2.14(08)	2.07(13)	2
Fe6	200	1.93(18)	2.07(08)	2.00(13)	2
Fe7	200	1.90(17)	2.03(08)	1.96(13)	2
Fe_{hex}	300	2.23(07)	2.39(04)	2.31(06)	6

Table 4.20: Bond valence sum of the Fe-sites at 200, K

the Y4 position is not split the BVS is 2.90(2). For the Yttrium and Oxygen valence the given errors are only the statistical errors from the uncertainties of the atomic positions, they do not consider the uncertainty of the d_{0i}-parameters. Considering that the uncertainty of d_{0i} will results in similar error as for the Fe positions, the valences are reasonably close to the ideal values.

Site	BVS
O1	2.06(1)
O2	2.11(1)
O3	2.09(1)
O4	2.07(1)
O5	2.15(1)
O6	2.01(1)
O7	1.96(1)

Site	BVS
O8	1.73(1)
O9	1.79(1)
O10	1.81(1)
O11	1.84(1)
O12	2.11(1)
O13	1.98(1)
O14	1.82(1)

Site	BVS
Y1	3.12(1)
Y2	3.07(1)
Y3	3.11(1)
Y4	3.20(2)

Table 4.21: Bond valence sum of the Y-sites at 200, K

If the structure is refined without the center of symmetry in spacegroup P1, as given in Appendix A.5, the received charge order pattern (cf. Tab. A.9) is the same as for the refinement in $P\bar{1}$ and still obeys a center of symmetry. All Fe sites connected by inversion in P1 show similar valences. It is therefore justified to choose $P\bar{1}$ as spacegroup. The refinement in P1 also showed large correlations (>0.9) of atomic coordinates from sites connected in $P\bar{1}$ by inversion, which also is an indication that the structure has an inversion center.

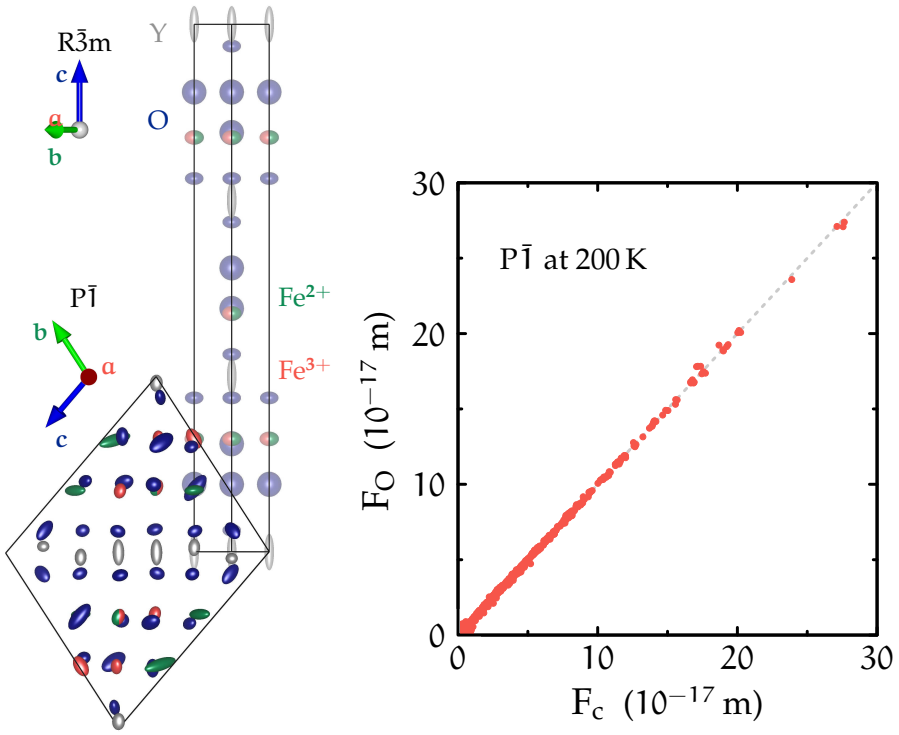

(a) comparison of R3̄m and P1̄ structures

(b) F_{obs} vs F_{calc}

Figure 4.25: (a) $YFe_2O_{4-\delta}$ structure at 210 K in relation to the R3̄m structure view along the hexagonal $[-1, 1, 0]$-axis (b) Plot of the observed structure factors F_{obs} versus the calculated F_{calc} of the R3̄m structure at 210 K.

4.8.5 Discussion

In the past the structure evaluation of $YFe_2O_{4-\delta}$ was dominated by electron diffraction [159, 162, 163, 165–169] and some powder diffraction experiments focusing mostly on the peak splitting of the structural reflections of R3̄m [160, 161, 164, 170, 187, 224].

Our propagation vector of $\left(\frac{2}{7}\frac{2}{7}\frac{3}{7}\right)$ is the same as the one suggested in [168] at 100 K, although one year later the group [169] changed the propagation vector to $(\frac{\bar{1}}{14}\frac{2}{7}\frac{1}{14})$. In the $(-2h, h, \ell)$-plane they observe reflections on lines $(\frac{2}{7}\frac{1}{7}\ell)$. Their diffraction image of the $hh\ell$-plane shows reflections on $(\frac{1}{7}\frac{1}{7}\ell)$ lines, although they say that these reflections do not lie exactly in the $hh\ell$-plane. It is remarkable that they still only observe 7 lines between (000) and (110) or $(\bar{2}10)$, the higher harmonics of odd order of $(\frac{\bar{1}}{14}\frac{2}{7}\frac{1}{14})$ seem to be missing, which makes it unclear why they change to a $\frac{1}{14}$-propagation. In our X-ray diffraction data regardless of whether we choose the $hh\ell$-plane or some symmetrically equivalent in R3̄m we never observe reflections which cannot be described with the $\left(\frac{2}{7}\frac{2}{7}\frac{3}{7}\right)$ propagation vector, its higher harmonics and symmetrically equivalent vectors, which correspond to the 6 twins.

The only structural solution suggested in the literature is from Blasco *et al.* [170] and is based on Rietveld refinement of synchrotron powder X-ray diffraction data. As we, they observe two distinct charge ordered phases between 240 and 80 K. For the 210 K structure they

observe superstructure reflections of the form $(\frac{h}{7}\frac{k}{7}\frac{\ell}{7})$ compatible with the propagation vector of $\left(\frac{2}{7}\frac{2}{7}\frac{3}{7}\right)$ we found by single crystal X-ray diffraction. Based on the room temperature structure they use representation analysis based on ISODISTORT [171] from the ISOTROPY Software Suite [172] to predict a structural model for the Rietveld refinement. From here their journey gets somehow strange instead of starting with the most primitive case of the single irreducible representation GP$(\frac{1}{7}\frac{1}{7}\frac{9}{7})$ they start with a superposition of two IRs SM$(a, -2a, 0)$ and LD$(0, 0, g)$ with $a = \frac{1}{7}$ and $g = \frac{9}{7}$ without saying why it is necessary to introduce a second primary order parameter [170]. Also one would expect reflections belonging only to one of these IRs with propagation vectors of $(\frac{1}{7}\frac{1}{7}0)$ or $(0, 0, \frac{9}{7})$, which neither they nor we observe. Their received solutions have extremely large unit cells, the refined cell has a volume of 4333.924(5) Å ^{3} with 25 formula units (the volume is falsely given as 43339.24(5) Å ^{3}). The other solution is so large Fullprof could not handle it, with a volume of 30404 Å ^{3} [170]. From the 185.000 structures of the Inorganic Crystal Structure Database [225] 5268 structures have a unit cell volume over 4000 Å ^{3} of which 758 were refined by powder diffraction, none of those was refined in a triclinic spacegroup.

To handle such a big structure, they refine symmetry adapted modes step by step and discard all mode amplitudes which are smaller than their uncertainty, in the end they have 72 mode amplitudes [170]. In comparison the triclinic seven times enlarged superstructure, we use, has 79 free parameters (75 atomic coordinates and 3 displacement parameters and 1 scale factor (if twinning is not considered). It is hard to justify a separate step by step refinement of single modes through such a small reduction of the needed parameters.

For the 80 K phase they observe a superposition of two phases, as we do. Their phase is characterized by a combination of the 200 K phase and additional superstructure peaks of the form $(\frac{h}{4}\frac{k}{2}\frac{\ell}{4})$. Considering only the latter, they present a list of the "simplest cells" compatible with these reflections, received from ISODISTORT, to me it is unclear how these cells where received. They end up with a model with 504 fractional coordinates, a similar amount as in their 200 K structure. They observe the following reflections which cannot be described with the propagation vector $\left(\frac{1}{4}\frac{1}{4}\frac{3}{4}\right)$: $(\frac{1}{2}, \bar{1}, 8)$, $(\frac{\bar{1}}{2}, 0, 5)$ and $(\frac{1}{2}\bar{1}3)$ [170]. None of these reflections, or in R$\bar{3}$m symmetrically equivalent reflections, are observed in our single crystal X-ray data. If one considers false indexing of the powder pattern, the closest reflections to $(\frac{1}{2}, \bar{1}, 8)$ with $|\mathbf{Q}| = 2.70$ are $(\frac{\bar{3}}{4}, \frac{1}{4}, 9.25)$ with $|\mathbf{Q}| = 2.71$ or $(\frac{3}{4}\frac{3}{4}\frac{\bar{3}}{4})$ with $|\mathbf{Q}| = 2.69$ and for $(\frac{\bar{1}}{2}, 0, 5)$ with $|\mathbf{Q}| = 1.64$ the closest reflection is $(\frac{\bar{1}}{4}, \frac{\bar{1}}{4}, 5.25)$ with $|\mathbf{Q}| = 1.60$. It is unclear if they really mean $(\frac{1}{2}, \text{integer}, \text{integer})$ reflections, or if this is a mistake, since in their powder pattern no reflection is marked with such indices. Also $(\frac{1}{2}, \text{integer}, \text{integer})$ reflections cannot be created with L-propagation $(\frac{\bar{1}}{2}\frac{1}{2}\frac{1}{2})$, which they stated they used [170]. Reflections with L-propagation are equivalent to the second harmonic of $\left(\frac{1}{4}\frac{1}{4}\frac{3}{4}\right)$. Their refinement of the room temperature structure in R$\bar{3}$m shows a by 10% too low intensity on all high intensity peaks [170], which might be an indication for the not accounted 2D charge order, which is still present at room temperature and is also not accounted in our refinement of the room temperature structure.

Figure 4.26 shows the charge order pattern of our solution at 200 K, where the upper part of the figure is the view of the Fe bilayer along $\mathbf{c}_{\text{hex}}$ and the lower part a view along the

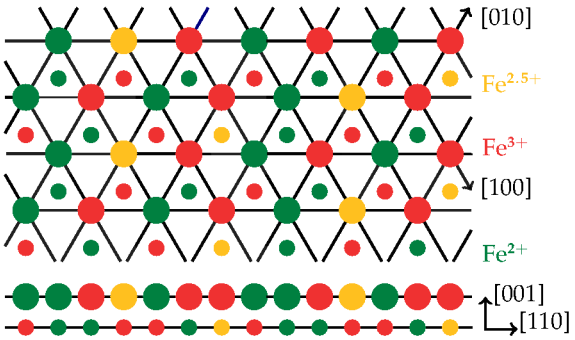

Figure 4.26: Charge order structure at 200 K, where the mixed $Fe^{2.5+}$ is marked in yellow. The upper part is the view along $\mathbf{c}_{\text{hex}}$ and the lower part is a view along $[1, \bar{1}, 0]_{\text{hex}}$.

perpendicular direction $[1, \bar{1}, 0]_{\text{hex}}$. The corresponding pattern for 160 K is shown in Figure 4.21b. In the 200 K pattern exists a mixed $Fe^{2.5+}$ site marked in yellow beside the Fe^{2+} (green) and Fe^{3+} (red) sites.

Table 4.20 shows that three sites are clearly Fe^{2+}, so three electrons from the 3.5 electrons we have to distribute can be considered as localized to the Fe5, Fe6 and Fe7 positions. This leaves only half an electron for the other four sites. The Fe1, Fe2 and Fe3 sites show a valence slightly below 3, while the Fe4 position shows an intermediate valence around 2.5. Adding up the deviations from the integer valence, these sites share approximately 1 electron, which is 0.5 more than what is left by the localized Fe^{2+} positions, this is just at the upper border of the sum of the error bars on the BVS of these sites.

As stated before the electrons on the Fe^{2+} sites are localized and the 0.5 remaining electron is shared between the three Fe^{3+} and the $Fe^{2.5+}$ sites. Especially form the lower part of Figure 4.26, it is obvious that these four sites are right next to each other, which makes the electron hopping between them reasonable. For the mixed $Fe^{2.5+}$ site four neighbors in the bilayer are Fe^{3+} and three are Fe^{2+}. The localized Fe^{2+} positions restrict the electron movement on diagonal lines in Figure 4.26 roughly along $[1, 2, 0]_{\text{hex}}$. This is further discussed in Section 4.11.

4.8.6 Mode decomposition

For the 200 K phase lowering the the symmetry to $P\bar{1}$ with the transformation matrix as given in Eqn. (4.20) the 6c site symmetry resolves into seven Fe positions and another 7 connected by inversion. With the propagation vector $\mathbf{p} = \left(\frac{2}{7}\frac{2}{7}\frac{3}{7}\right)$, the fourth harmonic is the negative of the third harmonic, therefore $n = 3$ in Eqn. (4.16). The Fe positions connected through translation in the $R\bar{3}m$ cell are identified as:

$$\begin{aligned} &Fe1^{3+}_{\text{tric}} = (1, 2, z)_{\text{hex}} \quad Fe2^{3+}_{\text{tric}} = (1, 1, z)_{\text{hex}} \quad Fe3^{3+}_{\text{tric}} = (3, 3, z)_{\text{hex}} \quad Fe4^{2.5+}_{\text{tric}} = (0, 0, z)_{\text{hex}} \\ &Fe5^{2+}_{\text{tric}} = (2, 3, z)_{\text{hex}} \quad Fe6^{2+}_{\text{tric}} = (2, 2, z)_{\text{hex}} \quad Fe7^{2+}_{\text{tric}} = (0, 1, z)_{\text{hex}} \end{aligned} \tag{4.25}$$

Without losing information we can set $z = 0$ since it will only add a constant phase to all contributions, this corresponds to an origin shift and we are free to choose a basis. This sets an Fe Atom at the Origin. At 160 K this lead by chance to a column with only zeros.

Separation of Eqn. (4.16) into sine and cosine terms leads to:

$$\mathrm{Val} = A \cdot \sin(2\pi \mathbf{p} \cdot \mathbf{r}) + B \cdot \cos(2\pi \mathbf{p} \cdot \mathbf{r}) + C \cdot \sin(2\pi \cdot 2\mathbf{p} \cdot \mathbf{r}) + D \cdot \cos(2\pi \cdot 2\mathbf{p} \cdot \mathbf{r}) \quad (4.26)$$

$$+E \cdot \sin(2\pi \cdot 3\mathbf{p} \cdot \mathbf{r}) + D \cdot \cos(2\pi \cdot 3\mathbf{p} \cdot \mathbf{r}) + G \quad (4.27)$$

Choosing one Fe position at the origin chooses the phase so that this Fe atom is not influenced by the mode belonging to the sine, this is also the phase choice used by ISODISTORT [171].

$$\begin{pmatrix} 1 \\ 1 \\ 1 \\ 0 \\ -1 \\ -1 \\ -1 \end{pmatrix} = \begin{pmatrix} -0.781831 & 0.623490 & -0.974928 & -0.222521 & -0.433884 & -0.900969 & 1 \\ -0.433884 & -0.900969 & 0.781831 & 0.623490 & -0.974928 & -0.222521 & 1 \\ -0.974928 & -0.222521 & 0.433884 & -0.900969 & 0.781831 & 0.623490 & 1 \\ 0 & 1 & 0 & 1 & 0 & 1 & 1 \\ 0.433884 & 0.900969 & -0.781831 & 0.623490 & 0.974928 & -0.222521 & 1 \\ 0.781831 & 0.623490 & 0.974928 & -0.222521 & 0.433884 & -0.900969 & 1 \\ 0.974928 & -0.222521 & -0.433884 & -0.900969 & -0.781831 & 0.623490 & 1 \end{pmatrix} \cdot \begin{pmatrix} A \\ B \\ C \\ D \\ E \\ F \\ G \end{pmatrix} \quad (4.28)$$

Since we have 7 equations and 7 variables and the determinant of the matrix in Eqn. (4.28) is not zero the system can be solved by inverting the matrix and multiplying the inverse matrix from the left with the column vector on the left side of Eqn. (4.28).

Which leads to: A=−1.21, B = 0, C = 0.14, D = 0, E = −0.35, F = 0 and G = 0. So we have only modes which leave one point unchanged (sine) with a large contribution from the first harmonic GP1=$\left(\frac{2}{7}\frac{2}{7}\frac{3}{7}\right)$ and a small part from the second harmonic GP2 = $\left(\frac{3}{7}\frac{3}{7}\frac{1}{7}\right)$ and a medium contribution from the third harmonic GP3 = $\left(\frac{1}{7}\frac{1}{7}\frac{9}{7}\right)$.

The mode decomposition using ISODISTORT [171] from the ISOTROPY Software Suite [172] of the distorted cell is given in Table 4.22.

mode	GM1+	GM3+	GP1 $\left(\frac{2}{7}\frac{2}{7}\frac{3}{7}\right)$	GP2 $\left(\frac{3}{7}\frac{3}{7}\frac{1}{7}\right)$	GP3 $\left(\frac{1}{7}\frac{1}{7}\frac{9}{7}\right)$
A_s	0.09	0.12	1.11	0.71	0.49
A_p	0.03	0.05	0.42	0.27	0.19
exp. A_s	0	0	1.21	0.14	0.35

Table 4.22: Mode amplitudes (sum) from mode decomposition of the distorted 200 K structure determined using ISODISTORT [171]. As is the amplitude of the triclinic CO cell and $A_p = A_s \cdot \sqrt{V_p/V_s}$ where V_p is the volume of the primitive parent structure and V_s the volume of the primitive CO supercell.

Table 4.23 shows the distortion mode amplitudes along $\mathbf{c}_{hex}$ for the Fe sites separated for sine and cosine contributions. It is clear that in contrast to the mode decomposition of the charge order pattern, the distorted structure leads to non-zero contributions from the cosine parts of the modes belonging to the general point $\left(\frac{2}{7}\frac{2}{7}\frac{3}{7}\right)$ and its higher harmonics. The mode amplitude for the mode of the general point $\left(\frac{2}{7}\frac{2}{7}\frac{3}{7}\right)$ in Table 4.22 is the largest, which confirms that $\left(\frac{2}{7}\frac{2}{7}\frac{3}{7}\right)$ is the preferable as propagation vector instead of $\left(\frac{1}{7}\frac{1}{7}\frac{9}{7}\right)$. The GP3 distortion of

mode	GP1 $\left(\frac{2}{7}\frac{2}{7}\frac{3}{7}\right)$	GP2 $\left(\frac{3}{7}\frac{3}{7}\frac{1}{7}\right)$	GP3 $\left(\frac{1}{7}\frac{1}{7}\frac{9}{7}\right)$
sine A_s	-0.053	-0.1114	-0.019
cosine A_s	-0.111	0.0536	-0.046

Table 4.23: Sine and cosine mode amplitudes (A_s) for distortions along $\mathbf{c}_{hex}$ from mode decomposition of the distorted 200 K structure determined using ISODISTORT [171].

Y and Fe is small, which explains the observed intensity distribution, where the reflections belonging to GP3 are the weakest. To understand which modes drive the charge order, one has to analyze the influence of different modes on the the bond valence sum, because only distortions changing the BVS are correlated with the charge order.

For this we have calculated the BVS for distorted structures based on the modes from the refined structure with one mode scaled by a factor of $\frac{1}{2}$. For GP2 and GP3 this brings the mode amplitudes closer to the values calculated from the charge pattern.

Surprisingly the amplitude reductions of either GP1, GP2 or GP3 all have a similar effect on th BVS. The reduction of GP1, which is the main distortion mode, brings all valences closer together to 2.5, which is not surprising since it reassembles the rhombohedral case. All reductions lower the charge on the former mixed Fe4 site to around 2.6 and turn the former 2+ site Fe6 in a clear 3+ site. Fe1 and Fe2 show now a 2.5 valence and Fe3, Fe5 and Fe7 are identified as 2+. The conclusion is that all three distortion modes collectively determine the charge order of $YFe_2O_{4-\delta}$ at 200 K, which is consistent with the valence mode decomposition (Table 4.22), although the amplitude of GP2 is rather different. The charge order seems to be very fragile and not completely frozen.

4.9 Phase stability in magnetic fields

To test if a magneto structural transitions, as in $LuFe_2O_{4-\delta}$ [31], exists in $YFe_2O_{4-\delta}$ we conducted an experiment in pulsed magnetic fields up tp 30 T. The experimental setup is described in Section 2.5. Figure 4.27a shows the raw detector images of the (113)-reflection at 160 K measured with the Pixrad detector for one second. The splitting of the reflection due to the charge order domain structure can be resolved, which could not be realized with the laboratory X-ray diffraction. Figure 4.27b and (c) compare the Pilatus Si and the Pixirad CdTe detectors against each other. The $(\frac{1}{2}\frac{1}{2}\frac{3}{2})$ reflection is shown measured for 0.40 ms at the peak of a 30 T field pulse. The reflection is clearly observable, which indicates that no charge order phase change was induced through the magnetic field. Due to the high X-ray energy of 20 keV the CdTe detector obeys a 6 times better quantum efficiency than the Silicon detector.

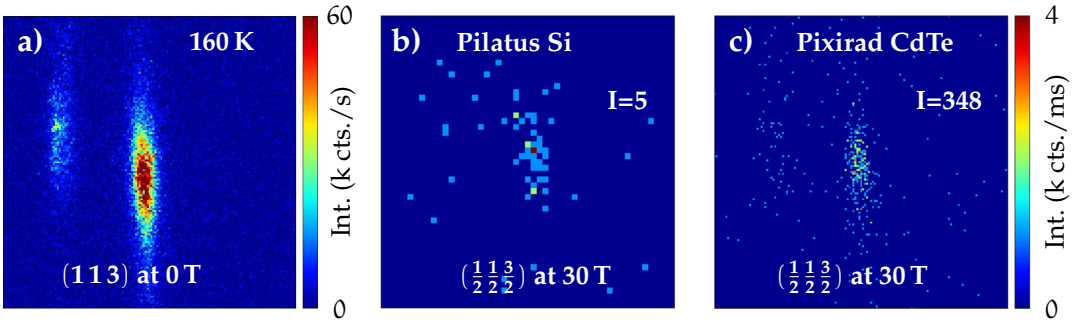

Figure 4.27: Detector images at 160 K of (a) (1 1 3) in zero field and (b),(c) $(\frac{1}{2}\frac{1}{2}\frac{3}{2})$ in 30 T with different detectors.

Figure 4.28 shows the Intensity of the $(\frac{1}{2}\frac{1}{2}\frac{3}{2})$ superstructure reflection at 160 K measured time resolved during a 20 T field pulse. The green curve shows the time dependence of the magnetic field pulse calculated from the current discharge of the capacitor bank. The red curve shows the triggers for the Pilatus detector, which was set to measure for 0.4 ms every 5 ms in such a way that one image is measured exactly during the maximum of the field pulse. The Pilatus detector had to be used because it was the only detector which had a fast enough reading time to gather images during the pulse and right before and after the pulse. The Pixirad detector, which has a better quantum efficiency because of the CdTe-sensor instead of Si used in the Pilatus, is too slow to collect images in close proximity to the peak. To compensate for the bad quantum efficiency of the Si-detector, the Intensities from several pulses were averaged to gain a better statistics. Since the magnet needs to cool for 12 minutes after each 30 T pulse, this procedure is quite time consuming and the necessary beamtime could be drastically reduced if a fast CdTe detector could be used. As can be seen in Figure 4.28 no field induced decrease of the intensity is observed on the charge ordered superstructure reflections. Also if the field was increased to 30 T the reflection did not change its intensity. The field strength necessary to alter the magnetic state will be reduced close to the Néel temperature. Therefore we increased the temperature to 205 K, which is in the hysteretic region of the

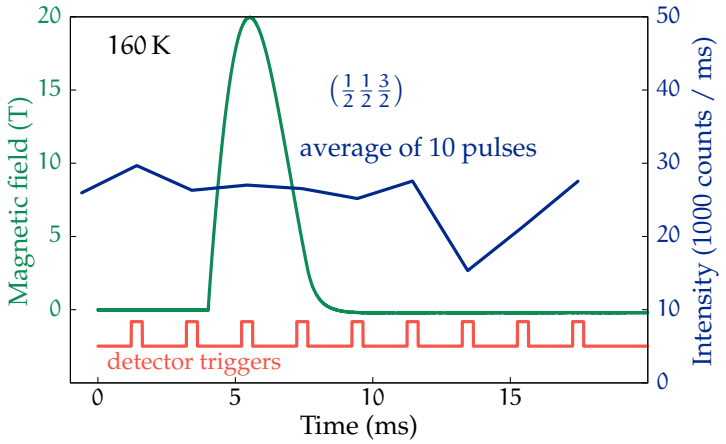

Figure 4.28: Average of 10 field pulses of the Intensity of $(\frac{1}{2}\frac{1}{2}\frac{3}{2})$ measured for 0.4 ms each at at 9 time positions during a 20 T field pulse.

magnetization (Figure 4.6) but no metamagnetic transition could be induced. The same was tried on charge order reflections at 225 K during cooling, without any induced transitions.

A further increase of the temperature closer to the Neel temperature during warming could not be realized since the sample was destroyed in a 30 T field pulse at 205 K. This might be caused by the increased magnetization, or the sample had a metamagnetic transition to a ferrimagnetic phase and was then destroyed by the forces from different domains. But this is speculative. The remains of the sample where checked with single crystal X-ray diffraction, but no changes to the state before the experiment were observed.

Considering that the magnetic moment of the sample was not perpendicular to the magnetic field but tilted 12° in field direction, the effective field is reduced by a factor $1-\sin(12°)$. Therefore we can state that $YFe_2O_{4-\delta}$ shows either no metamagnetic transitions up to 24 T or the charge order is not influenced by changes of the magnetic structure. The latter seems unlikely considering that the temperature induced charge order transitions are also magnetic transitions.

4.10 The magnetic phases of $YFe_2O_{4-\delta}$

4.10.1 Neutron diffraction

Before we come to a general discussion of the charge order we will also examine the magnetic structure of stoichiometric $YFe_2O_{4-\delta}$. The following introduction in Chapter 4.10.1 is a repetition of the results obtained in my diploma thesis [20], where the details can be found.

All neutron diffraction experiments were performed on the same 42 mg $YFe_2O_{4-\delta}$ single crystal grown during my diploma thesis. The crystal was always preoriented using Laue X-ray diffraction. The measurements presented in Figure 4.29 were all measured at DNS (see Sec. 2.3.9). $YFe_2O_{4-\delta}$ shows three different magnetic states, the transition temperatures follow the macroscopic magnetization and coincide with the charge order transitions. Above the ordering transition at 228.5 on cooling (248.5 K on warming) only diffuse magnetic scattering along $\left(\frac{1}{3}\frac{1}{3}\ell\right)$ and $\left(\frac{2}{3}\frac{2}{3}\ell\right)$ is observed (right part of Figure 4.29e indicating a random stacking of still antiferromagnetically ordered layers. Below this transition temperature two 3D ordered magnetic phases are observed, the transition between both lies around 180 K on cooling in accordance with the macroscopic magnetization (Figure 4.6). Figure 4.29a and (b) show a part of the reciprocal hhℓ-map in the spin flip channel with the neutron polarization perpendicular to the scattering plane. So only magnetic scattering is visible.

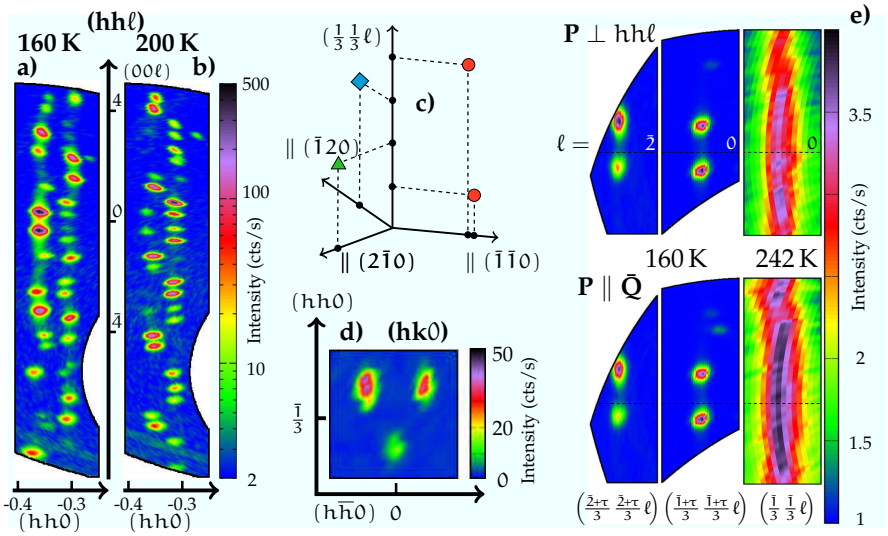

Figure 4.29: (a) Spin flip channel of the (hhℓ)-plane at 160 and (b) at 200 K
(c) Sketch of domain contributions (reproduced from [30])
(d) Spin flip channel of the (hk0)-plane at 200 K
(e) cuts from hhℓ-plane for $\mathbf{P} \perp$ hhℓ (top) and $\mathbf{P} \parallel \tilde{\mathbf{Q}}$ (bottom)
((a), (b) and (e)) reproduced from [20]).

The scattering pattern at 200 and 160 K consists of peaks arranged in two lines along $\left(\frac{1}{3}\frac{1}{3}\ell\right)$, which are shifted slightly in the positive and negative direction along (hh0). A similar pattern is observed along the $\left(\frac{2}{3}\frac{2}{3}\ell\right)$-line (cf. Appendix A.6 and A.7). The intensity distribution of the

peaks changes drastically while cooling from 200 K to 160 K . To determine the direction of the magnetic moment, polarization analysis was used. Figure 4.29e shows parts of the $hh\ell$-plane at 160 K and 242 K, measured with different neutron polarizations. The upper part of the figure is the spin flip channel measured with the neutron polarization **P** pointing out of the scattering plane $hh\ell$. In this configuration, scattering from magnetic moments lying in the $hh\ell$-plane will lead to spin flip scattering, which is shown here. In contrast to this the lower part of Figure 4.29e also shows the spin-flip channel but the polarization **P** is parallel to the average scattering vector $\tilde{\mathbf{Q}}$. Since only the magnetization **M** perpendicular to **Q** can be measured $\mathbf{P} \parallel \tilde{\mathbf{Q}}$ induces $\mathbf{M}_{\perp \mathbf{Q}} \perp \mathbf{P}$ so all magnetic scattering regardless of the moment direction will be spin flip. This is a rough approximation since in a multi detector experiment the polarization cannot be parallel to all **Q** vectors. The chosen region of reciprocal space is close enough to **P** to justify this approximation. As can be seen from the comparison of the different polarization choices at 242 K, the measurement with $\mathbf{P} \parallel \tilde{\mathbf{Q}}$ shows a higher intensity than the one with $\mathbf{P} \perp hh\ell$ indicating a magnetic moment not lying in the $hh\ell$- plane. The intensity difference corresponds to a deviation of 30° from an ideal Ising spin system with $\mathbf{c}_{\text{hex}}$ as the easy axis. In the case of the 3D ordered phase (left and center image of Figure 4.29e) no intensity variation is observed indicating that the spins are pointing parallel to $\mathbf{c}_{\text{hex}}$. The deviation from the Ising character above the charge order transition could be explained by a disorder of the Fe^{3+} spins. The Fe^{2+} spins are aligned parallel $\mathbf{c}_{\text{hex}}$ due to spin orbit coupling and the orbital moment. If the Fe^{3+} spins above the CO transition point in random directions, this is an average deviation of 60° from $\mathbf{c}_{\text{hex}}$. Since half of the Fe ions are Fe^{2+}, with a moment parallel $\mathbf{c}_{\text{hex}}$, the mean deviation for all Fe ions from $\mathbf{c}_{\text{hex}}$ will be 30° as observed in polarized neutron diffraction.

The anisotropy observed in magnetization measurements [158, 226] also indicates an Ising spin system and this is a generally accepted consent [19, 31, 198, 226–231] even before de Groot *et al.* [123] determined the spin-structure of $LuFe_2O_{4-\delta}$. It was confirmed with several methods including magnetization measurements [226], polarization analysis in resonant X-ray diffraction [75], where a large orbital moment is observed [198], density functional theory and Monte Carlo calculations [231], and the observation of Ising pancake like domains in magnetic force microscopy [230, 232]. Nevertheless it was never directly tested with polarized neutron scattering in $LuFe_2O_{4-\delta}$. This experimental confirmation of the generally assumed Ising character of the $RFe_2O_{4-\delta}$-system, drastically reduces the possible spin structures in $YFe_2O_{4-\delta}$, since there are only two spin states for each Fe site left. if full order is assumed.

4.10.2 A multi domain state

The assumed incommensurate shift of the magnetic Bragg peaks from the $\left(\frac{1}{3}\frac{1}{3}\ell\right)$-line resembles a similarity to the contributions of three domains to the CO-pattern of $LuFe_2O_{4-\delta}$ suggested in [30]. Angst *et al.* provided as explanation for the observed intensity variation on the $\left(\frac{1}{3}\frac{1}{3}\ell\right)$-line, the incommensurable shifting of peaks along $(\bar{1}\bar{1}0)$, $(\bar{1}20)$ and $(2\bar{1}0)$ as shown in Figure 4.29c originating from three domains arranged in a 120° pattern.

To test whether such a domain arrangement can explain the shifting and intensity vari-

ations of our magnetic scattering, measurements of a plane perpendicular to $hh\ell$-should be examined since it should show a peak arrangement in an equilateral triangle around $\left(\frac{1}{3}\frac{1}{3}\ell\right)$. Therefore we measured the $(hk0)$-plane shown in Figure 4.29d, as expected there is an equilateral triangle observed. Through the broad resolution ellipsoid of the DNS experiment (see Sec. 2.3.9) the hhl-plane shows also reflections which lie above or below the plane. To determine the spin structure the exact position of the magnetic reflections and their integrated intensity have to be known, the DNS instrument cannot offer this in a reasonable timeframe.

4.10.3 The spin structure at 200 K

To receive the integrated intensities necessary for a refinement of the spin structure, we went to the D10 beamline at the ILL, which is a four circle diffractometer with an area detector, which allows fast collection of magnetic reflections (see Sec. 2.3.10). The area detector is especially necessary since the magnetic unit cell could not be determined from the DNS data and therefore the exact positions where reflections are expected where unknown. We therefore systematically scanned an area of the reciprocal space around the $\left(\frac{1}{3}\frac{1}{3}\ell\right)$ and $\left(\frac{2}{3}\frac{2}{3}\ell\right)$ lines. Since polarization analysis is not available at D10 and its use would unnecessary increase the measurement time, charge order reflections were also collected in this scans. Since the polarization analysis at DNS showed no magnetic intensity on charge order or structural reflections, overlap of these with magnetic reflections could be excluded. Nevertheless CO-reflections are often in close proximity to magnetic reflections, so that every detector image had to be inspected manually to exclude regions with CO-reflections. In some cases powder rings from the aluminum sample holder had to be excluded. To get integrated intensities rocking scans were done on previously determined reflection positions. We collected 706 omega scans, each consisting of around 25 detector images, on magnetic and structural reflections including charge order superstructure reflections. To speed up the integration process a python program was written, which shows all frames belonging to a specific omega scan, the integration of these images and the integrated intensity versus Ω. On the basis of these images, manual integration masks were chosen for all images which showed contamination from neighboring reflections or aluminum rings. The integration was done automatically considering these masks by fitting pseudovoigt functions with constant background to the rocking curves. The fitting curves were plotted together with the data to check if the parameters were reasonable. Figure 4.30 shows the output of the python program for a typical magnetic reflection.

The reflections were corrected for the Lorentz factor, which is for an ω-scan in Euler geometry [233],

$$L = \frac{1}{\sin(2\theta)} \qquad \text{with} \qquad I_{real} = L \cdot I_{obs} \tag{4.29}$$

and corrects for the different angular velocities of the motion of reflections with different lengths of $\mathbf{Q}$ [67]. This is only exact for reflections lying in the center of the area detector, which is the case for all used reflections (cf. e.g. Fig. 4.30). Together with the non-infinitesimal size of the reflection and surface thickness of the Ewald sphere, this leads to different times

reflections with different $|\mathbf{Q}|$ will stay in reflection condition. Short scattering vectors lead to shorter times, decreasing the observed intensity, the Lorentz factor corrects for that.

The measured intensities have to be corrected for several other reasons. The magnetic form factor originates from the fact that the magnetic interaction of the neutron takes part with the electron shell of the atom and not the point size nucleus. It reduces the measured intensities at higher $\mathbf{Q}$, following Eqn. (4.30).

$$I_{real} = f_m(\mathbf{Q})^{-2} \cdot I_{obs} \quad \text{with } f_m(\mathbf{Q}) \text{ as defined in Eqn. (2.51)} \tag{4.30}$$

Only the magnetic moment perpendicular to $\mathbf{Q}$ contributes to the intensity of a reflection [234]. The magnetic moment in $YFe_2O_{4-\delta}$ in the 3D ordered phase is pointing in $\mathbf{c}_{hex}$ direction. Therefore the measured intensities have to be corrected as $I_{real} = W_{M_\perp} \cdot I_{obs}$ with

$$W_{M_\perp} = \frac{1}{|\sin(\alpha)|} \quad \text{with } \alpha = \arccos\left(\frac{\mathbf{Q}\cdot\mathbf{M}}{|\mathbf{Q}|\cdot|\mathbf{M}|}\right) \tag{4.31}$$

where the scalar product is taken in Cartesian coordinates.

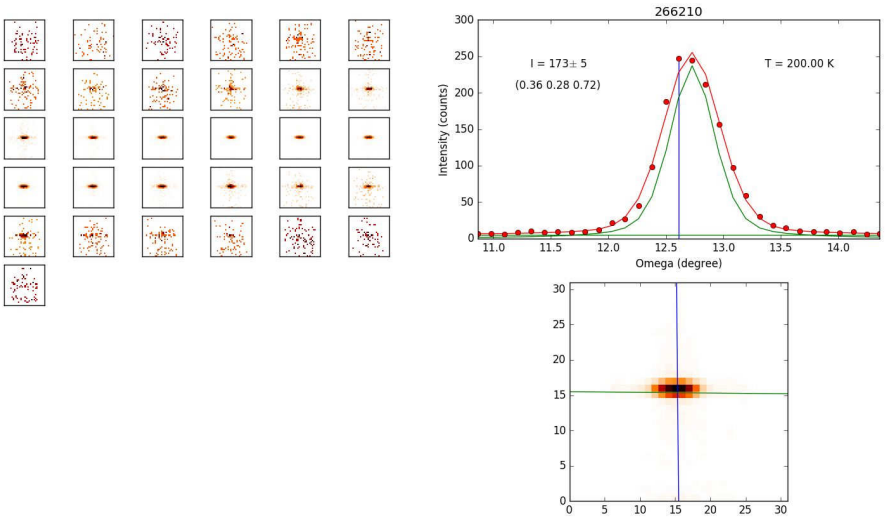

Figure 4.30: Output of the python program written for the D10 data integration on a typical magnetic reflection. The left part shows the single detector images of the ω-scan, the image at the bottom shows the pixelwise integration of all these images, the cross marks the detector center. The upper right image shows the integration of the left images in dependence of omega with a PseudoVoigt fit and a constant background, the blue line marks the center of the omega scan. The red curve is the best fit and the green curve the initial fit suggested by the *guess()* function of the *lmfit* package.

The thermal motion of the atoms will lead to an intensity decrease described by the Debye-Waller factor [235], assuming an isotropic thermal displacement of the Fe-ions the intensity decrease can be described as,

$$I_{obs} = I_{real} \cdot \exp\left(-\frac{1}{3}\langle u^2\rangle |Q|^2\right) \tag{4.32}$$

with $\langle u^2\rangle = 0.008\,\text{Å}^2$, the mean square displacement of an Fe atom received from X-ray diffraction.

The integration process showed that charge order reflections could be observed but the intensities were too weak to be used for structure refinement. Unfortunately at the time of the experiment we were not clear about the charge order structure and we collected mostly first order reflections of the propagation vector $(\frac{1}{7}\frac{1}{7}\frac{9}{7})$, since these are only the fourth order of the final propagation vector $(\frac{2}{7}\frac{2}{7}\frac{3}{7})$ they tend to be weak and could not be measured in reasonable counting times. Therefore only the 175 structural reflections belonging to the $R\bar{3}m$ cell were used in the structural refinement. The much stronger first order reflections of $(\frac{2}{7}\frac{2}{7}\frac{3}{7})$ were regularly observed in omega scans on close magnetic reflections but were only indexed during the integration after the experiment.

Figure 4.31 shows the relative absolute difference in intensities between Friedel mates of all measured reflections of the hexagonal structure in comparison to the relative uncertainty of the measured intensities. In Figure 4.31 the scattering angle is increasing from the left to the right. No systematic deviations could be observed and the difference between the Friedel mates is comparable to the measurement uncertainty. Considering the small amount of reflections where Friedel mates were measured and the statistical uncertainty an empirical absorption correction was not feasible. No reflection was measured several times with different azimuths. Therefore an analytical absorption correction was done in Jana2006 using Gaussian grid and indexed crystal facets. The crystal is small (10 mm^3) and the linear attenuation factor at $\lambda = 2.36\,Å$ is only $0.104\,cm^{-1}$, the ratio between the longest and shortest face distances is less than 4.2 ((100) vs. (001)), which results in transmission factors between 0.97 and 0.99 for the structural reflections. The influence on the differences in intensities between the Friedel mates is much less than the size of the points in Figure 4.31 and therefore not shown. Since the absorption correction had no reasonable effect on the refinement and introduces some uncertainty because of the general problem of an analytical absorption correction on a twinned crystal, due to partly illumination, no absorption correction was sued in the refinement.

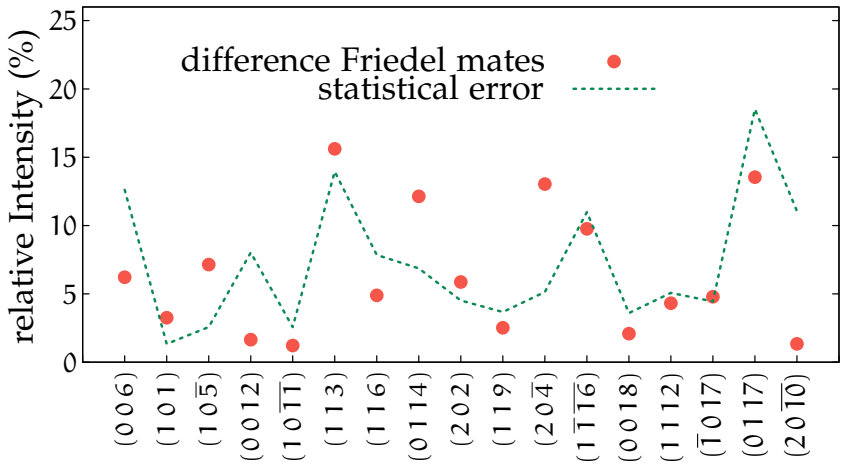

Figure 4.31: Relative difference between the Friedel mates of structural reflections in comparison to the measurement uncertainty (the error is a continuous line for visibility).

Integrated intensities of 330 magnetic reflections were collected, 179 had to be discarded

because the integration was not reliable, because of close CO reflections, not broad enough omega scans, aluminum lines, or they belong to a propagation based on the 160 K CO, which will be discussed in Sec. 4.10.5. Finally, only 151 magnetic reflections were used for the structural refinement.

All magnetic reflections can be indexed with a propagation vector of $(0\frac{3}{2}1)$ in the triclinic cell of the 200 K $P\bar{1}$ charge order supercell, in hexagonal notation this corresponds to $(\frac{5}{14}\frac{5}{14}\frac{18}{14})$. It is worthwhile to notice that if higher harmonics are considered this is equivalent to $(0\frac{1}{2}0)$ in the triclinic cell. The multiple domains from the CO-structure have of course to be considered. Due to the small amount of usable reflections a restriction to the reflections of only one domain as in the X-ray diffraction structure solution is unreasonable. Since the magnetic reflections show no overlap the handling of the twins is straight forward. The 151 magnetic reflections are distributed almost evenly over the six domains. The number of reflections for twin1 to twin6 are 21, 20, 22, 16, 27, 23.

Jana2006 will be used for the refinement of the magnetic structure. The magnetic cell can be described with a two times in **b**-direction enlarged CO cell and in the following all spin moments from the 14 Fe sites are considered as free variables, the spin direction is fixed in $\mathbf{c}_{\text{hex}}$ direction.

The magnetic structure refinement option of Jana2006 assumes that the initial structure is not twinned and all twinning is induced through the magnetic order. To overcome this the twinning matrices from the 200 K CO structure have to be transformed to the new magnetic cell, which was done with the cell transformation dialog of Jana2006 [64, 222]. After a new magnetic structure was created with the representation analysis option of Jana2006 [64, 222], the twinning matrices had to be written to the m50 file. Also the twin flags, identifying to which domain a reflections belongs to, had to be set by hand in the m95 file, since Jana2006 [64, 222] assumes an untwinned structure at the beginning of the representation analysis. As the polarization analysis at 160 K shows $YFe_2O_{4-\delta}$ is a true Ising-spin-system and only spin-models with $\mathbf{S} \parallel \mathbf{c}_{\text{hex}}$ have to be considered.

Representation analysis based on the magnetic propagation vector $(0\frac{1}{2}0)$, which is a special point, and the triclinic CO cell (Sec. 4.8) leads to two irreducible representations both with magnetic space group $P_s\bar{1}$. Each with 7 distinct Fe sites, one has no origin shift the other a shift by $(0, \frac{1}{2}0)_{\text{tric}}$. If one considers three possible spin values $\{-1, 0, 1\}$, where zero is allowed as a value to provide some degree of disorder, this gives 3^7 possible spin states. Since the magnetic propagation vector is $(0, \frac{1}{2}, 0)$ a full anti-ferromagnetic order would be possible, nevertheless, the refinement is not restricted to this case. The moments were restricted to point along $\mathbf{c}_{\text{hex}}$ in the refinement and the moments were free on each site.

Since only a 175 structural reflections and no CO reflections were usable, a refinement of the 75 atomic coordinates and 25 isotropic displacement parameters is not possible. Therefore the atomic coordinates were fixed to the values from the structure determined by X-ray diffraction in Section 4.8 . One isotropic displacement parameter was used for all atoms. Introducing different displacements parameters for Y, Fe and Oxygen did not lead to a significant improvement of the refinement and was therefore not done to reduce the number of free parameters. All Fe positions were treated with the magnetic form factor of Fe^{3+}, because in

$LuFe_2O_{4-\delta}$ it was found that the Fe^{2+} position shows a similar magnetic moment through the strong orbital moment [123, 194, 198]. In $LuFe_2O_{4-\delta}$ the introduction of different Fe^{2+} and Fe^{3+} form factors lead to an minor improvement of the spin structure solution, where for Fe^{2+} not only the spin moment was considered [123].

The representation analysis lead to two possible structures if the inversion symmetry is conserved. One structure belongs to the irreducible representation Y1+ the other to Y1- in the notation of Miller and Love [236] and the difference between the structures is an origin shift by $(0\frac{3}{2}1)$.

The representation analysis in the version of Jana2006 from July 2017[1], both possibilities are listed and additionally the non-centrosymmetric solution.

While the refinement based on the 200 K $P\bar{1}$ structure lead to a very good weighted R value of 5.7 for all reflections and 6.6 for the magnetic reflections, the refined moments were totally unrealistic since some were larger than 15 μ_B, regardless of which of the two representations were used. One reason for this could be that some of the magnetic measured intensities were wrong, which is unlikely since questionable reflections were excluded. The other reason would be that the placement of the Fe atoms in the 200 K CO structure is wrong. Some of the Fe ions in the 200 K structure obey huge anisotropic displacement parameters and it could be that these prevent the description by isotropic displacement parameters or that splitted positions are necessary. Using a CO structure based on a refinement of the X-ray data with isotropic displacement parameter, as a basis for the magnetic refinement, did lead to very large R-values >30 and unreasonable moments as well. Also introducing spin only magnetic form factors for Fe^{2+} and Fe^{3+} did not lead to an improvement.

For $LuFe_2O_{4-\delta}$ it was found that a refinement based on the CO structure or the hexagonal structure lead to similar results [75]. Therefore, to exclude any problem with the 200 K CO structure solution of $YFe_2O_{4-\delta}$ it is feasible to refine the magnetic structure based on $R\bar{3}m$ cell. Therefore we integrated only the 200 K X-ray data under neglect of the superstructure data and refined the structure in $R\bar{3}m$. Not surprisingly the received R-values are pretty large $R_{obs} = 16.7$ and $wR_{all} = 22.9$ and the Yttrium shows the strong anisotropic displacement as observed in the room temperature structure in Figure 4.14a.

This structure was then transformed following the CO propagation vector $(\frac{2}{7}\frac{2}{7}\frac{3}{7})$ using the transformation matrices given in Eqn. (4.20), by the use of ISODISTORT [171]. It would also be possible to refine the structure based on the $R\bar{3}m$ cell and the magnetic propagation vector $(\frac{5}{14}\frac{5}{14}\frac{18}{14})$. Changing to the CO cell allows one to copy and paste the reflection files with the twin indexation from the previous refinement. Again the structure for magnetic refinement was created using the representation analysis of Jana2006 [64, 222] with the magnetic propagation vector of $(0\frac{3}{2}1)$ in the triclinic notation. The refinement converges with reasonable magnetic R-values around 10, but the refinement is completely insensitive to the magnetic structure, the errors on the magnetic moments are larger than the received values.

To exclude any problems with the 200 K CO cell in the magnetic refinement and also overparameterization in the refinement we will now examine the most simple magnetic structure,

[1] March version showed only the one without origin shift

produced on the assumption that the magnetic structure is based on the primitive rhombohedral cell and the transformation between the cells is described by the magnetic propagation vector $\left(\frac{5}{14}\frac{5}{14}\frac{18}{14}\right)$.

The second harmonic of $\left(\frac{5}{14}\frac{5}{14}\frac{18}{14}\right)$ is $\left(\frac{5}{7}\frac{5}{7}\frac{18}{7}\right)$, which is a charge order position, the same is true for other higher harmonics of even order. From the polarized neutron experiment at DNS magnetic intensity on charge order reflections can be excluded (cf. Appendix A.6). The third harmonic is symmetry equivalent to $\left(\frac{1}{14}\frac{1}{14}\frac{27}{14}\right)$, here we have no data to determine if this harmonic is present. The fifth harmonic is symmetry equivalent to $\left(\frac{\bar{3}}{14}\frac{\bar{3}}{14}\frac{3}{14}\right)$ and the seventh harmonic to $\left(\frac{1}{2}\frac{1}{2}0\right)$, for both vectors no peaks are observed (cf. Appendix A.6). There are some small peaks present on $\left(\frac{1}{2}\frac{1}{2}0\right)$ due to the $\left(\frac{\lambda}{2}\right)$ contamination of (110). They are present also in the non-spinflip channel and at different temperatures.

It is therefore reasonable to refine the magnetic structure without considering higher harmonics, although a contribution from the third harmonic cannot be excluded.

Representation analysis using the $R\bar{3}m$ cell and the magnetic propagation vector $\left(\frac{5}{14}\frac{5}{14}\frac{18}{14}\right)$ gives one irreducible representation with magnetic space group $P_s\bar{1}$, assuming a single active **k**-vector, this leads to two structures, which differer from each other by having no origin shift (Case I) or a shift of $\left(\frac{\bar{1}}{3}\frac{\bar{1}}{6}\frac{1}{3}\right)_{hex}$ (Case II), which is $\left(0\frac{1}{2}0\right)_{CO}$. In the primitive magnetic cell this corresponds to an origin shift by $\left(00\frac{1}{2}\right)$ the transformation matrix from the hexagonal to the magnetic cell can be found in Appendix A.2. If the structure of Case II is described in a cell without origin shift the inversion means mirroring on $\left(00\frac{1}{4}\right)$ instead of (000), which leads to a moment distribution for the general positions of the group as given in Table 4.24. In Case I (000) the moment is not inverted by the inversion operation and in Case II it is inverted with the spacial inversion.

This means that for all 14 Fe ions in the in $\mathbf{b}_{tric}$ direction doubled CO cell, which are connected by spatial inversion to the other 14 Fe ions, there exist two cases; either all moments are reversed or no moment is reversed.

And the magnetic structure factor can be calculated as,

$$F = \sum_{j=1}^{14} S_j \cdot \exp\left[2\pi i \mathbf{Q}\cdot\mathbf{r}(Fe_j)\right] = \begin{cases} \sum_j S_j \cdot 2\cos\left[2\pi i \mathbf{Q}\cdot\mathbf{r}(Fe_j)\right] & \text{for Case I} \\ \sum_j S_j \cdot 2i\sin\left[2\pi i \mathbf{Q}\cdot\mathbf{r}(Fe_j)\right] & \text{for Case II} \end{cases} \tag{4.33}$$

here j runs over the 14 Fe ions connected by translation in the in $\mathbf{b}_{tric}$-direction doubled CO cell.

Since we consider a magnetic structure based on the primitive rhombohedral cell, the spin moment of 13 of the Fe positions in Eqn. (4.33) are given by the application of the magnetic propagation vector.

The 7 Fe positions of the CO cell in hexagonal notation connected by translation are given in Eqn. (4.25). The other 7 positions in the magnetic cell, the in $\mathbf{b}_{tric}$ direction doubled CO cell, are received by applying a translation of $\left(\frac{5}{3}\frac{4}{3}\frac{1}{3}\right)_{hex}$, which is $(0,1,0)_{tric}$. For the calculation the ideal positions from the hexagonal cell were used.

position ($P_s\bar{1}$)	moment (Case I (000))	moment (Case II $(00\frac{1}{2})$)
$(x, y, z))$	**S**	**S**
$(x, y, z + \frac{1}{2})$	**−S**	**−S**
$(\bar{x}, \bar{y}, \bar{z})$	**S**	**−S**
$(\bar{x}, \bar{y}, \bar{z} + \frac{1}{2})$	**−S**	**S**

Table 4.24: General positions of the Group $P_s\bar{1}$ and the moments for the structure without origin shift (000) (Case I) and with origin shift $(00\frac{1}{2})$ (Case II).

The spin moments which can be received from application of the propagation vector, were calculated following Eqn. (4.34),

$$S_i = \Re\left[\exp\left(-2\pi i\mathbf{k}\cdot\mathbf{R}(Fe_i) + i\phi\right)\right] \tag{4.34}$$

where $\mathbf{k} = [\frac{5}{14}, \frac{5}{14}, \frac{18}{14}]$ is the magnetic propagation vector in the hexagonal cell and $\mathbf{R}(Fe_i)$ is the lattice part of the different Fe positions following $\mathbf{r}(Fe_i) = \mathbf{R}_i + \mathbf{r}'$, where $\mathbf{R}_i$ is a hexagonal lattice vector and $\mathbf{r}' = [0, 0, z]$ is the position of the Fe ion in the hexagonal unitcell. For the calculation of the spin moments the origin is therefore chosen to be at $\mathbf{R}(Fe4) = (0, 0, 0)$, where the numbering corresponds to the Fe positions in Table 4.16 and Eqn. (4.25) and the moment of Fe_4 is determined by the phase ϕ as $S_4 = cos(\phi)$.

Since in Equation (4.34) $\mathbf{R}(Fe8) = \mathbf{R}(Fe1) + \left(\frac{5}{3}, \frac{4}{3}, \frac{1}{3}\right)_{hex}$ the moment of Fe8 is received as

$$S_8 = \Re\Big[\exp(-2\pi i\mathbf{k}\cdot\mathbf{R}(Fe_1) + \left(\frac{5}{3}\frac{4}{3}\frac{1}{3}\right) + i\phi)\Big] = S_1\cdot\Re\Big[\exp(-2\pi i\mathbf{k}\cdot\left(\frac{5}{3}\frac{4}{3}\frac{1}{3}\right))\Big] \tag{4.35}$$

and $\left(\frac{5}{3}\frac{4}{3}\frac{1}{3}\right)\cdot\left(\frac{5}{14}\frac{5}{14}\frac{18}{14}\right) = \frac{3}{2}$ the moment of Fe_8 is the negative moment of Fe_1:

$$S_8 = S_1\cdot\Re[\exp(-3\pi)] = -S_1 \tag{4.36}$$

In analog to F8 this is valid for the other 6 Fe positions in Eqn. (4.25) and we have only 7 distinct S_i-values the others are given by inversion.

The magnetic moments were then used to calculated the intensity for the 21 magnetic reflections observed in the first domain for the two cases given in 4.33. In the calculation ϕ and the Debye-Waller factor (Eqn. (4.32)) were used as free variables. Using the average Debye-Waller factor received from the isotropic mean displacement of the Fe ions in X-ray diffraction $\langle u^2\rangle = 0.008\text{Å}^2$, lead to large differences between the observed and calculated intensities at higher $|\mathbf{Q}|$. The calculated intensities were also corrected with the Lorentz factor Eqn. (4.29), the factor for only observing the component $\mathbf{M}_{\perp\mathbf{Q}}$ Eqn. (4.31) and the magnetic form factor Eqn. (4.30). For the latter the dipole approximation Eqn. (2.51) is used with a mixed value for Fe^{2+} and Fe^{3+}.

The calculated and the measured magnetic intensities were normed on $(0\frac{5}{2}0)$ and then fitted to determine the optimum values for ϕ and the Debye-Waller factor. Figure 4.32 shows the intensities of the reflections of the first domain, together with the calculated intensities

for the two cases defined in Equation Eqn. (4.33). In Figure 4.32 $|\mathbf{Q}|$ is increasing from left to right, the decrease of the intensity at higher $|\mathbf{Q}|$ is caused by the magnetic form factor (cf. 2.6b) and the Debye-Waller factor. For case I the parameters were determined as $\langle u^2 \rangle = 0.189$Å and $\phi = 0.193 \cdot \pi$ and for case II $\langle u^2 \rangle = 0.190$Å and $\phi = 0.697 \cdot \pi$. The absolute phase difference between both cases is nearly $\frac{\pi}{2}$.

The thermal displacement factor of $\langle u^2 \rangle = 0.190$Å is unrealistic, in comparison to the factor received from refinement of the 200 K structure $\langle u^2 \rangle = 0.008$Å, even if the 200 K structure is refined with the hexagonal cell the mean isotropic displacement increases only to $\langle u^2 \rangle = 0.02$Å as it includes now the distortions rendering the Fe sites different in the CO cell. As the thermal displacement parameter is, beside the phase shift, the only fitting parameter, it is likely that the parameter accounts for some other problem in the magnetic model. For example, if the assumption of a mixed magnetic form factor for Fe^{2+} and Fe^{3+} considering also the orbital contributions is wrong, this can lead to wrong intensities at higher $|\mathbf{Q}|$, which are then corrected by the Debye-Waller factor.

	$Fe1^{3+}$	$Fe2^{3+}$	$Fe3^{3+}$	$Fe4^{2.5+}$	$Fe5^{2+}$	$Fe6^{2+}$	$Fe7^{2+}$
Case I	0.98	-0.74	0.96	0.82	-0.37	-0.49	-0.07
Case II	-0.17	-0.66	0.27	-0.58	-0.92	0.88	1.00

Table 4.25: Magnetic moment for the distinct Fe positions and the two cases, a value of 1 is full spin.

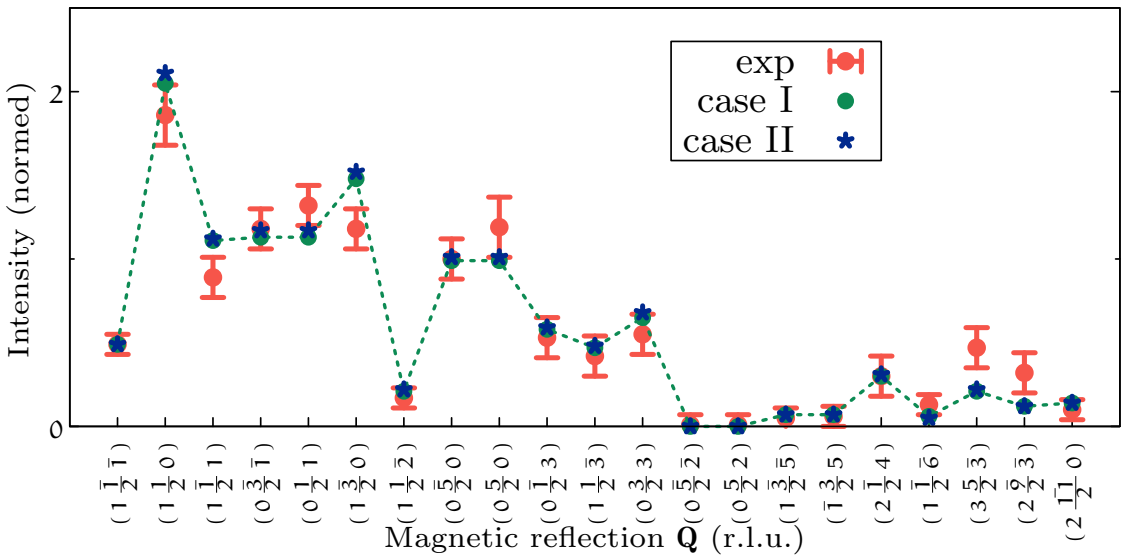

Figure 4.32: Measured and calculated intensities of reflections from the first domain normed to the intensity of $(0, -2.5, 0)$. They are ordered with $\mathbf{Q}$ increasing on the x-axis. exp is the measured intensity, case I is the calculated intensity for the cell with (000) as origin and case II is the calculated intensity for the structure with the origin at $(0\frac{1}{2}0)_{CO}$.

Figure 4.33 shows the spin structures for the two $P_s\bar{1}$ structures distinguished by the different origin shift. The shown cell is the in **b**-direction doubled charge order cell from Section 4.8, from which the Fe valences are also shown. Comparing only the absolute values of the moments, it is obvious that in the case I structure the Fe^{3+} ions are close to full spin and in the case II structure the Fe^{2+} ions have almost full spin (cf. Table 4.25).

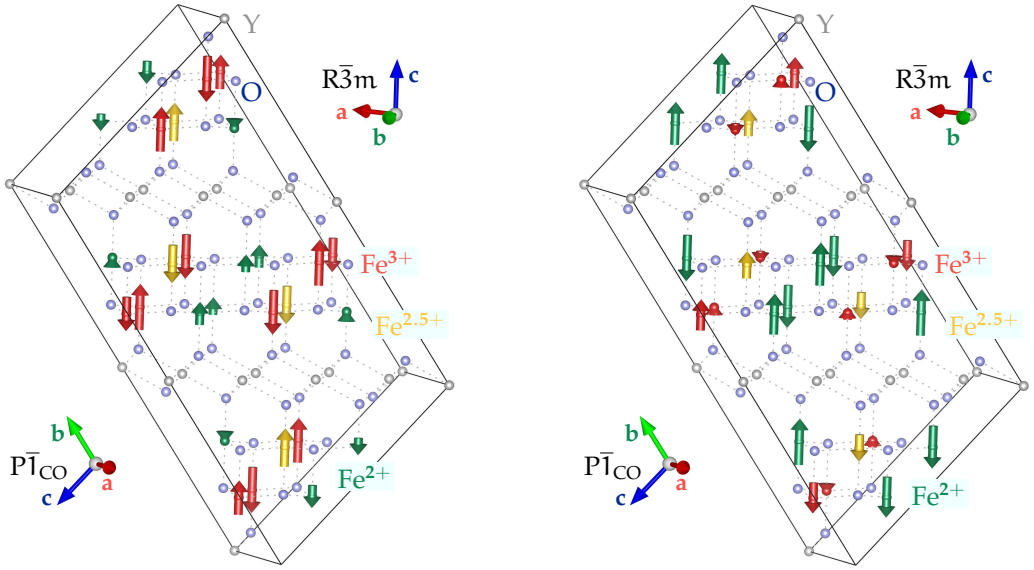

(a) Case I (000) (b) Case II $(00\frac{1}{2})$

Figure 4.33: The two possible spin structures of $YFe_2O_{4-\delta}$ at 200 K. Figure (a) is for Case I with no origin shift and Figure (b) is for Case II with an origin shift of $\left(\frac{\bar{1}}{3}\frac{\bar{1}}{6}\frac{1}{3}\right)_{hex}$ as defined in Eqn. (4.33).

If the Fe^{2+} orbital moment is quenched, the total moment of Fe^{2+} is only the spin moment of $4\mu_B$, which is slightly less than the moment of Fe^{2+} $5\mu_B$. The difference is too small to explain the reduced moment on the Fe^{2+} sites in the case I structure (cf. Tab.). From the XMCD measurements (Sec. 4.4) on stoichiometric $YFe_2O_{4-\delta}$ we could not received the orbital moment, but for the non-stoichiometric sample a large orbital moment is observed. This is also the case for stoichiometric $LuFe_2O_{4-\delta}$ [9, 190, 193–198].

In the case I structure the Fe^{3+} moments are close to the full moment. The Fe^{3+} sites are less localized in the 200 K charge order structure than the Fe^{2+} sites (cf. Sec. 4.8.5) and obey some degree of disorder. It is reasonable that this disorder also affects magnetic structure through spin charge coupling and decreases the average moment on the Fe^{3+} sites. The large magnetic anisotropy observed in $YFe_2O_{4-\delta}$ (Sec. 4.4) and $LuFe_2O_{4-\delta}$ [9], which is caused by spin orbit coupling and an unquenched Fe^{2+} moment [198, 231], will lead to a higher tendency for the Fe^{2+} spin moments to align parallel to $\mathbf{c}_{hex}$.

Above the charge order transition a deviation from the Ising character is observed (cf. Sec. 4.10.1). If now at 200 K the Fe^{3+} moments still show some degree of disorder, the assumption of all spins pointing parallel $\mathbf{c}_{hex}$ might not be justified. Although since the model fits the observed intensities quite well, such a deviation should be small. The small frequency

dependent shift of the high temperature transition of $YFe_2O_{4-\delta}$ observed in AC susceptibility (cf. Sec. 4.3.1) is an indication for some degree of disorder in the magnetic states of $YFe_2O_{4-\delta}$ also in the 200 K phase, although it tells us nothing about the valence of the disordered Fe ions.

The spin order of $YFe_2O_{4-\delta}$ at 200 K is characterized by the propagation vector $(0\frac{3}{2}1)$ in the triclinic cell of the 200 K $P\bar{1}$ charge order supercell, in hexagonal notation this corresponds to $(\frac{5}{14}\frac{5}{14}\frac{18}{14})$. A contribution of higher harmonics could be excluded for even order, the fifth and seventh harmonics. For the third harmonic we cannot exclude a contribution to the magnetic distortions. Representation analysis based on the rhombohedral cell lead to two structures with spacegroup $P_s\bar{1}$, one has no origin shift the other one by $\left(\frac{\bar{1}}{3}\frac{\bar{1}}{6}\frac{1}{3}\right)_{\text{hex}}$. Both structures lead to almost the same diffraction pattern (cf. Fig. 4.32) and match well with the observed intensities. One main difference between the spin structures is that for the structure with origin shift, the Fe^{3+} ions have almost full spin and for the other structure the Fe^{2+} ions. Considering the disorder of the Fe^{3+} ions in the 200 K CO cell, the scenario with a reduced moment on the Fe^{3+} positions due to disorder seems more likely. In the future it might be possible to distinguish between the two solutions through introduction of different moments and form factors for Fe^{2+} and Fe^{3+}, more importantly a refinement of the structure based on the distorted 200 K CO structure. Inclusion of the third harmonic, from which a contribution could not be excluded, could also allow one to distinguish the two structures through their diffraction pattern. The refinement could also be improved by the inclusion of reflections from different domains, which was omitted here to avoid an influence of problems with the domain population determination.

4.10.4 Temperature dependence of the spin order

To further elucidate the interplay between the 160 K and 200 K spin magnetic phases we have evaluated the temperature dependence of different magnetic and structural reflections.

Figure 4.34 shows the temperature dependence of the hexagonal structural reflections (110) and (003), while the (003) reflection shows almost no change of intensity at the 240 K charge order transition, the (110) reflection shows an intensity increase while cooling through the charge order transition. Normally one would expect that the intensity of the structural reflection drops while cooling through the charge order transition since some intensity is shifted to the superstructure reflections. This behavior can be explained by the increase of mosaicity below the charge order transition, which reduces extinction and was also observed on the low temperature transition of $LuFe_2O_{4-\delta}$ [31].

The charge order transition changes both the in-plane and out-of-plane ordering from $(\frac{1}{3}\frac{1}{3}\ell)$ and diffuse along ℓ to a propagation of $(\frac{2}{7}\frac{2}{7}\frac{3}{7})$. The transition from the disorder along ℓ to an ordered structure creates only a very small drop in the intensities of (003), while the in-plane change of the propagation has a much stronger effect. More interesting in terms of the magnetic order is of course the temperature dependence of magnetic reflections, which can be described by two different types. Figure 4.35 shows the temperature dependence of the $(0.37, 0.37, 0.37)_{\text{hex}}$ and $(0.36, 0.35, 4.36)_{\text{hex}}$ reflections. All curves start with cooling from

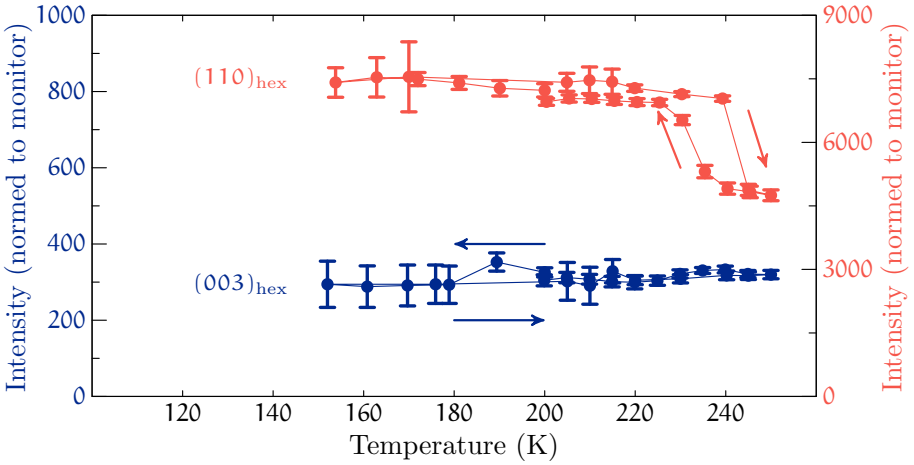

Figure 4.34: Temperature dependence the structural (110) and (003) reflection (hexagonal notation). Both measurements starts with cooling from 200 K.

200 K. The two reflections show quite different behavior. The temperature dependence of the $(0.37, 0.37, 0.37)$ reflection follows the lower temperature transition in the magnetization curve (Figure 4.6), while the temperature dependence of $(0.36, 0.35, 4.36)_{hex}$ follows the higher temperature transition in the magnetization.

At 200 K on cooling the magnetic reflections from the type of $(0.37, 0.37, 0.37)$, which we attribute to the 160 K phase have a low intensity, but are still observable. Considering the $\frac{1}{4}$-propagation of the 160 K charge order cell they can be described as $(\frac{3}{8}\frac{3}{8}\frac{3}{8})$ in the hexagonal notation.

On the other hand the $(0.36, 0.35, 4.35)$-type reflections, which we attribute to the 200 K phase, have a high intensity at 200 K during cooling, with the $\frac{1}{7}$-propagation this corresponds to $(-0.01, 2.52, -0.03)$ in the charge order cell, which was attributed to be $(0, 2.5, 0)$. On the other hand $(0, 2.5, 0)$ is $(0.36, 0.36, 4.29)$ in the hexagonal cell, which could mean that the reflection was falsely indexed. The temperature dependency of the $(0.36, 0.35, 4.35)$ reflection is the same as $(0.29, 0.35, -0.71)$ and $(0.37, 0.28, 0.29)$, so they should all belong to the same phase and it is likely that the variation of the ℓ-coordinate of 4.25 instead of 4.28 is just a measurement uncertainty and the magnetic propagation vector is correct.

While the 160 K reflections are still observable at 200 K they are too far away from magnetic or structural reflections of th 200 K phase, to be falsely indexed and used in the refinement. Since the reflections of the 160 K phase are still observable a part of the sample seems to be in the phase with a $(\frac{1}{4}\frac{1}{4}\frac{3}{4})$ charge order propagation. This was never observed in our X-ray diffraction experiments, which could be explained due to the much smaller sample mass and different cooling times. Although with the large amount crystals tested, we should have observed this by chance. We observed such a superposition of the two phases at 100 K in single crystal X-ray diffraction and it was also observed at higher temperatures in powder X-ray diffraction by Balsco *et al.* [170]. A superposition of the two phases, if not attributed, would lead to a too strong intensity of the $R\bar{3}m$ structural reflections in comparison to the 200 K

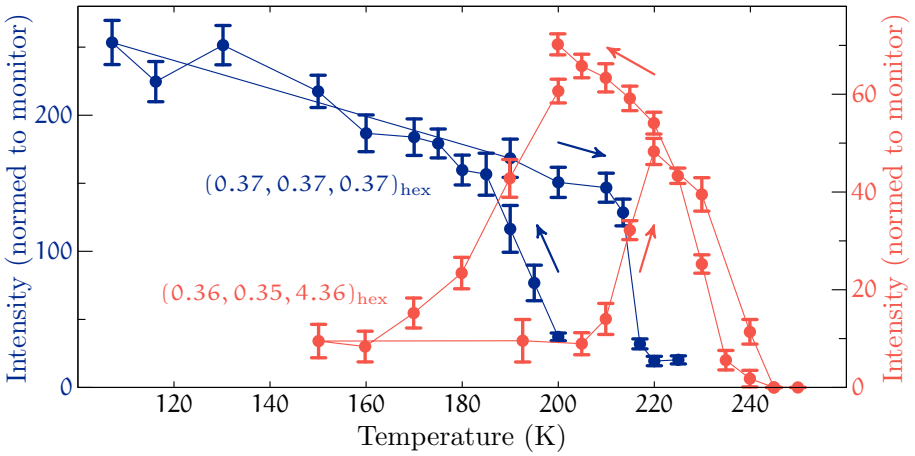

Figure 4.35: Temperature dependence of the two types of magnetic reflections. Both measurements starts with cooling from 200 K.

charge order and magnetic reflections. Since the charge order breaks the R$\bar{3}$m symmetry, the intensity distribution would also be affected. The only way to handle such a superposition would be to measure also the reflections belonging to the $(\frac{1}{4}\frac{1}{4}\frac{3}{4})$ propagation at 200 K, which was not done in our experiment, besides the three reflections measured for temperature dependence.

In contrast to the well separated phases observed in X-ray diffraction, the observations in neutron diffraction at 200 K and 160 K show a superposition of the two CO-phases, although the phases observed in X-ray diffraction are dominant. This is most likely due to the larger sample volume and different cooling times.

4.10.5 The spin structure at 160 K

The experiment at TriCs (see Sec. 2.3.11) to determine the magnetic cell at 160 K was performed shortly before the experiment at 200 K. Since the magnetic propagation of the 160 K phase was unknown at that time we collected three-dimensional maps along $(\frac{1}{3}\frac{1}{3}\ell)$, $(\frac{2}{3}\frac{2}{3}\ell)$ and symmetry equivalent lines. In these maps 71 reflections were identified and the integrated intensities of these were measured with rocking scans and a point detector. From the 71 measured reflections 38 can be described with a propagation vector of $(0\frac{1}{2}\frac{1}{2})$ in the triclinic 160 K CO, cell if six twin components are considered. Most of the reflections can be described with a propagation vector of $(\frac{3}{8}\frac{3}{8}\frac{45}{8})_{\mathrm{hex}}$ based on the R$\bar{3}$m cell, but some reflections like $(\bar{1}\frac{5}{2}\frac{1}{2})_{\mathrm{CO}}$ are higher harmonics of $(\frac{3}{8}\frac{3}{8}\frac{45}{8})_{\mathrm{hex}}$. Eleven reflections are charge order reflections of the 160 K phase, 17 are magnetic reflections from the 200 K phase and 5 reflections could not be attributed to any of these propagations. The five reflections are $(0.61, -0.38, -3.62)$, $(0.36, 0.39, -0.58)$, $(-0.14, 0.68, 1.41)$ $(-0.32, 0.63, 1.53)$ and $(-0.56, 0.85, 1.01)$ in hexagonal notation. The magnetic structure at 160 K consists of a superposition of the 200 K structure and one with a propagation vector of $(0\frac{1}{2}\frac{1}{2})_{\mathrm{CO}}$. The superposition is expected from the temperature dependence shown in Figure 4.35, although it is surprising that it is stronger at 160 K

than at 200 K. Representation analysis based on the 160 K charge order structure and the propagation vector $(0\frac{1}{2}\frac{1}{2})_{CO}$ leads to two irreducible representations, which both give a structure in spacegroup $P_s\bar{1}$, and are distinct only by either having no origin shift or a shift of $\left(00\frac{1}{2}\right)$. The transformation matrix between the 160 K CO cell and the magnetic cell is given in Eqn. (4.37).

$$\mathbf{B} = \begin{pmatrix} 1 & 0 & 0 \\ 0 & -1 & -1 \\ 0 & 0 & -2 \end{pmatrix} \text{ and } \mathbf{p} = \begin{pmatrix} 0 \\ 0 \\ 0 \end{pmatrix} \text{ or } \begin{pmatrix} 0 \\ 0 \\ \frac{1}{2} \end{pmatrix} \tag{4.37}$$

Comparing the intensities of the reflections that were measured in at least two domains, lead to very different domain populations, if different reflections from the same domain were used. The small amount of magnetic or CO reflection does not allow the removal of outliers. To exclude any problems with domain population scaling, only one domain was considered for the following calculations.

Assuming that all spins have full moments, that the system has a magnetic space group, and considering the four Fe sites from the CO cell, there are 8 different spin arrangements for each structure $(\frac{4^2}{2})$. As for the phase at 200 K, the origin shift between the two cells results in two cases; one connected to the sine and one to the cosine in Equation Eqn. (4.33). The measured integrated intensities were corrected for the magnetic form factor, Debye Waller factor, Lorentz factor and that only $\mathbf{M}_{\perp\mathbf{Q}}$ contributes to magnetic scattering.

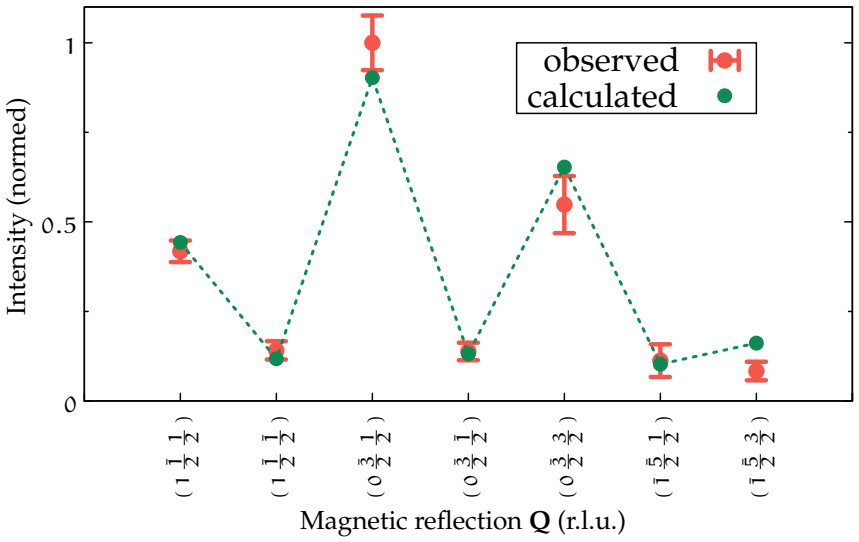

Figure 4.36: Measured and calculated intensities of reflections from one domain normed to the Intensity of $(0, -2.5, 0.5)$. They are ordered with $\mathbf{Q}$ increasing on the x-axis. observed is the measured intensity, calculated is the calculated intensity for the cell with no origin shift.

Comparing measured and calculated integrated intensities of the 16 different spin structures lead to only one structure, which is compatible in regard of relative intensities between different reflections. Figure 4.36 shows the measured intensities and the calculated intensities for this spin structure.

The structure is based on the cell with spacegroup $P_s\bar{1}$ with no origin shift and a spin structure as given in Table 4.26.

$Fe1^{3+}$	$Fe2^{2+}$	$Fe3^{2+}$	$Fe4^{3+}$
-1	1	1	-1

Table 4.26: Magnetic moment for the distinct Fe positions at 160 K, a value of 1 is full spin.

Figure 4.37 shows the spin structure in the magnetic $P_s\bar{1}$ cell, the red cell is the 160 K charge order cell.

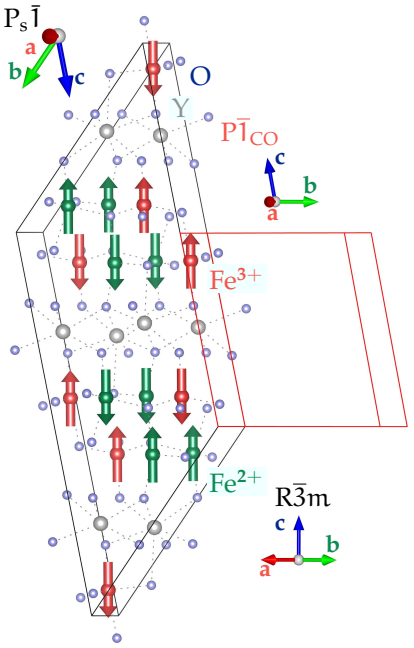

Figure 4.37: Spin structures of $YFe_2O_{4-\delta}$ at 160 K, $P_s\bar{1}$ with no origin shift.

In the 160 K spin structure, both of the distinct Fe^{2+} sites have a parallel spin in a direction opposing both Fe^{3+} spins. In contrast to the 200 K spin structure the 160 K spin structure can be well described with full spin moments indicating a complete spin order, which is in accordance with the full charge order and the stronger localization at 160 K.

The spin model could be improved by inclusion of different domains and a refinement of the Debye Waller factor, which is omitted here because of time reasons.

Nevertheless we were able to determine for the first time the spin structure of $YFe_2O_{4-\delta}$ at 160 K, which is based on a propagation vector of $\left(0\frac{1}{2}\frac{1}{2}\right)_{CO}$ and has the spacegroup $P_s\bar{1}$ with no origin shift in regard to the 160 K charge order structure.

4.11 General Discussion

We will now go back to the charge order structures of $YFe_2O_{4-\delta}$ and compare the two low temperature structures of $YFe_2O_{4-\delta}$. Figure 4.38 shows the 200 K and 160 K structures in comparison, the view is along the hexagonal $[1\bar{1}0]$ axis and [001] is pointing upwards. The mixed valence in the 200 K structure is colored yellow. The most obvious observation is that the anisotropic displacement parameters at 200 K are much larger, as one would expect at higher temperatures. They also show a stronger anisotropy sometimes not fulfilling the Hirshfeld test, which tests if the displacement parameters of two ions in a bond have similar values along the bonding direction [73]. This can be a hint for an error in the structure, however in our case it is more likely an indication for non-attributed disorder. The Hirshfeld test is valid for the phononic contribution to the displacement ellipsoids, if they describe a disordered position, the test fails. In the case of the Y4 position, the disorder was attributed to a split position and indeed the refinement could be further enhanced by splitting Fe sites. To avoid over parameterization in the refinement this splitting is omitted.

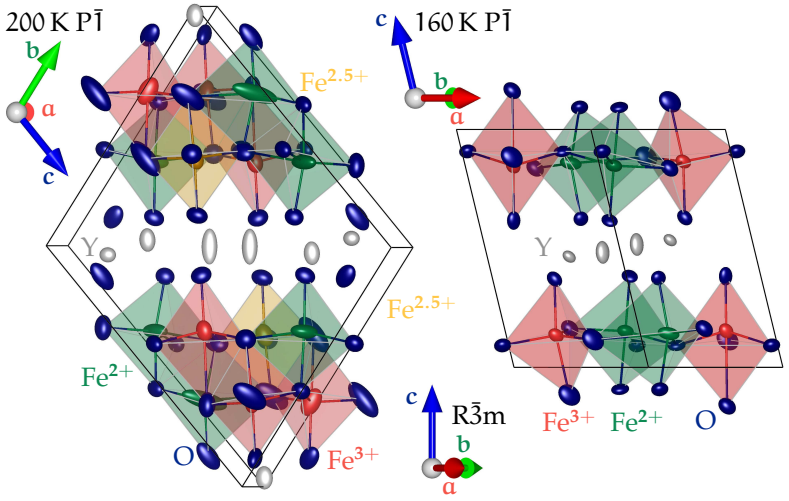

Figure 4.38: View of the P$\bar{1}$ 200 K (left) and 160 K structures along the hexagonal [1-10] axis with [001] pointing upwards.

The transition from the 200 K P$\bar{1}$ structure to the 160 K P$\bar{1}$ structure can be be described by the transformation (4.38).

$$\begin{pmatrix} \mathbf{a}' \\ \mathbf{b}' \\ \mathbf{c}' \end{pmatrix}_{200\,\mathrm{K}} = \underbrace{\mathbf{B}_{200\,\mathrm{K}} \cdot \mathbf{B}_{160\,\mathrm{K}}^{-1}}_{\mathbf{B}_{160\,\mathrm{K}\,\mathrm{to}\,200\,\mathrm{K}}} \cdot \begin{pmatrix} \mathbf{a} \\ \mathbf{b} \\ \mathbf{c} \end{pmatrix}_{160\,\mathrm{K}} \tag{4.38}$$

with:

$$\mathbf{B}_{160\,\mathrm{K\ to\ 200\,K}} = \begin{pmatrix} -1 & 0 & 0 \\ 0 & -1 & -1 \\ \frac{1}{2} & -\frac{3}{2} & 1 \end{pmatrix} \tag{4.39}$$

In contrast to us, Blasco *et al.* [170] observe the low temperature phase only in superposition with the 200 K phase, this might be explained by the much larger sample volume, a different oxygen stoichiometry or even different cooling times [159].

In Mössbauer spectroscopy a decrease of the Mössbauer line width is observed with decreasing temperature [174], compatible with the more localized charge distribution at 160 K compared to the 200 K structure. Also the occurrence of a very broad sextet, additional to the Fe^{2+} and Fe^{3+} sextets in the spectrum at 220 K on warming and 190 K on cooling [174], which is attributed to Fe^{3+} is compatible with our model of 3 localized Fe^{2+} and 4 partly localized Fe^{3+} from which one is closer to $Fe^{2.5+}$. The fact that these features can still be resolved also indicates that the hopping frequency between the non-localized charges has to be below 10^8 Hz, characteristic for the Mössbauer effect [174]. It is worthwhile to notice that the spectrum of non-stoichiometric $YFe_2O_{4-\delta}$ [173] is completely different from that of the stoichiometric one [174] due to the charge order of Fe^{2+} and Fe^{3+}.

It is also observed that the cooling rate has an influence on the low temperature Mössbauer spectrum [160] and therefore also on the charge order structure, which would explain why for example Blasco *et al.* [170] observed a superposition of different phases below 200 K, in contrast to the single phase we observe at 160 K. We observe a superposition of the 200 K and 160 K phase at 100 K in X-ray diffraction if the sample is cooled fast to 100 K, with slower cooling rates the reflections of the 200 K phase vanish. A general superposition of the two phases is observed in neutron diffraction. The latter is most likely caused by the larger sample volume or different cooling times, quenching some of the phases. In contrast to the powder X-ray diffraction at 200 K, where a monoclinic structure is observed [160] Mössbauer spectroscopy shows the same hyperfine splitting as for the triclinic low temperature phase, if the sample is kept at 200 K for over an hour [160]. This is compatible with our finding that both structures at 200 K and 160 K are triclinic. Although the structure is questionable Blasco *et al.* [170] also found both phases to be triclinic, based on synchrotron powder X-ray diffraction. The resistivity of $YFe_2O_{4-\delta}$ shows a continuous increase during cooling with jumps at both charge order transition temperatures [178, 179]. This can be well explained with the increased localization of the Fe electrons at both transition points. The resistivity also obeys the thermal hysteresis observed in magnetization measurements [181]. For a non-stoichiometric single crystal a jump in the resistivity is only observed in the $\mathbf{c}_{hex}$-plane at the broad 250 K magnetic transition [178], which can be ascribed to in-plane charge order. The hopping frequency of the electrons between Fe^{2+} and Fe^{3+} increases with increasing temperature [175], which accounts for the general lowering of the resistance with increasing temperature.

A partial Fe charge order with non-localized electrons on mixed valence sites is also found in $K_{0.6}FeF_3$ and leads to charge-order-induced polarization [237] and ferroelasticity [238],

although it is very different to $YFe_2O_{4-\delta}$ since the mixed valence site is distinct by a different site symmetry. Another example for a partial charge order is the weak metallic $AgNiO_2$, where a charge order of Ni^{2+} and $Ni^{3.5+}$ sites is observed [239, 240] and the partial CO lifts the orbital degeneracy under the presence of charge fluctuations [241]. The average valence at 200 K from Table 4.20 is 2.38, while at 160 K the valence is 2.47 (Table 4.11), the rhombohedral room temperature structure has a Fe valence of 2.31. With decreasing temperature the Fe average BVS as well as the site specific BVS is shifted to lower values at both phase transitions.

As stated in [19] the ratios of the Fe distances in the bilayer and between different bilayers are supposed to determine the realized charge order.

For a full three dimensional CO four interactions are necessary [19, 242, 243]; these are the Fe in-plane intra nearest neighbor interaction $V_{ab_{NN}}$, the out of plane intra nearest neighbor interaction $V_{c_{NN}}$, the interlayer out of plane nearest neighbor interaction V_{inter} between different bilayers and the next nearest neighbor interaction to the second layer of a different bilayer $V_{interNNN}$. The latter will not be discussed and is therefore omitted in Figure 4.39a, which shows the interactions used in this thesis, it also includes the next nearest neighbor interaction inside the bilayer $V_{c_{NNN}}$, which is used in the single bi-layer model from Nagano *et al.* [79] and will use to elucidate the effect of different ionic rare earth radii.

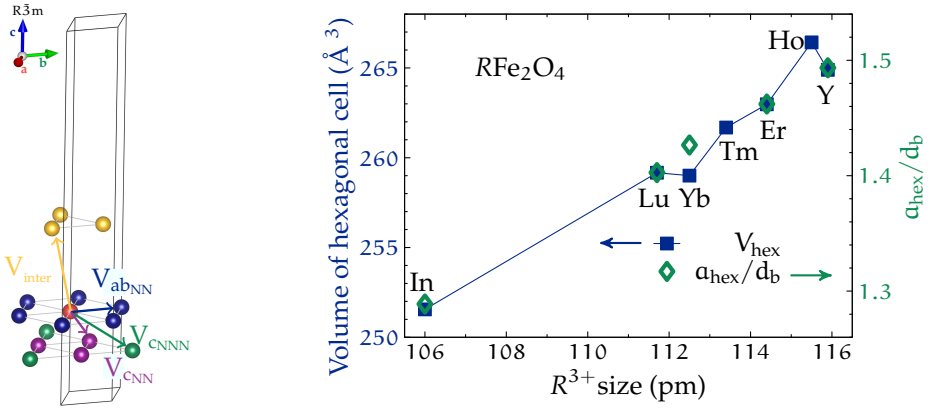

(a) Fe-interactions

(b) Cell volumne and Fe-Fe distance ratio vs R^{3+}-radius [19]

Figure 4.39: (a) Different Fe-interactions in the hexagonal cell. (b) Dependence of $\frac{ab_{NN}}{d_b}$ and the cell volume from the rare-earth ion radius R^{3+} (reproduced from [19], data based on [194, 226, 244–248]).

In a first approximation the strength of the Coulomb interaction is proportional to $\frac{1}{r}$ where r is the distance between the two Fe atoms. In a very rough model considering only the charge differences compared to the mean valence case, the interaction is repulsive between Fe ions of the same valence and attractive for different valences.

As stated in [19] the size change of the rare earth ion changes the bilayer thickness d_b as given in Eqn. (4.40), as well as the intralayer Fe-Fe distance ab_{NN}, which is the hexagonal a_{hex} lattice parameter. The ratio between the two $\frac{ab_{NN}}{d_b}$ shows a linear connection to both the R^{3+} ion radius and the volume of the hexagonal unit cell, as shown in Figure 4.39b.

Table 4.27 gives the relevant Fe-Fe distances in $YFe_2O_{4-\delta}$, $LuFe_2O_{4-\delta}$ and $YbFe_2O_{4-\delta}$ as well as relevant ratios between them, here the bilayer thickness is given as:

$$d_b = \sqrt{(c_{NN})^2 - \frac{(ab_{NN})^2}{3}} \tag{4.40}$$

$YFe_2O_{4-\delta}$	ab_{NN}	c_{NN}	c_{NNN}	$\frac{ab_{NN}}{c_{NN}}$	$\frac{ab_{NN}}{c_{NNN}}$	$\frac{c_{NN}}{c_{NNN}}$	$\frac{a_{hex}}{d_b}$
295 K	3.5152(4)	3.116(3)	4.6974(4)	1.128(1)	0.7483(1)	0.6633(1)	1.487(2)
210 K	3.526(23)	3.140(13)	4.716(38)	1.123(8)	0.748(7)	0.666(6)	1.475(20)
160 K	3.564(50)	3.166(27)	4.75(09)	1.126(18)	0.750(18)	0.665(13)	1.481(50)
$LuFe_2O_{4-\delta}$	ab_{NN}	c_{NN}	c_{NNN}	$\frac{ab_{NN}}{c_{NN}}$	$\frac{ab_{NN}}{c_{NNN}}$	$\frac{c_{NN}}{c_{NNN}}$	$\frac{a_{hex}}{d_b}$
295 K	3.440(1)	3.158(2)	4.670(1)	1.0893(8)	0.7366(3)	0.6762(5)	1.401(1)
210 K	3.434(6)	3.158(8)	4.665(4)	1.084(3)	0.734(1)	0.677(2)	1.390(8)
$YbFe_2O_{4-\delta}$	ab_{NN}	c_{NN}	c_{NNN}	$\frac{ab_{NN}}{c_{NN}}$	$\frac{ab_{NN}}{c_{NNN}}$	$\frac{c_{NN}}{c_{NNN}}$	$\frac{a_{hex}}{d_b}$
295 K	3.455(1)	3.138(4)	4.667(3)	1.101(1)	0.7403(5)	0.672(1)	1.426(1)

Table 4.27: Distances between Fe positions in $YFe_2O_{4-\delta}$, $YbFe_2O_{4-\delta}$ [249] and $LuFe_2O_{4-\delta}$ [9] (averaged in case of CO cells).

In the model with three interactions in [79], the nearest neighbor interaction along $\mathbf{c}_{hex}$ V_{cNN} is the strongest and the ratio between V_{cNN} and the next nearest neighbor interaction V_{cNNN} mainly determines which charge order is established. At $T = 0$, under the assumption the potential follows $\frac{1}{r}$, for $\frac{c_{NN}}{c_{NNN}} > 0.5$ the propagation of the form $(\tau\tau\ell)$ will be based on $\tau = \frac{1}{2}$, while for $\frac{c_{NN}}{c_{NNN}} < 0.5$ it will be based on $\tau = \frac{1}{4}$ at $T = 0\,K$. Thus increasing the out of plane nearest neighbor interaction in comparison to the out of plane next nearest neighbor interaction inside the bilayer results in lowering of τ.

With the temperature reduction in $YFe_2O_{4-\delta}$ the ratio $\frac{c_{NN}}{c_{NNN}}$ does not change, considering the large standard deviation, caused by the wide spread of Fe-Fe distances at low temperature (cf. Tab. 4.27).

Looking at the different rare earth ions the ratio $\frac{c_{NN}}{c_{NNN}}$ is slightly lowered if the ions size increases from Lu^{3+} over Yb^{3+} to Y^{3+}. This will lead to a propagation with a lower τ as observed in $YFe_2O_{4-\delta}$.

Under the assumption that the potential is proportional to $\frac{1}{r}$, $\frac{V_{cNNN}}{V_{abNN}}$ in [79] corresponds to $\frac{ab_{NN}}{c_{NNN}}$ in Table 4.27. Figure 4.40b shows the mean-field phase diagram for $RFe_2O_{4-\delta}$ reproduced from [79] for $\frac{ab_{NN}}{c_{NN}} = 1.2$, this is larger than the experimentally found value of 1.08 for $LuFe_2O_{4-\delta}$ or 1.13 for $YFe_2O_{4-\delta}$, although they considered a value of 1.2 applicable for $LuFe_2O_{4-\delta}$. In this phase diagram lowering the ratio $\frac{ab_{NN}}{c_{NNN}}$ leads to a reduction of τ in the propagation of the charge order $(\tau\tau\ell)$ from 0.5 over 0.33 to 0.25. $LuFe_2O_{4-\delta}$ and $YbFe_2O_{4-\delta}$ both show a clear preference for a charge order with $\tau = \frac{1}{3}$, while in $YFe_2O_{4-\delta}$ at room temperature diffuse lines at $h = 0.333(16)$ (cf. Fig. 4.13b), are observed and at 210 K τ is lowered to $\frac{2}{7}$ and at 160 K again lowered to $\frac{1}{4}$. The ratio $\frac{ab_{NN}}{c_{NNN}}$ is increased if one goes from $LuFe_2O_{4-\delta}$ over $YbFe_2O_{4-\delta}$ to $YFe_2O_{4-\delta}$ (cf. Tab. 4.27), which would in the phase diagram (Fig. 4.40b)

correspond to an increase of τ. The opposite is observed in experiment, which leads to the conclusion that the phase diagram reproduced in 4.40b cannot describe the $RFe_2O_{4-\delta}$-system.

A reduction of the ratio $\frac{c_{NN}}{c_{inter}}$ increases the intralayer interaction in contrast to the interlayer interaction, since c_{NN} is the Fe-Fe distance inside a bilayer and c_{inter} the Fe-Fe distance between different bilayers. Inside the standard deviations $YFe_2O_{4-\delta}$, $LuFe_2O_{4-\delta}$ and $YbFe_2O_{4-\delta}$ have the same value of $\frac{c_{NN}}{c_{inter}} = 0.50$ (not given in the table) and therefore the ratio cannot be used to determine the CO of the $RFe_2O_{4-\delta}$ system. In the model of Harris *et al.* [242] and Yamada *et al.* [243] this interaction is necessary to determine the phase relation between different Fe layers, but following [214] is not necessary to determine the in plane-propagation τ.

Lowering the ratio of $\frac{ab_{NN}}{c_{NN}}$ decreases the interaction between the two layers in the bilayer in comparison to a single layer and shifts τ to higher values, which can be seen in the phase diagram at $T = 0\,K$ from Naka *et al.* [214] in Fig. 4.40c, the points for $YFe_2O_{4-\delta}$, $YbFe_2O_{4-\delta}$ and $LuFe_2O_{4-\delta}$ were added from Table 4.27. This is a general shift to larger τ in $(\tau\tau\ell)$ if the ion size decreases from Y^{3+} over Yb^{3+} to Lu^{3+}, as it is observed in experiment. At higher temperatures the red line is expanded to a region in which the $\tau = \frac{1}{3}$ CO is stable as can be seen in the phase diagram in Figure 4.40b, which corresponds to the dotted line in Figure 4.40c.

Experimentally we found that at elevated temperature $LuFe_2O_{4-\delta}$ and $YbFe_2O_{4-\delta}$ lie in this zone and show a $\tau = \frac{1}{3}$ charge order, while $YFe_2O_{4-\delta}$ with the higher $\frac{ab_{NN}}{c_{NN}}$ is still in the phase where $\tau = \frac{1}{4}$ is favored. The experimental values of $\frac{c_{NN}}{c_{NNN}}$ for all three R^{3+} lie clearly above the border of $\frac{c_{NN}}{c_{NNN}} = 0.5$ (red line in Fig. 4.40c), which would correspond to $\tau = \frac{1}{2}$ at $T = 0\,K$. This is an indication that the rough approximation of $V \propto \frac{1}{r}$ is not valid. If one assumes screened potentials $V \propto \frac{1}{r}e^{-\frac{r}{\lambda_s}}$, with λ_s the screening length, the points would all be moved in the direction of the blue region both vertically and horizontally. Even if at non-zero temperature only the red line, where three charge orders with $\tau = \frac{1}{4}$, $\frac{1}{3}$ and $\frac{1}{2}$ are degenerate, is broadened as shown in Fig. 4.40b to a region where a $\tau = \frac{1}{3}$ CO is stable, $YFe_2O_{4-\delta}$ would have a $\tau = \frac{1}{3}$ propagation. From experiment we can therefore conclude, that a pure $V = \frac{1}{r}$ potential cannot explain the observed charge orders.

Lowering of the $\frac{ab_{NN}}{d_b}$ also increases the intralayer interaction as does a lowering of $\frac{c_{NN}}{c_{NNN}}$, therefore a lowering of τ can also be expected, which is what is observed if one changes from $LuFe_2O_{4-\delta}$ over $YbFe_2O_{4-\delta}$ to $YFe_2O_{4-\delta}$ (cf. Tab. 4.27).

In regard of the temperature changes in $YFe_2O_{4-\delta}$, cooling from the $\tau = \frac{1}{3}$ room temperature short-range correlations at the phase transition at 228.5 K τ is lowered to $\frac{2}{7}$, but with this structure no full charge order is possible as long as the structure is centrosymmetric. This is because of the mean Fe valence of 2.5, which cannot be distributed as Fe^{2+} and Fe^{3+} on the 7 distinct sites of the 210 K CO structure, as long as the structure is centrosymmetric. A centrosymmetric structure is very likely because the CO pattern determined by BVS is always centrosymmetric, even if the structure is refined in the non-centrosymmetric space group P1. On further cooling the electron hopping is reduced and a full charge order is favored, as can be seen in the BVS at 160 K, which shows a stronger localization. Since a full localization of

the Fe electrons is not possible with $\tau = \frac{2}{7}$ it is further lowered to $\tau = \frac{1}{4}$, which leads to the fully charge ordered structure determined at 160 K.

To explore how far the charge order correlations in $YFe_2O_{4-\delta}$ reach, one has to look at the width of superstructure peaks observed in X-ray diffraction. The resolution from the SuperNova diffractometer is not high enough to allow any determination of charge order correlation lengths based on the peak with. Our only synchrotron measurement on $YFe_2O_{4-\delta}$ was a resonant scattering experiment reported in my diploma thesis [20]. During this experiment we made some reciprocal space scans at 120 K to determine the peak width. At 120 K $YFe_2O_{4-\delta}$ shows the same charge order as at 160 K, so the results are representative for the 160 K phase. Figure 4.40 shows the intensity of a reciprocal space scan along (00ℓ) through the superstructure reflection $(\frac{1}{2}, \frac{1}{2}, 13.5)$ at 120 K and the structural reflection $(0, 0, 18)$ at 10 K.

The peak width of the $(\frac{1}{2}, \frac{1}{2}, 13.5)$ superstructure reflection along (00ℓ) was corrected for the width of the structural reflection, to take into account instrumental resolution and mosaicity. From this a correlation length of 22 unit cells along **c** was determined, which corresponds to 66 Fe bilayers. This is larger than typical correlation lengths observed in $LuFe_2O_{4-\delta}$ 7 [232] or 9 Fe bilayers [250] .

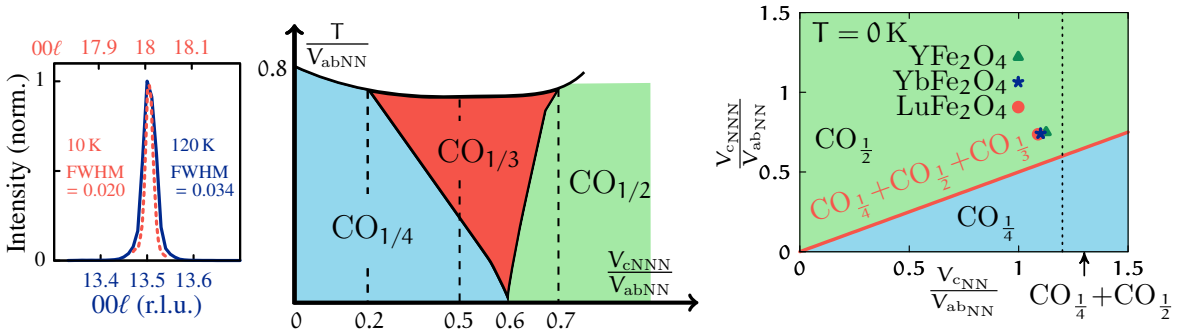

(a) reciprocal space scan (b) phase diagram [79] (c) phase diagram [214]

Figure 4.40: (a) Scan through $(\frac{1}{2}, \frac{1}{2}, 13.5)$ along $(0, 0, \ell$ at 120 K and $(0, 0, 18)$ at 10 K. The ℓ-position of the 120 K peak was corrected, based on the 10 K UB-matrix. Figure from own published work [40].
(b) Mean-field phase diagram for $RFe_2O_{4-\delta}$ (Reprinted with permission from A. Nagano et al., Phys. Rev. Lett. 99, 217202 (2007) Copyright (2007) by the American Physical Society [79]) (c) Mean-field phase diagram at $T = 0$ for $RFe_2O_{4-\delta}$ (Reprinted with permission from M.Naka et al., Phys. Rev. B 77, 224441 (2008) Copyright (2008) by the American Physical Society [214], points added from Table 4.27, assuming $V \propto \frac{1}{r}$, the dotted line corresponds to Figure (b).

The ℓ-coordinate in the propagation vector $(\frac{1}{4}\frac{1}{4}\frac{1}{2})$ is not received from the model in [214], but simply originates from an assumed out of phase stacking of the two layers. It is worthwhile to have a look at the different propagation vectors with $\tau = \frac{1}{4}$, $(\frac{1}{4}\frac{1}{4}0)$ is a special point Σ, the two smallest cells compatible with this propagation vector have spacegroup P2/m with 3 Fe positions or P2/c with 2 Fe positions. The P2/m cell with 3 distinct Fe sites cannot have a full charge order of Fe^{2+} and Fe^{3+}. The P2/c cell can have a full charge order. If small distortion modes amplitudes are introduced in the structure received from ISODISTORT [171],

the received charge order pattern is not the one from Naka *et al.* [214], which is reproduced in Figure 4.21b, where a Fe^{2+} ion in the upper layer has always a majority of Fe^{3+} in the triangle surrounding it in the lower layer and vice versa. The propagation vector $(\frac{1}{4}\frac{1}{4}\frac{1}{2})$ is a general point, the two smallest compatible cells both have two k-vectors active. The solution with spacegroup C2/m has 9 distinct Fe positions and therefore cannot have a full charge order. The second solution with spacegroup C2/c has 6 Fe sites, but we were not able to reproduce the pattern from Fig. 4.21b, by introduction of small distortions.

The very small frequency dependent shift of the AC susceptibility of the higher temperature transition of $YFe_2O_{4-\delta}$ is an indication for some partial magnetic order, this would be compatible with a not fully localized CO at 200 K in conjunction with different Fe^{3+} and Fe^{2+} magnetic moments.

In the $\tau = \frac{1}{3}$ charge order the nearest neighbor coulomb interaction cancels out in a non distorted triangular lattice [251]. The $\tau = \frac{1}{3}$ charge is rather stabilized by both thermal and quantum fluctuations, causing the interlayer electron transfer [251]. Let us now consider a distortion of the triangular lattice, which alters the potential along [110] different from the one along [100]. For the non-distorted case with full frustration, the $\tau = \frac{1}{3}$ charge order is energetically favorable [252]. If now increasing distortions are introduced the $\tau = \frac{1}{4}, \frac{1}{2}$ charge orders, which are based on Coulomb interaction are favored [252]. The distortions of the Fe layers in $YFe_2O_{4-\delta}$ (cf. Sec. 4.8.3 and 4.7.4) are much stronger than in $LuFe_2O_{4-\delta}$ [9, 75], this can be well seen in the large standard deviations of the ab_{NN}-distances in Table 4.27, which reassemble the huge spread of Fe-Fe distances in $YFe_2O_{4-\delta}$. The stronger distorting of the triangular lattice in $YFe_2O_{4-\delta}$ leads to a preference for the Coulomb based $\tau = \frac{1}{4}$ charge order in contrast to the quantum $\tau = \frac{1}{3}$ in $LuFe_2O_{4-\delta}$.

Naka *et al.* [253] found that a reduced cluster size in the cluster mean-field method on a model with interaction spin-less fermions on a single bilayer, does not lead to a $\tau = \frac{1}{4}$ charge order in contrast to their calculations on static charges [79]. If one considers that the correlation length in $YFe_2O_{4-\delta}$ is found to be much larger (66 bilayers) than in $LuFe_2O_{4-\delta}$ (7-9 bilayers [232, 250]), this can be another explanation why $LuFe_2O_{4-\delta}$ favours the $\tau = \frac{1}{3}$ charge order.

Considering the temperature dependence of the charge order in $YFe_2O_{4-\delta}$, Nagano *et al.* [79] found by Monte Carlo calculations for $\frac{V_{cNN}}{V_{a\,bNN}} = 1.2$ and $\frac{V_{cNNN}}{V_{a\,bNN}} = 0.6$, which they assume applicable for $RFe_2O_{4-\delta}$, that with decreasing temperature the dominant charge-correlation function changes from $\tau = \frac{1}{3}$ over $\tau = \frac{1}{2}$ to $\tau = \frac{1}{4}$. Although it does not reassemble the $\tau = \frac{2}{7}$ CO we observe, it predicts a two step transition with $\tau = \frac{1}{3}$ as start- and $\tau = \frac{1}{4}$ as end-member, as observed in $YFe_2O_{4-\delta}$. This is also conform with the observation that the temperature of the charge ordering transition in $YFe_2O_{4-\delta}$ (228 and 190 K) is lower than those of the $\tau = \frac{1}{3}$ CO in $LuFe_2O_{4-\delta}$ (320 K).

The magnetic structure of $YFe_2O_{4-\delta}$ at 200 K is described based on the rhombohedral structure and a propagation vector of $\left(\frac{5}{14}\frac{5}{14}\frac{18}{14}\right)_{hex}$, leading to the magnetic space group $P_s\bar{1}$. The diffraction pattern is compatible with two structures one without origin shift and the other with a shift of $\left(\frac{\bar{1}}{3}\frac{\bar{1}}{6}\frac{1}{3}\right)_{hex}$. The structure with origin shift has almost full moments on the

Fe^{2+} sites and reduced moments on the Fe^{3+} sites, which seems to be the more likely scenario, considering the partial disorder of the Fe^{3+} sites in the charge order structure. In contrast to this the 160 K spin structure is described based on the 160 K CO cell by a propagation vector of $(0\frac{1}{2}\frac{1}{2})_{CO}$ and a cell with spacegroup $P_s\bar{1}$ and no origin shift in relation to the CO cell. In hexagonal coordinates the main propagation is $(\frac{3}{8}\frac{3}{8}\frac{45}{8})_{hex}$, although higher harmonics are also present.

Considering the periodicity τ in $(\tau\tau\ell)_{hex}$, at room temperature we observed diffuse magnetic scattering at $\tau = 0.333$, at 200 K τ increases to 0.357 and τ increases further at 160 K to $\tau = 0.375$. This is in contrast to the charge order periodicity, which decreases with decreasing temperature from $\tau = 0.333$ at room temperature over 0.286 at 200 K to $\tau = 0.25$ at 160 K. This is also in contrast to $LuFe_2O_{4-\delta}$ where both the charge order and spin order periodicity at room temperature and low temperature is at $\tau = \frac{1}{3}$ (a small incommensurability of $\Delta\tau = +0.0028$ is observed), although in contrast to $YFe_2O_{4-\delta}$ charge and spin order occur at different temperatures [75]. This might be an indication that spin charge coupling plays a more important role in stabilizing the charge and spin structure in $YFe_2O_{4-\delta}$ than in $LuFe_2O_{4-\delta}$.

The strong orbital magnetic moment observed above the CO transition and in non-stoichiometric $YFe_2O_{4-\delta}$ excludes long-range orbital magnetic order. Since both magnetic transitions are also structural transitions, it is possible that at low temperature the Fe^{3+} orbital moment is quenched. The XMCD signal of the antiferromagnetic states is too weak to use sum rules. In resonant X-ray diffraction at 120 K a small anisotropy is observed [20], which could be connected to orbital order and is theoretically expected for the $RFe_2O_{4-\delta}$ system [78, 79]. The XMCD signal at 200 K (cf. Fig. 4.12) shows a much larger signal for the Fe^{2+} ions than for Fe^{3+}, indicating a higher net magnetic moment of Fe^{2+} along the field direction than the Fe^{3+} moment antiparallel to the field direction.

Since the magnetic structure is antiferromagnetic this cannot be directly linked to the moment sizes. One can conclude that Fe^{2+} is more easily polarized by a magnetic field, but it is unclear for which spin structure (full Fe^{2+} moments or decreased moments) this is the case. At 160 K the XMCD signals for both Fe^{2+} and Fe^{3+} have a similar size indicating an equal contribution to the net magnetic moment, which is compatible with the fully ordered antiferromagnetic spin structure given in Figure 4.37.

5

Summary and Outlook

In this thesis two materials, which were proposed as potential multiferroics, were investigated; i) $YFe_2O_{4-\delta}$, which shows complex charge order and ii) $Ni_{0.42}Mn_{0.58}TiO_3$, which is a XY-spin glass with toroidal moments. Single crystals of $Ni_{0.42}Mn_{0.58}TiO_3$ where grown with the traveling floating zone method and the Ni/Mn-stoichiometry was determined by powder and single crystal X-ray diffraction to be between 0.403 and 0.432. The spin glass state can only be established for a Ni/Mn-ratio between 0.4 and 0.5 (cf. Fig. 3.1). By a frequency shift of the AC-susceptibility it was shown that our single crystals obey the spin glass phase below 10 K, which was further proven through a magnetic memory-test. The single crystals show the same magnetic anisotropy as observed in [35], where the spins freeze first in the $\mathbf{c}_{\text{hex}}$-plane. A magnetoelectric effect based on toroidal moments could not be reproduced after applying the same cooling in crossed magnetic and electric fields inside the $\mathbf{c}_{\text{hex}}$-plane as reported in [35]. This was most likely caused by the imperfect isolating of the sample and joule heating caused by the application of the electric field, which warmed the sample over the spin glass transition at 10 K. Neutron diffraction showed magnetic diffuse lines along $(1, 0, \ell)$ with enhanced intensity on the positions expected for $NiTiO_3$ and $MnTiO_3$. Polarization analysis confirmed that the spins lie inside the $\mathbf{c}_{\text{hex}}$-plane. It would be interesting in the future to improve the setup for a measurement in electric fields using the MPMS, to isolate the sample from the contacts to avoid joule heating and possibly reproduce the results from [35]. If the effect cannot be reproduced, one has to further explore different Ni/Mn stoichiometries since [35] do not specify how the ratio was determined.

The main part of this thesis is dedicated to the determination of the charge order structures of $YFe_2O_{4-\delta}$ at 160 K and 200 K. At room temperature $YFe_2O_{4-\delta}$ has the rhombohedral spacegroup $R\bar{3}m$, but shows additional diffuse scattering along $\left(\frac{1}{3}\frac{1}{3}\ell\right)$ as indication for 2D order inside the Fe-layers, which are still randomly stacked. Cooling below the first magnetic transition at 228.5 K, 3D charge order of the Fe-ions occurs. This charge order is based on a propagation vector of $\left(\frac{2}{7}\frac{2}{7}\frac{3}{7}\right)$ and a reduction of the symmetry to $P\bar{1}$. From single crystal X-ray diffraction the crystallographic structure of $YFe_2O_{4-\delta}$ was solved and refined. The lost symmetry elements lead to 6 twin domains. Since the atomic form factors of Fe^{2+} and Fe^{3+} are too close to be directly distinguished by X-ray diffraction, bond valence sum analysis was applied to determine the valence of the Fe ions. The charge order at 200 K is incomplete, as one would

expect from a distribution of the mean Fe valence of 2.5 on 7 distinct sites. While three sites show a strong localization and are therefore Fe^{2+} the other four sites share the 0.5 electrons left, with a preference for the electron to be at one site. The valence pattern is found to be centrosymmetric even if the structure is refined in the non-centrosymmetric spacegroup P1, which makes a centrosymmetric structure very likely. The determined structure is triclinic in contrast to the early suggestion of a monoclinic phase [160]. In contrast to the triclinic structure suggested by Blasco *et al.* [170] based on representation analysis and powder X-ray diffraction our structure has a 7-times lower volume and can explain all reflections shown in [170]. Mode decomposition shows that three modes belonging to the general point $\left(\frac{2}{7}\frac{2}{7}\frac{3}{7}\right)$ and its higher harmonics are necessary to describe the charge order.

The spin order of $YFe_2O_{4-\delta}$ at 200 K is characterized by the propagation vector $\left(\frac{5}{14}\frac{5}{14}\frac{18}{14}\right)$ in hexagonal notation. A contribution of higher harmonics could be excluded for even order harmonics and the fifth and seventh harmonic. Two cells both with spacegroup $P_s\bar{1}$ are compatible with this propagation, one has no origin shift the other one by $\left(\frac{\bar{1}}{3}\frac{\bar{1}}{6}\frac{1}{3}\right)_{hex}$. A refinement of the neutron diffraction data based on the $R\bar{3}m$ structure could not distinguish between the two structures. Since the structure with orgin shift shows almost full moments on the stronger localized Fe^{2+} positions, it is considered to be more likely. In the future the refinement of the spin structure could be improved through inclusion of reflections from different domains and the introduction of the distortions of the 200 K CO cell in the refinement. Nevertheless we were able for the first time to determine the spin structure of $YFe_2O_{4-\delta}$.

Cooling through the second magnetic transition at 180 K, the propagation of the charge order changes to $\left(\frac{1}{4}\frac{1}{4}\frac{3}{4}\right)$ and the structure also obeys the triclinic centrosymmetric spacegroup $P\bar{1}$ with 6 twin domains due to the lost symmetry elements (relative to the $R\bar{3}m$ structure). Again by BVS the Fe valence was determined and a full charge disproportionation into Fe^{2+} and Fe^{3+} was found, which is in accordance with the results on $LuFe_2O_{4-\delta}$ [9, 76] and conform with Mössbauer spectroscopy [160, 174] and is in contrast to the previously suggested multimodal valence [193] based on XANES measurements on $LuFe_2O_{4-\delta}$. The 160 K charge order phase is insensitive to magnetic fields up to 24 T in contrast to $LuFe_2O_{4-\delta}$ where metamagnetic transitions were observed [123]. Mode decomposition shows that the CO pattern is mainly based on the single mode of the general point $\left(\frac{1}{4}\frac{1}{4}\frac{3}{4}\right)$. For the low temperature phase a correlation of the CO over 66 Fe bilayers was determined, which is much larger than the typical lengths observed in $LuFe_2O_{4-\delta}$; 7 [232] or 9 [250] Fe bilayers.

The lowering of τ in the propagation $(\tau\tau\ell)$ from $\frac{1}{3}$ observed in $LuFe_2O_{4-\delta}$ and $YbFe_2O_{4-\delta}$ to $\frac{2}{7}$ and on further cooling to $\frac{1}{4}$ in $YFe_2O_{4-\delta}$, is explained by the larger ionic radius of Y^{3+}, which reduces the intrabilayer Fe-Fe distances and increases the interlayer spacing inside a bilayer. This experimental observation therefore confirms the theoretical prediction from Naka *et al.* [214] (cf. Fig. 4.40c) where an enhancement of the intralayer interaction in relation to the interlayer interaction is expected to lower τ.

At 160 K the magnetic structure is based on a propagation vector of $\left(0\frac{1}{2}\frac{1}{2}\right)_{CO}$ and has the spacegroup $P_s\bar{1}$ with no origin shift in regard to the 160 K charge order structure. From the 16 possible spin structures with full moments, only one matches the relative intensities ob-

served in neutron diffraction and the spin structure with both Fe^{3+} spins, in the magnetic cell, pointing in the same direction and the two Fe^{2+} in the other direction is realized.

In conclusion the most relevant achievement of this thesis is the determination of the two low temperature charge order structures of $YFe_2O_{4-\delta}$, which are both found to be triclinic. This gives also new input for the structure determination of $LuFe_2O_{4-\delta}$ and $YbFe_2O_{4-\delta}$. The second important achievement is the establishment of the spin structures of $YFe_2O_{4-\delta}$ at 200 K and 160 K for the first time.

Bibliography

[1] C. Ederer and N. Spaldin, "Magnetoelectrics - a new route to magnetic ferroelectrics", Nat. Mater. **3**, 849 (2004) (cited on page 1).

[2] M. Bibes and A. Barthelemy, "Multiferroics: towards a magnetoelectric memory", Nat. Mater. **7**, 425 (2008) (cited on page 1).

[3] H. Schmid, "Some symmetry aspects of ferroics and single phase multiferroics", J. Phys.: Condens. Matter **20**, 434201 (2008) (cited on pages 1, 25, 26).

[4] N. Spaldin, "Magnetic materials: fundamentals and applications" (Cambridge University Press, 2010) (cited on page 1).

[5] P. Weiss, "L'hypothèse du champ moléculaire et la propriété ferromagnétique", Journal de Physique Théorique et Appliquée **6**, 661 (1907) (cited on page 1).

[6] N. A. Hill, "Why are there so few magnetic ferroelectrics?", J. Phys. Chem. B **104**, 6694 (2000) (cited on page 1).

[7] R. N. P. Choudhary and S. K. Patri, "Multiferroics: an introduction", in AIP Conf. Proc. Vol. 1063, edited by S. M. Bose, S. N. Behera, and B. K. Roul, 1 (2008), p. 263 (cited on page 1).

[8] N. Ikeda, H. Ohsumi, K. Ohwada, K. Ishii, T. Inami, K. Kakurai, Y. Murakami, K. Yoshii, S. Mori, Y. Horibe, and H. Kito, "Ferroelectricity from iron valence ordering in the charge-frustrated system $LuFe_2O_4$", Nature **436**, 1136 (2005) (cited on page 2).

[9] J. de Groot, T. Mueller, R. A. Rosenberg, D. J. Keavney, Z. Islam, J.-W. Kim, and M. Angst, "Charge order in $LuFe_2O_4$: an unlikely route to ferroelectricity", Phys. Rev. Lett. **108**, 187601 (2012) (cited on pages 2, 14, 22, 45–47, 50, 51, 55, 62, 63, 73, 92, 101, 104, 108).

[10] D. Niermann, F. Waschkowski, J. de Groot, M. Angst, and J. Hemberger, "Dielectric properties of charge-ordered $LuFe_2O_4$ revisited: the apparent influence of contacts", English, Phys. Rev. Lett. **109**, 016405 (2012) (cited on page 2).

[11] A. Ruff, S. Krohns, F. Schrettle, V. Tsurkan, P. Lunkenheimer, and A. Loidl, "Absence of polar order in $LuFe_2O_4$", English, Eur. Phys. J. B, **85**, 30296 (2012) (cited on page 2).

[12] S. Lafuerza, J. García, G. Subías, J. Blasco, K. Conder, and E. Pomjakushina, "Intrinsic electrical properties of $LuFe_2O_4$", Phys. Rev. B **88**, 085130 (2013) (cited on page 2).

[13] E. J. W. Verwey, "Electronic conduction of magnetite (Fe_3O_4) and its transition point at low temperatures", Nature **144**, 327 (1939) (cited on page 2).

[14] M. S. Senn, J. P. Wright, and J. P. Attfield, "Charge order and three-site distortions in the Verwey structure of magnetite", Nature **481**, 173 (2012) (cited on page 2).

[15] K. Yamauchi, T. Fukushima, and S. Picozzi, "Ferroelectricity in multiferroic magnetite Fe_3O_4 driven by noncentrosymmetric Fe^{2+} / Fe^{3+} charge-ordering: first-principles study", Phys. Rev. B **79**, 212404 (2009) (cited on page 2).

[16] F. Schrettle, S. Krohns, P. Lunkenheimer, V. A. M. Brabers, and A. Loidl, "Relaxor ferroelectricity and the freezing of short-range polar order in magnetite", Phys. Rev. B **83**, 195109 (2011) (cited on page 2).

[17] T. Nagata, P.-E. Janolin, M. Fukunaga, B. Roman, K. Fujiwara, H. Kimura, J.-M. Kiat, and N. Ikeda, "Electric spontaneous polarization in $YbFe_2O_4$", Appl. Phys. Lett. **110**, 052901 (2017) (cited on page 2).

[18] S. Ghosh, U. Chowdhury, S. Roy, and R. Bandyopadhyay, "Detection of low ppm carbon monoxide with charge ordered $LuFe_2O_4$ gas sensor – a novel sensing mechanism", Ceram. Int. **42**, 14944 (2016) (cited on page 2).

[19] M. Angst, "Ferroelectricity from iron valence ordering in rare earth ferrites?", Phys. Status Solidi RRL **7**, 383 (2013), (for the reprint of Fig. 4.39b © 2013 WILEY-VCH Verlag GmbH & Co. KGaA, Weinheim) (cited on pages 2, 46, 83, 100).

[20] T. Mueller, "Charge and spin order in highly stoichiometric $YFe_2O_{4-\delta}$ single crystals", Diplomarbeit (RWTH Aachen, 2012) (cited on pages 2–4, 14, 18, 40, 42, 50, 51, 66, 82, 103, 105, 137, 138).

[21] N. A. Spaldin, M. Fiebig, and M. Mostovoy, "The toroidal moment in condensed-matter physics and its relation to the magnetoelectric effect", J. Phys.: Condens. Matter **20**, 434203 (2008) (cited on pages 2, 25, 28).

[22] D. G. Sannikov, "Phenomenological theory of the magnetoelectric effect in some boracites", J. Exp. Theor. Phys. **84**, 293 (1997) (cited on page 2).

[23] Y. F. Popov, A. M. Kadomtseva, D. V. Belov, G. P. Vorob'ev, and A. K. Zvezdin, "Magnetic-field-induced toroidal moment in the magnetoelectric Cr_2O_3", J. Exp. Theor. Phys. **69**, 330 (1999) (cited on page 2).

[24] Y. Yamaguchi, T. Nakano, Y. Nozue, and T. Kimura, "Magnetoelectric effect in an XY-like spin glass system $Ni_xMn_{1-x}TiO_3$", Phys. Rev. Lett. **108**, 057203 (2012) (cited on pages 2, 25, 26, 30–33, 35).

[25] H. Tonomoto, K. Kimura, and T. Kimura, "Magnetoelectric glass nature in magnetoplumbite-type $BaCo_6Ti_6O_{19}$", J. Phys. Soc. Jpn. **85**, 033707 (2016) (cited on page 2).

[26] H. A. Dabkowska and A. B. Dabkowski, "Crystal growth of oxides by optical floating zone technique", in *Springer handbook of crystal growth*, edited by G. Dhanaraj, K. Byrappa, V. Prasad, and M. Dudley (Springer Nature, 2010), pp. 367–391 (cited on page 3).

[27] S. Kimura and K. Kitamura, "Floating zone crystal growth and phase equilibria: a review", J. Am. Ceram. Soc. **75**, 1440 (1992) (cited on page 3).

[28] I. Shindo, N. Kimizuka, and S. Kimura, "Growth of YFe_2O_4 single crystals by floating zone method", Mater. Res. Bull. **11**, 637 (1976) (cited on pages 3, 37, 40).

[29] J. Iida, S. Takekawa, and N. Kimizuka, "Single crystal growth of $LuFe_2O_4$, $LuFeCoO_4$ and $YbFeMgO_4$ by the floating zone method", J. Cryst. Growth **102**, 398 (1990) (cited on page 3).

[30] M. Angst, R. P. Hermann, A. D. Christianson, M. D. Lumsden, C. Lee, M.-H. Whangbo, J.-W. Kim, P. J. Ryan, S. E. Nagler, W. Tian, R. Jin, B. C. Sales, and D. Mandrus, "Charge order in $LuFe_2O_4$: antiferroelectric ground state and coupling to magnetism", Phys. Rev. Lett. **101**, 227601 (2008) (cited on pages 3, 82, 83).

[31] A. D. Christianson, M. D. Lumsden, M. Angst, Z. Yamani, W. Tian, R. Jin, E. A. Payzant, S. E. Nagler, B. C. Sales, and D. Mandrus, "Three-dimensional magnetic correlations in multiferroic $LuFe_2O_4$", Phys. Rev. Lett. **100**, 107601 (2008) (cited on pages 3, 24, 80, 83, 93).

[32] H. Williamson, T. Mueller, M. Angst, and G. Balakrishnan, "Growth of $YbFe_2O_4$ single crystals exhibiting long-range charge order via the optical floating zone method", J. Cryst. Growth **475**, 44 (2017) (cited on pages 3, 46).

[33] N. Kimizuka, A. Takenaka, Y. Sasada, and T. Katsura, "A series of new compounds $A^{3+}Fe_2O_4$ (A = Ho, Er, Tm, Yb, and Lu)", Solid State Commun. **15**, 1321 (1974) (cited on page 3).

[34] H. L. Williamson, "Magnetic and charge order in $LuFe_2O_4$ and $YbFe_2O_4$ multiferroics", Master thesis (University of Warwick, 2012) (cited on pages 3, 46).

[35] Y. Yamaguchi and T. Kimura, "Magnetoelectric control of frozen state in a toroidal glass", Nat. Commun. **4**, 2063 (2013) (cited on pages 3, 25, 26, 28, 32, 33, 35, 36, 107).

[36] H. Takei, "Preferentially orientated precipitation in $MnTiO_3$ single crystals", English, J. Mater. Sci. **16**, 1310 (1981) (cited on pages 3, 28).

[37] K. Kuribayashi, R. Takahashi, Y. Inatomi, S. Ozawa, and M. S. V. Kumar, "Containerless processing of metastable multiferroic composite in R-Fe-O system (R: Rare-earth element)", Int. J. Microgravity Sci. Appl. **33**, 330215 (2016) (cited on page 4).

[38] Y. B. Kang and H. G. Lee, "Experimental study of phase equilibria in the MnO -"TiO_2"- "Ti_2O_3" system", Isij International **45**, 1543 (2005) (cited on page 4).

[39] D.-P. Chen, X.-L. Wang, Y. Du, S. Ni, Z.-B. Chen, and X. Liao, "Growth mechanism and magnetic properties of highly crystalline NiO nanocubes and nanorods fabricated by evaporation", Crystal Growth & Design **12**, 2842 (2012) (cited on page 4).

[40] T. Mueller, J. de Groot, J. Strempfer, and M. Angst, "Stoichiometric $YFe_2O_{4-\delta}$ single crystals grown by the optical floating zone method", J. Cryst. Growth. **428**, 40 (2015) (cited on pages 4, 39–42, 44, 103).

[41] "Physical Property Measurement System: Vibrating Sample Magnetometer (VSM) Option User's Manual" (Quantum Design 6325 Lusk Boulevard San Diego, CA 92121 USA, 2003) (cited on page 5).

[42] "Magnetic Property Measurement System: SQUID VSM User's Manual" (Quantum Design 6325 Lusk Boulevard San Diego, CA 92121 USA, 2009) (cited on page 5).

[43] M. Faraday, "Experimental researches in electricity", edited by Richard and J. E. Taylor, 2nd ed., Vol. 1 (Printers and Publishers of the University of London, 1849) (cited on page 5).

[44] J. Clarke and A. I. Braginski, eds., "The SQUID handbook", Vol. 1 and 2 (Wiley-Blackwell, 2005) (cited on page 5).

[45] K. Binder and A. P. Young, "Spin glasses: experimental facts, theoretical concepts, and open questions", Rev. Mod. Phys. **58**, 801 (1986) (cited on pages 5, 30).

[46] D. Martien, "Introduction to AC susceptibility - AC magnetic measurements" (Quantum Design Aplication Notes) (cited on page 5).

[47] M. Schmitz, "Strain and electric field mediated manipulation of magnetism in $La_{(1-x)}Sr_xMnO_3/BaTiO_3$ heterostructures", PhD thesis (RWTH Aachen, 2015) (cited on page 5).

[48] C. Cohen-Tannoudji, B. Diu, and F. Laloe, "Quantum mechanics", Vol. 2 (John Wiley & Sons, 1977) (cited on page 6).

[49] S. Blügel, "Scattering theory: born series", in *Scattering methods for condensed matter research: towards novel applications at future sources*, Vol. 33, edited by M. Angst, T. Brückel, D. Richter, and R. Zorn, Lecture Notes of the 43rd IFF Spring School 2012 (Schriften des Forschungszentrums Jülich Reihe Schlüsseltechnologien, 2013) Chap. A2 (cited on page 7).

[50] T. Brückel, D. Richter, G. Roth, A. Wischnewski, and R. Zorn, eds., "Laboratory course neutron scattering lectures", Vol. 16 (Schriften des Forschungszentrums Jülich Reihe Schlüsseltechnologien, 2015) (cited on pages 8, 16–18, 129).

[51] B. W. Batterman and C. Henderson, "Dynamical diffraction of X rays by perfect crystals", Rev. Mod. Phys. **36**, 681 (1964) (cited on page 8).

[52] M. Angst, "Material analysis by synchrotron radiation and neutrons", Lecture notes (RWTH Aachen, 2015) (cited on pages 8, 9).

[53] E. Rebhan, "Theoretische Physik: Relativistische Quantenmechanik, Quantenfeldtheorie und Elementarteilchentheorie" (Springer-Verlag, Berlin Heidelberg, 2010) (cited on page 10).

[54] S.-L. Chang, "X-ray multiple-wave diffraction - theory and application" (Springer-Verlag, Berlin Heidelberg, 2004) (cited on page 10).

[55] U. Shmueli, "Reciprocal space in crystallography", in *International tables for crystallography*, Vol. B (International Union of Crystallography, 2006) Chap. 1.1, pp. 2–9 (cited on page 11).

[56] Rigaku Oxford Diffraction, (2015), CrysAlisPro Software system, version number 1.171.37.35, Rigaku Corporation, Oxford, UK (cited on pages 12, 55, 56, 66).

[57] H. A. Hauptman, "The phase problem of X-ray crystallography: overview", in *Electron crystallography* (Springer Netherlands, 1997), pp. 131–138 (cited on page 13).

[58] H. Shenk, "An introduction to direct methods. the most important phase relationships and their application in solving the phase problem", edited by C. A. Taylor, University College Cardiff Press Cardiff, Wales: International Union of Crystallography, 2001 (cited on page 13).

[59] A. Altomare, G. Cascarano, C. Giacovazzo, A. Guagliardi, M. C. Burla, G. Polidori, and M. Camalli, "SIR92 – a program for automatic solution of crystal structures by direct methods", J. Appl. Crystallogr. **27**, 435 (1994) (cited on page 13).

[60] G. Oszlányi and A. Süto, "Ab initio structure solution by charge flipping", Acta Cryst. A **60**, 134 (2004) (cited on page 13).

[61] L. Palatinus, "Ab initio determination of incommensurately modulated structures by charge flipping in superspace", Acta Cryst. A **60**, 604 (2004) (cited on page 13).

[62] G. Oszlányi and A. Sütő, "The charge flipping algorithm", Acta Crystallogr. A **64**, 123 (2007) (cited on page 13).

[63] L. Palatinus and G. Chapuis, "Superflip - a computer program for the solution of crystal structures by charge flipping in arbitrary dimensions.", J. Appl. Cryst. **40**, 786 (2007) (cited on pages 13, 48, 56, 68).

[64] V. Petříček, M. Dušek, and L. Palatinus, "Crystallographic computing system JANA2006: general features", Z. Kristallogr. **229(5)**, 345 (2014) (cited on pages 13, 48, 56, 70, 87, 88).

[65] V. Petříček and M. Dušek, "JANA98 the crystallographic computing system" (Institute of Physics Academy of Sciences of the Czech Republic, 2000) (cited on page 13).

[66] A. J. C. Wilson, "Largest likely values for the reliability index", Acta Cryst. **3**, 397 (1950) (cited on page 14).

[67] W. Massa, "Kristallstrukturbestimmung" (Vieweg Verlag, Friedr, & Sohn Verlagsgesellschaft mbH, 2011) (cited on pages 14, 84).

[68] P. Müller, R. Herbst-Irmer, A. L. Spek, T. R. Schneider, and M. R. Sawaya, "Crystal structure refinement: a crystallographer's guide to SHELXL", edited by P. Müller (Oxford University Press, 2006) (cited on pages 14, 69).

[69] M. Ladd and R. Palmer, "Structure determination by X-ray crystallography" (Springer US, 2013) (cited on page 14).

[70] W. Clegg, A. J. Blake, J. M. Cole, J. S. O. Evans, P. Main, S. Parsons, and D. J. Watkin, "Crystal structure analysis: principles and practice", edited by W. Clegg (Oxford University Press, 2009) (cited on page 14).

[71] F. L. Hirshfeld and D. Rabinovich, "Treating weak reflexions in least-squares calculations", Acta Crystallogr. A **29**, 510 (1973) (cited on page 14).

[72] L. Arnberg, S. Hovmöller, and S. Westman, "On the significance of 'non-significant' reflexions", Acta Crystallogr. A **35**, 497 (1979) (cited on page 14).

[73] F. L. Hirshfeld, "Can X-ray data distinguish bonding effects from vibrational smearing?", Acta Crystallogr. A **32**, 239 (1976) (cited on pages 14, 98).

[74] J. Strempfer, "Anomalous and resonant X-ray scattering: spin, charge and orbital order", in *Scattering methods for condensed matter research: towards novel applications at future sources - Schriften des Forschungszentrums Jülich . Reihe Schlüsseltechnologien / Key Technologies, Vol. 33*, edited by M. Angst, T. Brückel, D. Richter, and R. Zorn (Forschungszentrum Jülich GmbH Zentralbibliothek, Verlag, 2012) Chap. D11 (cited on page 14).

[75] J. de Groot, "Charge, spin and orbital order in the candidate multiferroic material $LuFe_2O_4$", PhD thesis (RWTH Aachen, 2012) (cited on pages 14, 21–23, 51, 55, 62, 83, 88, 104, 105).

[76] A. M. Mulders, S. M. Lawrence, U. Staub, M. Garcia-Fernandez, V. Scagnoli, C. Mazzoli, E. Pomjakushina, K. Conder, and Y. Wang, "Direct observation of charge order and an orbital glass state in multiferroic $LuFe_2O_4$", Phys. Rev. Lett. **103**, 077602 (2009) (cited on pages 14, 15, 45, 62, 108).

[77] S. M. Lawrence, "X-ray and neutron scattering of multiferroic $LuFe_2O_4$", PhD thesis (Curtin University, 2011) (cited on page 14).

[78] A. Nagano and S. Ishihara, "Spin-charge-orbital structures and frustration in multiferroic RFe_2O_4", J. Phys.: Condens. Matter **19**, 145263 (2007) (cited on pages 14, 41, 105).

[79] A. Nagano, M. Naka, J. Nasu, and S. Ishihara, "Electric polarization, magnetoelectric effect, and orbital state of a layered iron oxide with frustrated geometry", Phys. Rev. Lett. **99**, 217202 (2007) (cited on pages 14, 41, 63, 100, 101, 103–105).

[80] I. D. Brown, "The chemical bond in inorganic chemistry : the bond valence model", IUCr Monographs on Crystallography Volume 12 (Oxford Univ. Press, Oxford, 2006) (cited on page 15).

[81] I. D. Brown, "Bond valence theory", Struct. Bond. **158**, 11 (2014) (cited on page 15).

[82] L. Pauling, "Atomic radii and interatomic distances in metals", J. Am. Chem. Soc. **69**, 542 (1947) (cited on page 15).

[83] I. D. Brown and D. Altermatt, "Bond-valence parameters obtained from a systematic analysis of the inorganic crystal structure database", Acta Cryst. B **41**, 244 (1985) (cited on pages 15, 61, 62).

[84] N. E. Brese and M. O'Keeffe, "Bond-valence parameters for solids", Acta Cryst. B **47**, 192 (1991) (cited on page 15).

[85] S. Lafuerza, G. Subías, J. García, J. Blasco, G. Nisbet, K. Conder, and E. Pomjakushina, "Determination of the sequence and magnitude of charge order in $LuFe_2O_4$ by resonant X-ray scattering", Phys. Rev. B **90**, 085130 (2014) (cited on pages 15, 62, 63).

[86] S. Lafuerza, G. Subías, J. Blasco, J. García, G. Nisbet, K. Conder, and E. Pomjakushina, "Determination of the charge-ordered phases in $LuFe_2O_4$", Epl **107**, 47002 (2014) (cited on pages 15, 62, 63).

[87] S. M. Kanowitz and G. J. Palenik, "Bond valence sums in coordination chemistry using oxidation-state-independent R_0 values. a simple method for calculating the oxidation state of iron in Fe-O complexes", Inorg. Chem. **37**, 2086 (1998) (cited on pages 15, 61, 62).

[88] W. Liu and H. H. Thorp, "Bond valence sum analysis of metal-ligand bond lengths in metalloenzymes and model complexes. 2. Refined distances and other enzymes", Inorg. Chem. **32**, 4102 (1993) (cited on pages 15, 61).

[89] S. V. Krivovichev, "Derivation of bond-valence parameters for some cation-oxygen pairs on the basis of empirical relationships between r_o and b", Z. Kristallogr. **227**, 575 (2012) (cited on page 15).

[90] A. Dianoux and G. Lander, eds., "Neutron data booklet" (Institute Laue-Langevin, 2003) (cited on page 16).

[91] P. J. Brown, A. G. Fox, E. N. Masle, M. A. O'Keefe, and B. T. M. Willis, "Intensity of diffracted intensities", in *International tables for crystallography*, Vol. C, edited by E. Prince (International Union of Crystallography (IUCr), 2006) Chap. 6.1, pp. 554–595 (cited on page 17).

[92] P. J. Brown, "Magnetic form factors", in *International tables for crystallography*, Vol. C, edited by E. Prince (International Union of Crystallography (IUCr), 2006) Chap. 4.4, pp. 454–461 (cited on pages 17, 18).

[93] D. L. Price, "Introduction to neutron scattering", in *Methods in experimental physics, neutron scattering*, Vol. 23, Part A, edited by D. L. Price and K. Sköld (Academic Press INC., 1987) Chap. 1, pp. 1–97 (cited on page 17).

[94] S. Lovesey, "Theory of neutron scattering from condensed matter", Vol. 2, International series of monographs on physics (Clarendon Press Oxford, 1984) (cited on pages 17, 129).

[95] C. Zeyen, R. Chagnon, F. Disdier, and H. Morin, "A helium-flow cryostat (3 to 300 K) for neutron four-circle spectrometry", Revue de Physique Appliquée **19**, 789 (1984) (cited on page 19).

[96] K. Prokeš and F. Yokaichiya, "Elastic neutron diffraction on magnetic materials", in *Handbook of magnetic materials*, Vol. 25, edited by E. Brück (Elsevier, 2016) Chap. 2, p. 109 (cited on page 19).

[97] J. Schefer, M. Kännecke, A. Murasik, A. .Czopnik, T. Strässle, P. Keller, and N. Schlumpf, "Single-crystal diffraction instrument TriCS at SINQ", Physica B **276-278**, 168 (2000) (cited on page 20).

[98] H. S. Bennett and E. A. Stern, "Faraday effect in solids", Phys. Rev. **137**, A448 (1965) (cited on pages 20, 21).

[99] G. Schütz, W. Wagner, W. Wilhelm, P. Kienle, R. Zeller, R. Frahm, and G. Materlik, "Absorption of circularly polarized X rays in iron", Phys. Rev. Lett. **58**, 737 (1987) (cited on page 20).

[100] J. Stöhr, "Exploring the microscopic origin of magnetic anisotropies with X-ray magnetic circular dichroism (XMCD) spectroscopy", J. Magn. Magn. Mater. **200**, 470 (1999) (cited on page 20).

[101] P. A. van Aken and B. Liebscher, "Quantification of ferrous/ferric ratios in minerals: new evaluation schemes of fe $l_2$3 electron energy-loss near-edge spectra", English, Physics and Chemistry of Minerals **29**, 188 (2002) (cited on page 20).

[102] G. van der Laan and A. I. Figueroa, "X-ray magnetic circular dichroism—a versatile tool to study magnetism", Coord. Chem. Rev. **277-278**, 95 (2014) (cited on page 20).

[103] A. Rogalev, F. Wilhelm, N. Jaouen, J. Goulon, and J.-P. Kappler, "X-ray magnetic circular dichroism: historical perspective and recent highlights", in *Magnetism: a synchrotron radiation approach*, Vol. 697, edited by E. Beaurepaire, H. Bulou, F. Scheurer, and J.-P. Kappler, Lect. Notes Phys. (Springer-Verlag, Berlin Heidelberg, 2006), pp. 71–93 (cited on pages 20, 21).

[104] F. de Groot and A. Kotani, "X-ray magnetic circular dichroism", in *Core level spectroscopy of solids*, Vol. 6, edited by D. Sarma, G. Kotliar, and Y. Tokura, Advances in Condensed Matter Science (CRC Press, 2008) Chap. 7, pp. 287–334 (cited on pages 21, 22).

[105] F. Baudelet, C. Giorgetti, S. Pizzini, C. Brouder, E. Dartyge, A. Fontaine, J. Kappler, and G. Krill, "Study of 5d magnetism in rare-earth-transition-metal (Fe, Co) intermetallic compounds by magnetic circular X-ray dichroism", J. Electron. Spectrosc. Relat. Phenom. **62**, 153 (1993) (cited on page 21).

[106] C. Kapusta, P. Fischer, and G. Schütz, "Magnetic X-ray absorption spectroscopy", J. Alloys Compd. **286**, 37 (1999) (cited on page 21).

[107] S. W. Lovesey and S. P. Collins, "X-ray scattering and absorption by magnetic materials" (Clarendon Press Oxford, 1996) (cited on page 21).

[108] P. Zeeman, "Ueber einen Einfluss der Magnetisierung auf die Natur des von einer Substanz emittirten Lichtes", Verhandlungen der Physikalischen Gesellschaft zu Berlin, 128 (1896) (cited on page 21).

[109] J. C. Lang, "Characterization of materials", in *X-ray magnetic circular dichroism*, edited by E. N. Kaufmann (John Wiley and Sons, Inc., 2012), p. 1536 (cited on page 21).

[110] F. Baudelet, "X-ray magnetic circular dichroism", in *Neutron and X-ray spectroscopy* (Springer Nature, 2006), pp. 103–130 (cited on page 21).

[111] B. T. Thole, P. Carra, F. Sette, and G. van der Laan, "X-ray circular dichroism as a probe of orbital magnetization", Phys. Rev. Lett. **68**, 1943 (1992) (cited on page 22).

[112] P. Carra, B. T. Thole, M. Altarelli, and X. Wang, "X-ray circular dichroism and local magnetic fields", Phys. Rev. Lett. **70**, 694 (1993) (cited on page 22).

[113] M. Altarelli, "Orbital-magnetization sum rule for X-ray circular dichroism: a simple proof", Phys. Rev. B **47**, 597 (1993) (cited on page 22).

[114] A. Ankudinov and J. J. Rehr, "Sum rules for polarization-dependent X-ray absorption", Phys. Rev. B **51**, 1282 (1995) (cited on page 22).

[115] C. T. Chen, Y. U. Idzerda, H.-J. Lin, N. V. Smith, G. Meigs, E. Chaban, G. H. Ho, E. Pellegrin, and F. Sette, "Experimental confirmation of the X-ray magnetic circular dichroism sum rules for iron and cobalt", Phys. Rev. Lett. **75**, 152 (1995) (cited on page 22).

[116] A. Rogalev, K. Ollefs, and F. Wilhelm, "X-ray Magnetic Circular Dichroism", in *X-ray absorption and X-ray emission spectroscopy*, edited by J. A. V. Bokhoven and C. Lamberti (John Wiley & Sons, Ltd, 2016) Chap. 23, pp. 671–694 (cited on page 22).

[117] P. Kirkpatrick and A. V. Baez, "Formation of optical images by X-rays", J. Opt. Soc. Am. **38**, 766 (1948) (cited on page 23).

[118] T. Funk, A. Deb, S. J. George, H. Wang, and S. P. Cramer, "X-ray magnetic circular dichroism—a high energy probe of magnetic properties", Coord. Chem. Rev. **249**, 3 (2005) (cited on page 23).

[119] J. W. Freeland, J. C. Lang, G. Srajer, R. Winarski, D. Shu, and D. M. Mills, "A unique polarized x-ray facility at the advanced photon source", Rev. Sci. Instrum. **73**, 1408 (2002) (cited on page 23).

[120] D. Keavney, "Polarized soft X-ray science at the APS", Workshop on Soft X-ray Beamlines at the NSLS-II Brookhaven, NY, February 4, 2008 (cited on page 23).

[121] J. Iida, S. Kakugawa, G. Kido, Y. Nakagawa, S. Takekawa, and N. Kimizuka, "High field magnetization of single crystals YFe_2O_4, $YbFe_2O_4$ and $LuFe_2O_4$", Physica B **155**, 307 (1989) (cited on page 24).

[122] X. S. Xu, M. Angst, T. V. Brinzari, R. P. Hermann, J. L. Musfeldt, A. D. Christianson, D. Mandrus, B. C. Sales, S. McGill, J.-. Kim, and Z. Islam, "Charge order, dynamics, and magnetostructural transition in multiferroic $LuFe_2O_4$", Phys. Rev. Lett. **101**, 227602 (2008) (cited on page 24).

[123] J. de Groot, K. Marty, M. D. Lumsden, A. D. Christianson, S. E. Nagler, S. Adiga, W. J. H. Borghols, K. Schmalzl, Z. Yamani, S. R. Bland, R. de Souza, U. Staub, W. Schweika, Y. Su, and M. Angst, "Competing ferri- and antiferromagnetic phases in geometrically frustrated $LuFe_2O_4$", Phys. Rev. Lett. **108**, 037206 (2012) (cited on pages 24, 83, 88, 108).

[124] Z. Islam, D. Capatina, J. P. C. Ruff, R. K. Das, E. Trakhtenberg, H. Nojiri, Y. Narumi, U. Welp, and P. C. Canfield, "A single-solenoid pulsed-magnet system for single-crystal scattering studies", Rev. Sci. Instrum. **83**, 035101 (2012) (cited on page 24).

[125] Z. Islam, H. Nojiri, J. P. C. Ruff, R. K. Das, D. Capatina, and J. C. Lang, "Precision X-ray diffraction studies in high pulsed magnetic fields at the advanced photon source", Synchrotron Radiat. News **25**, 5 (2012) (cited on page 24).

[126] D. Capatina, Z. Islam, E. Trakhtenberg, H. Nojiri, and Y. Narumi, "Mechanical design of a dual-cryostat instrument for a high-field pulsed magnet", Diamond Light Source Proceedings **1**, e42 (2011) (cited on page 24).

[127] H. Kawamura and M. Tanemura, "Chiral order in a two-dimensional XY spin glass", Physical Review B **36**, 7177 (1987) (cited on page 25).

[128] H. Kawamura, "The ordering of XY spin glasses", J. Phys.: Condens. Matter **23**, 164210 (2011) (cited on page 25).

[129] S. Blundell, "Magnetism in condensed mater", Oxford Master Series in Condensed Matter Physics (OUP Oxford, 2001) (cited on page 25).

[130] R. S. Solanki, S.-H. Hsieh, C. H. Du, G. Deng, C. W. Wang, J. S. Gardner, H. Tonomoto, T. Kimura, and W. F. Pong, "Correlations and dynamics of spins in an XY-like spin-glass $Ni_{0.4}Mn_{0.6}TiO_3$ single-crystal system", Phys. Rev. B **95**, 024425 (2017) (cited on page 25).

[131] C. Ederer and N. A. Spaldin, "Towards a microscopic theory of toroidal moments in bulk periodic crystals", Phys. Rev. B **76**, 214404 (2007) (cited on pages 25, 27, 28).

[132] G. Shirane, S. J. Pickart, and Y. Ishikawa, "Neutron diffraction study of antiferromagnetic $MnTiO_3$ and $NiTiO_3$", J. Phys. Soc. Jpn. **14**, 1352 (1959) (cited on pages 25, 26, 35).

[133] S. Chi, F. Ye, H. D. Zhou, E. S. Choi, J. Hwang, H. Cao, and J. A. Fernandez-Baca, "Magnetoelectric coupling tuned by competing anisotropies in $Mn_{1-x}Ni_xTiO_3$", Phys. Rev. B **90**, 144429 (2014) (cited on pages 25, 35).

[134] H. Kawano, H. Yoshizawa, A. Ito, and K. Motoya, "Two successive spin glass transitions in nondiluted Heisenberg-like spin glass $Ni_{0.42}Mn_{0.58}TiO_3$", J. Phys. Soc. Jpn. **62**, 2575 (1993) (cited on pages 25, 33).

[135] A. Ito, H. Kawano, H. Yoshizawa, and K. Motoya, "Magnetic properties and phase diagram of $Ni_xMn_{1-x}TiO_3$", J. Magn. Magn. Mater. **104-107, Part 3**, 1637 (1992) (cited on page 26).

[136] H. Yoshizawa, H. Kawano, H. Mori, S. Mitsuda, and A. Ito, "Phase diagram of a Heisenberg-like spin glass $Ni_xMn_{1-x}TiO_3$", Physica B **180-181, Part 1**, 94 (1992) (cited on page 26).

[137] B. B. Van Aken, J.-P. Rivera, H. Schmid, and M. Fiebig, "Observation of ferrotoroidic domains", Nature **449**, 702 (2007) (cited on page 27).

[138] R. P. Liferovich and R. H. Mitchell, "Rhombohedral ilmenite group nickel titanates with Zn, Mg, and Mn: synthesis and crystal structures", Phys. Chem. Miner. **32**, 442 (2005) (cited on pages 29, 30).

[139] J. Tholence, "On the frequency dependence of the transition temperature in spin glasses", Solid State Commun. **35**, 113 (1980) (cited on page 30).

[140] H. Vogel, "The temperature dependence law of the viscosity of fluids", Phys. Z. **22**, 645 (1921) (cited on page 30).

[141] G. S. Fulcher, "Analysis of recent measurements of the viscosity of glasses", J. Am. Ceram. Soc. **8**, 339 (1925) (cited on page 30).

[142] S. Shtrikman and E. Wohlfarth, "The theory of the Vogel-Fulcher law of spin glasses", Phys. Lett. A **85**, 467 (1981) (cited on page 30).

[143] K. Jonason, E. Vincent, J. Hammann, J. P. Bouchaud, and P. Nordblad, "Memory and chaos effects in spin glasses", Phys. Rev. Lett. **81**, 3243 (1998) (cited on page 31).

[144] V. M. Nield and D. A. Keen, "Diffuse neutron scattering from crystalline materials", Vol. 14, Oxford Series on Neutron Scattering in Condensed Matter (Oxford University Press, 2001) (cited on page 34).

[145] H. J. Silverstein, E. Skoropata, P. M. Sarte, C. Mauws, A. A. Aczel, E. S. Choi, J. van Lierop, C. R. Wiebe, and H. Zhou, "Incommensurate crystal supercell and polarization flop observed in the magnetoelectric ilmenite $MnTiO_3$", Phys. Rev. B **93**, 054416 (2016) (cited on page 34).

[146] J. Ko and C. T. Prewitt, "High-pressure phase transition in $MnTiO_3$ from the ilmenite to the $LiNbO_3$ structure", Phys Chem. Miner. **15**, 355 (1988) (cited on page 35).

[147] A. M. Arévalo-López and J. P. Attfield, "Weak ferromagnetism and domain effects in multiferroic $LiNbO_3$-type $MnTiO_3$-II", Phys. Rev. B **88**, 104416 (2013) (cited on page 35).

[148] C. J. Fennie, "Ferroelectrically induced weak ferromagnetism by design", Phys. Rev. Lett. **100**, 167203 (2008) (cited on page 35).

[149] X. Deng, W. Lu, H. Wang, H. Huang, and J. Dai, "Electronic, magnetic and dielectric properties of multiferroic $MnTiO_3$", J. Mater. Res. **27**, 1421 (2012) (cited on page 35).

[150] N. Mufti, G. R. Blake, M. Mostovoy, S. Riyadi, A. A. Nugroho, and T. T. M. Palstra, "Magnetoelectric coupling in $MnTiO_3$", Phys. Rev. B **83**, 104416 (2011) (cited on page 35).

[151] C. Xin, Y. Wang, Y. Sui, Y. Wang, X. Wang, K. Zhao, Z. Liu, B. Li, and X. Liu, "Electronic, magnetic and multiferroic properties of magnetoelectric $NiTiO_3$", J. Alloys Compd. **613**, 401 (2014) (cited on page 35).

[152] T. Acharya and R. N. P. Choudhary, "Structural, ferroelectric, and electrical properties of $NiTiO_3$ ceramic", J. Electron. Mater. **44**, 271 (2014) (cited on page 35).

[153] R. Singh, T. Ansari, R. Singh, and B. Wanklyn, "Electrical conduction in $NiTiO_3$ single crystals", Mater. Chem. Phys. **40**, 173 (1995) (cited on page 36).

[154] N. Kimizuka and T. Katsura, "Standard free energy of formation of $YFeO_3$, $Y_3Fe_5O_{12}$, and a new compound YFe_2O_4 in the Fe–Fe_2O_3–Y_2O_3 system at 1200 °C", J. Solid State Chem. **13**, 176 (1975) (cited on pages 37, 40, 43).

[155] K. Kitayama, M. Sakaguchi, Y. Takahara, H. Endo, and H. Ueki, "Phase equilibrium in the system Y-Fe-O at 1100 °C", J. Solid State Chem. **177**, 1933 (2004), (Fig 4.2 Reprinted with permission from Elsevier) (cited on pages 37, 39, 40).

[156] K. Jacob and G. Rajitha, "Nonstoichiometry, defects and thermodynamic properties of $YFeO_3$, YFe_2O_4 and $Y_3Fe_5O_{12}$", Solid State Ionics **224**, 32 (2012) (cited on pages 37, 40, 41).

[157] W. Piekarczyk, W. Wepper, and A. Rabenau, "Solid state electrochemical study of phase equilibria and thermodynamics of the ternary system Y-Fe-O at elevated temperatures", Z. Naturforsch. A **34**, 430 (1979) (cited on page 37).

[158] T. Sugihara, K. Siratori, I. Shindo, and T. Katsura, "Parasitic ferrimagnetism of YFe_2O_4", J. Phys. Soc. Jpn. **45**, 1191 (1978) (cited on pages 37, 42, 43, 83).

[159] N. Ikeda, R. Mori, S. Mori, and K. Kohn, "Structure transition and charge competition on YFe_2O_4", Ferroelectrics **286**, 175 (2003) (cited on pages 37–39, 75, 99).

[160] M. Inazumi, Y. Nakagawa, M. Tanaka, N. Kimizuka, and K. Siratori, "Magnetizations and Mössbauer spectra of YFe_2O_{4-x}", J. Phys. Soc. Jpn. **50**, 438 (1981) (cited on pages 38–43, 75, 99, 108).

[161] Y. Nakagawa, M. Inazumi, N. Kimizuka, and K. Siratori, "Low-temperature phase transitions and magnetic properties of YFe_2O_4", J. Phys. Soc. Jpn. **47**, 1369 (1979) (cited on pages 37, 40, 42, 75).

[162] Y. Matsui, "Extra electron reflections observed in YFe_2O_4, $YbFe_2O_2$, $Yb_2Fe_3O_7$ and $Yb_3Fe_4O_{10}$", J. Appl. Crystallogr. **13**, 395 (1980) (cited on pages 37, 39, 75).

[163] S. Mori, S. Shinohara, Y. Matsuo, Y. Horibe, K. Yoshii, and N. Ikeda, "Effect of oxygen vacancies on charge ordered structure in $YFe_2O_{4-\delta}$", Jpn. J. Appl. Phys. **47**, 7595 (2008) (cited on pages 37–39, 75).

[164] N. Ikeda, R. Mori, K. Kohn, M. Mizumaki, and T. Akao, "Dielectric and structure properties of charge competing system YFe_2O_4", Ferroelectrics **272**, 309 (2002) (cited on pages 37, 39, 75).

[165] N. Ikeda, S. Mori, and K. Kohn, "Charge ordering and dielectric dispersion in mixed valence oxides RFe_2O_4", Ferroelectrics **314**, 41 (2005) (cited on pages 37, 39, 75).

[166] Y. Horibe, K. Kishimoto, S. Mori, and N. Ikeda, "Dielectric anomaly and structural phase transitions in $YFe_2O_{4-\delta}$", Integr. Ferroelectr. **67**, 151 (2004) (cited on pages 37–39, 75).

[167] Y. Horibe, K. Kishimoto, S. Mori, and N. Ikeda, "Nano-sized domains related to dielectric anomaly in $YFe_2O_{4-\delta}$", J. Electron Microsc. **54**, i87 (2005) (cited on pages 37–39, 75).

[168] Y. Horibe, K. Yoshii, N. Ikeda, and S. Mori, "Oxygen-deficient effect on charge ordering in spin- and charge-frustrated ferrite $YFe_2O_{4-\delta}$", Phys. Rev. B **80**, 092104 (2009) (cited on pages 37–39, 75).

[169] Y. Horibe, N. Ikeda, K. Yoshii, and S. Mori, "Direct observation of low-temperature superstructure in spin- and charge-frustrated ferrite $YFe_2O_{4-\delta}$", Phys. Rev. B **82**, 184119 (2010) (cited on pages 37, 39, 75).

[170] J. Blasco, S. Lafuerza, J. García, G. Subías, V. Cuartero, J. L. García-Muñoz, C. Popescu, and I. Peral, "Characterization of competing distortions in YFe_2O_4", Phys. Rev. B **93**, 184110 (2016) (cited on pages 38, 73, 75, 76, 94, 99, 108).

[171] B. J. Campbell, H. T. Stokes, D. E. Tanner, and D. M. Hatch, "*ISODISPLACE*: a web-based tool for exploring structural distortions", J. Appl. Crystallogr. **39**, 607 (2006) (cited on pages 38, 51, 64, 67, 76, 78, 79, 88, 103).

[172] "ISOTROPY software suite iso.byu.edu" (cited on pages 38, 51, 63, 67, 76, 78).

[173] T. Sugihara, M. Abe, and T. Katsura, "Magnetic and Mössbauer studies of a new compound YFe_2O_4", J. Phys. Soc. Jpn. **40**, 1211 (1976) (cited on pages 38, 42, 99).

[174] M. Tanaka, M. Kato, N. Kimizuka, and K. Siratori, "Mössbauer study of stoichiometric YFe_2O_4", J. Phys. Soc. Jpn. **47**, 1737 (1979) (cited on pages 38, 44, 99, 108).

[175] M. Tanaka, K. Siratori, and N. Kimizuka, "Mössbauer study of RFe_2O_4", J. Phys. Soc. Jpn. **53**, 760 (1984) (cited on pages 38, 99).

[176] A. Narayanasamy, T. Nagarajan, P. Muthukumarasamy, and N. Kimizuka, "Mössbauer studies of a series of new compounds RFe_2O_4 (R = Y, Ho, Er, Tm, Yb)", Phys. Status Solidi A **66**, 377 (1981) (cited on page 38).

[177] M. Kishi, Y. Nakagawa, M. Tanaka, N. Kimizuka, and I. Shindo, "Low-temperature transitions of RFe_2O_4", J. Magn. Magn. Mater. **31-4**, 807 (1983) (cited on page 38).

[178] M. Tanaka, J. Akimitsu, Y. Inada, N. Kimizuka, I. Shindo, and K. Siratori, "Conductivity and specific heat anomalies at the low temperature transition in the stoichiometric YFe_2O_4", Solid State Commun. **44**, 687 (1982) (cited on pages 39, 44, 99).

[179] A. Enomura, S. Asai, Y. Ishiwata, T. Inabe, Y. Sakai, N. Tsuda, M. Tanaka, and K. Siratori, "Seebeck coefficient of YFe_2O_4", J. Phys. Soc. Jpn. **52**, 4286 (1983) (cited on pages 39, 99).

[180] Y. Sakai, K. Kaneda, N. Tsuda, M. Tanaka, and K. Siratori, "Seebeck coefficient of YFe_2O_4 at lower transition temperature", J. Phys. Soc. Jpn. **54**, 4089 (1985) (cited on page 39).

[181] Y. Sakai, K. Kaneda, N. Tsuda, and M. Tanaka, "Electrical resistivity of YFe_2O_4", J. Phys. Soc. Jpn. **55**, 3181 (1986) (cited on pages 39, 99).

[182] K. Siratori, N. Môri, H. Takahashi, G. Oomi, J. Iida, M. Tanaka, M. Kishi, Y. Nakagawa, and N. Kimizuka, "Effect of the pressure and the rare-earth substitution on the verwey transition of YFe_2O_4", J. Phys. Soc. Jpn. **59**, 631 (1990) (cited on page 39).

[183] T. Matsumoto, N. Mori, J. Iida, M. Tanaka, K. Siratori, F. Izumi, and H. Asano, "Crystal structures of the two dimensional antiferromagnets RFe_2O_4 (R = Y, Er) and their magnetic properties under pressure", Physica B **180-181, Part 2**, 603 (1992) (cited on pages 39, 41, 48, 49).

[184] J. Akimitsu, Y. Inada, K. Siratori, I. Shindo, and N. Kimizuka, "Two-dimensional spin ordering in YFe_2O_4", Solid State Commun. **32**, 1065 (1979) (cited on page 39).

[185] S. Funahashi, J. Akimitsu, K. Siratori, N. Kimizuka, M. Tanaka, and H. Fujishita, "Two-dimensional spin correlation in YFe_2O_4", J. Phys. Soc. Jpn. **53**, 2688 (1984) (cited on pages 39, 40).

[186] S. Funahashi, Y. Morii, and H. R. Child, "Two-dimensional neutron diffraction of YFe_2O_4 and $CoCr_2O_4$", J. Appl. Phys. **61**, 4114 (1987) (cited on page 39).

[187] S. Katano, T. Matsumoto, S. Funahashi, J. Iida, M. Tanaka, and J. Cable, "Crystal and magnetic structure of stoichiometric YFe_2O_4", Physica B **213-214**, 218 (1995) (cited on pages 40, 75).

[188] J. Bourgeois, M. Hervieu, M. Poienar, A. M. Abakumov, E. Elkaim, M. T. Sougrati, F. Porcher, F. Damay, J. Rouquette, G. Van Tendeloo, A. Maignan, J. Haines, and C. Martin, "Evidence of oxygen-dependent modulation in $LuFe_2O_4$", Phys. Rev. B **85**, 064102 (2012) (cited on page 41).

[189] T. Sekine and T. Katsura, "Phase equilibria in the system Fe–Fe_2O_3–Lu_2O_3 at 1200 °C", J. Solid State Chem. **17**, 49 (1976) (cited on page 41).

[190] H. J. Noh, H. Sung, J. Jeong, J. Jeong, S. B. Kim, J. Y. Kim, J. Y. Kim, and B. K. Cho, "Effect of structural distortion on ferrimagnetic order in $Lu_{1-x}L_xFe_2O_4$ (L=Y and Er; x=0.0, 0.1, and 0.5)", Phys. Rev. B **82**, 024423 (2010) (cited on pages 45–47, 92).

[191] D. H. Kim, J. Hwang, E. Lee, J. Kim, B. W. Lee, H.-K. Lee, J.-Y. Kim, S. W. Han, S. C. Hong, C.-J. Kang, B. I. Min, and J.-S. Kang, "Interplay between R 4f and Fe 3d states in charge-ordered RFe_2O_4 (R = Er, Tm, Lu)", Phys. Rev. B **87**, 184409 (2013) (cited on pages 46, 47).

[192] H. L. Williamson, (unpublished), PhD thesis (2017) (cited on page 46).

[193] S. Lafuerza, J. García, G. Subías, J. Blasco, J. Herrero-Martin, and S. Pascarelli, "Electronic states of RFe_2O_4 (R = Lu, Yb, Tm, Y) mixed-valence compounds determined by soft X-ray absorption spectroscopy and X-ray magnetic circular dichroism", Phys. Rev. B **90**, 245137 (2014) (cited on pages 46, 47, 92, 108).

[194] K. Kuepper, M. Raekers, C. Taubitz, M. Prinz, C. Derks, M. Neumann, A. V. Postnikov, F. M. F. de Groot, C. Piamonteze, D. Prabhakaran, and S. J. Blundell, "Charge order, enhanced orbital moment, and absence of magnetic frustration in layered multiferroic $LuFe_2O_4$", Phys. Rev. B **80**, 220409 (2009) (cited on pages 46, 47, 88, 92, 100).

[195] C. Derks, "Characterization of $RScO_3$, $LuFe_2O_4$ and M_72Fe_30 based molecules by x-ray spectroscopic techniques", PhD thesis (Universität Osnabrück, 2012) (cited on pages 46, 92).

[196] M. Raekers, "An x-ray spectroscopic study of novel materials for electronic applications", PhD thesis (Universität Osnabrück, 2009) (cited on pages 46, 92).

[197] C. Taubitz, "Investigation of the magnetic and electronic structure of Fe in molecules and chalcogenide systems", PhD thesis (Universität Osnabrück, 2010) (cited on pages 46, 92).

[198] K. T. Ko, H. J. Noh, J. Y. Kim, B. G. Park, J. H. Park, A. Tanaka, S. B. Kim, C. L. Zhang, and S. W. Cheong, "Electronic origin of giant magnetic anisotropy in multiferroic $LuFe_2O_4$", Phys. Rev. Lett. **103**, 207202 (2009) (cited on pages 46, 47, 83, 88, 92).

[199] J. Jeong, H.-J. Noh, and S. B. Kim, "Effects of structural distortion induced by Sc substitution in $LuFe_2O_4$", J. Korean Phys.Soc. **64**, 1701 (2014) (cited on page 47).

[200] L. Sohncke, "Entwicklung einer Theorie der Kristallstruktur" (Teubner Verlag, Leipzig, 1879) (cited on page 47).

[201] L. Sohncke, "Die unbegrenzten regelmäsigen Punktsysteme als Grundlage einer Theorie der Krystallstructur", Verhandlungen des Naturwissenschaftlichen Vereins zu Karlsruhe, **Heft 7** (1876) (cited on page 47).

[202] W. J. A. M. Peterse and J. H. Palm, "The anisotropic temperature factor of atoms in special positions", Acta Crystallogr. **20**, 147 (1966) (cited on page 48).

[203] W. F. Kuhs, "Atomic displacement parameters", in *International tables for crystallography*, Vol. D, edited by A. Authier (International Union of Crystallography (IUCr), 2013) Chap. 1.9, pp. 231–245 (cited on page 48).

[204] M. Isobe, N. Kimizuka, J. Iida, and S. Takekawa, "Structures of $LuFeCoO_4$ and $LuFe_2O_4$", Acta Crystallogr. **C46**, 1917 (1990) (cited on page 48).

[205] B. H. Toby, "R factors in Rietveld analysis: how good is good enough?", Powder Diffraction **21**, 67 (2006) (cited on page 48).

[206] R. H. Blessing, "Outlier treatment in data merging", J. Appl. Cryst. **30**, 421 (1997) (cited on page 55).

[207] P. Müller, "Practical suggestions for better crystal structures", Crystallogr. Rev. **15**, 57 (2009) (cited on page 60).

[208] R. D. Shannon, "Revised effective ionic radii and systematic studies of interatomic distances in halides and chalcogenides", Acta Cryst. A **32**, 751 (1976) (cited on page 62).

[209] S. Lafuerza, J. García, G. Subías, J. Blasco, and V. Cuartero, "Strong local lattice instability in hexagonal ferrites RFe_2O_4 (R = Lu, Y, Yb) revealed by X-ray absorption spectroscopy", English, Phys. Rev. B **89**, 045129 (2014) (cited on pages 62, 73).

[210] H. Seo, J. Merino, H. Yoshioka, and M. Ogata, "Theoretical aspects of charge ordering in molecular conductors", J. Phys. Soc. Jpn. **75**, 051009 (2006) (cited on page 63).

[211] J. Merino, H. Seo, and M. Ogata, "Quantum melting of charge order due to frustration in two-dimensional quarter-filled systems", Phys. Rev. B **71**, 125111 (2005) (cited on page 63).

[212] C. Hotta, N. Furukawa, A. Nakagawa, and K. Kubo, "Phase diagram of spinless fermions on an anisotropic triangular lattice at half-filling", J. Phys. Soc. Jpn. **75**, 123704 (2006) (cited on page 63).

[213] S. Nishimoto, M. Shingai, and Y. Ohta, "Coexistence of distinct charge fluctuations in θ-(BEDT-TTF)$_2$X", Phys. Rev. B **78**, 035113 (2008) (cited on page 63).

[214] M. Naka, A. Nagano, and S. Ishihara, "Magnetodielectric phenomena in a charge- and spin-frustrated system of layered iron oxide", Phys. Rev. B **77**, 224441 (2008) (cited on pages 63, 64, 102–104, 108).

[215] E. Kroumova, J. M. Perez-Mato, and M. I. Aroyo, "WYCKSPLIT: a computer program for determination of the relations of Wyckoff positions for a group-subgroup pair", J. Appl. Crystallogr. **31**, 646 (1998) (cited on page 64).

[216] K. Friese and A. Grzechnik, "Data reduction and analysis", at the workshop *Methods of high-pressure single-crystal X-ray diffraction*, a satellite workshop of the 26th European Crystallographic Meeting, Darmstadt, 2010 (cited on page 69).

[217] H. D. Flack, M. Sadki, A. L. Thompson, and D. J. Watkin, "Practical applications of averages and differences of friedel opposites", Acta Crystallogr. A **67**, 21 (2010) (cited on page 69).

[218] U. Shmueli, H. D. Flack, and J. C. H. Spence, "Methods of space-group determination", in *International tables for crystallography*, Vol. A (International Union of Crystallography, 2016), pp. 107–131 (cited on page 69).

[219] M. Vijayan and S. Ramaseshan, "Isomorphous replacement and anomalous scattering", in *International tables for crystallography*, Vol. B (International Union of Crystallography, 2010), pp. 282–296 (cited on page 69).

[220] S. Parsons, P. Pattison, and H. D. Flack, "Analysing Friedel averages and differences", Acta Crystallogr. A **68**, 736 (2012) (cited on page 69).

[221] R. E. Marsh, "Centrosymmetric or noncentrosymmetric?", Acta Crystallogr. B **42**, 193 (1986) (cited on page 69).

[222] V. Petříček, M. Dušek, and L. Palatinus, "Crystallographic computing system Jana2006: solution and refinement of twinned structures", Zeitschrift für Kristallographie - Crystalline Materials **231**, 583 (2016) (cited on pages 70, 87, 88).

[223] K. Momma and F. Izumi, "*VESTA3* for three-dimensional visualization of crystal, volumetric and morphology data", J. Appl. Crystallogr. **44**, 1272 (2011) (cited on page 73).

[224] T. Matsumoto, N. Môri, J. Iida, M. Tanaka, and K. Siratori, "Magnetic properties of the two dimensional antiferromagnets RFe_2O_4 (R=Y, Er) at high pressure", J. Phys. Soc. Jpn. **61**, 2916 (1992) (cited on page 75).

[225] Inorganic Crystal Structure Database - ICSD `https://icsd.fiz-karlsruhe.de` (cited on page 76).

[226] J. Iida, M. Tanaka., Y. Nakagawa, S. Funahashi, N. Kimizuka, and S. Takekawa, "Magnetization and spin correlation of 2-dimensional triangular antiferromagnet $LuFe_2O_4$", J. Phys. Soc. Jpn. **62**, 1723 (1993) (cited on pages 83, 100).

[227] N. Ikeda, T. Nagata, J. Kano, and S. Mori, "Present status of the experimental aspect of RFe_2O_4 study", J. Phys.: Condens. Matter **27**, 053201 (2015) (cited on page 83).

[228] F. Wang, J. Kim, Y.-J. Kim, and G. D. Gu, "Spin-glass behavior in $LuFe_2O_{4+\delta}$", Phys. Rev. B **80**, 024419 (2009) (cited on page 83).

[229] J. Iida, Y. Nakagawa, and N. Kimizuka, "Field-heating effect - anomalous thermomagnetization curves observed in hexagonal $LuFe_2O_4$", J. Phys. Soc. Jpn. **55**, 1434 (1986) (cited on page 83).

[230] W. Wu, V. Kiryukhin, H.-J. Noh, K.-T. Ko, J.-H. Park, W. Ratcliff, P. A. Sharma, N. Harrison, Y. J. Choi, Y. Horibe, S. Lee, S. Park, H. T. Yi, C. L. Zhang, and S.-W. Cheong, "Formation of pancakelike ising domains and giant magnetic coercivity in ferrimagnetic $LuFe_2O_4$", Phys. Rev. Lett. **101**, 137203 (2008) (cited on page 83).

[231] H. J. Xiang, E. J. Kan, S.-H. Wei, M.-H. Whangbo, and J. Yang, "Origin of the ising ferrimagnetism and spin-charge coupling in $LuFe_2O_4$", Phys. Rev. B **80**, 132408 (2009) (cited on pages 83, 92).

[232] S. Park, Y. Horibe, Y. J. Choi, C. L. Zhang, S.-W. Cheong, and W. Wu, "Pancakelike Ising domains and charge-ordered superlattice domains in $LuFe_2O_4$", Phys. Rev. B **79**, 180401 (2009) (cited on pages 83, 103, 104, 108).

[233] J. Pickworth Glusker and K. N. Trueblood, "Crystal structure analysis : a primer", 3rd ed., IUCr texts on crystallography 14 (Univ. Press, Oxford, 2010) (cited on page 84).

[234] T. Chatterji, "Neutron scattering from magnetic materials" (Elsevier Science, 2005) (cited on page 85).

[235] C. Kittel, "Introduction to solid state physics", 8th ed. (Wiley, New York, NY, 2005) (cited on page 85).

[236] S. C. Miller and W. F. Love, "Tables of irreducible representations of space groups and co-representations of magnetic space groups" (Boulder, Colo., Pruett Press, 1967) (cited on page 88).

[237] F. Mezzadri, S. Fabbrici, E. Montanari, L. Righi, G. Calestani, E. Gilioli, F. Bolzoni, and A. Migliori, "Structural properties and multiferroic phase diagram of $K_{0.6}Fe^{II}_{0.6}Fe^{III}_{0.4}F_3$ fluoride with TTB structure", Phys. Rev. B **78**, 064111 (2008) (cited on page 99).

[238] K. Yamauchi and S. Picozzi, "Interplay between charge order, ferroelectricity, and ferroelasticity: Tungsten bronze structures as a playground for multiferroicity", Phys. Rev. Lett. **105**, 107202 (2010) (cited on page 99).

[239] E. Wawrzyńska, R. Coldea, E. M. Wheeler, T. Sörgel, M. Jansen, R. M. Ibberson, P. G. Radaelli, and M. M. Koza, "Charge disproportionation and collinear magnetic order in the frustrated triangular antiferromagnet AgNiO2", Phys. Rev. B **77**, 094439 (2008) (cited on page 100).

[240] G. L. Pascut, R. Coldea, P. G. Radaelli, A. Bombardi, G. Beutier, I. I. Mazin, M. D. Johannes, and M. Jansen, "Direct observation of charge order in triangular metallic $AgNiO_2$by single-crystal resonant X-ray scattering", Phys. Rev. Lett. **106**, 157206 (2011) (cited on page 100).

[241] E. Wawrzyńska, R. Coldea, E. M. Wheeler, I. I. Mazin, M. D. Johannes, T. Sörgel, M. Jansen, R. M. Ibberson, and P. G. Radaelli, "Orbital degeneracy removed by charge order in triangular antiferromagnet $AgNiO_2$", Phys. Rev. Lett. **99**, 157204 (2007) (cited on page 100).

[242] A. B. Harris and T. Yildirim, "Charge and spin ordering in the mixed-valence compound $LuFe_2O_4$", Phys. Rev. B **81**, 134417 (2010) (cited on pages 100, 102).

[243] Y. Yamada, K. Kitsuda, S. Nohdo, and N. Ikeda, "Charge and spin ordering process in the mixed-valence system $LuFe_2O_4$: charge ordering", Phys. Rev. B **62**, 12167 (2000) (cited on pages 100, 102).

[244] M. Phan, N. Frey, M. Angst, J. de Groot, B. Sales, D. Mandrus, and H. Srikanth, "Complex magnetic phases in $LuFe_2O_4$", Solid State Commun. **150**, 341 (2010) (cited on page 100).

[245] Y. Sun, Y. Liu, F. Ye, S. Chi, Y. Ren, T. Zou, F. Wang, and L. Yan, "A magnetoelectric multiglass state in multiferroic $YbFe_2O_4$", J. Appl. Phys. **111**, 07D902 (2012) (cited on page 100).

[246] J. Bourgeois, G. André, S. Petit, J. Robert, M. Poienar, J. Rouquette, E. Elkaïm, M. Hervieu, A. Maignan, C. Martin, and F. Damay, "Evidence of magnetic phase separation in $LuFe_2O_4$", Phys. Rev. B **86**, 024413 (2012) (cited on page 100).

[247] M. Tanaka, H. Iwasaki, K. Siratori, and I. Shindo, "Mössbauer study on the magnetic structure of $YbFe_2O_4$: a two-dimensional antiferromagnet on a triangular lattice", J. Phys. Soc. Jpn. **58**, 1433 (1989) (cited on page 100).

[248] S. Nakamura, H. Kitô, and M. Tanaka, "An approach to specify the spin configuration in the RFe_2O_4 (R=Y, Ho, Er, Tm, Yb, and Lu) family: ^{57}Fe Mössbauer study on a single crystal $LuFe_2O_4$", J. Alloys Compd. **275-277**, 574 (1998) (cited on page 100).

[249] K. Kato, I. Kawada, N. Kimizuka, and T. Katsura, "Crystal-structure of $YbFe_2O_4$", Zeitschrift Fur Kristallographie **141**, 314 (1975) (cited on page 101).

[250] J. Wen, G. Xu, G. Gu, and S. M. Shapiro, "Magnetic-field control of charge structures in the magnetically disordered phase of multiferroic $LuFe_2O_4$", Phys. Rev. B **80**, 020403 (2009) (cited on pages 103, 104, 108).

[251] T. Watanabe and S. Ishihara, "Quantum dielectric fluctuation in electronic ferroelectricity studied by variational Monte-Carlo method", J. Phys. Soc. Jpn. **79**, 114714 (2010) (cited on page 104).

[252] T. Watanabe and S. Ishihara, "Quantum fluctuation and geometrical frustration effects on electric polarization", J. Phys. Soc. Jpn. **78**, 113702 (2009) (cited on page 104).

[253] M. Naka, H. Hashimoto, and S. Ishihara, "Dynamical properties of interacting charge system on frustrated lattices", Physica B: condensed Matter **460**, 68 (2015) (cited on page 104).

Aken along

A Appendix

A.1 Spin operator

This explanation is a reproduction of Appendix A in Chapter 7 of [50] and can be similarly found in [94].
The spin operator $\hat{\boldsymbol{\sigma}}$ is given as

$$\hat{\boldsymbol{\sigma}} = (\hat{\boldsymbol{\sigma}}_x, \hat{\boldsymbol{\sigma}}_y, \hat{\boldsymbol{\sigma}}_z) \tag{A.1}$$

where x, y, z are the Cartesian axes and with the Pauli spin matrices

$$\hat{\boldsymbol{\sigma}}_x = \begin{pmatrix} 0 & 1 \\ 1 & 0 \end{pmatrix} \qquad \hat{\boldsymbol{\sigma}}_y = \begin{pmatrix} 0 & -i \\ i & 0 \end{pmatrix} \qquad \hat{\boldsymbol{\sigma}}_z = \begin{pmatrix} 1 & 0 \\ 0 & -1 \end{pmatrix} \tag{A.2}$$

for a spin $\frac{1}{2}$ particle the spin up $|+\rangle$ and spin down $|-\rangle$ states can be represented as:

$$|+\rangle = \begin{pmatrix} 1 \\ 0 \end{pmatrix} \qquad |-\rangle = \begin{pmatrix} 0 \\ 1 \end{pmatrix} \tag{A.3}$$

leading to the following algebra:

$$\hat{\boldsymbol{\sigma}}_x |+\rangle = |-\rangle \qquad \hat{\boldsymbol{\sigma}}_x |-\rangle = |+\rangle \tag{A.4}$$

$$\hat{\boldsymbol{\sigma}}_y |+\rangle = i|-\rangle \qquad \hat{\boldsymbol{\sigma}}_y |-\rangle = -i|+\rangle \tag{A.5}$$

$$\hat{\boldsymbol{\sigma}}_z |+\rangle = |+\rangle \qquad \hat{\boldsymbol{\sigma}}_z |-\rangle = -|-\rangle \tag{A.6}$$

A.2 Transformation matrix to magnetic cell at 200 K

The transformation matrix from the hexagonal cell to the magnetic $P_s\bar{1}$ cell at 200 K received from representation analysis is given as:

$$\mathbf{B} = \begin{pmatrix} -1 & -2 & 0 \\ 2.33333 & 0.666667 & -0.333333 \\ 3.33333 & 0.666667 & 0.666667 \end{pmatrix} \text{ and } \mathbf{p} = \begin{pmatrix} 0 \\ 0 \\ 0 \end{pmatrix} \text{ or } \begin{pmatrix} \frac{\bar{1}}{3} \\ \frac{\bar{1}}{6} \\ \frac{1}{3} \end{pmatrix} \tag{A.7}$$

A.3 $YFe_2O_{4-\delta}$ atomic parameters with Fe^{2+} and Fe^{3+} form factors

Table A.1 gives the atomic positions and thermal displacement parameters at 160 K considering different form factors for Fe^{2+} and Fe^{3+} assigned after the results from the bond valence sum analysis. Table A.2 is a reproduction of Table 4.7 for direct comparison.

Site	x	y	z	U11	U22	U33	U12	U13	U23
Y1	.24416(8)	.36549(7)	.46537(7)	.0044(3)	.0056(3)	.0038(3)	-.0009(2)	.0003(2)	-.0006(2)
Y2	-.25810(8)	.12406(7)	.48338(7)	.0045(3)	.0072(3)	.0134(3)	-.0004(2)	.0016(2)	.0022(2)
Fe1	.34550(12)	.02464(11)	.13478(9)	.0051(4)	.0066(4)	.0050(4)	.000	.0009(3)	-.0009(3)
Fe2	-.11926(13)	.32993(13)	.14233(9)	.0085(4)	.0094(5)	.0044(4)	.0026(3)	.000	-.0008(3)
Fe3	.60415(14)	.50141(12)	.84774(9)	.0094(4)	.0111(5)	.0041(4)	-.0032(3)	.0009(3)	-.0006(3)
Fe4	.14568(12)	.21070(11)	.84667(9)	.0051(4)	.0071(4)	.0059(4)	-.0007(3)	.0012(3)	-.0006(3)
O1	.5830(6)	.3923(5)	.6171(4)	.0069(18)	.0061(18)	.0044(19)	. 000	-.0017(14)	.0023(15)
O2	.3900(6)	.0701(5)	.3706(4)	.0061(18)	.0049(18)	.0062(18)	.000	.000	.000
O3	.0969(6)	.1651(5)	.6171(4)	.0043(18)	.0061(18)	.0090(19)	.000	.0029(15)	.000
O4	.3419(6)	.0201(5)	.8837(5)	.0060(19)	.012(2)	.012(2)	.0031(16)	.000	.000
O5	-.1223(6)	.3570(5)	.3753(4)	.0052(18)	.0070(18)	.0055(18)	.000	.0020(14)	.000
O6	-.1419(6)	.1866(5)	.9077(4)	.0096(19)	.0102(19)	.0050(19)	-.0019(16)	.0021(15)	.000
O7	.2124(6)	.2721(5)	.1631(4)	.0069(18)	.0080(18)	.0074(19)	.000	.000	.000
O8	.2971(6)	.4531(5)	.9078(4)	.0081(19)	.0095(19)	.0034(19)	.000	.000	.0022(15)

Table A.1: Atomic positions and thermal displacement parameters at 160 K using different atomic form factors for Fe^{2+} and Fe^{3+}.

Site	x	y	z	U11	U22	U33	U12	U13	U23
Y1	.24420(8)	.36552(7)	.46534(7)	.0041(3)	.0051(3)	.0034(3)	-.0009(2)	.00023(20)	-.0007(2)
Y2	-.25807(8)	.12408(7)	.48336(7)	.0042(3)	.0064(3)	.0131(3)	-.0007(2)	.0016(2)	.0022(2)
Fe1	.34540(12)	.02463(11)	.13480(9)	.0049(4)	.0064(4)	.0043(4)	.000	.0007(3)	-.0012(3)
Fe2	-.11930(13)	.32994(13)	.14234(9)	.0081(4)	.0089(4)	.0037(4)	.0028(3)	.000	-.0011(3)
Fe3	.60414(14)	.50140(12)	.84774(9)	.0088(4)	.0105(4)	.0035(4)	-.0036(3)	.0008(3)	-.0007(3)
Fe4	.14569(12)	.21055(11)	.84667(9)	.0050(4)	.0066(4)	.0053(4)	-.0006(3)	.0011(3)	-.0008(3)
O1	.5829(6)	.3919(5)	.6171(4)	.0059(18)	.0051(18)	.0046(19)	.000	-.0015(14)	.0028(15)
O2	.3900(6)	.0696(5)	.3708(4)	.0063(18)	.0050(18)	.0046(17)	.000	.000	.000
O3	.0966(6)	.1647(5)	.6168(4)	.0045(18)	.0074(18)	.0069(19)	.000	.0021(14)	.000
O4	.3419(6)	.0197(5)	.8837(4)	.0049(18)	.012(2)	.013(2)	.0026(16)	.000	.0023(17)
O5	-.1225(6)	.3566(5)	.3753(4)	.0049(18)	.0053(18)	.0051(18)	.000	.0024(14)	.000
O6	-.1419(6)	.1861(5)	.9076(4)	.0081(19)	.0110(19)	.0047(19)	-.0020(16)	.0016(15)	.000
O7	.2125(6)	.2723(5)	.1628(4)	.0071(18)	.0065(18)	.0070(19)	.000	.000	.000
O8	.2970(6)	.4530(5)	.9080(4)	.0072(19)	.0094(19)	.0030(19)	-.0022(15)	.000	.0024(15)

Table A.2: Atomic positions and thermal displacement parameters of the refined 160 K structure using the average Fe form factor.

A.4 Refinement in P1 at 160 K

In the following the refined structure parameters are given for a refinement in the non-centrosymmetric spacegroup P1.

a (Å)	b (Å)	c (Å)	α (°)	β(°)	γ (°)
6.0928(4)	7.1500(5)	8.4611(6)	103.285(6)	96.372(6)	90.207(6)

Table A.3: Lattice parameters of the $P\bar{1}$ cell at 160 K

Parameter	this work
Spacegroup	P1
R_{int}/R_{σ} (%)	4.2/3.9
R_{obs}/wR_{obs} (%)	3.9/4.75
R_{all}/ wR_{all} (%)	4.71/5.28
GOF_{obs}/ GOF_{all}	1.83/1.87
unique Reflections obs / all	2235 / 1919
parameters	258
diff. peak and hole (e/Å ^{3})	1.89 / -1.22
ρ_{calc} (g/cm^3)	4.931

Twin	population (%)
1	0.79(2)
2	0.048(10)
3	0.064(12)
4	0.043(7)
5	0.005(8)
6	0.051(7)

Table A.4: Refinement parameters at 160 K in P1

Site	T (K)	BVS (2+)	BVS (3+)
$Fe1_1$	160	2.86(7)	3.06(7)
$Fe1_2$	160	2.64(6)	2.82(7)
$Fe2_1$	160	2.06(5)	2.20(6)
$Fe2_2$	160	2.02(5)	2.17(5)
$Fe3_1$	160	2.06(5)	2.20(6)
$Fe3_2$	160	2.03(5)	2.17(5)
$Fe4_1$	160	2.84(8)	3.04(8)
$Fe4_2$	160	2.61(7)	2.79(7)

Table A.5: Fe Bond valence sum calculations for the P1 structure, the standard deviation is propagated from the standard deviation of the mean of d_{0i} as given in Table 2.1 and from the uncertainties of the bond lengths.

Site	x	y	z	U11	U22	U33	U12	U13	U23
$Y1_1$	0.2444(4)	0.3662(4)	0.4679(4)	0.0052(15)	0.0079(16)	0.015(2)	-0.0011(12)	0.0034(13)	0.0038(15)
$Y1_2$	-0.2443(4)	-0.3656(3)	-0.4656(3)	0.0046(14)	0.0023(16)	0.0038(15)	0.0005(12)	0.0001(11)	-0.0009(13)
$Y2_1$	-0.2576(4)	0.1237(4)	0.4829(4)	0.0057(16)	0.0061(16)	0.0147(17)	-0.0003(12)	0.0025(12)	0.0031(14)
$Y2_2$	0.2577(5)	-0.1247(4)	-0.4854(4)	0.0046(14)	0.0052(15)	0.0184(16)	0.0000(11)	0.0034(11)	0.0030(13)
$Fe1_1$	0.3436(7)	0.0238(6)	0.1340(5)	0.010(2)	0.008(3)	0.004(2)	0.0037(18)	-0.0009(15)	0.0005(17)
$Fe1_2$	-0.3467(6)	-0.0258(6)	-0.1367(5)	0.003(2)	0.006(3)	0.003(2)	-0.0047(17)	0.0014(14)	-0.0015(18)
$Fe2_1$	-0.1202(7)	0.3295(7)	0.1428(6)	0.013(2)	0.007(2)	0.012(2)	0.0010(18)	0.0008(17)	0.000(2)
$Fe2_2$	0.1214(7)	-0.3260(7)	-0.1421(5)	0.011(2)	0.022(3)	-0.002(2)	0.0125(19)	0.0004(15)	0.0004(18)
$Fe3_1$	0.6073(8)	0.5001(7)	0.8485(6)	0.018(3)	0.018(3)	0.000(2)	-0.008(2)	0.0030(18)	-0.004(2)
$Fe3_2$	-0.6053(7)	-0.5004(7)	-0.8477(5)	0.011(2)	0.009(2)	0.007(2)	-0.0045(19)	0.0008(16)	0.0013(17)
$Fe4_1$	0.1451(7)	0.2111(6)	0.8465(5)	0.014(2)	0.013(3)	-0.0006(18)	-0.0050(19)	0.0018(15)	0.0006(17)
$Fe4_2$	-0.1472(7)	-0.2109(6)	-0.8476(5)	0.0022(19)	0.001(3)	0.011(2)	0.0035(17)	0.0010(15)	-0.0007(18)
$O1_1$	0.589(3)	0.395(3)	0.621(2)	0.000(7)	0.003(9)	0.011(9)	-0.003(6)	0.012(6)	0.003(7)
$O1_2$	-0.580(3)	-0.390(3)	-0.614(2)	0.009(8)	0.008(10)	0.006(10)	0.006(7)	-0.014(6)	0.008(8)
$O2_1$	0.389(3)	0.073(3)	0.369(2)	0.000(8)	0.001(8)	0.022(9)	0.009(6)	-0.003(6)	0.009(7)
$O2_2$	-0.393(3)	-0.071(3)	-0.3724(19)	0.006(9)	0.017(11)	-0.012(6)	-0.006(8)	0.000(5)	-0.004(6)
$O3_1$	0.098(3)	0.156(3)	0.620(2)	-0.003(8)	0.016(10)	0.009(10)	0.010(7)	0.008(6)	0.005(7)
$O3_2$	-0.094(3)	-0.170(3)	-0.615(2)	0.006(8)	-0.006(7)	0.007(9)	-0.006(6)	-0.004(6)	0.004(6)
$O4_1$	0.334(4)	0.018(4)	0.888(3)	0.027(12)	0.045(15)	0.032(14)	0.029(11)	0.006(10)	0.009(11)
$O4_2$	-0.344(3)	-0.017(3)	-0.879(2)	-0.001(8)	0.003(8)	0.001(8)	-0.005(6)	-0.001(6)	0.002(6)
$O5_1$	-0.118(3)	0.357(3)	0.380(2)	-0.001(8)	-0.003(9)	0.022(10)	0.003(6)	0.009(6)	0.000(7)
$O5_2$	0.125(3)	-0.355(3)	-0.369(2)	0.014(9)	0.011(10)	-0.007(8)	-0.009(7)	-0.003(6)	0.000(7)
$O6_1$	-0.140(3)	0.187(3)	0.910(2)	-0.005(8)	0.032(12)	0.012(11)	-0.014(8)	-0.008(7)	0.005(9)
$O6_2$	0.146(3)	-0.185(3)	-0.905(2)	0.038(12)	-0.002(9)	-0.001(9)	0.009(8)	0.012(8)	-0.004(7)
$O7_1$	0.212(3)	0.275(2)	0.159(2)	0.007(10)	-0.004(8)	0.023(10)	-0.009(7)	0.001(7)	-0.019(7)
$O7_2$	-0.214(3)	-0.270(3)	-0.163(2)	0.007(10)	0.026(12)	0.016(10)	0.009(8)	0.006(7)	0.021(9)
$O8_1$	0.298(3)	0.449(3)	0.908(2)	0.008(9)	0.007(10)	0.000(9)	-0.007(7)	0.005(7)	-0.003(7)
$O8_2$	-0.295(3)	-0.458(3)	-0.907(2)	0.021(10)	0.011(10)	0.007(9)	0.009(8)	0.002(7)	0.007(7)

Table A.6: Atomic positions and thermal displacement parameters of the refined 160 K structure refined in P1.

A.5 Refinement in P1 at 200 K

In the following the refined structure parameters are given for a refinement in the non-centrosymmetric spacegroup P1.

a (Å)	b (Å)	c (Å)	α (°)	β(°)	γ (°)
6.0814(3)	9.8419(4)	11.0698(6)	105.407(4)	100.456(4)	95.814(4)

Table A.7: Lattice parameters of the $P\bar{1}$ cell at 200 K

Parameter	this work
Spacegroup	P1
R_{int}/R_{σ} (%)	12.1/15.3
R_{obs}/wR_{obs} (%)	5.6/9.4
R_{all}/ wR_{all} (%)	24.2/15.9
GOF_{obs}/ GOF_{all}	1.29/1.15
unique Reflections obs / all	35244 / 10038
parameters	456
diff. peak and hole (e/Å ^{3})	14 / -17
ρ_{calc} (g/cm^3)	4.9584

Twin	population (%)
1	0.280(10)
2	0
3	0.224(6)
4	0.275(5)
5	0.025(5)
6	0.195(5)

Table A.8: Refinement parameters at 200 K in P1, The large peaks which are still present are very close to the origin and are an indication for a problem with the split Y4 position and the assumption of the same ADP for both $Y4_1$ and $Y4_2$. The next largest peak is much smaller.

Site	T (K)	BVS (2+)	BVS (3+)	BVS (2.5+)
$Fe1_1$	200	2.64(5)	2.83(5)	2.74(5)
$Fe1_2$	200	2.69(5)	2.88(6)	2.79(5)
$Fe2_1$	200	2.57(5)	2.75(5)	2.66(5)
$Fe2_2$	200	2.45(5)	2.62(6)	2.54(5)
$Fe3_1$	200	2.71(5)	2.89(6)	2.80(5)
$Fe3_2$	200	2.61(5)	2.79(5)	2.70(5)
$Fe4_1$	200	2.33(5)	2.49(5)	2.41(5)
$Fe4_2$	200	2.47(5)	2.64(5)	2.56(5)
$Fe5_1$	200	2.04(4)	2.18(4)	2.11(4)
$Fe5_2$	200	1.96(4)	2.10(4)	2.03(4)
$Fe6_1$	200	1.96(5)	2.10(5)	2.03(5)
$Fe6_2$	200	1.93(4)	2.06(4)	2.05(4)
$Fe7_1$	200	1.85(4)	1.98(4)	1.915(4)
$Fe7_2$	200	1.95(4)	2.08(4)	2.02(4)

Table A.9: Bond valence sum of the Fe-sites at 200, K for the P1 structure

Site	x	y	z	U11	U22	U33	U12	U13	U23
$Y1_2$	-0.7205(7)	-0.4292(7)	-0.4272(6)	0.0037(6)	0.0252(11)	0.0077(6)	0.0015(6)	0.0005(4)	-0.0058(6)
$Y2_1$	0.1386(7)	0.3016(7)	0.2718(6)	0.0056(5)	0.0073(6)	0.0084(6)	-0.0002(5)	0.0016(5)	0.0006(5)
$Y2_2$	-0.1393(7)	-0.2970(7)	-0.2748(6)	0.0032(5)	0.0111(7)	0.0091(7)	-0.0005(5)	0.0022(5)	-0.0012(6)
$Y3_1$	0.5679(7)	0.1210(6)	0.1583(6)	0.0055(5)	0.0061(6)	0.0069(6)	0.0016(4)	0.0017(4)	0.0034(5)
$Y3_2$	-0.5714(7)	-0.1216(7)	-0.1581(6)	0.0033(5)	0.0077(7)	0.0066(6)	-0.0007(4)	0.0010(4)	0.0015(5)
$Y4_1$	-0.0027(8)	0.0205(8)	-0.0135(7)	0.0047(10)	0.0134(16)	0.0112(14)	0.0044(10)	0.0036(9)	0.0036(11)
$Y4_2$	0.0016(8)	-0.0242(7)	0.0164(6)	0.0030(9)	0.0072(12)	0.0070(11)	-0.0021(8)	-0.0010(8)	-0.0029(10)
$Fe1_1$	0.6760(8)	-0.2088(7)	0.1430(6)	0.0059(7)	0.0076(10)	0.0097(9)	0.0025(7)	-0.0003(7)	0.0002(8)
$Fe1_2$	-0.6752(8)	0.2084(7)	-0.1421(6)	0.0155(10)	0.0110(11)	0.0070(9)	0.0038(8)	-0.0008(8)	0.0018(8)
$Fe2_1$	0.1150(7)	0.6558(7)	0.0082(6)	0.0036(7)	0.0190(13)	0.0037(7)	-0.0012(7)	0.0010(6)	-0.0053(7)
$Fe2_2$	-0.1185(8)	-0.6533(7)	-0.0088(6)	0.0119(10)	0.0248(15)	0.0144(11)	0.0019(9)	0.0039(8)	0.0090(10)
$Fe3_1$	0.3971(8)	0.2329(7)	0.5824(6)	0.0083(8)	0.0118(11)	0.0123(10)	-0.0019(8)	-0.0018(7)	0.0041(9)
$Fe3_2$	-0.4000(8)	-0.2344(7)	-0.5860(6)	0.0093(8)	0.0059(9)	0.0066(8)	0.0000(7)	0.0029(6)	-0.0014(7)
$Fe4_1$	0.9669(8)	0.3632(7)	0.7315(6)	0.0117(9)	0.0113(12)	0.0132(10)	0.0014(8)	0.0034(8)	0.0044(9)
$Fe4_2$	-0.9658(8)	-0.3622(7)	-0.7299(6)	0.0047(7)	0.0069(10)	0.0106(9)	0.0005(6)	-0.0005(6)	-0.0031(8)
$Fe5_1$	0.8486(8)	0.0610(7)	0.4137(6)	0.0124(8)	0.0117(10)	0.0112(9)	-0.0067(7)	-0.0063(6)	0.0066(8)
$Fe5_2$	-0.8386(9)	-0.0642(7)	-0.4187(6)	0.0423(16)	0.0184(14)	0.0227(14)	-0.0176(11)	-0.0184(11)	0.0180(12)
$Fe6_1$	0.2691(9)	-0.0472(7)	0.3110(7)	0.0375(17)	0.0167(14)	0.045(2)	0.0188(12)	0.0377(16)	0.0194(14)
$Fe6_2$	-0.2635(9)	0.0503(7)	-0.3121(7)	0.048(2)	0.0196(15)	0.043(2)	0.0190(14)	0.0372(18)	0.0240(15)
$Fe7_1$	0.4744(8)	0.4879(7)	0.1357(6)	0.0241(12)	0.0114(10)	0.0141(10)	-0.0031(8)	-0.0047(8)	0.0100(9)
$Fe7_2$	-0.4668(8)	-0.4828(7)	-0.1310(6)	0.0317(14)	0.0123(11)	0.0155(10)	0.0108(10)	0.0155(10)	0.0085(9)

Table A.10: Atomic positions and thermal displacement parameters of the refined 200 K structure refined in P1.

Site	x	y	z	U11	U22	U33	U12	U13	U23
$O1_1$	0.4883(19)	0.3483(14)	0.2300(13)	0.004(3)	0.011(4)	0.019(5)	0.005(3)	0.004(3)	0.011(4)
$O1_2$	-0.4778(18)	-0.3507(13)	-0.2308(11)	0.007(3)	0.005(4)	0.005(3)	-0.001(2)	0.002(2)	-0.001(3)
$O2_1$	0.8368(18)	0.2200(14)	0.3435(13)	0.004(3)	0.008(4)	0.014(4)	0.003(3)	0.005(3)	0.002(3)
$O2_2$	-0.8322(19)	-0.2205(14)	-0.3473(12)	0.009(3)	0.009(4)	0.006(4)	-0.002(3)	-0.002(3)	0.004(3)
$O3_1$	-0.127(2)	0.2079(16)	0.0835(13)	0.013(4)	0.022(5)	0.016(4)	-0.001(4)	0.003(3)	0.015(4)
$O3_2$	0.1226(18)	-0.2067(14)	-0.0901(11)	0.005(3)	0.012(4)	0.001(3)	-0.007(3)	-0.001(2)	-0.005(2)
$O4_1$	0.225(2)	0.0753(16)	0.2030(15)	0.010(4)	0.012(5)	0.026(6)	0.002(3)	0.011(4)	0.000(4)
$O4_2$	-0.220(2)	-0.0756(14)	-0.2012(13)	0.008(3)	0.006(4)	0.017(5)	-0.002(3)	0.007(3)	0.001(4)
$O5_1$	0.6645(19)	-0.0856(13)	0.0360(11)	0.007(3)	0.005(3)	0.007(3)	0.001(3)	-0.006(2)	-0.009(2)
$O5_2$	-0.665(2)	0.0810(14)	-0.0354(12)	0.019(4)	0.014(4)	0.008(3)	0.005(3)	-0.001(3)	0.010(3)
$O6_1$	0.382(2)	0.3539(15)	0.4766(13)	0.008(3)	0.013(4)	0.013(4)	-0.006(3)	-0.002(3)	0.004(4)
$O6_2$	-0.3848(18)	-0.3588(14)	-0.4778(11)	0.008(3)	0.013(4)	0.007(4)	0.009(3)	0.003(3)	0.007(3)
$O7_1$	0.4336(17)	0.6360(13)	0.0358(10)	0.005(3)	0.012(4)	0.003(3)	0.001(3)	-0.001(2)	0.003(3)
$O7_2$	-0.444(2)	-0.6390(14)	-0.0407(13)	0.022(5)	0.005(4)	0.020(5)	-0.004(3)	0.005(4)	0.006(4)
$O8_1$	0.900(2)	0.5135(16)	0.8791(18)	0.014(5)	0.006(4)	0.040(8)	0.001(3)	0.007(5)	-0.003(5)
$O8_2$	-0.899(3)	-0.5081(18)	-0.8728(18)	0.014(5)	0.019(6)	0.039(8)	-0.004(4)	0.007(5)	0.006(6)
$O9_1$	0.012(2)	0.2329(17)	0.8567(17)	0.018(5)	0.018(6)	0.040(8)	-0.003(4)	0.016(5)	0.014(6)
$O9_2$	-0.013(2)	-0.2360(15)	-0.8587(15)	0.021(5)	0.012(5)	0.028(6)	0.008(4)	0.022(5)	0.005(4)
$O10_1$	0.295(2)	0.3424(16)	0.7258(14)	0.016(4)	0.013(5)	0.013(5)	-0.003(4)	0.003(4)	0.005(4)
$O10_2$	-0.288(2)	-0.3395(15)	-0.7270(12)	0.009(3)	0.011(5)	0.009(4)	0.001(3)	0.002(3)	0.003(3)
$O11_1$	0.594(2)	-0.0635(13)	0.2749(12)	0.012(4)	0.003(3)	0.008(3)	-0.001(3)	-0.002(3)	-0.005(3)
$O11_2$	-0.591(2)	0.0685(16)	-0.2744(13)	0.013(4)	0.024(6)	0.013(4)	0.003(4)	0.002(3)	0.008(4)
$O12_1$	0.960(2)	0.4921(15)	0.6243(13)	0.014(4)	0.013(5)	0.016(4)	0.006(3)	0.007(3)	0.010(4)
$O12_2$	-0.9562(19)	-0.4915(14)	-0.6196(12)	0.008(4)	0.006(4)	0.009(3)	-0.003(3)	-0.002(3)	0.003(3)
$O13_1$	0.1911(19)	0.0692(14)	0.4743(12)	0.014(4)	0.006(4)	0.008(4)	-0.002(3)	0.000(3)	0.003(3)
$O13_2$	-0.1963(19)	-0.0702(14)	-0.4779(12)	0.010(4)	0.008(4)	0.009(4)	-0.002(3)	-0.006(3)	0.003(3)
$O14_1$	0.709(2)	0.2215(15)	0.6208(14)	0.013(4)	0.008(5)	0.026(6)	-0.004(3)	-0.006(4)	0.007(4)
$O14_2$	-0.713(2)	-0.2226(16)	-0.6206(13)	0.015(5)	0.016(5)	0.011(4)	0.000(4)	-0.004(3)	0.008(4)

Table A.11: Atomic positions and thermal displacement parameters of the refined 200 K structure refined in P1.

A.6 Neutron diffraction 200 K

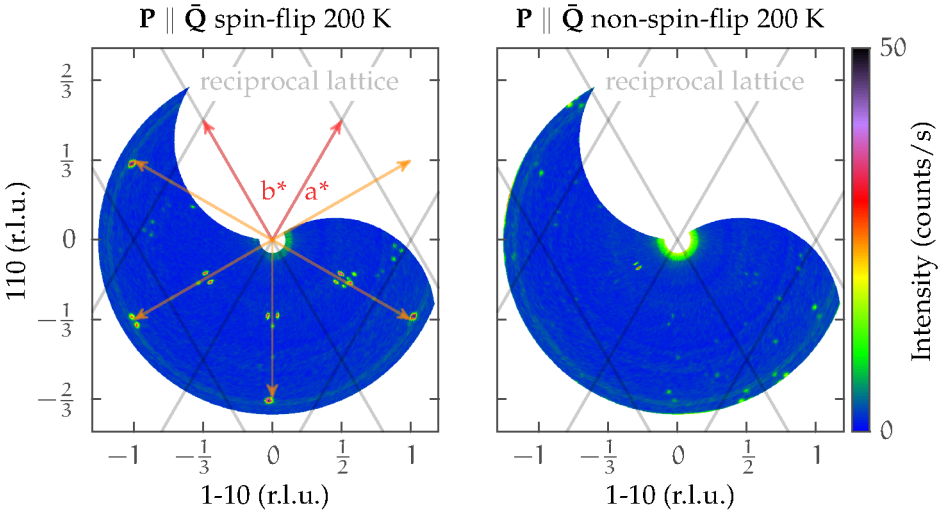

Figure A.1: Reciprocal hk0-plane of $YFe_2O_{4-\delta}$ with neutron polarization **P** parallel the average scattering vector $\bar{\mathbf{Q}}$ in spin-flip (a) and non-spin-flip channel (b). The gray lines correspond to the R$\bar{3}$m reciprocal lattice and the arrows to the $\left[\frac{1}{3}\frac{1}{3}0\right]$ direction and symmetry equivalent.

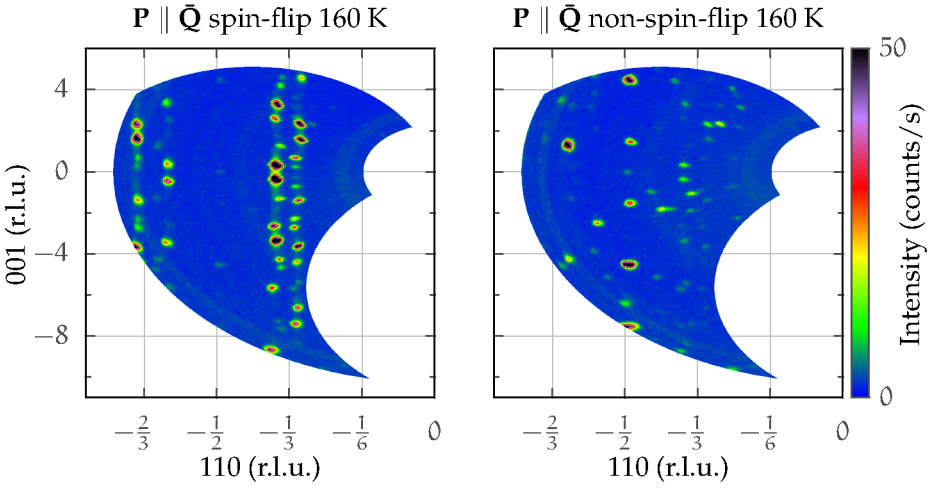

Figure A.2: Reciprocal hhl-plane of $YFe_2O_{4-\delta}$ with neutron polarization **P** parallel the average scattering vector $\bar{\mathbf{Q}}$ in spin-flip (a) and non-spin-flip channel (b). Reproduced from [20].

A.7 Neutron diffraction 160 K

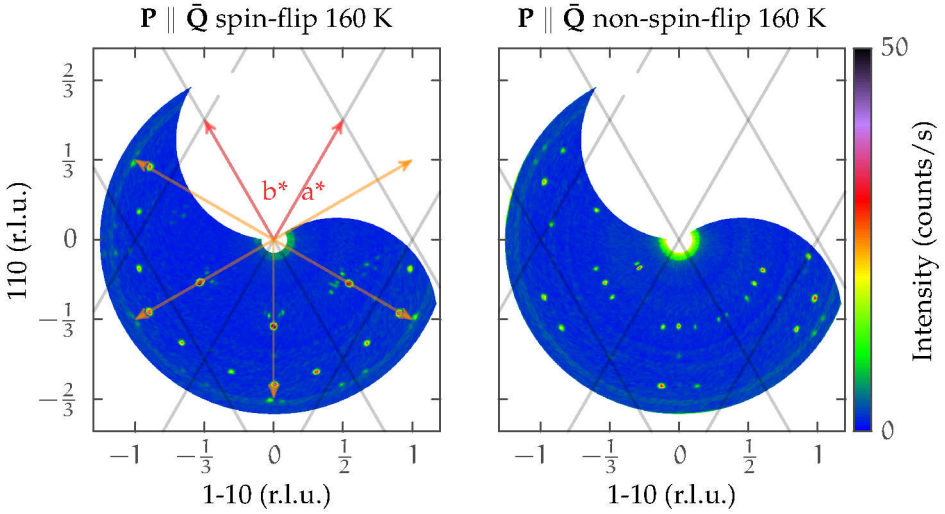

Figure A.3: Reciprocal hk0-plane of $YFe_2O_{4-\delta}$ with neutron polarization **P** parallel the average scattering vector $\bar{\mathbf{Q}}$ in spin-flip (a) and non-spin-flip channel (b). The gray lines correspond to the R$\bar{3}$m reciprocal lattice and the arrows to the $[\frac{1}{3}\frac{1}{3}0]$ direction and symmetry equivalent.

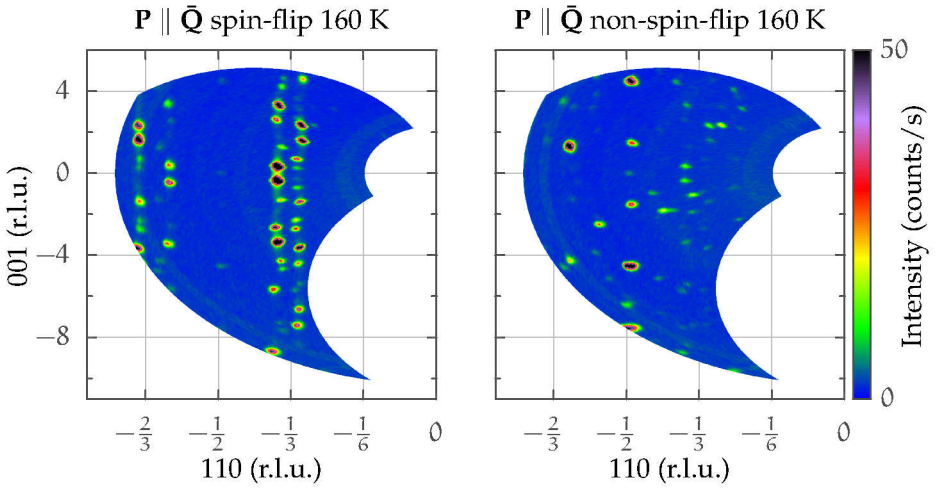

Figure A.4: Reciprocal hhl-plane of $YFe_2O_{4-\delta}$ with neutron polarization **P** parallel the average scattering vector $\bar{\mathbf{Q}}$ in spin-flip (a) and non-spin-flip channel (b). Reproduced from [20].

Acknowledgments

I would like to thank the whole **JCNS-2 / PGI-4** institute for a pleasant working atmosphere and the amazing support. Additionally I would like to thank the following people in particular:

Prof. Dr. Manuel Angst for the well mentoring during this research and for giving me the freedom to find my own solutions, for fruitful discussions, encouragement and useful critiques during the whole thesis.
Prof. Dr. Uwe Klemradt for his agreement to be the second reviewer of this thesis.
Prof. Dr. Thomas Brückel for the opportunity to perform this research in his wonderful institute.
Hailey Williamson, Dr. Pankaj Thakuria, Sabreen Hammouda, Georgi Khazaradze, Dr. Joost de Groot, Dr. Shilpa Adiga for assistance during beamtimes. I really enjoyed being in a working group with you.
Markus Waschk for his help during the 4-ID-C beamtime and common lunches.
Dr. Karen Friese for her help with the structure solution.
Dr. Zahirul Islam for the introduction to time resolved diffraction and the assistance during the 6-ID-B beamtime at the APS.
Dr. Yixi Su and Dr. Kirill Nemkowski for their help, discussions and ideas during the DNS exper- iment at FRM II.
Dr. Richard Rosenberg, Dr. David Keavney and Dr. John Freeland for the assistance during both 4-ID-C beamtime at the APS.
Dr. Bachir Ouladdiaf for the assistance during the D10 beamtime at ILL.
Dr Jürg Schefer for the assistance during the TRICS beamtime at SINQ.
Dr. Douglas Robinson for the assistance during the 6-ID-D beamtime at the APS.
Dr. Jörg Strempfer, Dr. Dinesh Kumar Shukla, Dr. Sonia Francoual for their help during the experiment at the P09 PETRA-III beamline at DESY.
Jörg Perßon for introduction to crystal growth and Laue Diffraction
Dr. Vaclav Petricek for his help with Jana2006.
Berthold Schmitz, Frank Gossen and Micha Hölzle for technical support whenever there was a need.
Barbara Daegener for any help with the administration and deadline reminders.
Dr. Susanne Mayer for the on-site crystal alignment for the DNS experiments.
Dr. Arthur Glavic for his program to plot and analyze DNS Data.
Support from the initiative and networking fund of Helmholtz Association by funding the Helmholtz University Young Investigator Group "Complex Ordering Phenomena in Multifunctional Oxides" is gratefully acknowledged. This research used resources of the Advanced Photon Source, a U.S. Department of Energy (DOE) Office of Science User Facility operated for the DOE Office of Science by Argonne National Laboratory under Contract No. DE-AC02-06CH11357.

This work is based on experiments performed at the Swiss spallation neutron source SINQ, Paul Scherrer Institute, Villigen, Switzerland.

This work is based upon experiments performed at the DNS instrument operated by JCNS at the Heinz Maier-Leibnitz Zentrum (MLZ), Garching, Germany.

And finally I would like to thank **my family** for the support and love they gave to me.